Nanoporous Silica Nanoparticles and Bone Morphogenetic Protein 2 for Bone Regeneration

Von der Naturwissenschaftlichen Fakultät der

Gottfried Wilhelm Leibniz Universität Hannover

zur Erlangung des Grades

Doktorin der Naturwissenschaften

(Dr. rer. nat)

genehmigte Dissertation

von

Alexandra Satalov, M. Sc.

2017

Referent: Prof. Dr. Peter Behrens

Korreferentin: Prof. Dr. Andrea Hoffmann

Tag der Promotion: 27.11.2017

Kurzzusammenfassung

Verletzungen des Bewegungsapparates, bestehend aus Knochen, Muskeln, Knorpel, Sehnen, Bändern, Gelenken und dem Bindegewebe, sind weltweit unter den häufigsten Ursachen für chronische Schmerzen und körperliche Funktionseinschränkungen. Klassische Therapiemethoden versagen oft bei der Wiederherstellung der Funktionalität des betroffenen Gewebes. Das Ziel des Tissue Engineerings ist es, die Chancen einer erfolgreichen Heilung und Regeneration der verletzten Gewebe und Gewebeübergänge zu verbessern. Die Freisetzung von Wachstumsfaktoren aus einem Scaffold (Gerüst für das Wachstum von Gewebe) ist dabei einer der vielversprechenden Ansätze.

In der vorliegenden Arbeit wurden komplexe Systeme auf der Basis von nanoporösen Silica-Nanopartikel (NPSNPs) zur kontrollierten Beladung und Freisetzung des Wachstumsfaktors bone morphogenetic protein 2 (BMP-2) entwickelt, die im Bereich des Tissue Engineerings und der Regeneration vom Knochengewebe eingesetzt werden sollen. Sphärische NPSNPs wurden mit Hilfe des Tensid-gesteuerten Sol-Gel-Verfahrens hergestellt. Die Oberfläche der NPSNPs wurde nachträglich mittels post-synthetischer Reaktionen mit unterschiedlichen organischen Silankopplungsreagenzien verändert, um die Beladungsmenge und die Freisetzungskinetik von BMP-2 gezielt zu steuern.

Vor der BMP-2-Beladung wurde festgestellt, dass auf der Oberfläche von aminopropylsilyl-modifizierten NPSNPs hydrolytisch stabile Spezies vorlagen, die einen Verschluss der Poren verursachten. Dieser Porenverschluss konnte in Folge weiterer postsynthetischer Reaktionen wieder rückgängig gemacht werden. Diese Ergebnisse sind entscheidend für die Weiterentwicklung der NPSNP-basierten Freisetzungs-systeme.

Nach der Beladung von BMP-2 auf die Oberfläche von unterschiedlich modifizierten NPSNPs zeigte sich, dass die Anwesenheit von hydrophoben Funktionalitäten, ungeachtet der Ladung, ein entscheidendes Kriterium für eine erfolgreiche BMP-2-Beladung darstellte. Abhängig von der Oberflächenmodifizierung der NPSNPs zeigten die BMP-2-beladenen NPSNPs drei verschiedene Arten der Freisetzung: eine anfänglich schnelle (burst), eine konstante (sustained) oder eine langsame (retention) BMP-2-Freisetzung. Obwohl die Zusammenhänge zwischen der Art der funktionellen Gruppe und der Freisetzungskinetik nicht vollständig geklärt werden konnten und weiterer Untersuchungen bedürfen, bieten diese Ergebnisse einen ersten Ansatz für die Entwicklung von NPSNP-basierten Systemen für eine gezielte Freisetzung von Wachstumsfaktoren für die Anwendung im Bereich des Tissue Engineerings.

Erste Zellkulturuntersuchungen von BMP-2-beladenen NPSNPs (verglichen mit ungebundenen BMP-2) zeigten eine gewisse Tendenz, die Expression von „frühen" Genen, die auf eine anfängliche osteogene Differenzierung von Knochenmark-stammzellen hinweisen, auszulösen. Die Untersuchungen der Zelltoxizität von verschiedenen NPSNPs gegenüber Myoblasten und Knochenmarkstammzellen zeigten, dass die nicht modifizierten NPSNPs bei keiner der getesteten Konzentrationen und zu keinem Zeitpunkt zelltoxisch waren. Die unterschiedlich modifizierten NPSNPs hatten bis zur einen Konzentration von 10 µg ml^{-1} keinen zelltoxischen Effekt auf beide Zelllinien innerhalb von 7 Tagen.

In Hinblick auf den gewünschten Einsatz zur Regeneration des Knochengewebes in großen Knochendefekten und in Knochen-Sehnen-Übergängen beschäftigte sich ein weiterer Teil der Arbeit mit der Herstellung von biofunktionalisierten Implantaten mit einer gezielten Freisetzung von kleinen Dosen von BMP-2 (Nanogramm) unter Zuhilfenahme von unterschiedlich modifizierten, BMP-2-beladenen NPSNPs und dreidimensionalen, porösen Scaffolds aus Kollagen- oder Poly(ε-caprolactone) (PCL)-Fasern. Trotz der ersten, vielversprechenden Ergebnisse bedürfen sowohl die Kollagen- als auch die PCL-basierten Freisetzungssysteme weiterer Optimierung bezüglich der freigesetzten BMP-2-Mengen, damit eine erfolgreiche osteogene Differenzierung von Stammzellen erreicht werden kann.

Abstract

Injuries of the musculoskeletal system, which is made up of the bones of the skeleton, muscles, cartilage, tendons, ligaments, joints and the connective tissue, are among increasing health care issues of the ageing population worldwide. Classical treatments often fail to restore the functionality of the damaged tissue leading to chronical pain and physical disabilities. Thus, the limitations of the current therapies point to the clinical need for effective healing strategies providing a target for innovative tissue engineering approaches. Among these approaches, growth factor delivery from a scaffold is one of the promising approaches for tissue regeneration.

In this work, sophisticated nanoplatforms for the controlled loading and delivery of the growth factor bone morphogenetic protein 2 (BMP-2) were developed by using nanoporous silica nanoparticles (NPSNPs) for applications in the field of bone tissue engineering and regeneration. Spherical NPSNPs were synthesised by the sol-gel method with the aid of a structure-directing surfactant. Subsequently, NPSNPs were modified by post-synthetic reactions with different organosilane coupling reagents to obtain NPSNPs with versatile surface chemistries and by that, to control the loading capacities and release kinetics of BMP-2.

Before loading of the BMP-2, it was shown that hydrolytically highly stable moieties were present on the surface of aminopropylsilyl-modified NPSNPs; these moieties caused pore clogging. However, this pore clogging could be removed by post-synthetic reactions, an important finding with regard to the construction of NPSNP-based drug delivery devices.

After the loading of BMP-2 on the surface of differently modified NPSNPs, it was shown that the presence of hydrophobic functionalities on the surface of the NPSNPs was the major governing factor controlling BMP-2 loading capacities regardless of the positive or negative charge of the terminal functional groups. Furthermore, BMP-2 delivery systems based on NPSNPs showed three types of BMP-2 release behaviour: fast initial (burst), sustained and slow release (retention), depending on the modification of the NPSNPs. Notwithstanding that the reasons for the different release behaviours could not be fully clarified yet and need further investigations, these results pave the way for engineered NPSNP-based delivery systems with desired growth factor release kinetics for tissue engineering.

First studies on the potential for bone regeneration revealed that BMP-2-loaded NPSNPs were slightly more effective in upregulating early targeted gene expression in human bone marrow-derived mesenchymal stem cells after a short exposure time of 2 h as compared to free BMP-2. In addition, cytotoxicity investigations performed with all types of NPSNPs showed that all concentrations of non-modified NPSNPs, as well as all types of modified NPSNPs were not cytotoxic up to a concentration of 10 μg ml^{-1} towards mouse myoblasts (C2C12) cells and human bone marrow-derived mesenchymal stem cells within a period of 7 days.

With regard to the possible application to regenerate bone tissue in case of large bone defects or of a rupture of the tendon-bone junction, BMP-2-loaded NPSNPs with different modifications were successfully integrated into three-dimensional and porous scaffolds made up of either collagen or poly(ε-caprolactone) (PCL) fibres, respectively. As a result, biofunctionalised implants were developed providing a controlled release of small doses (nanogram range) of BMP-2. Despite the promising results, both collagen- and PCL-based scaffolds need further optimisation regarding the released amounts of BMP-2 to successfully induce osteogenic differentiation of mesenchymal stem cells.

Keywords: nanoporous silica nanoparticles, bone morphogenetic protein 2, growth factor delivery, scaffolds, osteogenic differentiation, bone regeneration, tendon-bone interface regeneration

List of contents

List of figures

List of tables

List of abbreviations

APTES	(3-aminopropyl)triethoxysilane
BCP	biphasic calcium phosphate
BET	Brunauer-Emmett-Teller
BJH	Barett, Joyner, Halenda
BSA	bovine serum albumin
BM-MSCs	bone marrow-derived mesenchymal stem cells
BMPs	bone morphogenetic proteins
BRE	BMP-responsive element
°C	degree Celsius
CaP	calcium phosphate
CAPS	*N*-cyclohexyl-2-aminopropanesulfonic acid
CHES	*N*-cyclohexyl-2-aminoethanesulfonic acid
CHO cells	Chinese Hamster Ovary cells
cm	centimetre
CTAB	cetyltrimethyl ammonium bromide
C/S	Carbon/sulphur
DAPI	4',6-diamidino-2-phenylindole
DBM	demineralised bone matrix
DBU	1,8-Diazobicyclo[5.4.0]undec-7-en
DCC	*N*, *N*- dicyclohexylcarbodiimide
DFG	Deutsche Forschungsgemeinschaft
DEA	diethanolamine
DLS	dynamic light scattering
DMEM	Dulbecco's modified Eagle's medium
DMF	*N*, *N*-dimethylformamide
DMHA	*N*, *N*-dimethylhexadecylamine
DNA	deoxyribonucleic acid
ECM	extracellular matrix
EDC	ethylcarbodiimide
E. coli	*Escherichia coli*
e.g.	for example
ELISA	enzyme-linked immunosorbent assay
et al.	lat.: at alii (and others)
FCS	fetal calf serum
FDA	Food and Drug Administration
FGF	fibroblast growth factor
FITC	fluorescein isothiocyanate
FTIR	Fourier transform infrared
h	hour
HAp	hydroxyapatite
hASCs	human adipose-derived mesenchymal stem cells
HEPES	4-(2-hydroxyethyl)piperazine-1-ethanesulfonic acid
HRP	horseradish peroxidase
Id	*inhibitor of differentiation*
IGF	insulin-like growth factor
IL	interleukin

ISO	International Organization of Standardization
IUPAC	International Union of Pure and Applied Chemistry
kDa	kilo Dalton
kHz	kilo Hertz
kV	kilovolt
Luc	luciferase
MES	2-(*N*-morpholino)ethanesulfonic acid
mg	milligram
µg	microgram
min	minute
ml	millilitre
µl	microliter
mM	mill molar
mmol	mill mole
MOPS	2-(*N*-morpholino)propanesulfonic acid
MSCs	mesenchymal stem cells
MSNs	mesoporous silica nanoparticles
MTT	3-(4,5-dimethylthiazol-2-yl)-2,5-diphenyltetrazolium bromide
mV	millivolt
NADH	nicotinamide adenine dinucleotide
NHS	*N*-hydroxysuccinimide
NLDFT	non-local density functional theory
nm	nanometre
NPSNPs	nanoporous silica nanoparticles
PBS	phosphate buffered saline
PCL	poly(ε-caprolactone)
PDGF	platelet-derived growth factor
PEG	polyethylene glycol
pg	picogram
PGA	poly(glycolic acid)
pI	isoelectric point
PLA	poly(lactic acid)
PLGA	poly(lactic-co-glycolic acid)
qRT-PCR	quantitative real-time polymerase chain reaction
rh	recombinant human
SBA-15	Santa Barbara Amorphous-15
SBF	simulated body fluid
SDA	structure-directing agent
SEM	scanning electron microscopy
SI	supporting information
siRNA	small interfering ribonucleic acid
T	temperature
t	time
TEA	triethanolamine
TCP	tricalcium phosphate
TEOS	tetraethoxysilane
TEM	transmission electron microscopy
TGA	thermogravimetric analysis
TGF-β	transforming growth factor beta

TMB	1,3,5-trimethylbenzen
TMOS	tetramethoxysilane
TRIS	tris(hydroxymethyl)aminomethane
UV	ultra violet
VEGF	vascular endothelial growth factor
W	watt
wt.%	weight percent
XRD	X-ray diffraction

1 Introduction

Bone tissue has a unique ability to naturally heal and remodel itself without scarring [1, 2]. However, in large bone defects, caused by trauma, tumors, infections etc., this regenerative capability can fail to result in a permanent tissue damage and a loss of function unless surgeons manage to bridge the defect site [3]. The "gold standard" in bone defect treatments remains bone transplantation (grafting) of an autologous bone graft that is harvested from the pelvis or the iliac crest of the patient and used to fill the bone defect [4]. In addition, allografts and xenografts, bone tissue harvested from another patient or from an animal, provides an alternative treatment when only a limited amount of the autologous bone graft is available [5]. However, there is a risk of the rejection by the immune system, infections and transmission of donor diseases. Thus, the limitations of the current bone graft techniques point to the clinical need for an effective and sophisticated bone graft substitutes, providing a target for innovative bone tissue engineering strategies.

Another challenging issue in orthopaedics is the regeneration of tissue interfaces, the highly specialized and organized areas that connect two tissues with different biochemical and mechanical properties, in particular, cartilage-bone, tendon/ligament-bone and meniscus-bone tissues [6]. The interfaces show a unique gradual transition in structure, biochemical composition and cell types and enable a load transfer between the tissues that they connect. Most musculoskeletal injuries are associated with the ruptures of the interfacial zones, which are either caused by trauma, mostly acquired during sport activities, or by age-related tissue degeneration [7]. For example, tendon-bone ruptures are responsible for the rotator cuff tears that are among the most frequent injuries causing pain and limiting the mobility of the shoulder [8]. Classical treatments of the rotator cuff tears involve surgical intervention, pulling the torn tissue back to its original position and fixing it at the bone site. However, the risk of the failure of the surgical procedure is high (20% - 90%) [9]. At the moment, there is no satisfying therapeutic solution to restore the initial functionality of the torn rotator cuff.

To restore the architecture and functionality of both bone tissue and the tendon-bone interface is the challenging task for tissue engineering [10]. Common orthopaedic tissue engineering approaches include three-dimensional scaffolds, which provide structural support, a friendly microenvironment for the attachment of the cells, enabling cell ingrowth, proliferation and differentiation as well as vascularization, with a final goal to re-establish the form and functionality of the damaged tissues [11-13]. A wide range of inorganic materials, natural and synthetic polymers as well as their composites are able

to mimic the mechanical properties of the natural tissue and therefore, have been identified as suitable scaffolds for tissue regeneration [14-16]. Further, cells and/or growth factors can be integrated into the scaffolds providing biochemical functionalities. When the tendon-bone connection shall be re-established by using an engineered scaffold, the transition from a soft tissue like tendon to a hard tissue like bone presents a special challenge. The recent tissue engineering approaches focus on the fabrication of graded structures by mimicking the composition of the extracellular matrix in the individual tissue zones and by employing growth factor gradients and cells [17-20]. The mentioned cell- and growth factor-based approaches can also be used for bone regeneration [21-24].

Bone morphogenetic protein 2 (BMP-2) is one of the prominent osteoinductive growth factors, which shows promising osteogenic effects *in vitro* and in *vivo* [25, 26]. In combination with a scaffold, made of the natural polymer collagen, the medical product INFUSE® Bone Graft (Medtronic) was approved by the FDA for the interbody spinal fusion in 2002 [27]. However, more recently, concerns have been raised regarding the off-label use of the product due to severe side effects associated with the uncontrolled release of supraphysiological doses of BMP-2 [16]. Therefore, one of the aims of this work was the development of an optimized bone regenerative system enabling the delivery of low doses of the growth factor in a controlled manner and thus, offering a safer and less expensive solution for engineered tissue implants, by using nanoporous silica nanoparticles (NPSNPs).

NPSNPs are ideal candidates for the incorporation, adsorption and delivery of a variety of therapeutic agents, mostly drugs, growth factors and genes, for biomedical purposes due to their large pore volume, high specific area and tunable surface chemistry [28-32]. More recently, NPSNPs have demonstrated a great potential for adsorbing the growth factor BMP-2 and to deliver it, as shown by the osteogenic differentiation of mesenchymal stem cells *in vitro* [33, 34]. However, the mechanisms of how the surface chemistry of NPSNPs controls the growth factor loading capacity and release have not yet been fully understood, leaving behind a major hurdle to overcome if their widespread application for the delivery of growth factors is to be realized. To this end, within this work the surface chemistry of NPSNPs will be tailored by silanization with various organosilanes possessing different physicochemical properties, e.g. hydrophobicity/ hydrophilicity and surface charge. The BMP-2 loading capacity on differently modified NPSNPs and the BMP-2 release from the surface of the NPSNPs will be studied (chapter 4.2). In addition, with regard to the envisaged application in tissue engineering, the cytotoxicity of modified NPSNPs towards the murine cell line C2C12 BRE-Luc (BMP-Responsive-Element-Luciferase)-pGL3 and bone marrow-derived mesenchymal stem cells (BM-MSCs) will be assessed (chapter 4.4). Moreover, the differentiation progress

of BM-MSCs towards osteogenic lineage upon exposure to BMP-2-loaded NPSNPs will be examined by monitoring BMP-2-induced early targeted gene expression (chapter 4.3).

As stated earlier, one of the main goals of this work is the development of an optimized system providing a controlled release of small BMP-2 doses from scaffolds for bone and bone-tendon tissue regeneration. Two different types of nanocomposites will be developed with regard to the two different applications. Within the interdisciplinary research consortium "Biofabrication for NIFE", BMP-2-loaded NPSNPs will be integrated into porous collagen scaffolds (chapter 4.5). The success of the integration of NPSNPs into the scaffolds and the release behaviour of BMP-2 from the scaffolds will be examined subsequently. In addition, it will be studied how the BMP-2 release behaviour depends on the surface chemistry of NPSNPs. Furthermore, the ability of prepared collagen-NPSNP-BMP-2 nanocomposites to promote the osteogenic differentiation of human adipose tissue-derived stem cells (hASCs) in the three-dimensional environment of the nanocomposites will be evaluated under *in vitro* conditions with regard to the future application for bone regeneration.

A similar approach will be used to develop a graded implant for the tendon-bone interface regeneration in case of a rotator cuff rupture within the DFG research group FOR 2180 "Graded implants for tendon-bone junction". Within this research group, electrospun poly(ε-caprolactone (PCL) fibre mats with both aligned and unaligned fibres mimicking the natural tendon and bone tissues will be used as scaffolds. To provide graded bioactive functions, scaffolds will be equipped with NPSNPs or/and chitosan nanoparticles used for the controlled delivery of bioactive molecules: bone growth factor BMP-2, transcription factor Smad8 Linkerregion + Mad Homology Region 2 (Smad8 (L+MH2) and transforming growth factor (TGF)-β3 to regenerate the bone, tendon and the tissue of the transition zone in between, respectively. The present work deals with regeneration of the bone site of the tendon-bone junction (chapter 4.5). For this purpose, BMP-2-loaded NPSNPs will be integrated into three-dimensional, electrospun PCL fibre mats, which were previously functionalized by a chitosan-PCL graft copolymer to obtain a "shish-kebab" structured fibre surface and which were finally coated with alginate [35]. Subsequently, the integration of NPSNPs into the scaffolds and the release behaviour of BMP-2 from the NPSNPs previously loaded into the scaffolds will be evaluated. The results derived from the BMP-2 release will be compared with regard to the chosen modification of NPSNPs. This work will be a part of the first steps towards the fabrication of a graded implant for the treatment of a rotator cuff rupture.

Obviously, NPSNPs play a central role in the entire work. Therefore, two key parameters, namely degradation and hydrolytic stability of NPSNPs, will be investigated in a basic

study to enable the successful application of NPSNPs as delivery systems for therapeutic agents in biomedicine. While most studies on the degradation have focused on non-modified NPSNPs [36-38], the issue of the hydrolytic stability of the functional groups attached on the surface of NPSNPs has not been addressed yet. For this purpose, the hydrolytic stability of aminopropylsilyl moieties tethered on the surface of NPSNPs upon exposure to ultrapure water will be investigated (chapter 4.1). In this context, a novel approach to regain the porosity of aminopropylsilyl-modified NPSNPs, which is lost upon exposure to an aqueous medium, will be elaborated.

2 Theoretical background

2.1 Nanoporous silica nanoparticles

Nanoporous silica nanoparticles (NPSNPs) are considered promising candidates for the high loading and controlled delivery of pharmaceutical drug, therapeutic proteins and genes [39]. This chapter provides general information on the syntheses of first mesoporous silica materials followed by advanced syntheses of NPSNPs and their surface modification. Before reviewing the use of NPSNPs as delivery systems in biomedicine, such key parameters as the degradation, hydrolytic stability and biocompatibility of NPSNPs will be discussed. Finally, the potential biomedical applications of NPSNPs and the immobilization strategies for therapeutic biomolecules will be presented.

2.1.1   Synthesis of nanoporous silica nanoparticles

Nanomaterials have long become a subject of intense research due to their unique physical and chemical characteristics. According to the International Union of Pure and Applied Chemistry (IUPAC), nanomaterial's particle sizes should be in the range of 1 – 100 nm in at least one dimension. Among nanosized materials, nanoporous silica nanoparticles (NPSNPs), have shown a great potential for multiple applications; one of them is biomedicine [29, 31, 40-42]. The silica nanoparticles possess mesopores in the range of 2 – 50 nm [43]. Therefore, the term mesoporous (instead of nanoporous) silica nanoparticles (MSNs) is also often used in the literature.

Mesoporous silica material was first synthesized simultaneously by two independent groups of scientists in 1992 and was intended to be used as molecular sieves, adsorbent or catalyst [44, 45]. The idea to use mesoporous silica for drug delivery was proposed almost 10 years later, in 2001 [46]. Parallel to that, a deeper understanding of the synthesis mechanism of mesoporous silica materials had led to the ability to produce nanoporous silica nanoparticles of various sizes and morphologies with tunable pore structures [28].

Nanoporous silica nanoparticles can be synthesized by modifying the Stöber process and employing the micelle-forming surfactants, e.g. cetyltrimethylammonium bromide (CTAB) as an ionic surfactant and a non-ionic triblock co-polymers Pluronic P-123 or F-127, which serve as templates (also called structure-directing agents (SDAs)) [47, 48]. Two main synthesis mechanisms are considered effective to produce ordered mesostructures (Figure 1a). During the true liquid-crystal templating process, a lyotropic

liquid-crystalline phase is formed only by the SDA at high concentrations followed by the condensation of hydrolysed silica precursors forming a silica framework (Figure 1b). Tetraethoxysilane (TEOS) or tetramethoxysilane (TMOS) are usually used as silica sources. In contrast, liquid crystals can be formed by cooperative self-assembly of SDA with silica precursor species at lower SDA concentration. In this method, attractive interactions between the SDA and the silica precursors are essential [49].

In order to obtain ordered mesoporous silica material, the organic template should be removed. The most commonly used method is the calcination, in which organic SDAs can be decomposed at high temperatures under air atmosphere. However, overheating of the sample should be avoided in order to prevent structural collapse. For long-chain alkyl surfactants, the temperature of 550 °C is considered optimal to remove organic residues. As an alternative, SDAs can be extracted by using an acidic ethanol solution [48].
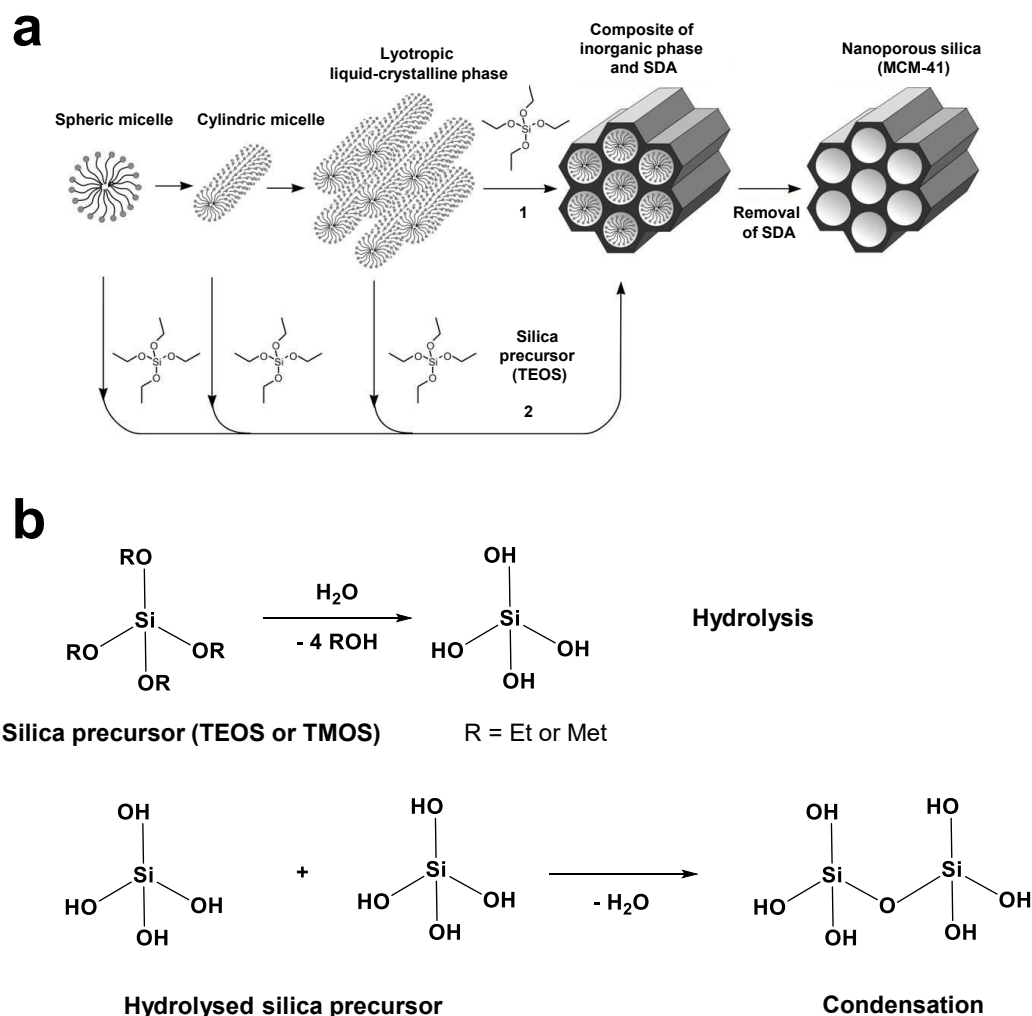
Figure 1: (a) Formation of mesoporous materials by structure-directing agents: 1) true liquid-crystal template mechanism and 2) cooperative self-assembly mechanism [49]. (b)Hydrolysis of the silica precursor (TEOS or TMOS) and their condensation.

During the synthesis of nanoporous silica nanoparticles with precise particle sizes and distinct morphology, two fundamental variables should be controlled [50, 51]. On the one hand, the relative rates of hydrolysis and condensation of the silica source can be adjusted by varying the pH. Hydrolysis of silica precursors ($Si(OR)_4$) could be catalysed both in acidic and basic conditions. The hydrolysis rate is lowest near neutral pH. The condensation rate of hydrolysed silica precursors is in line with their charge density. Above the isoelectric point of silica (pI ≈ 2) silica species become negative and the charge density increases along with the pH. In the pH range between 2 and 7 negatively charged silica species tend to assemble with positively charged SDAs, e.g. CTAB, via electrostatic interactions or with non-ionic templates, e.g. triblock co-polymers, via hydrogen bonding interactions. Under alkaline conditions (pH > 7) only electrostatic interactions between SDA and silica can be established [52]. The maximum of condensation rate is reached at pH 7.5 and, from there on, decreases with increasing pH due to the instability of silica at higher pH. During the syntheses of NPSNPs (pH≈10), however, cationic SDAs prevent silica species from dissolving by forming stable composites up to pH 12. Consequently, Mann and co-workers employed a fast pH-changing strategy yielding particles with the sizes below 500 nm [53]. Lin and co-workers could reduce the particle sizes to 200 nm through the fast addition of silica precursors to a diluted, preheated and rapidly stirred aqueous surfactant solution [54]. This group pioneered the development and coined the term mesoporous silica nanoparticles (MSCs) for drug delivery. The synthesis route for nanoporous silica nanoparticles in this work was adapted from [55]. The NPSNPs in the size range between 40 nm and 60 nm can be produced under basic conditions using diethanolamine (DEA), TEOS and CTAB through controlled hydrolysis and condensation of silica source.

On the other hand, the magnitude of the interactions between the growing silica polymer and the micelles can be controlled by choosing different templates, co-solvent or additives [51]. Reducing aggregation of silica species is crucial to achieve nanoparticles. Therefore, the direct contact of silanol groups should be prevented. Suzuki *et al*. demonstrated that the growth of silica particles could be suppressed by the addition of a non-ionic triblock co-polymer to the solution containing a silica precursor and an ionic surfactant. This synthesis route yielded mesoporous silica nanoparticles with a diameter of ca. 20 nm [56]. Other protective agents like polyethylene glycol (PEG) [57], tri- and diethanolamine (TEA [58] and DEA [55]) have been applied to reduce silica particle size. By using ethanol as co-solvent, mesoporous silica spheres with the mean size of about 500 nm were synthesized by Unger and co-workers [59].

Besides round-shaped NPSNPs, rod-like particles can be prepared by using different organic alkoxysilanes as co-structure directing agents [60]. In addition, through employing of different templates, twisted and helical ribbons [61], worm-like silica nanotubes [62] and mesoporous platelets can be synthesised [63].

Variation of pore sizes of NPSNPs is desired for incorporation of drugs or biomolecules for biomedical applications and can be achieved by choosing appropriate surfactants with differently long hydrophobic chains or special swelling agents. However, by using the first one, the variation is rather limited. Therefore, swelling agents such as *N, N*-dimethylhexadecyl-amine (DMHA) and 1,3,5-trimethylbenzene (TMB) were used to synthesize NPSNPs with large nanopores with a diameter of up to 9 nm for biomolecule loading [64]. By using TMB and a hydrothermal method NPSNPs with even larger nanopores (> 15 nm) could be obtained for gene delivery [65]. As an alternative, non-ionic triblock co-polymers Pluronic P65, P123 and F127 and cationic fluorocarbon surfactant (quencher for particle growth) can be used to synthesize NPSNPs with pore sizes in the range between 5 nm and 20 nm [66]. In order to further increase the volume for drug and biomolecule loading, many syntheses to prepare hollow silica nanoparticles were developed [67].

2.1.2 Surface modification of nanoporous silica nanoparticles

Surface modification of NPSNPs by covalent attachment of different functional groups allows to tailor and customize the surface chemistry of NPSNPs for the desired application. The standard procedure to introduce functional groups on the surface of NPSNPs is to use various, commercially available organic trialkoxysilanes. There are two different approaches: co-condensation and post-synthetic grafting [49, 51]. By employing the co-condensation method, the chosen organic alkoxysilane is directly added to the reaction mixture containing the silica precursor and the SDA leading to a homogeneously distributed integration of organosilane moieties into the silica framework of NPSNPs (Figure 2a) [68-70]. The main disadvantage of this method is that the removal of the SDA can only be attained by the extraction in acidic ethanol solution and not by calcination due to the organic nature of integrated trialkoxy groups. However, through the extraction, it is not possible to entirely remove the SDA, which would cause crucial cytotoxic effects when used for biomedical applications.
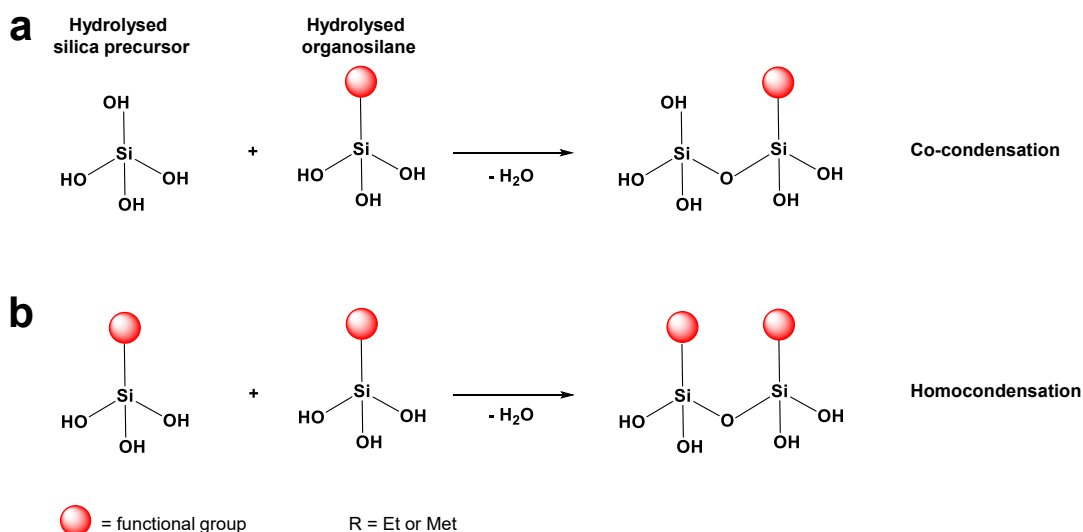
Figure 2: (a) Co-condensation of a hydrolysed silica precursor with a hydrolysed organosilane. (b) Homocondensation of two hydrolysed organosilanes.

In contrast, post-synthetic grafting refers to the subsequent modification of the surface of already formed NPSNPs with organic trialkoxysilanes. These reagents can be attached to the external and internal surface of NPSNPs by the reaction with the surface silanol groups. The main advantage of this method is that the SDA can be completely removed by calcination before the grafting process. However, it was shown that the distribution of the functional groups on the surface is less homogeneous when grafted than co-condensed [70].

If the grafting is performed before the removal of SDA, only the external surface of NPSNPs can be modified [71]. After the extraction of the SDA, the second type of trialkoxysilanes can be attached to the internal surface of NPSNPs. A selective modification of both surfaces can be achieved only by post-synthetic grafting.

One of the drawbacks of both methods is the intermolecular condensation (homocondensation) of the organic trialkoxysilanes. In case of co-condensation, the content of terminal organic groups that are incorporated into the silica network is generally lower than the initially added amount of trialkoxysilanes. This can be justified by the fact that trialkoxysilanes at high concentration tend to homocondensation and react with each other, instead of the condensation with the silica precursor (Figure 2a and b) [49]. In case of post-synthetic grafting, too high organosilane concentrations and excess of water can lead to homocondensation [72]. The condensed organosilane oligomers formed hereby can precipitate on the surface of NPSNPs causing pore blocking. Therefore, it is crucial to perform post-synthetic grafting in a water-free solvent, such as toluene, and at low concentrations of the organosilane.

2.1.3 Degradation of nanoporous silica nanoparticles

The degradation and hydrolytic stability of NPSNPs is one of the key parameters for their successful application as drug delivery systems. The degradation behaviour of NPSNPs has not only a major impact on the release kinetics of the drug but also on the toxicity of NPSNPs. Therefore, in several studies, structural parameters of NPSNPs of different sizes were studied upon immersion into different physiological media. Onida and co-workers showed a rapid decrease of the pore volume during the first hours of the immersion, while the mesopore structure remained intact (XRD measurements) [73]. The authors concluded a pore blocking caused by dissolved and re-deposited silica species. He *et al.*, who made similar observations, proposed a three-stage degradation behaviour of NPSNPs in simulated body fluid (SBF) [36]. According to this proposal, a rapid bulk degradation on hour-scale is followed by a slow degradation hindered by the deposition of calcium/magnesium silicate layer deposited on the particle surface. In addition, Kuroda and co-workers studied the degradation of NPSNPs with different sizes ranging from 20 nm to 80 nm in phosphate buffered saline (PBS) [37]. They showed that the degradation rates of colloidally stable NPSNPs were particle size-independent, but higher than those of non-porous silica nanoparticles and of NPSNPs aggregates, probably due to the large surface areas.

Subsequently, attempts have been made to prevent NPSNPs from fast degradation. Bein and co-workers compared the degradation behaviour of colloidally stable NPSNPs modified with different trialkoxysilanes or polyethylene glycol (PEG) in SBF [74]. They demonstrated that PEG modification could protect NPSNPs from rapid degradation. In another study, the authors reported that longer and denser polymer chains of PEG could effectively slow down the degradation of NPSNPs [38].

Furthermore, the hydrolytic stability of the attached functionalities on the NPSNP surface is an important parameter, since the drug should remain linked to the NPSNPs till it reaches the targeted site. Surprisingly, this issue has been addressed only by few studies, demonstration a rapid dissolution of the majority of the attached aminopropylsilyl moieties from the surface of non-porous silica nanoparticles and silicon wafer within few hours [75, 76]. These results clearly highlight the need for further studies on the degradation of organosilica-modified NPSNPs with regard to their application as drug delivery systems.

2.1.4 Biocompatibility of nanoporous and non-porous silica nanoparticles

Biocompatibility investigations are a prerequisite for the application of NPSNPs in the biomedical field. The term "biocompatibility" is used to describe both harmful and beneficial biological effects caused by nanoparticles, including cytotoxicity and *in vivo* toxicity, and in general all changes in cells or living organisms at molecular, cellular and histological levels [39]. In this chapter, the focus will lie on the cytotoxic effects caused by the exposure of silica nanoparticles.

The number of studies on the toxicity of nanoparticles has exponentially increased since 2000. However, as highlighted by Harald F. Krug, who critically reviewed more than 10 000 publications on the safety of nanomaterials appeared since 2001, the lack of standardized testing methods leads to incomparable and often contradictory results [77]. To assess the toxicology of different nanomaterials, a web-based data platform DaNa$^{2.0}$ (Data and knowledge on Nanomaterials) has been developed [78]. To create this data platform, only original literature was used that met the certain set of criteria established by the DaNa$^{2.0}$ expert team. These criteria include a detailed characterization of the physicochemical properties of studied nanomaterials as well as the description of sample preparation and testing parameters [79]. The following information on the DaNa$^{2.0}$ database can be found regarding the toxicology of amorphous silica nanoparticles. In contrast to crystalline SiO_2 nanoparticles, amorphous SiO_2 nanoparticles are considered harmless. In cell culture experiments, the exposure of very high doses of amorphous SiO_2 has resulted in cell-toxic reactions (references are not provided). However, the exposure of relevant doses (up to 50 µg ml^{-1}) of amorphous SiO_2 did not cause cytotoxic effects [80, 81]. Inflammation responses were detected only at high concentrations [81]. In general, the amount of information provided by the database on amorphous non-porous silica nanoparticles is rather low. No information is provided on the toxicity of NPSNPs. Therefore, an additional literature review was conducted.

In principle, nanoparticle characteristics such as the particle size and shape, porosity, functionality of the external surface and surface charge can affect cellular interactions *in vitro* and *in vivo* [30]. Since NPSNPs used in this work exhibit different functional groups on their surface and are porous, toxic effects related to the surface chemistry and charge as well as the porosity of NPSNPs are crucial to assess. In contrast, particle size and shape will have a low impact on the toxicity due to the attachment of NPSNPs on a scaffold.

It is commonly accepted that positively charged nanoparticles cause cytotoxicity by cell membrane damage, while negatively charged nanoparticles cause intracellular damage [82, 83]. In addition, nanoparticles with no charge (isoelectric point) exhibit least

unwanted cell interactions [84]. Since NPSNPs should be used as the delivery system for biomolecules, they need to have charged functional groups to interact with these biomolecules. However, it was difficult to assess the impact of the surface chemistry and charge of NPSNPs on the toxicity due to the lack of systematic studies.

The porosity of silica nanoparticles seems to play a role on haemolysis: the destruction of red blood cells. It has been found that NPSNPs show less haemolytic activity towards red blood cells than the non-porous silica nanoparticles of a similar size up to a concentration of 100 µg ml^{-1} [57, 85, 86]. This outcome was linked to the large surface area of NPSNPs. Due to the nanopores, the "cell-contactable surface area" of nanoporous silica nanoparticles is smaller than of non-porous silica nanoparticles. As a result, NPSNPs exhibit fewer silanol groups on the external surface and therefore, have fewer interactions with the red blood cells than their non-porous counterparts [86]. Further studies have shown that the haemolytic effect of NPSNPs was concentration- and size-dependent [87]. Starting from the particle concentration of 100 µg ml^{-1} increased haemolytic activity was demonstrated up to particle concentration of 1600 µg ml^{-1} by NPSNPs of different sizes (25 nm to 255 nm). The NPSNPs with the smallest particle size (25 nm) revealed the highest haemolytic activity. In general, interactions of NPSNPs with red blood cells are important, since NPSNP-bearing scaffolds are planned to be evaluated *in vivo* and will come in contact with blood.

As mentioned above, the cytotoxicity of nanoparticles was shown to be clearly dependent on the nanoparticle doses. It has been found that NPSNPs at high doses inhibit cellular and mitochondrial respiration [88] and caused cellular oxidative stress [89]. However, when cells are exposed to high particle concentrations, the cytotoxicity is probably caused by the coverage of the cells with nanoparticles, so that the supply of oxygen and nutrients to the cells as well as the removal of the cell waste is inhibited resulting in cell death [90, 91].

In addition, in several studies, it was shown that the cytotoxic effects of silica nanoparticles are cell-dependent and, therefore, cannot be generalized for all cell types. One possible explanation for that may be the difference in metabolic activity of different cell line [92]. While fibroblasts with long doubling times were less susceptible, tumour cells with short doubling times were more sensitive to nanoparticle exposure [92]. In another study, it was demonstrated that human vascular endothelial cells were more affected by silica nanoparticle exposure than the cervix carcinoma (HeLa) cells [93]. These studies clearly demonstrate that, in order to predict the potential toxic effect of nanoparticles in humans, cytotoxicity investigations on cell types with physiological relevance should be analysed. In this work, these would be the bone marrow-derived mesenchymal stem cells due to their participation in bone regeneration processes.

Despite the high number of studies related to the possible toxic effects caused by amorphous non-porous and nanoporous silica nanoparticles, systematic and harmonized studies are needed to ensure the safety of NPSNPs for their clinical applications as delivery systems for drugs and biomolecules [94].

2.1.5 Potential biomedical applications of nanoporous silica nanoparticles

Due to their high porosity, large surface area and pore volume, tuneable particle sizes and surface chemistry, NPSNPs are considered promising candidates for the high loading and controlled delivery of pharmaceutical drug, therapeutic proteins and genes [39]. By additional incorporation of a magnetic or/and fluorescent core into NPSNPs, multifunctional platforms can be developed and used for multimodal imaging and localized therapy (Figure 4) [95]. In the following section, the development from simple drug delivery systems based on mesoporous silica materials to sophisticated NPSNP-based delivery platforms for various therapeutic agents will be presented.

In the early 2000s, nanoporous silica materials were proposed as suitable candidates for drug incorporation and delivery. In 2001, Vallet-Regí and co-workers showed that bulk nanoporous materials with pore sizes of 2.5 nm and 1.8 nm are able to incorporate and release ibuprofen, an anti-inflammatory drug [46]. Subsequently, several studies have reported on the successful incorporation and release of some other drugs such as gentamicin [96], erythromycin [97], aspirin [98]. In principle, drug loading capacity essentially depends on the surface area of the porous material due to the drug adsorption on the surface [31]. Therefore, by increasing the surface area more drugs can be incorporated into the drug delivery system. However, if the increase of the surface area is not possible, the surface of the drug delivery system can be modified with various functional groups to achieve stronger drug-surface interaction [49, 99]. As a result, Song *et al*. demonstrated that by the introduction of the amino groups on the surface of the mesoporous silica material SBA-15, higher ibuprofen amounts were loaded in comparison to unmodified SBA-15 due to the electrostatic attraction between the amino groups and the carboxyl groups of ibuprofen [100]. In addition, the release rate of ibuprofen from modified material could be controlled as compared to unmodified SBA-15. In our group, high amounts of the antibacterial drug ciprofloxacin were incorporated into mesoporous silica layers by modifying the silica surface with sulfonic acid groups [101]. The release of ciprofloxacin was delayed by an additional coating of the drug-containing mesoporous silica layers with hydrophobic bis(trimethoxysilyl)hexane or dioctyltetramethyldisilazane to prolong the effective antibacterial activity. Surface modification with hydrophobic moieties to control drug release from the porous silica materials is a well-known approach. Tang *et al*. demonstrated that the release of

ibuprofen into an aqueous medium was slowed down, because of the difficult penetration of the aqueous medium into the pores [102].

Common drug release profile of mesoporous materials was proposed by Vallet-Regí and co-workers (Figure 3) [31]. The profile *a* is commonly observed for mesoporous silica materials before the modification as shown by Song *et al*. [103] and Ehlert *et al*. [101], displaying an initial burst release followed by a very slow drug release. This drug release behaviour is favourable to treat acute infections or inflammations. After the modification of the mesoporous silica materials with appropriate functionalities, the drug release can be slowed down and follows i) first-order kinetics with respect to drug concentration (profile *b*) or ii) zero-order kinetics that only depends on time (profile *c*). The former one is demonstrated by Song *et al*. after the modification with amino groups [103]. The latter one is demonstrated by Ehlert *et al*. after the additional coating [101]. This profile is also called sustained release and is highly desirable for long-term drug delivery. All three release profiles can also describe release kinetics of other therapeutics like proteins and genes.
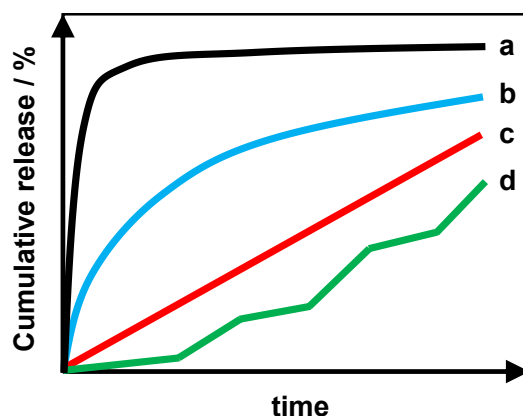
Figure 3: Drug release profiles of mesoporous materials. (a) Initial burst release followed by slow release, (b) first-order release kinetics, (c) zero-order release kinetics (sustained release) and (d) release profile of stimuli-responsive drug delivery systems, adapted from [31].

Besides pharmaceutical drugs, it is possible to incorporate membrane-impermeable peptides and proteins into NPSNPs and to transport them into the cell by cellular uptake [39]. The incorporation of these biomolecules is based on the same principles, namely strong electrostatic or hydrophobic interactions between the carrier/delivery system surface and the cargo molecules. In 2007, the incorporation of an enzyme, cytochrome C, into NPSNPs with an average pore size of 5.4 nm and its release into HeLa cells was attained by Lin and co-workers [104]. The enzyme was protected from degradation through loading into NPSNPs and remained its activity in catalysing the substrate after cellular internalization. However, it is not always necessary to transport proteins inside the cells. Instead, proteins can be loaded on the external surface of

NPSNPs and delivered to the cell surface, where they are detected by the cell receptors. Our group was successful in loading the growth factor bone morphogenetic protein 2 (BMP-2), which promotes the osteogenic differentiation of mesenchymal stem cells (MSCs), on the nanoporous amorphous silica layer and NPSNPs both modified with aminopropylsilyl groups [33, 105]. When MSCs were seeded on BMP-2 loaded silica layers or exposed to BMP-2 loaded NPSNPs, the promotion towards osteogenic differentiation could be demonstrated. However, the binding and release mechanisms of BMP-2 have not been investigated in aforementioned studies and are, therefore, one of the aims of the present work.

The intracellular transport (referred as transfection) of therapeutic genes such as small interfering (si)RNAs by using delivery carriers is a relatively new approach in gene therapy. The advantage of using siRNAs instead of drugs is the possibility to silence the expression of nearly any genes in the body [106]. Currently, this approach is being extensively investigated for anti-cancer treatment [107, 108]. Several studies have shown that NPSNPs modified with positively charged functionalities, usually polycation polymers, were able to incorporate and deliver negatively charged siRNAs into different types of cells [109-114].

Apart from siRNA delivery, more sophisticated drug delivery systems based on NPSNPs mostly for anti-cancer treatment are being developed. The main goal is to achieve the so-called "zero premature release" of the drug, which means that no drug release should occur before reaching the targeted site. One of the concepts to reach this goal is to temporarily close the nanopores of NPSNPs with so-called "gatekeepers". As soon as drug delivery systems reach the desired location, the pores (gates) will be opened by applying an external stimulus, and the drug will be released. In first stimuli-responsive drug delivery systems, surface-modified CdS nanocrystals were used as removable caps by attaching them through disulphide bonds to NPSNPs [54]. Through the cleavage of the bond by disulphide-reducing agents such as dithiothreitol and mercaptoethanol, the encapsulated drug could be released.
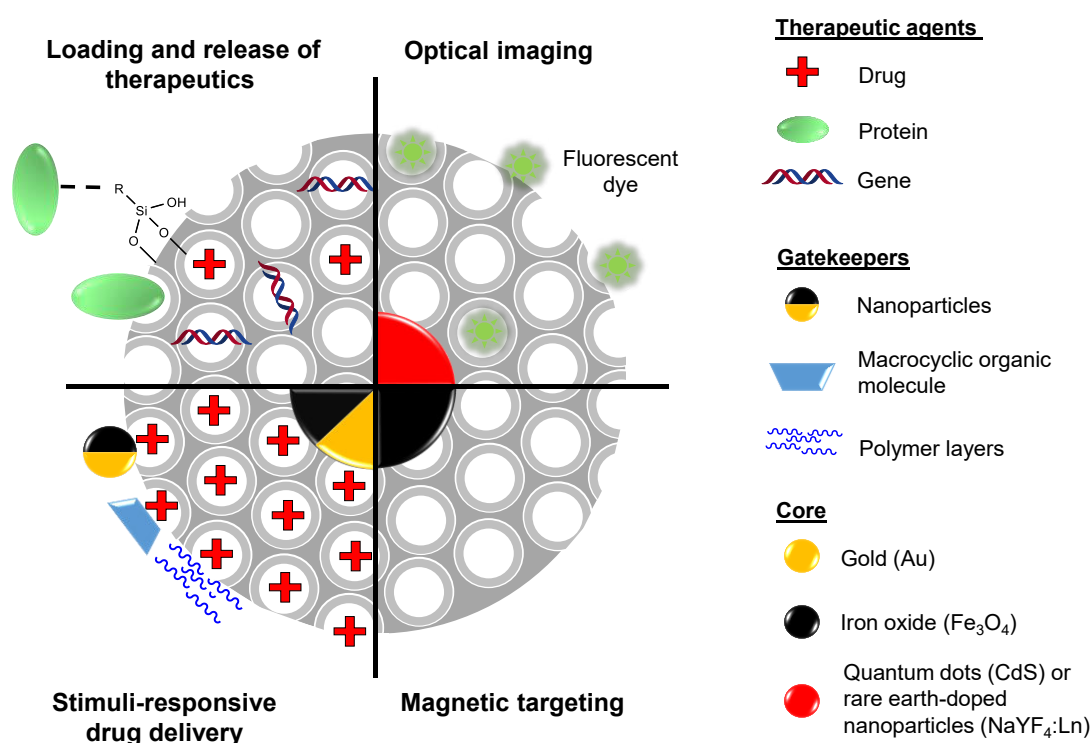
Figure 4: Multifunctional nanoplatform based on NPSNPs for delivering of various therapeutic agents, magnetic targeting and optical imaging.

Besides nanoparticles, diverse types of other gatekeepers such as macrocyclic and linear molecules as well as polymers have been investigated [32]. Depending on the chosen gatekeeper, stimuli-responsive drug delivery systems can respond to pH [115-117], ultrasound [118], radiation [119], temperature [120, 121] or to a combination of several stimuli [122, 123]. A comprehensive analysis of about 500 publications on multifunctional delivery systems based on NPSNPs performed by Aznar *et al.* demonstrates endless possibilities to design versatile smart nanoplatforms [124]. In our group, pH-sensitive stimuli-responsive drug delivery system based on NPSNPs for controlled release of chlorhexidine was developed for antibacterial application in dentistry [125]. The nanopores of NPSNPs were capped with the polymer poly(4-vinylpyridine) to prevent drug leakage at physiologic pH. At acidic pH caused by bacterial infection, the polymer strains become protonated, straighten up and release the antibacterial drug. A common release profile of such stimuli-responsive drug delivery systems is given in profile d. In this case, the release rate is controlled by the external stimuli, e.g. pH.

By incorporation of a magnetic core, mostly Fe_3O_4 nanoparticles, into the NPSNPs magnetic-responsive delivery systems can be obtained [126, 127]. In most cases, the ability of superparamagnetic iron oxide nanoparticles to generate thermal energy under an external magnetic field is used to release the drug. Additionally, the external magnetic

field can drive the magnetic drug delivery systems to the desired location, hold them untill the drug release is completed and finally remove them (targeted delivery) [128]. Moreover, gold nanoparticles can be embedded into NPSNPs and used for different applications such as ultrasound imaging [129] or photoinduced drug delivery [130]. For imaging purposes, fluorescent dyes, e.g. fluorescein isothiocyanate (FITC), can be attached to the surface of NPSNP-based drug delivery systems. However, they often suffer from photobleaching and quenching [131]. Alternatively, fluorescent quantum dots, e.g. CdS, CdSe or ZnS [132, 133], or luminescent rare earth-doped phosphors, $NaYF_4$:Ln with Ln = Yb^{3+}, Er^{3+} [134, 135] as nanoparticles can be incorporated into NPSNPs for *in vivo* imaging.

2.1.6 Strategies for protein immobilisation

Various biomolecules such as enzymes, antibodies, affinity proteins and cell-receptor ligands have been immobilized on the surface of different biomaterials for therapeutic, diagnostic, biosensor and bioprocess purposes [136]. The main goal is to bind biomolecules to a surface while maintaining its biological function. Generally, biomolecules can be immobilized by three major methods: physical adsorption, physical entrapment and covalent attachment [136]. Since physical entrapment can occur only in microcapsules and hydrogels and not in nanoparticles, it won't be discussed further.

During covalent attachment, biomolecules are tightly bound to the surface of the biomaterial through a chemical reaction [137]. A popular strategy to bind biomolecules on the surface of biomaterial surfaces or nanoparticles is the reaction of primary amines of biomolecules with *N*-hydroxysulfosuccinimide (*sulfo*-NHS) ester groups, which have been previously tethered on the biomaterial surface by a reaction of surface –COOH groups with 1-ethyl-3-(3-dimethylaminopropyl)carbodiimide (EDC) (Figure 5a) [138]. Covalent crosslinking of biomolecules is a rather expensive, time- and resource-consuming method that can lead to the loss of biological activity of biomolecules [139]. Moreover, in the case when biomolecules such as proteins should be released from the biomaterial surface, covalent attachment seems not suitable due to very strong conjugation between the biomaterial and the protein. In contrast, the biomolecule immobilization by physical adsorption is often more convenient and cost-effective method for biomolecule immobilization that allows for biomolecule desorption [136]. Since this method was chosen to immobilize growth factor BMP-2 on the surface of NPSNPs, it will be discussed in more detail.

The success of physical adsorption of a biomolecule, e.g. protein, on the surface of a biomaterial is determined by the properties of both protein and biomaterial, as well as by the environmental condition, in which protein adsorption occurs [140]. When a protein

arrives at the material surface, they interact with each other through intramolecular bonds: hydrogen bonding, electrostatic and hydrophobic interactions (Figure 5b-e). Which type of interactions is favoured, depends on both protein and biomaterial characteristics such as the hydrophilicity/hydrophobicity and the surface charge [141].
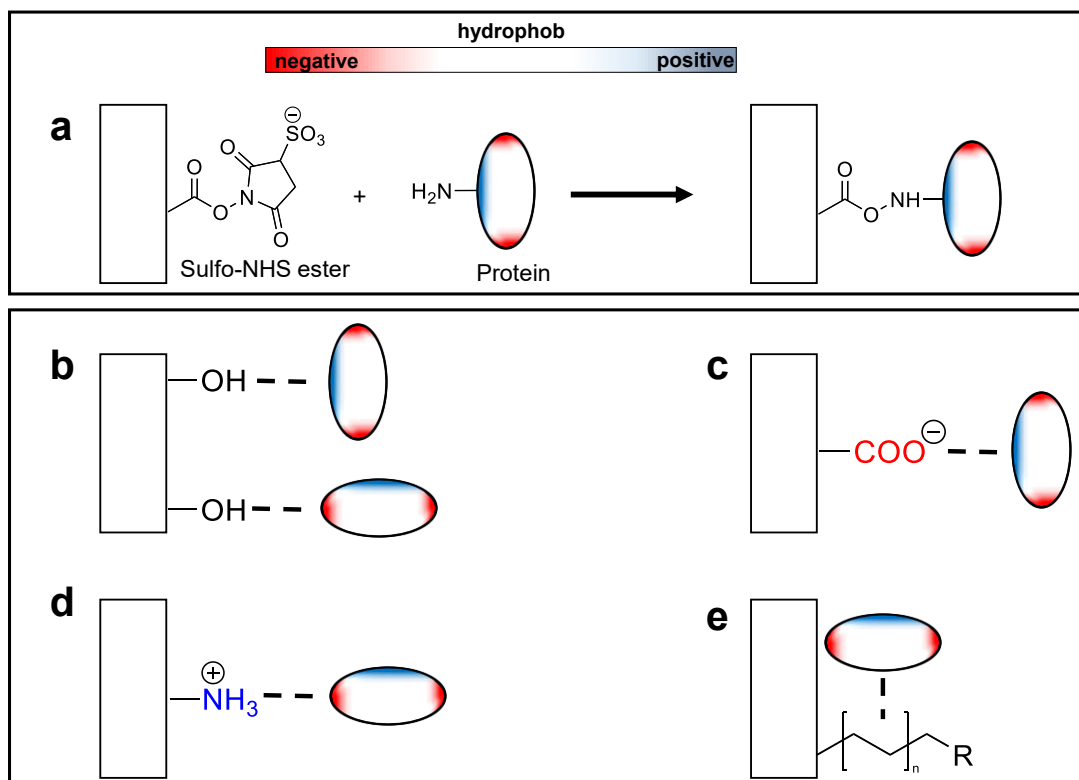
Figure 5: (a) Covalent attachment of a protein on biomaterial surface. Physical protein adsorption via (b) hydrogen bonding, (c) and (d) electrostatic and (e) hydrophobic interactions, adapted from [142]. R= −CH₃, −(CH₂)ₙ-CH₃, −NH₂, −SO₃H, etc.

The interaction via hydrogen bonding is rather weak, and thus, plays a minor role in protein adsorption. Electrostatic attraction occurs when positively/negatively charged protein domains interact with the oppositely charged surface regions of biomaterials. However, this way of interaction is not dominant for adsorption due to many conditions like pH and ionic strength of the medium, which can interrupt this process [141]. For hydrophobic proteins and surfaces, the hydrophobic interaction is the driving force for protein adsorption [143]. Before the adsorption, both the hydrophobic protein and the surface are surrounded by water molecules. However, these water molecules interact more with each other than with the hydrophobic regions and form an ordered cage, creating a situation with the decreased level of entropy. Disruption of these hydrate shells by adsorption is energetically favoured due to the increase of the entropy [141]. Since proteins are amphipathic species, which have both hydrophobic and hydrophilic

(charged) regions, and can undergo conformational changes during the adsorption, all three ways of interaction with biomaterial surfaces are possible [142].

Among other protein characteristics, protein size and structural stability (tendency to denaturation) play important roles in protein adsorption [141]. Large and structurally unstable proteins have more interactions with the biomaterial surface due to spreading on the surface in comparison to small or stable proteins.

While most properties are predetermined for proteins, for most biomaterials they can be tuned by surface modification [144]. As already mentioned, silica surfaces can be easily modified by silanization. Hereby, silanol groups on the surface of non-modified silica can react with trialkoxysilanes. There is a high number of commercially available trialkoxysilanes, which bear different functional groups such as $-NH_2$, $-COOH$, $-(CH_2)_n$-CH_3 etc. Upon chosen functional groups, hydrophobic or hydrophilic surfaces bearing positive or negative charge can be designed for desired protein (Figure 5c-d).

Moreover, the accessible surface area of biomaterials can be increased by employing nanoparticles instead of large solid surfaces and by introducing the porosity [141]. For example, while the surface area of a nonporous glass substrate is in the range of several cm^2, the external surface area of 1 gram of NPSNPs can be increased up to 300 m^2 resulting in the potential adsorption of higher protein amounts.

Finally, environmental conditions, in which protein adsorption occurs, can also have an impact on the amount and conformation of loaded proteins [145]. The temperatures above room temperature can significantly increase the amount of adsorbed proteins due to high diffusion of protein molecules. However, high temperatures can cause the denaturation of proteins and loss of the bioactivity. Besides the temperature, environmental pH is a crucial factor for proteins. Generally, the protein adsorption is the highest at pH ≈ pI (isoelectric point of a protein with no charge) probably due to the lack of electrostatic interactions with other protein molecules. However, at this pH aggregation and precipitation of proteins are common. Therefore, this method is not suitable for the adsorption of proteins on the surface of nanoparticles. Moreover, it is disadvantageous if electrostatic interactions between protein and the surface should be established. Lastly, the presence of other proteins or surfactants for protein stabilizing and prevention of aggregation can negatively affect protein adsorption by competing with or by binding on the main protein. The exact effect on protein adsorption has not been well studied yet.

2.2 Bone tissue regeneration

One part of the present work was performed within the interdisciplinary research consortium "Biofabrication for NIFE" and dealt with the development of innovative implants for bone tissue engineering. Therefore, this chapter provides general information on bone healing, classical therapy of critical bone defects and innovative bone regeneration strategies by exploiting key concepts of tissue engineering.

2.2.1 Bone healing

Bone tissue exhibits a unique capability to regenerate and repair after a small injury or fracture [146]. The most common pathway is indirect bone healing, which undergoes four stages and involves the expression of several thousands of genes (Figure 6). The detailed healing process was described in several reviews [22, 147, 148]. In this part, a brief summary of the indirect bone healing process is presented.

Immediately after the injury, a hematoma consisting of blood and bone marrow cells is formed and coagulates between and around broken bone ends forming a fibrinous clot [149]. Following the acute inflammation phase with the peak at 24 h after the injury, several pro-inflammatory cytokines including interleukin (IL) 1 and 6, etc. as well as members of the transforming growth factors (TGF)-β superfamily such as bone morphogenetic protein (BMP)-2, -4, -5 and 6 are secreted [150]. The hypoxic conditions during this healing phase induce the secretion of angiogenic factors such as vascular endothelial growth factor (VEGF), which stimulate the proliferation and differentiation of cell types needed for revascularization of the tissue [150]. Revascularization of healing tissue is essential for successful bone regeneration to re-establish gas and nutrition supply and to remove cell wastes [151].

During the healing stage which usually takes around 3 – 7 days after the injury, the hematoma is gradually replaced by granulation tissue rich in collagen fibres, cells and capillaries leading to soft callus formation (7 – 10 days) [147]. Hereby, mesenchymal stem cells are recruited from surrounding soft tissue and bone marrow and form cartilaginous tissue [148]. The formation of the cartilaginous matrix can be a result of insufficient blood supply, which restrains the osteogenic differentiation of MSCs, but allows for chondrogenic differentiation and proliferation [152, 153].

10 – 14 days after the injury, chondrocytes become hypertrophic, release calcium and undergo apoptosis [153]. The soft callus is resorbed by monocytes and replaced by osteoblasts differentiated from MSCs driven by BMPs [154]. These processes lead to the formation of hard callus (woven bone).

In order to completely restore the biomechanical properties of the newly formed bone tissue, hard callus is remodelled into a lamellar bone, which may take years for humans to achieve fully-loadable bone structure [146, 155]. Interestingly, during this phase, the secretion of BMP-2 is upregulated, while most members of TGF-β family are not present [154].
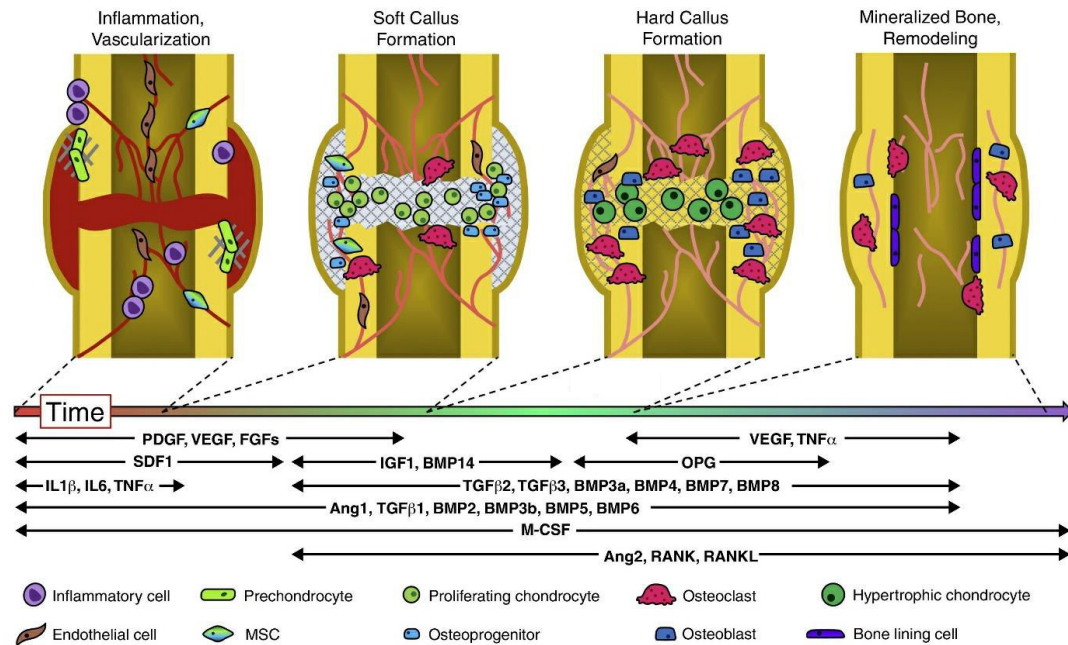
Figure 6: A spatiotemporal cascade of multiple endogenous factors controls normal bone regeneration during fracture repair in four stages. PDGF = platelet derived growth factor; VEGF = vascular endothelial growth factor; FGF = fibroblast growth factor; TNF = tumor necrosis factor; SDF = stromal cell-derived factor; IGF = insulin-like growth factor; BMP = bone morphogenetic protein; OPG = osteoprotegerin; IL = interleukin; TGF = transforming growth factor; Ang = angiopoietin; M-CSF = macrophage colony stimulating factor; RANK = receptor activator of nuclear factor κB; RANKL = RANK-ligand, from [156].

2.2.2 Classical treatments of critical bone defects and their limitations

Despite the remarkable potential for bone regeneration, large bone defects, caused by trauma, tumors, osteonecrosis, osteoporosis, spinal deformities or infections, can lead to significant bone loss with inferior healing capacities or painful non-union: permanent failure of bone healing [3]. A risk of the non-union can be high due to disorders associated with systemic inflammation, such as diabetes mellitus, sepsis, rheumatoid arthritis etc. [153].

Bone transplantation is currently the most common treatment for bone defects [4, 157, 158]. Based on the so-called diamond concept for a successful bone defect treatment, the bone transplant or bone graft should be osteoconductive, osteoinductive, osteogenic

and possesses mechanical properties similar to the bone [159]. The osteoconductive properties are provided by a rigid and cell-friendly scaffold, which allows the migration, attachment and proliferation of MSCs and other cells. Osteoinduction is defined as the promotion of MSCs differentiation into osteoblast and osteocytes (cell types present in the bone). The osteogenesis is given by the presence of cells that are able to form new bone tissue. In natural bones, these abilities are provided by the extracellular matrix (ECM), growth factors BMPs and osteoblasts, respectively [160]. Recent findings suggest that the established diamond concept should be modified to encompass the crosstalk between inflammatory cells and their secreted growth factors as well as the cells and the growth factor related to the bone healing, which is essential to the bone repair and remodelling (Figure 7) [3, 161]. However, all classic treatments of bone defects aim to limit the inflammation response disregarding the possible positive influence of inflammatory cells on bone repair capability.
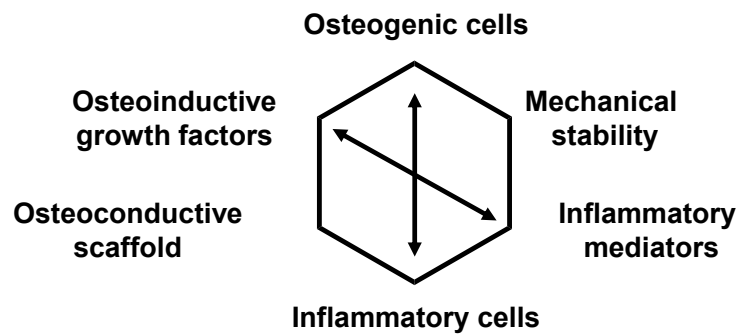
Figure 7: Modified diamond concept showing main factors influencing bone healing. Arrows demonstrate interactions between the cells and secreted growth factors and mediators, adapted from [3].

The current "gold standard" to treat critical size bone defects is the use of autologous bone grafts that are usually harvested from the iliac crest of the patient and consist of natural, immune-tolerated bone cells, an osteoconductive scaffold and osteoinductive growth factors [160]. However, this method provides a limited amount of bone and is not suitable for large or multiple bone defects. In these cases, allogenic bone grafts, which are decellularized bone harvested from other patients can be used instead [157]. Allogenic bone grafts (allografts) remain osteoconductive but lose their osteoinductive and osteogenic properties. In addition, allogenic bone grafts have the risk of disease transmission and immune reactions. As an alternative, demineralized bone matrix (DBM) is produced from cadaveric bones and is commercially available in form of chips, gel, putty or cement. DBM products are highly osteoinductive due to the presence of bone morphogenetic proteins (BMPs), while their osteoconductive properties are diminished [4]. Similar to allografts, DBM lacks osteogenic capability and mechanical strength.

The numerous drawbacks of the current treatments of bone defects call for an immediate response to develop a customized bone graft substitute with desirable biomechanical properties.

2.2.3 General bone tissue engineering approaches

The main tissue engineering goal is to restore damaged tissue and organs by employing biological, chemical and engineering approaches to clinical problems [162]. Traditionally, tissue engineering revolves around two main strategies: i) transplantation of an engineered scaffolds containing growth factors and cells grown *in vitro* and, and ii) combination of the engineered scaffold with growth factors to induce cell regeneration of the tissue *in vivo* [162].

Appropriate scaffolds for bone tissue engineering are typically made of porous biodegradable materials with special physicochemical properties that provide mechanical support and cell-friendly environment during the bone regeneration process. An ideal scaffold for bone regeneration should have following essential characteristics ([13, 16, 158]):

- *biocompatibility* as the ability to support normal cell activity without toxic effects to the host tissue; to allow the bone cells to adhere, proliferate and form ECM; to induce new bone formation and to form blood vessels for nutrients, gas and wastes transport;

- *biodegradability or -resorbability* as controlled degradation of the scaffold to create space for new tissue;

- *mechanical properties* should match the properties of the host bone tissue (strong differences between cancellous (inner) to cortical (outer) bone). Initial mechanical strength should enable handling during sterilization, packaging, transportation;

- *interconnected pore structure* to enable transport of nutrients, gas and wastes, and to guide new tissue ingrowth. Minimum pore size should be > 100 µm [163]. Optimal bone tissue ingrowth occurs when pore sizes are around 200-350 µm [164]. However, too porous structures can compromise mechanical properties;

- *ability to be sterilized* without the loss of above mentioned properties.

A wide range of inorganic materials, natural and synthetic polymers, as well as their composites have been identified as suitable scaffolds for bone regeneration. The advantages and disadvantages of the most prominent biomaterials are summarized in Table 1.

Table 1: Common scaffold materials used in bone tissue engineering [165].

Scaffolds	Advantages	Disadvantages	Examples
Inorganic materials	Resembles natural structure of bone (calcium phosphates); resorbable or non-resorbable; binds BMPs	Brittle; difficult to mould; exothermic	Hydroxyapatite (HAp), calcium phosphate (CaP) cements, bioactive glass
Natural polymers	Extremely biocompatible; possible natural affinity for growth factors	Disease transmission; difficult to sterilise; immune response	Collagen, gelatin, chitosan, alginate, hyaluronic acid, silk, fibrin
Synthetic polymers	Reproducible Manufacture; controlled release properties; easy to sterilise	Degradation products may be toxic; cell recognition; solvents or cross linkers may damage proteins	Poly(lactic acid) (PLA), poly(glycolic acid) PGA and their copolymers (PLGA) polyethylene glycol (PEG), poly(ε-caprolactone) (PCL)
Composite materials	Benefits depend on material exploited	More complex to manufacture	

Since collagen was used as one of the scaffold materials in this work, it will be described in more in detail. Among natural polymers, collagen is the most frequently used for bone regeneration [166]. Collagen is a fibrous protein (Figure 8) and is the main component of extracellular matrix of many tissues such as bone, cartilage, tendon, ligament, skin and so forth. Among all collagens, collagen type I is the most abundant of all. The extracellular matrix of bone consists of 90 % of type I and 5 % of type V collagen, making porous collagen scaffolds a suitable candidate for bone tissue engineering [15]. Advantageous characteristics of collagen are superior biocompatibility, biodegradability, regenerative characteristics such as osteoconduction and osseointegration. In addition, employing collagen is beneficial for cell adhesion, proliferation and differentiation [167]. In fact, two commercial products based on collagen scaffolds and osteoinductive factors, INFUSE® (rhBMP-2, Medtronic, Minneapolis, MN) [168] and OP-1™ (rhBMP-7, Stryker Biotech, Hopkinton, MA) [169], have received Food and Drug Administration (FDA)

approval for several surgical applications. The major disadvantage of collagen scaffolds, however, is the possible disease transmission, immunogenicity and lack of mechanical strength.
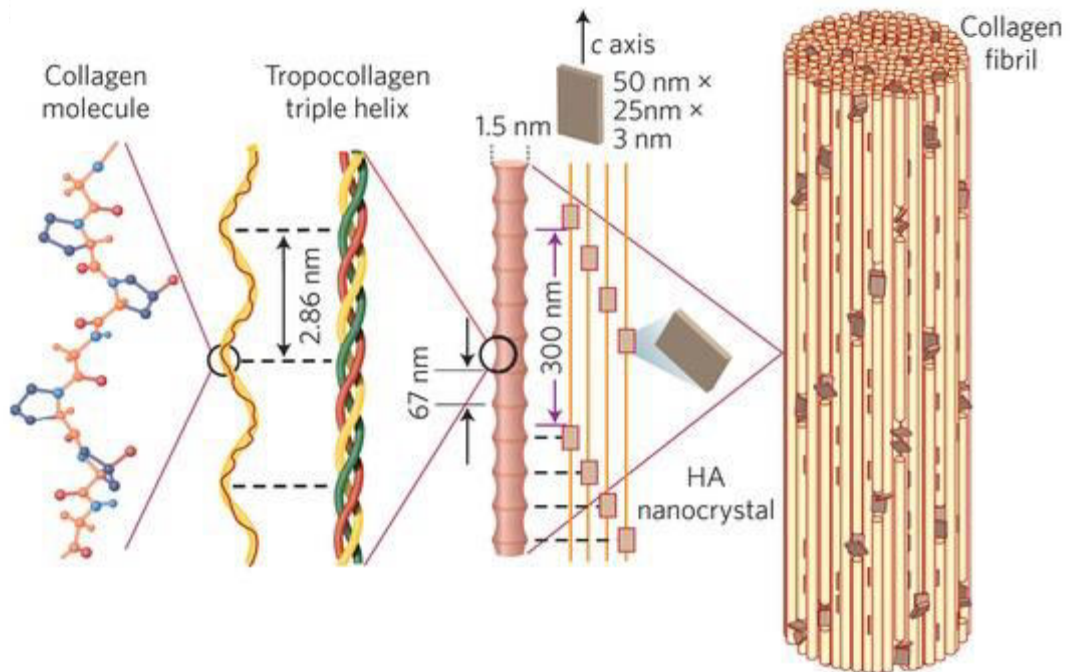
Figure 8: Collagen in the natural bone, adapted from [170].

One of the tissue engineering approaches is the cell-based therapy. Cellular regenerative tissue engineering strategies provide osteogenic properties to the scaffolds. Mesenchymal stem cells (MSCs) are a group of multi-potent adult-derived stem cells that can be isolated from organs and tissues including bone marrow, ligaments, muscular and adipose tissue [171]. The best characterized are the bone marrow-derived mesenchymal stem cells (BM-MSCs) [172, 173]. *In vitro* conditions have been found under which BM-MSCs are capable of self-renewal for many generations without the loss of their properties while possessing the ability to differentiate down the osteogenic, chondrogenic and adipogenic cell lineages [174]. In addition, adipose-derived mesenchymal stem cells (ASCs) have become an attractive and alternative multipotent stem line for bone tissue engineering [175, 176]. In contrast to BM-MSCs, they are abundant and can differentiate down the osteogenic cell lineage under suitable *in vitro* conditions [177]. To provide osteogenic and osteoinductive properties to the engineered scaffold for bone regeneration, MSCs can be i) delivered by seeding on injectable scaffolds [24, 178]; ii) pre-cultured on a scaffold *in vitro* and co-delivered with osteoinductive growth factors [179, 180] and iii) genetically modified to express osteogenic genes, seeded on the scaffold and delivered to the needed site [181, 182].

Another promising approach is the delivery of therapeutic growth factors using engineered scaffold/carriers described earlier to promote bone repair and regeneration. An ideal carrier material should protect growth factors from fast degradation, enable controlled time- and dose-dependent release of the growth factor and provide supportive scaffolds for cell migration, adhesion and proliferation and for vascularization.

As described previously, multiple growth factors are involved in regulating different phases of the bone regeneration process. Some of these growth factors, summarized in Table 2, have been extensively explored for bone healing in pre-clinical applications (reviewed by [148, 165, 183]).

Table 2: Growth factors involved into bone repair and regeneration, adapted from [158].

Growth factors	Tissue	Effects
Bone morphogenetic protein (**BMP**)-2 and -7 Transforming growth factor (**TGF**)-β3	Bone, cartilage	Bone-forming cell proliferation and differentiation; cartilage formation
Fibroblast growth factors (**FGF**)-1, -2 and -18 Platelet-derived growth factor (**PDGF**)-AA and -BB	Bone, muscle, blood vessels	Endothelial cell migration, proliferation and survival; increased osteogenic differentiation of mesenchymal stem cells
Insulin-like growth factor-1 (**IGF-1**)	Bone, cartilage, muscles	Osteoprogenitor cell proliferation and differentiation
Vascular endothelial growth factor (**VEGF**)	Bone, blood vessels	Endothelial cell migration and proliferation; recruitment, survival and activity of bone forming cells

In general, growth factors can be loaded onto carrier materials by non-covalent and covalent immobilization. In case of non-covalent immobilization, growth factors can be physically adsorbed to the surface of carrier materials through electrostatic, hydrophobic and hydrogen bonding interactions or entrapped/encapsulated within microcapsules, hydrogels and polymer matrixes. Covalent immobilization includes the chemical

attachment on solid surfaces, polymers or hydrogels [136]. The challenge is the development of controlled delivery systems of growth factors that mimic the physiological conditions required for bone regeneration [184].

Growth factors can be released from carrier materials by desorption through disruption of established growth-factor-carrier interactions, diffusion, convective fluid flow, carrier material degradation or a combination of these processes [184]. Many efforts have been made to control growth factor release by functionalization of the carrier materials and altering their degradation kinetics (review by [184, 185]). However, an ideal growth factor delivery system that can release one or multiple growth factors in the desired manner is yet to be developed.

2.3 Tendon-to-bone healing

One part of the work was performed within the DFG research group FOR 2180 "Graded implants for tendon-bone junction" and dealt with the development of a graded implant for bone-tendon bridging in case of a rotator cuff rupture. This chapter provides a short review of the current knowledge in tendon-bone junction biology, classical therapies and innovative tissue engineering approaches for the restoration of the tendon-bone junction after a rupture.

2.3.1 Tendon-bone junction biology

To fully understand the healing and regeneration of tendons and tendon-bone junction, it is important to understand their anatomic structures. The tendons are primarily composed of type I collagen, the most abundant collagen type in the body [186]. Similar to the bone, collagen molecules form collagen fibrils, which are assembled into parallel arrays of fibres (Figure 8). These fibres are then organized in parallel bundles, which are responsible for the tendon's tensile strength. In addition, small amounts of other collagen types, such as III and V, and proteoglycans participate in the organization and stabilization of tendon tissue.

The region where the tendon attaches to the bone is called enthesis. There are two different types of entheses in the body: fibrous and fibrocartilaginous [187], according to the absence or presence of fibrocartilage tissue at the tendon-bone junction, respectively. The fibrocartilaginous entheses are very common in the body and will be discussed in detail.

The fibrocartilaginous entheses are characterized by 4 distinct zones: 1) *tendon* comprised of collagen bundles containing sparse amount of tenocytes (tendon cells); 2)

non-mineralised fibrocartilage containing collagen fibres with embedded chondrocytes (cartilage cells); 3) *mineralised fibrocartilage* with mineralized extracellular matrix and perforating randomly aligned collagen fibres and 4) *bone* with its highly organized lamellar structure [188]. As can be seen, native tendon-bone transition is highly specialized and organized tissue.

2.3.2   Tendon failure and classical repair strategies

One of the functions of the tendon is to connect muscles on the one site and bones at the other side to generate a movement [189]. Tendon injuries can be acute as a result of trauma (e.g. during sports) or chronic as a result of accumulation of small repetitive tears that fail to heal [7]. As an example, the rotator cuff rupture is a frequent injury type for athletes due to sports trauma. However, the majority of patients with the rotator cuff ruptures are between 45 and 65 years old [190]. In these cases, the rupture occurs due to the age associated tissue degeneration. Noyes *et al.* revealed three primary modes of tendon failure: i) through ligament; ii) by tear out of the bone underlying the enthesis and iii) through the tendon-bone junction. The second mode is the most common in the mature skeleton because the bone underlying the enthesis (zone 4) is typically weaker than the transition zone between the tendon and the bone (zone 2 and 3) [191]. The relative avascularity of the fibrocartilage tissue and the bone loss at the injured site makes the healing process very slow [192].

The classical tendon repair often needs a surgical reconstruction, where the torn tissue is pulled back to its original position and fixed at the bone site. However, in cases of massive or large injury, chronic or re-tears and older patients, the risk of the failure of surgical treatment is high (20% − 90%) [9]. At the moment, there is no satisfying therapeutic solution to re-attach the tendon to the bone site and restore the initial functionality of the injured site.

2.3.3   Tissue engineering strategies to improve tendon-to-bone healing

Currently, tissue engineering approaches provide alternative strategies to accelerate and improve tendon-to-bone healing. The employed tissue engineered strategies are very similar to those for bone tissue engineering, which were already described in section 2.2.3.

This section provides a review of the current status of tissue engineering approaches for the repair of rotator cuff ruptures, which is the main goal of the DFG research group FOR 2180 "Graded implants for tendon-bone junction".

Current scaffold-based approaches for tendon-to-bone junction repair are summarized in Table 3. It can be seen, that three different approaches based on cell incorporation, growth factor release and gene transcription can be applied. All three approaches employ scaffolds made of degradable synthetic or natural polymers. In general, all polymer materials that are suitable for bone regeneration, summarized earlier in Table 1, can be also used to produce tissue-engineered scaffolds for tendon-bone repair. This also applies to the growth factors. All growth factors, which play a crucial role in bone regeneration, given in Table 2, can be used for tendon-bone junction restoration.

Table 3: Scaffold-based approaches for tendon-to-bone junction repair.

Scaffold composition	Scaffold design	Cell type/Growth factors	Ref.
Cell-based approach			
Unaligned, extruded/electrospun PCL nanofibres	Gradient of scaffold with incorporated TCP nanoparticles	Mouse preoblastic cells (MC3T3) *in vitro*	[19]
Gelatin-coated PCL nanofibers and plasma treated PLGA	Graded coating with calcium phosphate	MC3T3 cells *in vitro*	[20]
Growth factor-based approach			
Scaffold made of P$_{DL}$LA microparticles	Encapsulation of rhBMP-2 in microparticles	Mouse myoblasts C2C12	[18]
Alginate gel containing PLGA and silk fibroin microspheres	Encapsulation of rhBMP-2 and rhIGF-1 in microparticles	hBM-MSCs *in vitro*	[17]
PLLA scaffolds with incorporated PLGA microspheres	Encapsulation of PDGF-BB	-	[193]
Gene-based approach			

Scaffold composition	Scaffold design	Cell type/Growth factors	Ref.
Collagen sponge	Graded coating with poly-L-lysine (PLL) for the attachment of a Runx2/Cba1 encoding retrovirus	Primary fibroblasts from Wistar rats	[194]

As the tendon-bone interface is formed by 4 zones of different tissue, the reconstruction of this junction is a very challenging task. These challenges have motivated investigation into the development of a cell-free, graded implant for the rotator cuff repair by mimicking the highly complex organization of the tendon-bone connection employing the scaffold and growth factor-based approach within the DFG research group FOR 2180 "Graded implants for tendon-bone junction" (Figure 9a and b). For that, a scaffold with suitable structural, mechanical and biodegradation properties is produced by electrospinning of poly(ε-caprolactone) (PCL) into fibre mats, with both aligned and unaligned fibres mimicking the natural tendon and bone tissue, respectively. To provide bioactive function and further graded properties, scaffolds will be equipped with nanoporous silica nanoparticles or/and chitosan nanoparticles for the controlled delivery of bioactive molecules: BMP-2 for the bone side and TGF-β3 for the fibrocartilaginous transition. To restore the tendon side, the transcription factor Smad8 Linkerregion + Mad Homology Region 2 (Smad8 (L+MH2)) should be used. Thus, after the sterilization, a patient-safe and efficient implant should be fabricated, which can be easily translated into the clinic use to heal rotator cuff ruptures.

a

Muscle

Graded implant

25mm

30-40mm

Bone (Humerus head)

Tendon

b

Smad8 (L+MH2)   TGF-β3   BMP2

Tendon attachment by suture

Bone anchor

Tendon   Non-mineralized fibrocartilage   Mineralized fibrocartilage   Bone
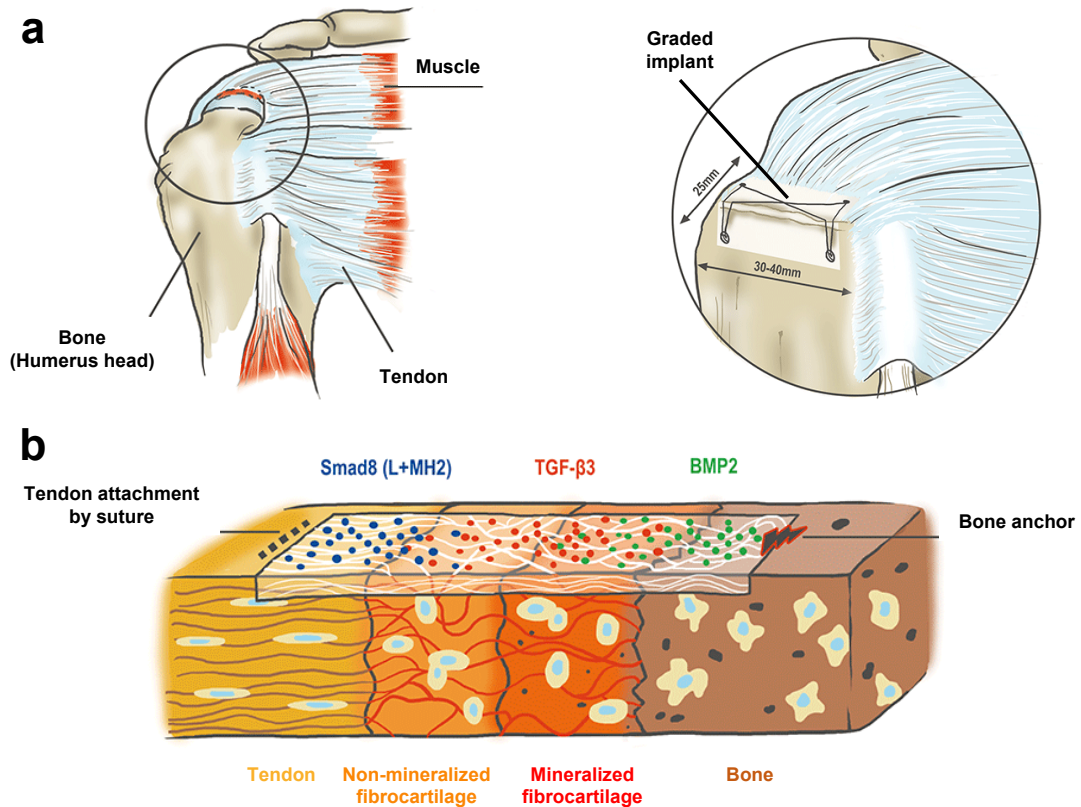
Figure 9: (a) Left: schematic illustration of the rotator cuff rupture (right shoulder, front view) and right: enlarged illustration of the tendon-bone defect site with the attached graded implant. (b) Schematic illustration of the graded implant in vivo. White lines represent electrospun PCL fibres. Blue, red and green dots represent different nanoparticles used as delivery systems for bioactive molecules, adapted from [195].

As PCL is to be used for implant fabrication, its characteristics will be briefly reviewed in this section. Among synthetic polymers, PCL, a family member of biodegradable aliphatic polyesters, has attracted considerable attention as biomaterial and drug delivery system in tissue engineering [196]. PCL was firstly synthesized in 1930s, by a ring-opening reaction of the cyclic monomer, ε-caprolactone (Figure 10a) [197]. It is a commercially available polymer that was approved by the U.S Food and Drug Administration (FDA) to be used in humans. PCL has excellent characteristics such as biodegradability, biocompatibility, and low cost of processing, enabling its fabrication in a variety of structures and forms to be used as a biomaterial. PCL fibre scaffolds with a three-dimensional porous structure and tunable pore sizes can be fabricated by the electrospinning process (Figure 10b) [35]. One of the advantages of this process is the simple modification of the physical, chemical and mechanical properties of PCL scaffolds by copolymerization or blending with other polymers. By altering these properties, engineered PCL-based scaffolds with desirable physicochemical properties and biodegradability can be provided for biomedical applications [197].

a

Cyclic ε-caprolactone   **Poly(ε-caprolactone) (PCL)**

b
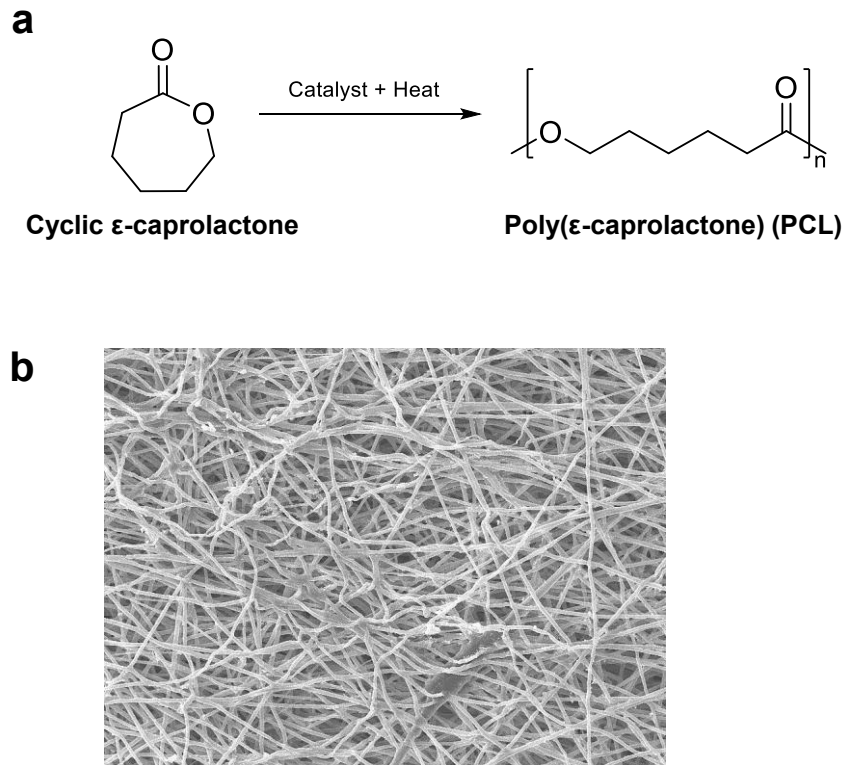
Figure 10: (a) Ring-opening polymerization of ε-caprolactone to poly(ε-caprolactone). (b) Scanning electron microscopy image of a three-dimensional electrospun PCL scaffold. The fibre diameter is about 3 µm.

Several studies have tested three-dimensional porous PCL fibre mats *in vitro* and *in vivo* for tissue engineering. *In vitro* studies could demonstrate a successful seeding, adhering, proliferation and differentiation of mesenchymal stem cells on PCL-based scaffolds [198-201]. *In vitro* studies of PCL-based scaffolds with different osteoinductive growth factors demonstrated a successful growth factor release and bone formation [21, 202, 203]. PCL/β-TCP composites have already been applied in pre-clinical spinal surgery, showing successful spine fusion in a pig [204].

2.4 Bone morphogenetic protein 2 (BMP-2)

This chapter presents an overview about BMPs and BMP-2 in particular ranging from the discovery to the applications in tissue engineering.

2.4.1 History of BMPs

In 1965, Urist postulated that a mix of proteins present in a demineralized bone matrix was responsible for bone regeneration when implanted subcutaneously in rodents and

rabbits [205]. Some years later, he identified and named these proteins as bone morphogenetic proteins (BMPs) [206]. During the decades of the 1980s and 1990s, several BMPs were isolated from bovine bone, and more than 20 morphogenetic proteins have been described in humans and other species [207, 208]. However, not all BMPs can induce *de novo* bone formation. Five BMPs, namely BMP-2, 4, 6, 7 and 9, exhibit high osteogenic activity [209]. Among these, BMP-2 is the most osteoinductive protein capable to induce the differentiation of mesenchymal stem cells (MSCs) into osteoblasts and chondrocytes both *in vitro* and *in vivo* [210, 211]. Since high quantities of human BMP-2 can be produced by recombinant technology using Chinese hamster ovary (CHO) and *Escherichia coli* (*E. coli*) cells [212, 213], recombinant human (rh) BMP-2 is used for various clinical studies for bone repair [214, 215]. In 2002, the clinical use of rhBMP-2 was approved by the U.S. Food and Drug Agency (FDA) and validated by the European Medicines Agencies for spinal fusion and long bone non-unions [216]. More recently, a much broader range of biological activity of different BMPs was recognized based on BMP expression studies. These studies demonstrated the essential role of BMPs in the embryogenesis and the development of organs, such as kidney, gut, lung, teeth, limb and testis, as well as in the homeostasis and regeneration of adult tissue [217]. Because of the growing number of different BMP functions, it was suggested to call BMPs "body morphogenetic proteins" [217].

2.4.2 Structure and physicochemical properties of BMP-2

BMPs are multifunctional growth factors that belong to the transforming growth factors beta (TGF-β) superfamily, with exception of BMP-1. Each active BMP is a homo- or heterodimer linked via disulphide bridges [218].

The crystallographic structure of native human BMP-2 was first reported by Scheufler *et al.* in 1999, demonstrating a homodimer with a dimension of 7 nm x 3.5 nm x 3 nm (Figure 11) [219]. Each BMP-2 monomer contains a cystine-knot forming three intrachain disulphide bridges. The folding topology of a monomer was described as a hand, where the α-helix is the wrist, the cystine-knot the palm and the β-sheets the fingers [220]. Two monomers are linked to a dimer by another covalent disulphide bond in an angle of approximately 40 °, creating a convex and concave side of the dimer (Figure 11b). The so-called cavity I, which has an excess of positive charge, is situated on the convex side. This cavity can function as a heparin binding site. The cavity II is located on the concave side and is smaller than cavity I. The charge of this cavity is negative and it is, therefore a possible interaction site for one of the BMP-receptors on the cell surface. In addition, two symmetrical finger-helix cavities are present in a BMP-2 dimer. The special shape and the negative charge of these cavities may form a specific epitope for receptor

interactions. Moreover, the surface of BMP-2 dimers possesses large hydrophobic areas, which could be responsible for the tendency to aggregate readily at physiological conditions.
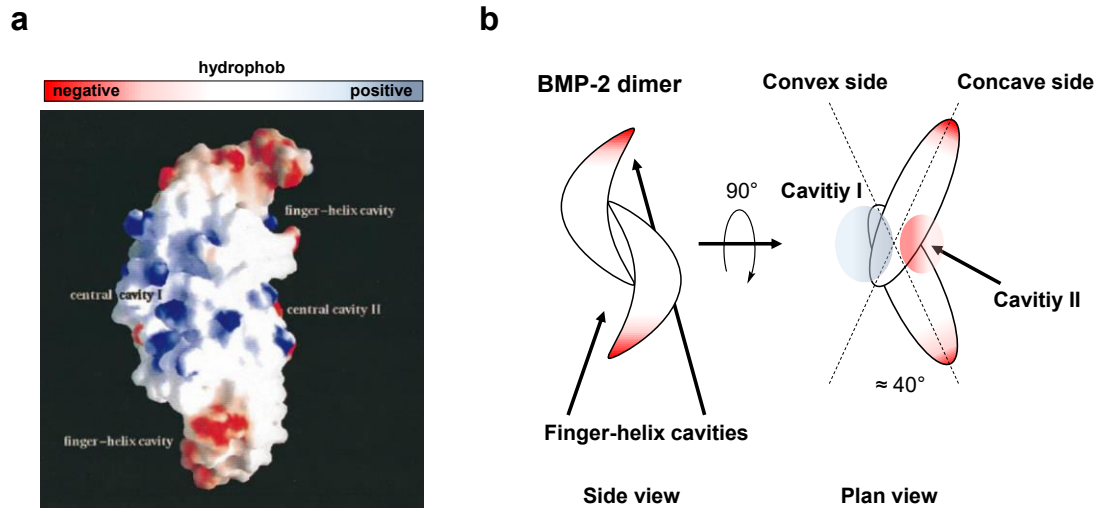
Figure 11: (a) Surface potential of a BMP-2 dimer. (b) Illustration of a BMP-2 dimer in the side and plan view for visualization of several cavities and their surface potentials as well as angles between BMP-2 monomers, adapted from [219].

RhBMP-2 produced in Chinese hamster ovary (CHO) cells or *Escherichia Coli* (*E. coli*) exhibits slightly different physicochemical properties. The isoelectric point (pI) of CHO-derived rhBMP-2 is with 9 slightly higher than the pI of *E. coli*-derived rhBMP-2 of 8.5 [221]. This behaviour is probably related to the fact that CHO-derived rhBMP-2 consists of two glycosylated monomers, whereas *E. coli*-derived BMP-2 does not possess any glycosylated units. This property could influence solubility of the rhBMP-2. However, it was demonstrated that both types of rhBMP-2 exhibit similar biological activities [222, 223]. Therefore, with regard to routine clinical application in bone regeneration, the use of *E. coli*-derived rhBMP-2 is more favourable due to its low-cost mass-production compared with the more costly production of CHO-derived rhBMP-2 [212, 224].

2.4.3 BMP signalling pathway and osteogenic differentiation of mesenchymal stem cells

The BMP-induced bone formation is driven by the Smad signalling pathway (Figure 12) [225, 226]. BMPs initiate their signalling cascade by binding to a dimeric complex of two specific cell-surface receptors, designated as receptor type I (BMPR-I) and type II (BMPR-II). There are three different types of BMPR-I and -II receptors. First, BMPs are bound to the BMPR-I followed by the recruitment of BMPR-II, which in turn phosphorylates the first one. Subsequently, BMP signal is transduced through the Smad-

dependent pathway, in which the expression of specific genes for osteogenesis is activated [227]. For that, Smad1/5/8 are phosphorylated and form a DNA binding heterodimer with the Smad4. Once entered the nucleus, the active heterodimer promotes the transcription of BMP target genes.
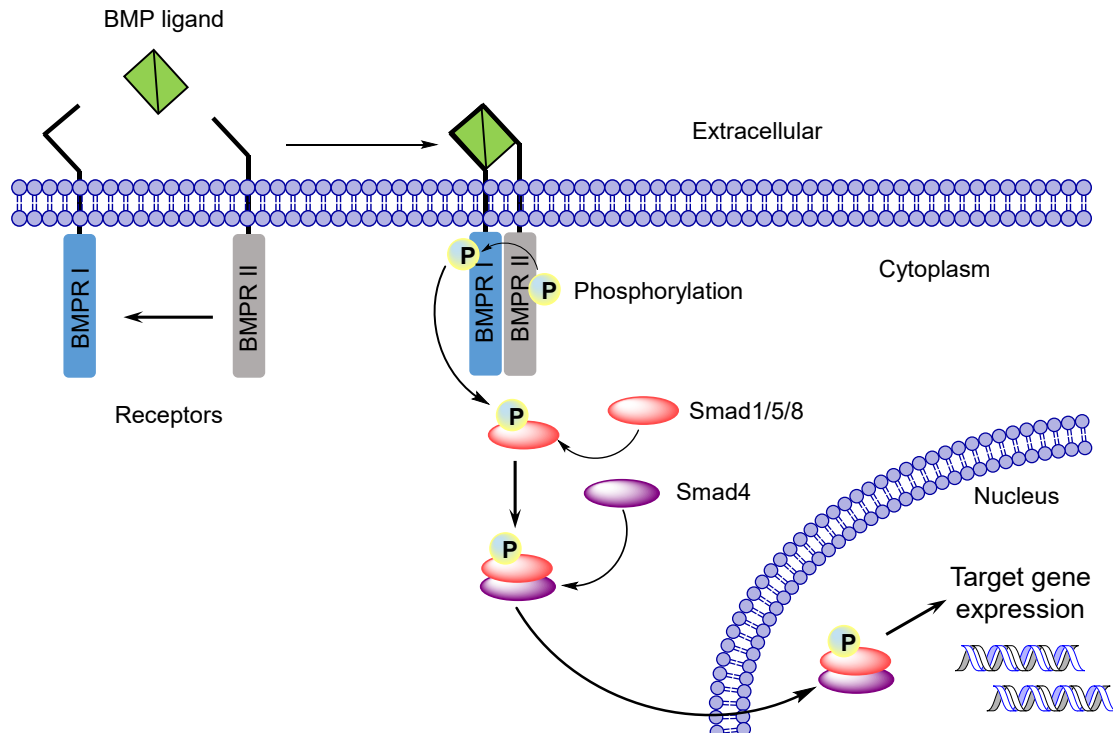
Figure 12: Cascade of BMP signalling through Smad-dependent pathway, adapted from [228].

Fine-tuning of BMP signalling is necessary to enable the coordination of biological responses. In vertebrates, BMP signalling is delicately controlled by a group of extracellular antagonists, including noggin [229] and chordin [230], which directly bind to the BMPs and hinder the interaction with the receptors. In addition, signalling can be prevented intracellularly by inhibitory (I)-Smads, such as Smad6 and Smad7, by interacting with the phosphorylated BMPR-I receptor or through competition with Smad4 [231]. Furthermore, at the membrane side, a pseudo-receptor BAMBI/Nma binds to the BMPR-II and prevents the BMP signal transduction [232]. Besides BMP signalling through Smad molecules, Smad-independent signalling pathways have been demonstrated to alternatively generate BMP signal transduction [233].

The progress of BMP-induced osteogenic differentiation of mesenchymal stem cells can be studied by the detection of specific osteogenic markers (Figure 13). The expression of immediate early genes, such as the *inhibitor of differentiation* (*Id*) *Id1* and *Id3*, and at later time points of such genes as *collagen type I*, *alkaline phosphatase*, *osteopontin*, *bone sialoprotein* and *osteocalcin,* provide evidence of successful osteogenesis [234].

Finally, osteogenic differentiation can be proven by the detection of mineralized matrix, which consists of hydroxyapatite and is formed only by differentiated cells [235].
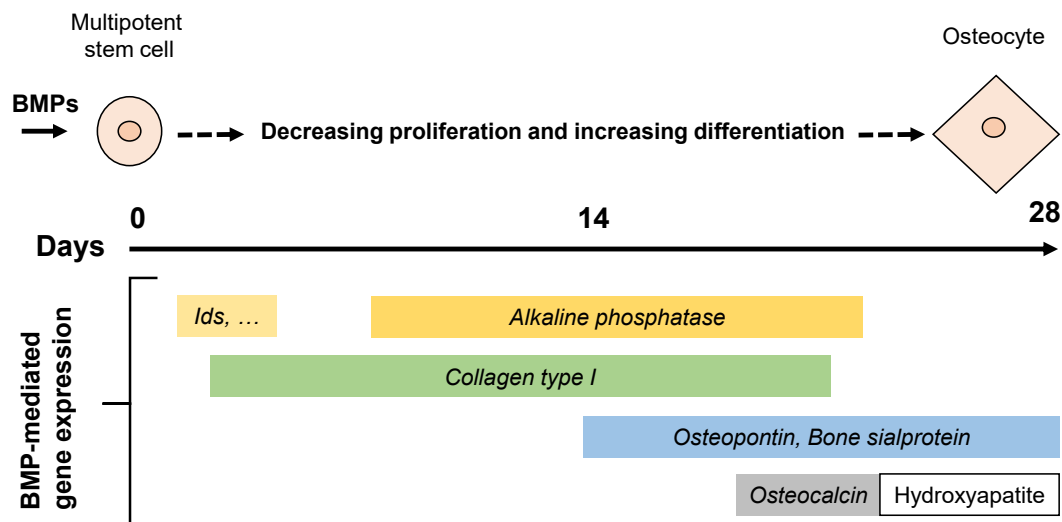
Figure 13: Schematic illustration of BMP-mediated expression of target genes during the osteogenic differentiation of mesenchymal stem cells, adapted from [209, 234, 236].

2.4.4 Strategies for BMP-2 incorporation and delivery for bone healing

There are three major categories of carrier material/scaffolds for BMP-2: inorganic materials, natural and synthetic polymers, and composites, which fulfil the key requirements as promising delivery systems for BMP-2, presented earlier in Table 1 [237-240].

Inorganic materials such as demineralized bone matrix (DBM) [205, 241], calcium phosphate ceramics (hydroxyapatite (HAp), β-tricalcium phosphate (β-TCP) and biphasic calcium phosphate (BCP)) and bioactive glasses [242] have been used as carriers for rhBMP-2 in pre-clinical animal studies due to their osteoconductive properties and similarity in mineral composition to human bones (Table 4). Since in most cases BMP-2 is not specifically bound to the inorganic carrier material matrix, the release is usually fast and uncontrolled. However, applications in bone regeneration require a release of BMP-2 for an adequate period of time to allow the cells to migrate to the injured area and to proliferate and differentiate [216].

Table 4: Selected carrier materials for BMP-2 delivery, BMP-2 dose, type of study and defect model.

Carrier	Carrier type	BMP-2 dose	Study	Defect model	Ref.
Ceramics					
HAp	Granules	1 and 3 mg	Mini pig	Posterolateral lumbar fusion	[243]
β-TCP	Granules	1-10 mg	Sheep	Posterolateral lumbar fusion	[244]
BCP		6, 9 and 12 mg	Nonhuman primate	Posterolateral lumbar intertransverse fusion	[245]
Natural polymers					
Collagen	Sponge	0.4 mg	Nonhuman primate	Anterior interbody fusion	[246]
	Sponge	6 and 12 mg	Human	Open tibia shaft fracture	[168]
Gelatin	Hydrogel	17 µg	Rabbit	Ulnar segment defect	[247]
Hyaluronic acid	Hydrogel	0.3 mg	Dog	Alveolar ridge defect	[248]
Alginate	Hydrogel	5 µg	Rat	Femoral bone defect	[249]
Chitosan	Hydrogel	2 µg	Rat	Calvarial bone defect	[250]
Silk	Hydrogel	0.3 mg	Rabbit	Maxillary sinus floor augmentation	[251]
Fibrin	Hydrogel	-	Rat	Calvarial bone defect	[252]
Synthetic polymers					
PLA-PEG	Injectable liquid	1 mg	Dog	Anterior thoracic spinal fusion;	[253]

Carrier	Carrier type	BMP-2 dose	Study	Defect model	Ref.
PLGA	Foam spheres	-	Rodents	Calvarial bone defect	[254]
PCL	Honeycomb porous scaffold	-	Rabbit	Ulna bone defect	[203]
	3-D scaffold	20 µg	Mouse	Subcutaneous implantation	[21]
Composites					
Collagen/BCP	Sponge/Granules	3 mg	Nonhuman primate	Posterolateral spinal fusion	[255]
PCL/β-TCP	Porous scaffold	0.6 mg	Pig	Anterior lumbar interbody fusion	[204]

As an alternative, different natural and synthetic polymers have been used for the development of a suitable delivery system for BMP-2. Collagen is a part of the extracellular matrix and the most prominent natural osteoinductive polymer used as a carrier for rhBMP-2 delivery [15]. However, it is well-known that a controlled delivery of BMP-2 from a collagen sponge is difficult to achieve due to the physical entrapment of BMP-2 in it. In addition, collagen scaffolds lack the mechanical strength. To overcome these challenges, collagen has been combined with ceramics to enhance mechanical properties and establish controlled BMP-2 release. The use of osteoinductive ceramics not only facilitates new bone formation but also helps to reduce the required BMP-2 dose for spinal fusion in monkeys [255]. In current clinical practice, rhBMP-2 adsorbed on an absorbable collagen sponge, is used for the treatment of interbody spinal fusion and open tibia fractures in orthopaedics, as well as of sinus and alveolar ridge augmentation in oral / maxillofacial surgery [245, 256]. A review of the literature on BMPs summarizes their current clinical applications [238]. Despite the global success, several negative side effects of rhBMP-2 have been reported associated with the usage of supraphysiological doses of rhBMP-2 (10-1000 fold higher than the concentration of native BMPs in the body) [257-260]. Recently, a medical product containing a very high amount of rhBMP-2 (AMPLIFY™, 40 mg rhBMP-2) has been associated with higher cancer risk in contrast to the control group [261]. Such high doses of rhBMP-2 are probably necessary due to the rapid protein degradation and diffusion, in particular, during the early stages of the post-surgical repair, notwithstanding that the natural amount of all BMPs in the bones is considered to be 1-2 µg per kg [262].

In addition to collagen, there are a number of other natural polymers such as gelatin, hyaluronic acid, alginate, chitosan, silk and fibrin in the form of a hydrogel or in combination with ceramics/synthetic polymers that can be considered as promising carriers for BMP-2 incorporation and release (Table 4).

Degradable synthetic polymers such as polylactic acid (PLA), polyglycolic acid (PGA), poly(DL-lactide-co-glycolide) (PLGA) and poly(ε-caprolactone) (PCL) are extensively used for BMP-2 delivery in tissue engineering due to their biocompatibility, hydrolytic biodegradability, simple fabrication and functionalization for desired physical, chemical and mechanical properties (Table 4). Despite the promising result of BMP-2 loaded carrier materials to promote bone healing in animal models, finding a suitable carrier with a low dose and controlled release kinetics of BMP-2 is still an active area of research. Future investigations are required to define the most suitable BMP-2 delivery system, dosage and release kinetics to improve the efficacy, efficiency and safety of future rhBMP-2-based medical products for bone healing.

3 Methods and materials

First, the working principles of the methods used for material characterization, protein quantification and cell culture investigations are described in this chapter. Next, the sources of different purchased chemicals and materials are given. In the following experimental part, the synthesis and modification routes of nanoporous silica nanoparticles as well as the protein loading and release procedures are presented in detail. In addition, specific parameters used for the characterization of the used materials are given.

3.1 Characterisation methods

3.1.1 Nitrogen physisorption

Nitrogen physisorption measurements were used to examine the surface area, pore volume and pore size distribution of nanoporous silica nanoparticles. The standard method applied for the surface area assessment is BET (Brunauer-Emmett-Teller), which is the most widely used for nonporous, macro- and nanoporous materials. The surface area of nanoporous materials calculated by BET is the effective area available for the adsorption of the adsorbable gas, in this case, nitrogen.

The BJH (Barett, Joyner, Halenda) method is the standard procedure for calculating the pore size distribution of porous materials. However, it was found that this method can underestimate the pore size of nanomaterials by 20-30%. To obtain more accurate results, the pore size distribution can be calculated by applying a molecular model of adsorption such as the non-local density functional theory (NLDFT). This and other methods based on DFT and molecular simulations should be used as standard methods for pore size analysis according to the International Standard Organization (ISO).

In this work, nitrogen adsorption-desorption measurements were performed at 77 K using Quantachrome Autosorb-1 apparatus (Quantachrome Instruments, Boynton Beach, Florida, USA) by NATALJA WENDT, JAN LIPPKE, NADJA SCHMIDT, MANDY JAHNS and ALEXANDER MOHMEYER. Samples were outgassed in dynamic vacuum at 100 °C for 1 day before starting the measurements. To determine the specific surface areas and pore volumes, the ASiQWin 2.0 software from Quantachrome was applied. The BET surface area was calculated from the adsorption data in the range of p/p_o = 0.05 to 0.3 for all samples. The pore volume was calculated at p/p_o = 0.9. The pore size distribution was determined by applying the NLDFT-N_2-silica adsorption branch kernel at 77 K, cylindrical pore model.

3.1.2 Fourier transform infrared (FTIR) spectroscopy

FTIR spectroscopy serves to analyse the molecule structure. This technique is based on the characteristic absorption of the electromagnetic radiation by molecules correlating with the vibration frequencies of the atoms of the molecules. Consequently, an IR spectrum is generated by recording the absorbed or transmitted radiation at the certain wavelength.

In this work, FTIR spectroscopy was used to provide insights into the successful modification of NPSNPs and integration of those into the PCL and collagen scaffolds. The samples were analysed by FTIR spectroscopy applying the attenuated total reflexion (ATR) technique and using Bruker Tensor 27 spectrometer (Bruker Optics GmbH, Germany). All spectra were recorded by the OPUS software (Bruker) in the range of between 500 cm^{-1} - 4000 cm^{-1} with a 2 cm^{-1} resolution.

3.1.3 Thermogravimetric (TG) and carbon/sulphur (C/S) analyses

TGA is one of several complementary techniques used to identify the composition of a sample. The weight loss of the analysed material is measured as a function of the increasing temperature in a defined atmosphere. The weight change is associated with the decomposition of organic components and allows for quantitative composition analysis.

TGA measurements were performed with non-modified and modified NPSNPs using a Netzsch 429 thermoanalyzer (Netzsch-Gerätebau GmbH, Selb, Germany) by KATHARINA NOLTE, SERGEJ SPRINGER and DENNES NETTELROTH. Samples were filled in alumina crucibles and heated up in a flow of air using a temperature ramp of 5 °C min^{-1} from 25 °C up to 1000 °C. The measured weight loss between 120 °C and 700 °C was associated with the decomposition of grafted organosilane groups and then converted into the amount of these groups per gram of nanoporous silica nanoparticles (Eq. 1 and 2).

$$m_{Organosilane} = m_0 \cdot \frac{wt.\%}{100\%} \tag{1}$$

$$n_{Organosilane} = \frac{m_{Organosilane}}{M_{Hydrolysed\ organosilane} \cdot (m_0 - m_{Organosilane})}, \tag{2}$$

where $m_{Organosilane}$ (mg) is the mass of decomposed organic groups, m_0 (mg) is the initial mass of the sample, $wt.\%$ (%) is the weight loss in the range of 120 °C and 700 °C, $n_{Organosilane}$ (mmol g^{-1}) is the molar amount of grafted organic groups on the surface of 1

gram of NPSNPs and $M_{Hydrolysed\ organosilane}$ (g mol^{-1}) is the molar mass of hydrolysed grafted organic groups.

PCL- or collagen-NPSNP nanocomposite samples were cut into small pieces and filled in alumina crucibles and heated in a flow of air using a temperature ramp of 5 °C min^{-1} from 25 °C up to 1000 °C. The measured weight loss between 120 °C and 700 °C was associated with the decomposition of organic components of the scaffolds. The amount of integrated NPSNPs was calculated from the weight of inorganic residues.

The carbon and sulphur content of non-modified and modified NPSNPs was determined by using ELTRA CS 2000 (Neuss, Germany) by CLAUDIA SCHULZE. For that, the sample was filled in a crucible and burned in a flow of oxygen. The resulting gases, CO_2 and SO_2, were detected by IR spectroscopy. Carbon and sulphur amounts of the analysed sample could be quantified by means of standard samples with known carbon and sulphur content.

3.1.4 Dynamic light scattering (DLS) and zeta potential

DLS is a well-established method, which is widely used to measure the size and the size distribution of a variety of particles, including nanoparticles, proteins and protein aggregates.

DLS measuring principle is based on the scattering of the light from particles and their inherent Brownian motion. The intensity of the elastic light scattering is proportional to the sixth power of the particle's radius when the particle size is smaller than the wavelength of the incident light. The intensity fluctuations of the scattered light occur due to the Brownian motion and provide information about the diffusion coefficient (D) of the particles in the medium. By using the STOKES-EINSTEIN relationship and the diffusion coefficient D, the hydrodynamic radius of spherical particles can be calculated by equation 3:

$$D = \frac{k_B \cdot T}{6 \cdot \pi \cdot \eta \cdot R} \tag{3}$$

D	Diffusion coefficient
k_B	Boltzmann's constant
T	Temperature
η	Solvent viscosity
R	Hydrodynamic radius

In addition, DLS is one of the methods that is used for monitoring and studying protein aggregation under various conditions and concentrations. This information can be helpful to control protein aggregation.

Zeta potential is the potential difference between the surface of a particle and the surrounding solvent and is a key indicator of the colloidal stability of dispersions. Electrophoresis is used to determine the zeta potential of a dispersion. In practice, an electric field is applied across the dispersion. The electrophoretic velocity, with which charged particles migrate towards the electrode with the opposite charge, is proportional to the electrophoretic mobility, which can be measured by means of the light scattering. By using the HENRY equation, the zeta potential of a dispersion can be calculated by equation 4:

$$\mu \cdot e = 2 \cdot \varepsilon \cdot \zeta \cdot f[ka]/3 \cdot \eta \tag{4}$$

$\mu \cdot e$	Electrophoretic mobility
ε	Dielectric constant
ζ	Zeta potential
$f[ka]$	HENRY function
η	Viscosity

In general, particle dispersions are considered colloidally stable, when zeta potential values are above + 20 mV or under – 20 mV resulting in an electrostatic repulsion of equally charged particles. However, by changing the pH of the solvent, zeta potential can be diminished, so that particle aggregation takes place. Besides particles, the zeta potential of proteins can be measured to study pH- and concentration-dependent protein aggregation.

All DLS and zeta potential measurements were performed using a Zetasizer Nano ZS and an MPT2 autotitrator (Malvern Instruments Ltd., Worcestershire, UK). A detailed description of the measurements is described in the sections 3.3.5, 3.3.6, 3.3.8 and 3.3.10.

3.1.5   Scanning and transmission electron microscopy (SEM and TEM)

Electron microscopy is a powerful tool to study the morphology of a sample. SEM and TEM are the most commonly used electron microscopes. Both microscopes work using an electron beam. In SEM, the electron beam scans the sample surface producing scattered electrons, which are used for sample imaging. In contrast, TEM uses transmitted electrons that pass through the thin sample. In addition, TEM offers greater magnification and higher resolution.

The SEM micrographs of PCL- and collagen-NPSNP nanocomposites were taken using JEOL JSM-6610LV (JEOL Ltd., Tokyo, Japan) by INGA WILLE. The nanocomposites were

cut into small pieces, attached to a double-coated carbon conductive tab on an aluminium specimen holder and sputter coated for 30 s with gold to prevent charging of the specimen.

TEM micrographs were taken using FEI Tecnai G2 F20 TMP (FEI, Oregon, USA) operated at 200 kV in the Laboratory of Nano and Quantum Engineering (LNQE). Dispersions of the particles in ethanol were dropped on a carbon-coated Cu grid and dried under reduced pressure overnight.

3.1.6 Enzyme-linked immunosorbent assay (ELISA) for BMP-2 quantification

ELISA is a plate-based assay used to detect and quantify peptides, proteins, antibody and hormones. The so-called "sandwich" ELISA is the most powerful because it is sensitive and robust. In the first step of ELISA, a capture antibody is passively bound to the surface of the well-plate. Then, the sample containing the protein (also called antigen) is given into the wells. After some time, the antigen that was not "captured" by the antibody is washed off and a biotin-conjugated detection antibody is added to the wells. After a certain incubation time, the antibody-antigen-antibody complex or so-called "sandwich" is formed. For the detection, streptavidin with a conjugated enzyme, mostly horseradish peroxidase (HRP), is used. The enzyme converts a chromogenic substrate to a detectable product. A suitable substrate is 3, 3', 5, 5'-tetramethyl-benzidine that is converted into the yellow 3, 3', 5, 5'-tetramethyl-benzidine diimine. If ELISA was performed properly, the intensity of the signal will be directly proportional to the amount of the captured antigen (Figure 14).
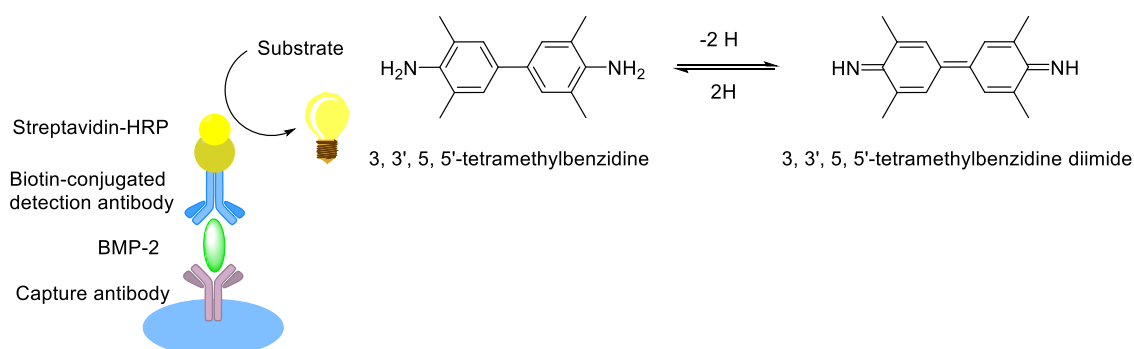
Figure 14: Schematic illustration of the "sandwich" ELISA, which was used for the detection of BMP-2, and oxidation of the substrate 3, 3`, 5, 5`-tetramethylbenzidine to the yellow 3, 3`, 5, 5`-tetramethylbenzidine diimine. The intensity of the yellow product is proportional to the BMP-2 amount.

In this work, the amount of BMP-2 after the absorption to the surface of NPSNPs and the release from them was quantified by a "sandwich" ELISA according to the manufacturer's instructions. The BMP-2 amount adsorbed on the surface of NPSNPs was determined by subtraction the BMP-2 amount in the supernatant from the initial BMP-2 amount. The released BMP-2 was detected directly in the release medium. For each particle type, the experiments were performed in triplicates. The results were reported as averages ± standard deviation of the mean.

3.1.7 BRE-Luc assay for BMP-2 quantification

The BRE-Luc assay is a highly sensitive and rapid cell-based assay for quantification of biologically active BMP-2 [263]. For that, stably transfected mouse myoblast cell line (C2C12) containing a BMP-responsive element (BRE) coupled to the firefly luciferase reporter gene (Luc) are needed. The addition of BMP-2 to the cells induces the BMP-related Smad signalling pathway within the cells. Subsequently, the luciferase reporter gene is switched on resulting in the production of luciferase. The activity of the produced luciferase was measured by using luciferin as substrate (Figure 15). The photons emitted during this reaction can be detected as luminescence after 24 h of exposure to BMP-2. The luminescence intensity is proportional to the BMP-2 amount. The main advantage of this assay compared to ELISA is the detection of biologically active BMP-2, which helps to assess the performance of BMP-2-loaded NPSNPs for future biomedical applications. The exact procedure of BRE-Luc assay performed in this work is given in section 3.3.11.
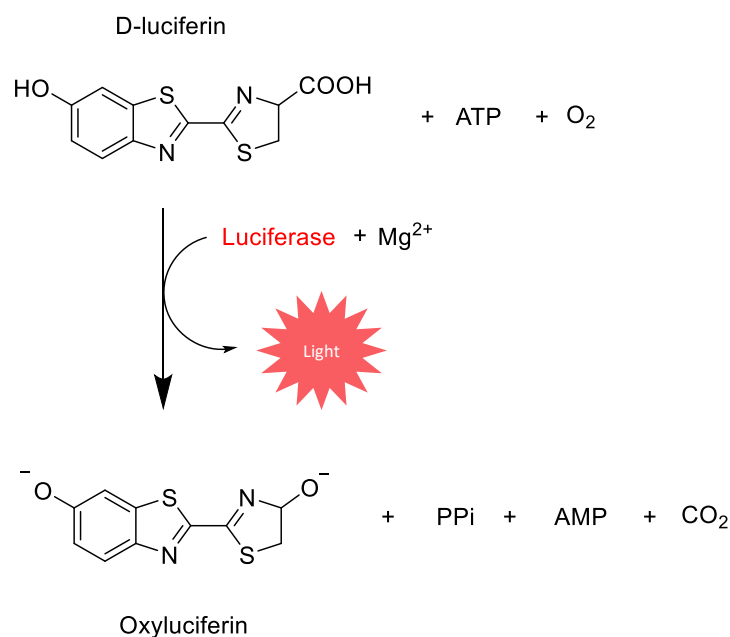
Figure 15: Conversion of luciferin into oxyluciferin by luciferase. The intensity of the luminescence is proportional to the BMP-2 amount.

3.1.8 Quantitative real-time polymerase chain reaction (qRT-PCR) for gene expression

The addition of BMP-2 to the mesenchymal stem cells triggers the expression of so-called immediate early genes, namely *Id1* and *Id3*. The quantification of the expressed genes was performed using quantitative real-time PCR. For that, messenger RNA was first isolated from the cells and then reverse-transcribed to complementary DNA with reverse transcriptase.

The principle of a basic PCR is the amplification of DNA by means of a thermostable polymerase. To begin the amplification the temperature is raised to 95 °C to denature the double-stranded DNA into single strands. After that, the reaction temperature is lowered down to 60 °C, which allows the primer to bind to the gene of interest. The primers are starting points for the polymerase reaction to generate new DNA strands of the desired gene sequence. After the copying process is completed, there are two copies of the gene instead of one at the beginning. These temperature changes are usually repeated for 40 cycles, generating copies of the target sequence exponentially.

The same principle of amplification is used in the quantitative real-time PCR. However, a sequence-specific DNA probe which is labelled with a fluorescent reporter and a quencher is additionally added to the reaction mixture. This probe binds downstream of the primer before the polymerase reaction and is fluorescently inactive. During the PCR the probe is cleaved by the polymerase. Subsequently, the fluorescent reporter and quencher are separated from each other resulting in a fluorescence signal, which increases and is measured after every PCR cycle in real-time. As a result, fluorescence intensity can be plotted against cycle number. The number of the cycle, at which the fluorescence signal passes a certain threshold, is called the threshold cycle (C_T). For quantification of the desired gene, the C_T of this gene is subtracted from the C_T of a normalized gene with the known quantity (Eq. 5):

$$\Delta C_T = \frac{E^{-C_T \text{ (target gene)}}}{E^{-C_T \text{ (normalized gene)}}} \tag{5}$$

Where *E* is the efficiency of PCR. It is set to 2, when the amount of DNA is doubled after one cycle of PCR (Eq. 6).

$$\Delta C_T = \frac{2^{-C_T \text{ (target gene)}}}{2^{-C_T \text{ (normalized gene)}}} = 2^{-(C_T \text{ (target gene)} - C_T \text{ (normalized gene)})} \tag{6}$$

When the expression of the target gene should be compared among different samples, the so-called $2\text{-}\Delta\Delta C_T$ method is used (Eq. 7). The $\Delta\Delta C_T$ values are often called as fold change.

$$\Delta\Delta C_T = \frac{\Delta C_T(\text{sample 1})}{\Delta C_T(\text{sample 2})} \qquad (7)$$

The procedure of the gene quantification by qRT-PCR is given in the section 3.3.14.

3.1.9 Cell viability assay

To investigate the cytotoxicity of non-modified and modified NPSNPs, a 3-(4,5-dimethylthiazol-2-yl)-2,5-diphenyltetrazolium bromide (MTT) assay is often used. Hereby, viable cells with active metabolism convert yellow water-soluble MTT into purple coloured formazan (Figure 16). The intense purple colour is detected by UV-Vis spectrophotometry at the absorbance maximum of 570 nm. Ideally, the quantity of formazan is proportional to the number of metabolic active viable cells and thus, to the cell viability. The exact cellular mechanism of MTT reduction into formazan is not well understood, but probably involves the oxidation of nicotinamide adenine dinucleotide (NADH) to NAD^+. A detailed description of the measurements is described in the section 3.3.13.
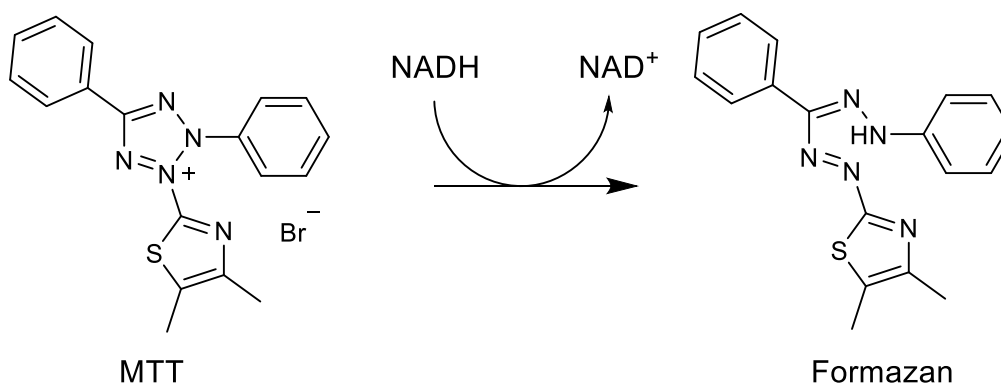
Figure 16: Reduction of yellow MTT into purple formazan by NADH. This reaction takes place only in viable cells with active metabolism.

3.1.10 Histochemical stainings

To investigate the three-dimensional osteogenic differentiation of human adipose-derived mesenchymal stem cells (hASCs) in collagen-NPSNP-BMP-2 nanocomposites, Alizarin Red S, Calcein and von Kossa stainings are often used (Figure 17). These staining principles are based on the detection of the extracellular calcium or phosphate

deposits, which are only present in differentiated osteoblasts. Calcium deposits can be specifically stained with Alizarin Red S and Calcein, showing bright orange-red colour or green fluorescence, respectively. Von Kossa staining indicates phosphate by the reaction with silver ions. After the exposure to UV light, silver ions are reduced to elementary silver, which can be visualized as brownish deposition on the cells.

In addition, cell nuclei can be stained with 4',6-diamidino-2-phenylindole (DAPI) demonstrating blue fluorescence (Figure 17).

To study the viability within the collagen scaffolds, live/dead cell viability assay can be performed. It is a fluorescence-based method to simultaneously distinguish between live and dead cells. Viable cells with intact esterase activity react with the cell-permeant Calcein AM producing an intense uniform green fluorescence. In contrast, ethidium homodimer enters only dead cells with a damaged membrane producing a bright red fluorescence.

Detailed description of the experiments for osteogenic differentiation of hASCs and different staining procedures are given in sections 3.3.25 and 3.3.26.
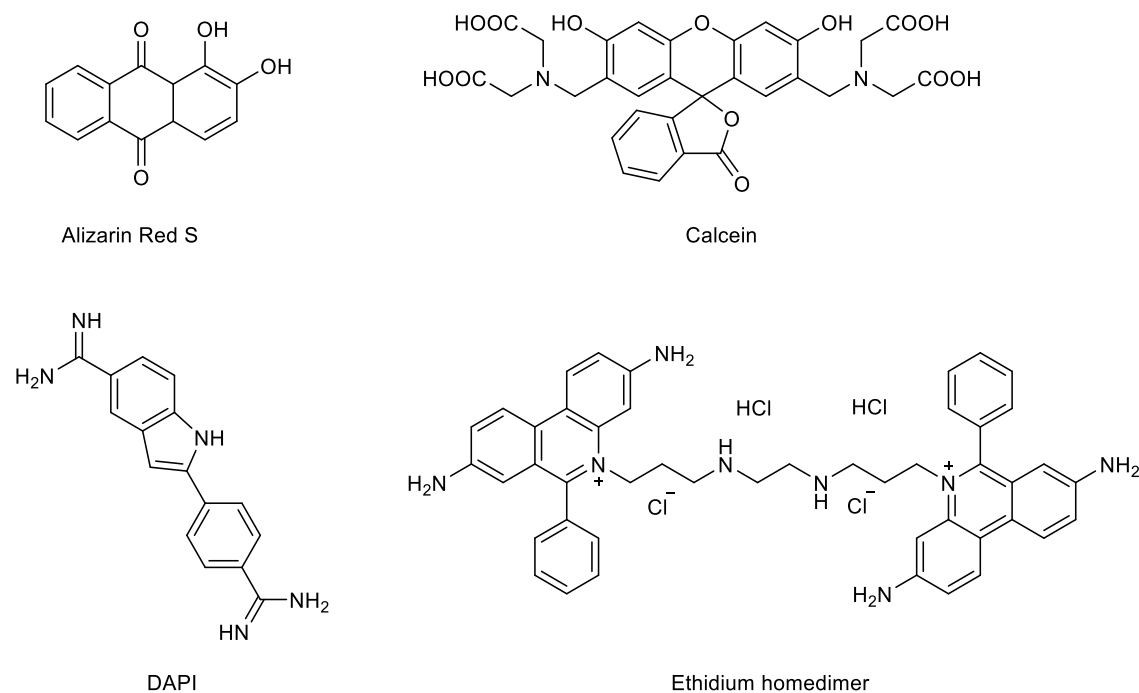
Figure 17: Molecular structures of different stainings.

3.2 Materials

3.2.1 Chemicals for the syntheses of non-modified and organosilane-modified nanoporous silica nanoparticles

All chemicals, including cetyltrimethylammonium bromide (CTAB), >98%; diethanolamine (DEA) puriss, >99%; tetraethylorthosilicate (TEOS), 98%; toluene, anhydrous, 99.8%; (3-aminopropyl)triethoxysilane (APTES), >98%; (3-mercaptopropyl)trimethoxysilane, 95%; 1,8-diazabicyclo[5.4.0]undec-7-ene (DBU), puriss, >99%; *N*,*N*-dimethylformamid (DMF), anhydrous, 99.8%; succinic anhydride, >99%; 2-(*N*-morpholino)ethanesulfonic acid monohydrate (MES), >99.5%; hydrogen peroxid solution (H_2O_2), meets analytical specification of Ph.Nord., 34.5-36.5%; were purchased from Sigma-Aldrich Chemie GmbH (Munich, Germany) and used without further purification. *N*-(6-aminohexyl)aminomethyltriethoxysilane, 92%; *N*-(6-aminohexyl)aminopropyltrimethoxysilane, 92%; were purchased from abcr GmbH (Karlsruhe, Germany). Absolute ethanol was purchased from Merck (Darmstadt, Germany). For all experiments ultrapure water (max. resistance at 25 °C 18.2 MΩ cm) purified by Milli-Q® integral system from Merck Millipore (Darmstadt, Germany).

3.2.2 BMP-2 and ELISA sources

The recombinant human (rh) BMP-2 was produced by BASTIAN QUAAS from the Institut für Technische Chemie, Leibniz Universität Hannover, Hannover, Germany. Hereby, the recombinant human (rh) BMP-2 was expressed in *Escherichia coli* (*E. coli*), isolated from the inclusion bodies, followed by *in vitro* refolding and purification as previously described by [224].

For investigations of collagen-NPSNP-BMP-2 nanocomposites *E.coli* derived rhBMP-2 (120-02) from PeproTech (Hamburg, Germany) was used.

BMP-2 standard TMB ELISA development kit (900-T255) for BMP-2 quantification and TMB ELISA buffer kit (900-T00) were purchased from PeproTech (Hamburg, Germany).

3.2.3 Chemicals for different buffers

Sodium acetate, ≥99%; 2-(*N*-morpholino)ethanesulfonic acid (MES), ≥99%; 2-(*N*-morpholino)propanesulfonic acid (MOPS), ≥99.5%; phosphate buffered saline (PBS), disodium hydrogen phosphate, ≥99% and potassium dihydrogen phosphate, ≥99% for Soerensen buffer, tris(hydroxymethyl)aminomethane (TRIS), ≥99.9%; *N*-cyclohexyl-2-

aminoethanesulfonic acid (CHES), ≥99%;   *N*-cyclohexyl-2-aminopropanesulfonic acid (CAPS), ≥99%; 1 M hydrochloric acid and sodium hydroxide solutions were purchased from Sigma-Aldrich Chemie GmbH (Munich, Germany) and used without further purification.

3.2.4 PCL, alginate and collagen sources

PCL (M_n=80.000) and chitosan (M_n=110.000-150.000) were purchased from Sigma-Aldrich Chemie GmbH (Munich, Germany).

Sodium alginate was purchased from Sigma Aldrich Chemie GmbH (Munich, Germany). Alginate was dissolved in deionized water (20 mg ml^{-1}) and dialyzed against deionized water. The product was lyophilized and characterized with ^{1}H-NMR spectroscopy.

The collagen scaffolds "KOLLAGEN resorb™" were purchased from RESORBA Medical GmbH (Nürnberg, Germany).

3.2.5 Chemicals for cell culture investigations

For the cell culture-based experiments the following chemicals and solvents were used: DMEM FG0415, DMEM F0445, penicillin/streptomycin, HEPES, glutamine, PBS, trypsin, were purchased from Biochrom (Berlin, Germany). FCS Hyclone, FCS South American, TRIzol, Taqman® Fast Advanced Master Mix, Taqman® gene expression assays for human RPS29 (Hs03004310_g1), Id1 (Hs03676575_s1) and Id3 (Hs00171409_m1) were purchased from Thermo Fisher Scientific (Waltham, USA). 2 ng ml^{-1} FGF-2 was purchased from PeproTech (Hamburg, Germany). Dexamethasone and 1-bromo-3-chloropropane were purchased from Sigma-Aldrich Chemie GmbH. Ascorbic acid, 2-propanol and ethanol p.a.abs. were purchased from Carl Roth (Karlsruhe, Germany). *β*-glycerophosphate-pentahydrate was purchased from Honeywell Fluka (Schwerte, Germany). Luciferase Cell Culture Lysis Reagent, Steady-Glo® Luciferase Assay System and CellTiter 96® Non-Radioactive Cell Proliferation Assay (MTT) was purchased from Promega (Madison, USA).

Live/Dead cell viability assay, Calcein and 4',6-diamidino-2-phenylindole (DAPI) stain kits were purchased from Thermo Fisher Scientific (Waltham, USA). Alizarin Red S and von Kossa stain kits were purchased from Sigma-Aldrich Chemie GmbH (Munich, Germany).

3.3   Experimental

3.3.1   Synthesis of nanoporous silica nanoparticles (NPSNPs)

Nanoporous silica nanoparticles (NPSNPs) were synthesized by the following procedure [55]: CTAB (3.16 g, 8.67 mmol) and DEA (0.23 g, 2.19 mmol) were first dissolved in 75 ml of ultrapure water and 13.4 ml of absolute ethanol followed by stirring the solution for 30 mins and heating up to 40 °C. Then TEOS (8.56 ml, 38.63 mmol) was added dropwise to the surfactant solution. The mixture was allowed to stir for 2 h, giving a white precipitate. Finally, the white suspension was centrifuged, washed several times with ultrapure water and absolute ethanol, and was dried over night at 60 °C. To remove the organic template, the dried product was calcined at 550 °C for 5 h with a heating rate of 1 K min^{-1}.

3.3.2   Modification of NPSNPs

To introduce functional groups on the surface of NPSNPs, a post-grafting technique was applied, adapted from [264]. First, calcined NPSNPs (500 mg) were dispersed in 20 ml of toluene. Next, (3-aminopropyl)trimethoxysilane (125 µl, 0.53 mmol) and 1,8-diazabicyclo[5.4.0]undec-7-ene (DBU) (75 µl, 0.50 mmol) were added to synthesize aminopropylsilyl-modified NPSNPs. After that, the suspension was heated up to 80 °C and stirred for 2 h. Subsequently, the particles were centrifuged, washed several times with ultrapure water and absolute ethanol, and dried at 60 °C overnight.

The same procedure was applied for the post-grafting with other silanizing agents (Figure 18). For the synthesis of mercaptopropylsilyl-modified NPSNPs (3-mercaptopropyl)-trimethoxysilane (125 µl, 0.67 mmol) and DBU (75 µl, 0.50 mmol) was added. For the synthesis of NPSNPs with −methyl-NH-hexyl-NH$_2$ and −propyl-NH-hexyl-NH$_2$ groups *N*-(6-aminohexyl)-aminomethyltriethoxysilane   (240 µl, 0.70 mmol)   and   *N*-(6-amino-hexyl)aminopropyltrimethoxysilane (191 µl, 0.7 mmol) with DBU (75 µl, 0.50 mmol) was added to the calcined NPSNPs (500 mg), respectively.
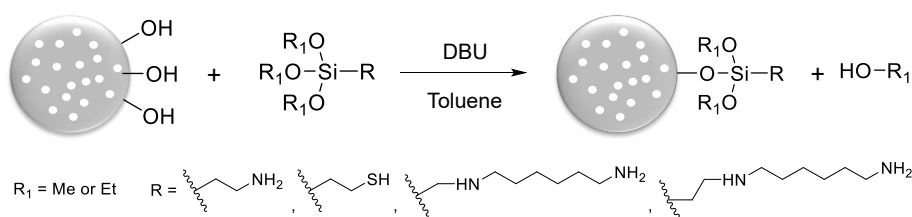
Figure 18: Modification of NPSNPs with different organosilanes.

To prepare sulfonic acid modified NPSNPs, previously synthesized mercaptopropylsilyl-modified NPSNPs (100 mg) were stirred in 10 ml of H_2O_2 ($\approx$35%) at room temperature for 12 h (Figure 19). Subsequently, the particles were centrifuged, washed several times with ultrapure water, and dried at 60 °C overnight.
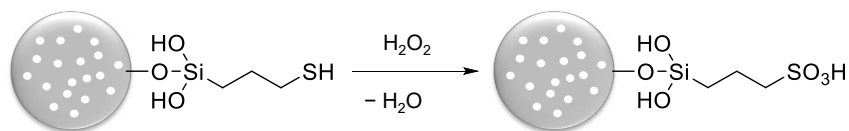
Figure 19: Synthesis of sulfonic acid modified NPSNPs.

For the preparation of carboxy-modified NPSNPs aminopropylsilyl-modified NPSNPs (400 mg) were suspended in 20 ml of DMF followed by an addition of succinic anhydride (2 g, 20.00 mmol) to the suspension (Figure 20). The suspensions were allowed to stir over night at room temperature. Finally, the particles were centrifuged, washed several times with ultrapure water and absolute ethanol, and dried at 60 °C over night.
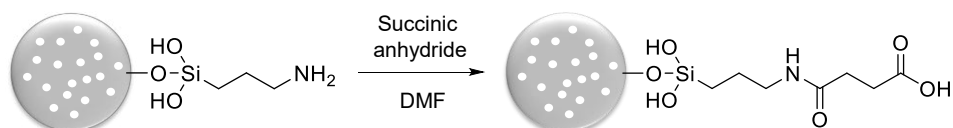
Figure 20: Synthesis of carboxy-modified NPSNPs.

3.3.3   Hydrolytic stability tests of aminopropylsilyl-modified NPSNPs

In order to investigate the hydrolytic stability, aminopropylsilyl-modified NPSNPs (500 mg) were suspended in 8 ml of ultrapure water and stirred for 64 h at room temperature. Then the particles were centrifuged and dried under low pressure.

3.3.4   Treatment of the immersed aminopropylsilyl-modified NPSNPs with DMF

To prove whether the porosity can be regained by stirring in DMF, 200 mg of the nanoporous silica nanoparticles after the hydrolytic stability tests were suspended in 10 ml of DMF and stirred at room temperature for 12 h or at 155 °C for 1 h.

3.3.5   pH-dependent zeta potential measurements of NPSNPs

pH-dependent zeta potential measurements were performed using a Zetasizer Nano ZS and a MPT2 autotitrator (Malvern Instruments Ltd., Worcestershire, UK). Hereby, 20 mg of each particle type were dispersed in 20 ml ultrapure water under ultrasound treatment for 10 min using a VWR Ultrasonic Cleaner (45 kHz, 60 W). The measurements were recorded starting from pH 10 until pH 2. The pH value was lowered in 0.5 steps. At each pH value the zeta potential was measured in triplicates, and the average pH was calculated.

3.3.6   Zeta potential and dynamic light scattering (DLS) measurements of NPSNPs

In addition, zeta potential and DLS measurements were performed with all particles types dispersed in MES buffer at pH 5. For this, 2 mg of the NPSNPs were sonicated for 10 min in 2 ml of MES buffer using a VWR Ultrasonic Cleaner (45 kHz, 60 W). 0.9 ml of each dispersion were transferred into polystyrene disposable cuvette. Particle scattering was detected with 173° angle detector. Affiliated zeta potential and DLS data were evaluated with the Zetasizer software from Malvern. The average zeta potential and particle size ± standard error of the mean were calculated from the triple measurements.

3.3.7   Preparation of different buffers for BMP-2

Sodium acetate (pH 4), MES (pH 5 and 6), MOPS (pH 6 and 7), PBS (pH 7), Soerensen (pH 7.4), Tris (pH 8), CHES (pH 9.5) and CAPS (pH 11) buffers with a concentration of 50 mM were prepared by dissolving an appropriate amount of the chemicals in 1 l of ultrapure water. The pH was adjusted with 1 M HCl or NaOH.

3.3.8   Characterisation of BMP-2 by zeta potential and DLS measurements

The zeta potential and size of BMP-2 was determined by using Zetasizer Nano ZS (Malvern Instruments Ltd., Worcestershire, UK). To measure the zeta potential, BMP-2 solution with a concentration of 130 µg ml^{-1} was necessary. This was the lowest BMP-2 concentration that could be measured by Zetasizer Nano ZS. Hereby, a so-called diffusion barrier technique was applied, in which first, the disposable zeta potential cell was filled with 900 µl of the buffer, and second, 100 µl of BMP-2 sample was placed of the bottom of the cell using long pipette tip. This technique protects the protein from

damage caused by the measurement. DLS measurements were carried out at different BMP-2 concentration (66, 33 and 16 µg ml^{-1}) in MES buffer at pH 5. In addition, DLS measurements of BMP-2 in different buffers, namely sodium acetate, MES, MOPS, PBS, Soerensen, TRIS, CHES and CAPS, were performed at a concentration of 25 µg ml^{-1}. Each solution was transferred into polystyrene disposable cuvette. Particle scattering was detected with 173° angle detector. Affiliated zeta potential and DLS data were evaluated with the Zetasizer software from Malvern. The average zeta potential and particle size ± standard error of the mean were calculated from the triple measurements.

3.3.9   BMP-2 loading on non-modified and differently modified NPSNPs

The loading of BMP-2 on the surface of NPSNPs were carried out under aseptic conditions. The NPSNPs were sterilized under UV light for 30 min, and BMP-2 solution was sterile-filtered. Non-modified and each type of differently modified NPSNPs (5 mg) were suspended in 0.5 ml of MES buffer under ultrasound treatment for 10 min using a VWR Ultrasonic Cleaner (45 kHz, 60 W). After that 0.5 ml of a BMP-2 solution (10 µg ml^{-1}) in MES buffer was added to the particle dispersion, and the mixture was shaken at 350 rpm and 4 °C for 24 h in a thermomixer (Biozym Scientific GmbH, Germany) to produce BMP-2-loaded NPSNPs. Then, the BMP-2-loaded NPSNPs were separated by centrifugation (10000 rpm, for 10 mins) and used for the subsequent release experiments. Taken together, 5 µg of BMP-2 were offered for loading on the surface of 5 mg NPSNPs resulting in the maximal theoretically adsorbed BMP-2 amount of 1 µg BMP-2 per 1 mg NPSNPs (1 µg mg^{-1}).
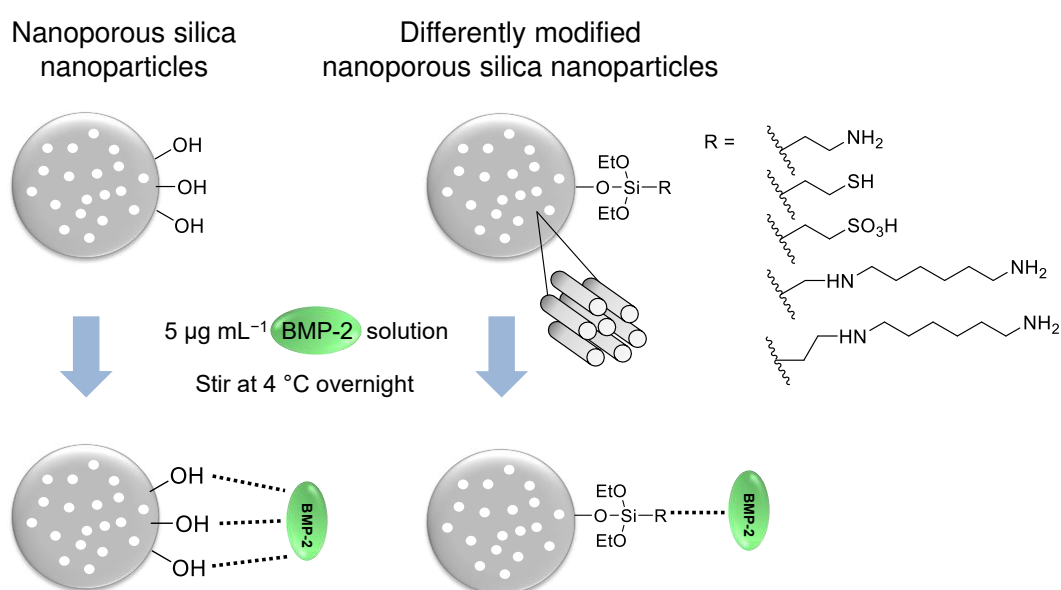
Figure 21: BMP-2 loading procedure on the surface of NPSNPs.

3.3.10 Characterisation of BMP-2-loaded NPSNPs by zeta potential and DLS

To study the changes of the surface chemistry and particle sizes of NPSNPs upon BMP-2 adsorption, each type of NPSNPs (50 µg) was mixed with different BMP-2 amounts, namely 0.05 µg, 0.25 µg, 1.25 µg and 2.5 µg, in MES buffer at pH 5. The total volume of each sample was 1 ml. The BMP-2-loaded NPSNPs were characterized by zeta potential and DLS measurements using Zetasizer Nano ZS (Malvern Instruments Ltd., Worcestershire, UK). 0.9 ml of each dispersion were transferred into polystyrene disposable cuvette. Particle scattering was detected with 173° angle detector. Affiliated zeta potential and DLS data were evaluated with the Zetasizer software from Malvern. The average zeta potential and particle size ± standard error of the mean were calculated from the triple measurements.

3.3.11 Quantification of adsorbed BMP-2 by BRE-Luc assay

The amount of the bioactive BMP-2 adsorbed on the surface of NPSNPs was determined by the cell-based BRE-Luc assay [263] . All BRE-Luc assays were performed by Laura Burmeister from the Klinik für Orthopädie im Annastift, Medizinische Hochschule Hannover, Germany. For that, stably transfected C3H10T1/2 cells containing BMP-responsive element coupled to the firefly luciferase reporter gene (BRE-Luc) were seeded at a density of 35,000 cells in 24-well plates using standard growth medium (DMEM F0445, 10% FBS South American Origin, 4 mM glutamine, 1% penicillin/streptomycin, 1 ml/well), after 4 h media was changed to serum-free growth medium, and the cells were cultured for 24 h. Next, 100 µl of BMP-2-loaded NPSNPs dispersed in MES buffer (5000 ng ml^{-1}) was added to the cells (dilution 1:5). After 24 h cells were washed with PBS and lysed with 70 µl Luciferase Cell Culture Lysis Reagent. The lysate was centrifuged at 4 °C for 10 min at 20,000 x g. Luciferase activity of the supernatant was measured in triplicate using 7.5 µl lysate and 25 µl Steady-Glo Luciferase Assay System reagent. Measurements of the luminescence intensity was performed after 5 min incubation with sensitivity being set to 135 and 1 sec integration time for all measurements using Synergy 2 from Biotek, (Winooski, USA). Since the luminescence intensity is directly proportional to the BMP-2 concentration in the range of 2-1000 ng ml^{-1}, the amount of adsorbed BMP-2 on the surface of NPSNPs could be determined directly by an appropriate calibration. Each experiment was performed in triplicates for each nanoparticle type. The averages ± standard deviation of the mean were calculated from these results.

3.3.12   Release of BMP-2 from the surface of NPSNPs

The release of BMP-2 was carried out with the previously BMP-2-loaded NPSNPs suspended in 1 ml of sterile-filtered MES buffer at pH 5 and 37 °C in a convection oven for a period of two weeks under aseptic conditions (Figure 22). At each time point, 200 µl of the supernatant was carefully removed without prior centrifugation and stored in vials at −20 °C for further analysis. The collected supernatant was replaced by 200 µl of the fresh MES buffer. The released BMP-2 amount in the supernatant was quantified by ELISA according to the manufacturer's instructions. For each particle type the experiments was performed in triplicates. The results were reported as averages ± standard error of the mean.
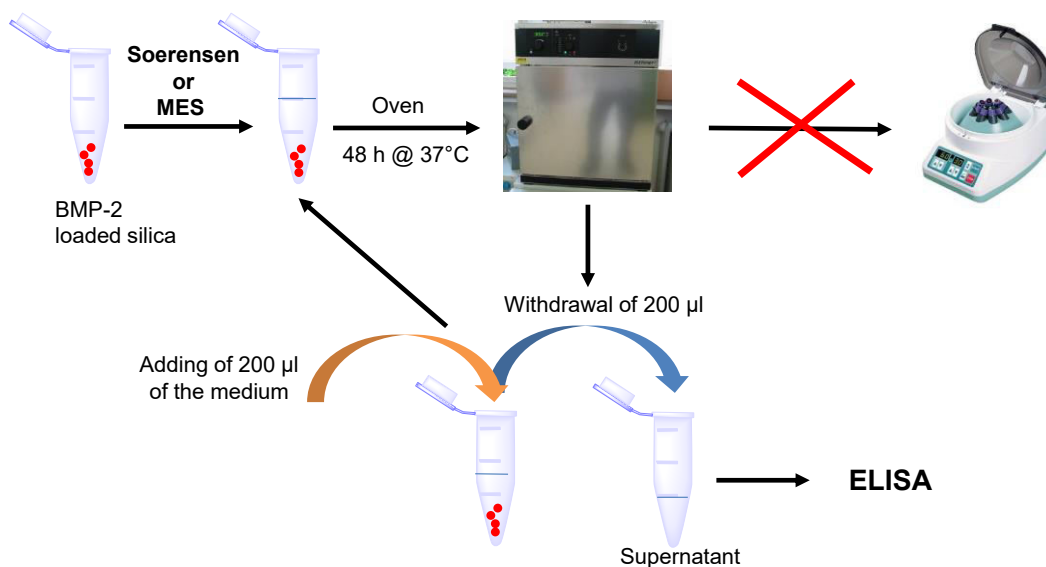
Figure 22: Schematic procedure of BMP-2 release from NPSNPs.

3.3.13   Cytotoxicity investigations

The cytotoxicity investigations were performed by LAURA BURMEISTER from the Klinik für Orthopädie im Annastift, Medizinische Hochschule Hannover, Germany.

For the cell culture experiments different media according to the cell type were used. Human bone marrow-derived stem cells (BM-MSCs) were cultivated in DMEM FG0415, 1% penicillin/streptomycin, 20 mM HEPES all purchased, 10% FCS Hyclone, 2 ng ml^{-1} FGF-2. The murine cell line C2C12 BRE-Luc (BMP-Responsive-Element-Luciferase)-pGL3 was cultivated in DMEM F0445, 1% penicillin/streptomycin, 4 mM glutamine and 10% FCS South American.

To evaluate the cytotoxicity of the differently modified NPSNPs cell viability assay, namely CellTiter 96® Non-Radioactive Cell Proliferation Assay analysing the oxidation

of NADH to NAD$^+$, was used. All cell types used in this study were analysed (BM-MSCs and C2C12 BRE-Luc). The cells were seeded at a density of 5000 c cm^{-2} in a 96 well plate. After 4 h the different NPSNPs solutions in concentrations between 0 and 1000 µg ml^{-1} were added to the cells. Measurement of cell viability took place after 1, 3 and 7 days. For the CellTiter 96® Non-Radioactive Cell Proliferation Assay 15 µl of dye solution were incubated for 4 h at 37°C followed by 1 h incubation of solubilisation solution at room temperature. Absorbance was recorded at 570 nm/630nm.

3.3.14 Gene expression of *Id1* and *Id3* and qRT-PCR

The gene expression and qRT-PCR investigations were performed by LAURA BURMEISTER from the Klinik für Orthopädie im Annastift, Medizinische Hochschule Hannover, Germany.

The addition of BMP-2 to stem cells triggers the expression of so called immediate early genes, namely *Id1* and *Id3*. To assess that, mesenchymal stem cells derived from bone marrow-derived stem cells were seeded at a density of 3000 c cm^{-2} and grown to confluence for 5 days. Then 250 µg ml^{-1} BMP-2-loaded NPSNPs were added to the cells and incubated for 2 h and 24 h. To isolate RNA the cells were harvested with 600 µl TRIzol and stored at −80 °C until further processing. Next, 60 µl 1-bromo-3-chloropropane were added to the TRIzol-harvested cells, mixed and centrifuged for 15 min at 20,000 x g and 4 °C. The supernatant was mixed with 300 µl 2-propanol to precipitate RNA, incubated for 5 min and centrifuged for 30 min at 20,000 x g and 4 °C. The obtained pellets were washed with 1 ml 80% ethanol and centrifuged for 15 min at 20,000 x g and 4 °C. After drying the pellets were dissolved in 20 µl dH$_2$O and incubated at 60 °C for 10 min to dissolve secondary structures. RNA concentration was determined using NanoDrop 2000c (Thermo Fisher Scientific).

Quantitative real-time-PCR was used to quantify the gene expression of *Id1* and *Id3* (*inhibitor of* differentiation *1* and *3*) using RPS29 (Ribosomal Protein S29) as housekeeping gene. The PCR was accomplished in a duplex run with TaqMan® Fast Advanced Master Mix using the StepOnePlus Real-Time PCR System (Applied Biosystems, Foster City, USA) with the following conditions: 20 s at 95 °C and 40 cycles of 1 s at 95 °C and 20 s at 60 °C. Differences between samples and controls were calculated based on 2-ΔΔCt method. Triplicate experiments were performed for all genes investigated.

3.3.15 Electrospinning of PCL scaffolds

A PCL solution of 17 wt.% in 2,2,2-trifluoroethanol was loaded into a syringe, which was connected by a Teflon tubing to an electrospinning emitter. A rotating steel drum covered with baking paper was used as a collector. The scaffolds were produced with a voltage of 25 kV for 2 h at a rotation speed of 8 m s^{-1}. The emitter to collector distance was at 25 cm. The solvent flow rate was set to 4 ml h^{-1}.

Poly(ε-caprolactone) (PCL) scaffolds used in this study were electrospun and coated by DOMINIC DE CASSAN from the Institut für Technische Chemie, Technische Universität Braunschweig, Germany.

3.3.16 Coatings of PCL scaffolds with chitosan-PCL graft copolymer ("shish-kebab" structures)

Preparation of the "shish-kebab" structures on the PCL scaffolds was performed according to literature [35]. For that, diluted solutions of chitosan-PCL graft copolymer have been used to form "shish-kebab" structures on the surface of the electrospun fibres by crystallization. To perform the coating, 0.5 wt.% of the copolymer was dissolved in 77 vol.% aqueous solution of acetic acid at 40° C for 1 h. After, the solutions were cooled down to room temperature, PCL fibres were plunged into the solution for 2 mins. Subsequently, the scaffolds were removed from the solutions and placed into a vacuum oven at room temperature for 24 h. During the process of solvent evaporation, the "shish-kebab" structures were formed.

3.3.17 Coating of "shish-kebab" structured PCL scaffolds with alginate

The prepared "shish-kebab"-structured PCL fibre mats were immersed into 5 mg ml^{-1} alginate solution for 2 mins. After that, fibre mats were rinsed with deionized water several times and subsequently dried in vacuum for 24 h at room temperature.

3.3.18 Determination of the total porosity of PCL$_{SK-Alg}$ scaffolds by a gravimetric method

The PCL$_{SK-Alg}$ scaffolds were punched out and had a diameter of 15 mm. The weight and the thickness of 20 round PCL$_{SK-Alg}$ scaffolds were measured using a laboratory scale and digital calliper (Top craft), respectively (Table S7, SI).

Based on the measured parameters and the density of bulk PCL total porosity of the electrospun PCL scaffolds could be determined using following equations [265]:

$$V = r^2 * \pi * h \tag{8}$$

$$V_{\mathrm{p}} = \frac{wt}{\rho_{\mathrm{PCL}}} \tag{9}$$

$$P_{\mathrm{Scaffold}} = \frac{V - V_p}{V} \times 100\%, \tag{10}$$

where r is the radius of the PCL$_{\text{SK-Alg}}$ scaffold, h is the average thickness of the PCL$_{\text{SK-Alg}}$ scaffold, V_{p} is the volume of the PCL$_{\text{SK-Alg}}$ fibres, wt is the average weight of the PCL$_{\text{SK-Alg}}$ scaffold, ρ_{PCL} is the density of the PCL, V is the total volume of the scaffold, P_{Scaffold} is the total porosity of the scaffold.

3.3.19 Preparation of PCL$_{\text{SK-Alg}}$-NPSNP nanocomposites without and with BMP-2

"Shish-kebab"-structured and alginate-coated PCL scaffolds measuring 15 mm in diameter, 0.35 mm in height and weighing roughly 14 mg were used for all *in vitro* experiments (Table S7, SI).

To prepare PCL$_{\text{SK-Alg}}$-NPSNP nanocomposites PCL$_{\text{SK-Alg}}$ scaffolds were simply immersed into a dispersion of NPSNPs (2 mg in 0.4 ml MES buffer) for 12 h. The unbound NPSNPs were washed off of the scaffolds with ultrapure water. The PCL$_{\text{SK-Alg}}$-NPSNP nanocomposites were dried under low pressure.

PCL$_{\text{SK-Alg}}$-NPSNP-BMP-2 nanocomposites were prepared to study the *in vitro* release of BMP-2. All further steps were carried out in a clean bench following aseptic techniques. For that, PCL$_{\text{SK-Alg}}$ scaffolds and NPSNPs were sterilized under UV light for 30 mins, and the BMP-2 dissolved in MES buffer was sterile-filtered. First, BMP-2 was loaded on the surface of NPSNPs according to the described previously procedure. Each type of differently modified NPSNPs (2 mg) were suspended in 0.2 ml of sterile-filtered MES buffer under ultrasonic treatment for 10 mins using a VWR Ultrasonic Cleaner (45 kHz, 60 W) to avoid particles agglomeration. After that 0.2 ml of a BMP-2 solution (10 µg ml^{-1}) in MES buffer was added to the particle dispersion, and the mixture was shaken at 350 rpm and 4 °C for 24 h in a thermomixer (Biozym Scientific GmbH, Germany) to produce BMP-2-loaded NPSNPs. Then, the BMP-2-loaded NPSNPs were separated by centrifugation at 10,000 rpm, dispersed in 0.4 ml MES buffer and loaded on the PCL$_{\text{SK-Alg}}$ scaffolds as described above. The removed supernatants were frozen at −20 °C for BMP-2 quantification by ELISA and BRE-Luc assay. Taken together, 2 µg BMP-2 were

offered for loading on the surface of 2 mg NPSNPs resulting in the theoretically adsorbed BMP-2 amount of 2 µg BMP-2 per 2 mg NPSNPs immobilized on one PCL$_{SK-Alg}$ scaffold.

3.3.20   Release of BMP-2 from PCL$_{SK-Alg}$-NPSNP-BMP-2 nanocomposites

The release of BMP-2 was carried out with the previously prepared PCL$_{SK-Alg}$-NPSNP-BMP-2 nanocomposites immersed into 1 ml of sterile-filtered phosphate buffered saline (PBS) containing 0.1% bovine serum albumin (BSA) and 0.02% Tween 20 as stabilizing agents for BMP-2, pH 7.4 and 37 °C in a convection oven for a period of five weeks under aseptic conditions without shaking (Figure 23). At each time point, the PCL$_{SK-Alg}$ scaffolds were removed and placed into a new vial containing 2 ml of fresh release medium. The release solution was stored in vials at −20 °C for further analysis. The released BMP-2 amount in the supernatant was quantified by ELISA according to the manufacturer's instructions. For each sample the experiments was performed in triplicates. The results were reported as averages ± standard deviation of the mean.
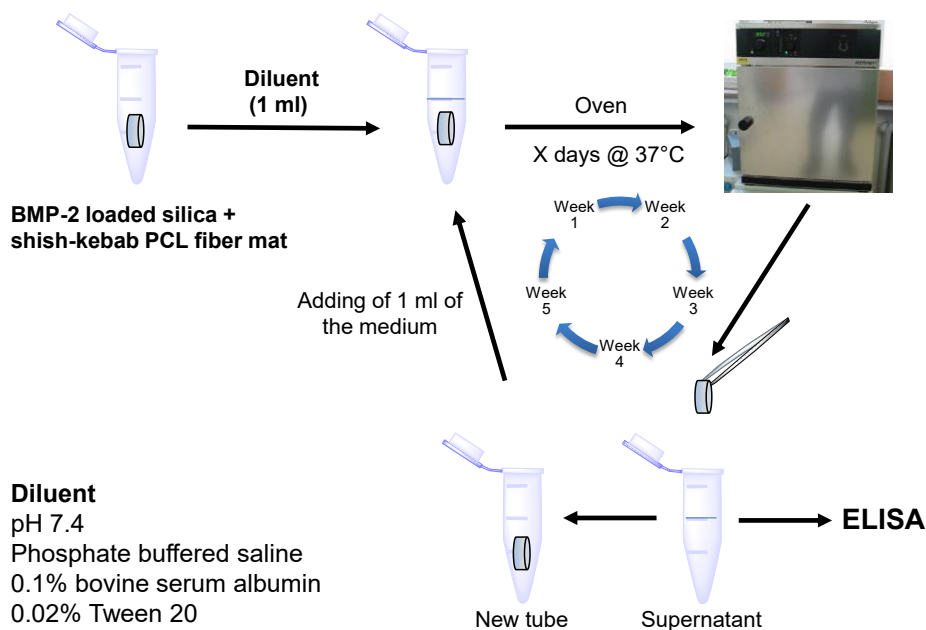
Figure 23: Schematic procedure of BMP-2 release from PCL$_{SK-Alg}$-NPSNP-BMP-2 nanocomposites.

3.3.21   Degradation of the PCL$_{SK-Alg}$-NPSNP nanocomposites for five weeks

For degradation investigations, PCL$_{SK-Alg}$-NPSNP nanocomposites were immersed into 1 ml of sterile-filtered PBS containing 0.1% BSA and 0.02% Tween 20 and placed in tightly closed plastic container (10 ml) (Figure 24). The *in vitro* degradation took place at 37 °C in a convection oven for a period of five weeks under aseptic conditions without

shaking. After 1, 2, 3 and 5 weeks of immersion small pieces were cut out of the samples, rinsed with ultrapure water and dried in vacuum at room temperature prior further characterization.
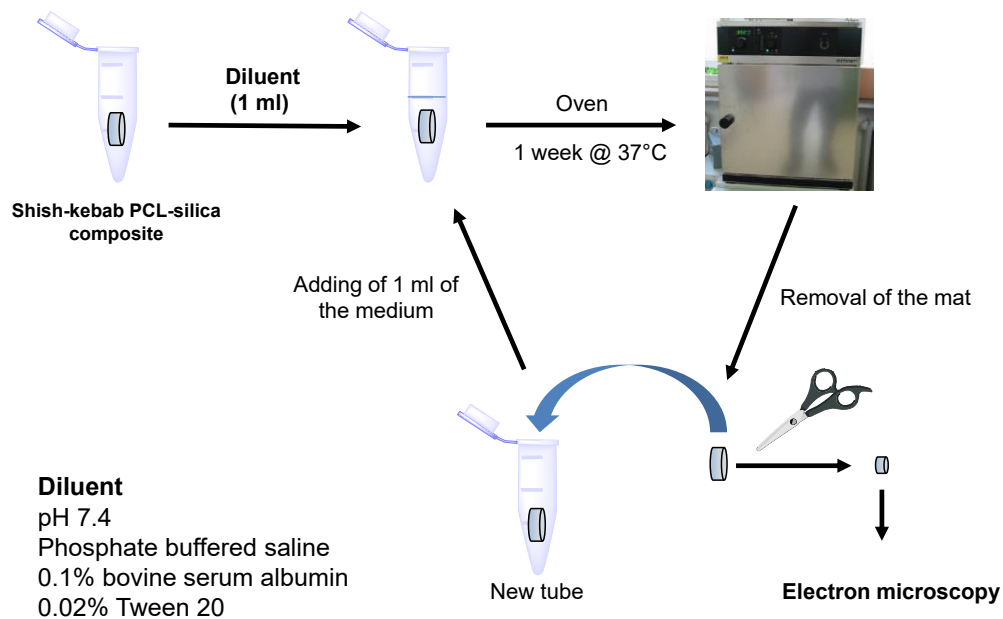
Figure 24: Schematic procedure of the degradation of PCL$_{SK-Alg}$-NPSNP-BMP-2 nanocomposites.

3.3.22 Preparation of collagen-NPSNP nanocomposites for TGA

Sterile "KOLLAGEN resorb™" scaffolds for wound dressing measuring 18 mm x 36 mm and weighing about 20 mg (2.8 mg collagen per 1 cm^2) were used for all experiments. Non-modified NPSNPs (20 mg) were dispersed in 10 ml ultrapure water and sonicated for 10 mins. PBS was omitted here, because of the precipitation of phosphate salts on the collagen. Next, collagen sponges (20 mg) were immersed into the nanoparticle dispersions. The dispersions were shaken at 350 rpm and room temperature for 1, 3, 19 and 24 h in a thermomixer (Biozym Scientific GmbH, Germany). After that, the collagen sponges were rinsed with ultrapure water to remove unbound NPSNPs and dried in a convection oven at 60 °C overnight.

3.3.23 Preparation of collagen-NPSNP-BMP-2 nanocomposites

Collagen-NPSNP-BMP-2 nanocomposites were prepared to study the release of BMP-2 (Figure 25). All further steps were carried out in a clean bench following aseptic techniques. For that, NPSNPs were sterilized under UV light for 30 mins.
To load BMP-2 on the surface of non-modified and aminopropylsilyl-modified NPSNPs, each type of NPSNPs (5 mg) were suspended in 0.5 ml of sterile-filtered phosphate

buffered saline (PBS) with 0.01% bovine serum albumin (BSA) under ultrasound treatment for 10 mins using a VWR Ultrasonic Cleaner (45 kHz, 60 W). BMP-2 was dissolved in phosphate buffered saline (PBS) with 0.01% bovine serum albumin (BSA) to a concentration of 10 µg ml^{-1}. After that, 0.5 ml of a BMP-2 solution (10 µg ml^{-1}) was added to the particle dispersion, and the mixture was shaken at 350 rpm and 4 °C for 24 h in a thermomixer (Biozym Scientific GmbH, Germany) to produce BMP-2-loaded NPSNPs. Then, the BMP-2-loaded NPSNPs were separated by centrifugation and the supernatants were frozen for later ELISA measurements.

Subsequently, collagen scaffolds were soaked in the dispersion of the BMP-2-loaded NPSNPs in 5 ml PBS containing 0.1% BSA and stirred for 24 h at room temperature. Taken together, 5 µg of BMP-2 were offered for loading on the surface of 5 mg NPSNPs resulting in the theoretically adsorbed BMP-2 amount of 5 µg BMP-2 per 5 mg NPSNPs and 1 collagen scaffold.
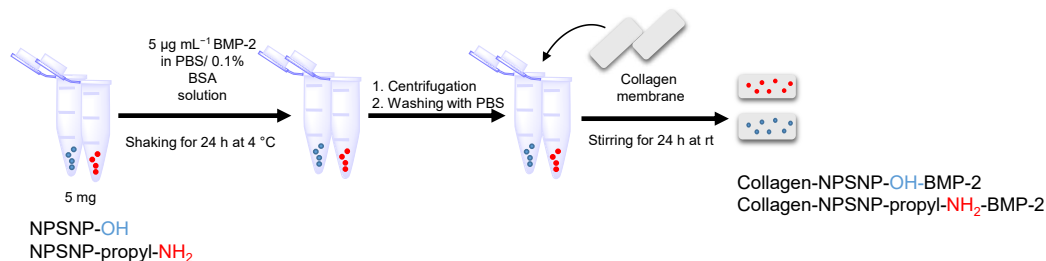
Figure 25: Schematic procedure of the preparation of collagen-NPSNP-BMP-2 nanocomposites.

3.3.24 Release of BMP-2 from the surface of collagen-NPSNP-BMP-2 nanocomposites

The release of BMP-2 was carried out with the previously prepared collagen-NPSNP-BMP-2 nanocomposites immersed into 2 ml of sterile-filtered PBS containing 0.1% BSA as stabilizing agent for BMP-2, pH 7.4 and 37 °C in a convection oven for a period of five weeks under aseptic conditions without shaking (Figure 26). At each time point, the collagen scaffold was removed and placed into a new vial containing 2 ml of fresh release medium. The left release solution was stored in vials at −20 °C for further analysis. The released BMP-2 amount in the supernatant was quantified by ELISA according to the manufacturer's instructions. For each sample the experiments was performed in triplicates.

Collagen-NPSNP-OH-BMP-2
Collagen-NPSNP-propyl-NH$_2$-BMP-2
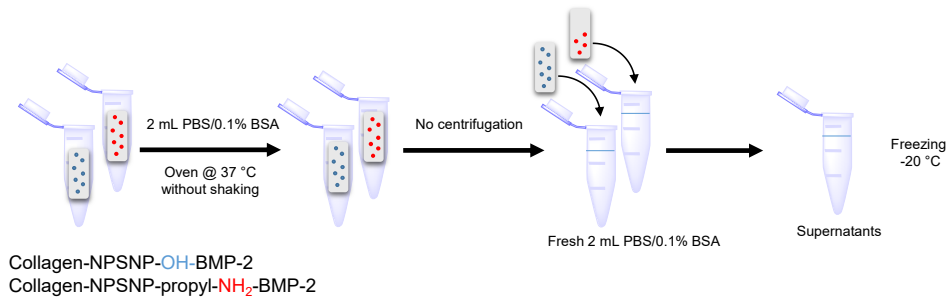
Figure 26: Schematic procedure of BMP-2 release from collagen-NPSNP-BMP-2 nanocomposites.

3.3.25 Osteogenic differentiation

Cell culture experiments were performed by VINCENT COGER from the Kerstin Reimers Labor für Regenerationsbiologie, Klinik für Plastische, Ästhetische, Hand- und Wiederherstellungs-chirurgie, Medizinische Hochschule Hannover, Germany.

Human adipose-derived mesenchymal stem cells (hASCs) were in DMEM with 10% fetal bovine serum and 1% penicillin/streptomycin and incubated at 37 °C with 5% CO$_2$ in a humidified atmosphere.

hASCs with a density of 10,000 cells per well were mixed with 100 µl rat tail collagen, seeded in a 96 well plate and cultivated for 1 day till a shrinkage of the collagen gel occurred.

In order to further support osteogenic differentiation, a medium with and without dexamethasone was used (DMEM with 10% fetal bovine serum, 1 M Hepes buffer, 1 M *β*-glycerolphosphate, 50 mg ml^{-1} L-ascorbat-2-phosphate, 20 µg ml^{-1} dexamethasone and 1% penicillin/streptomycin). The cell-seeded collagen gels were placed below the collagen scaffold samples in a 6 well plate and poured with the cell medium as shown in Figure 27. During cultivation of either 2 or 4 weeks, 20% of the medium was carefully removed and replaced by the fresh medium three times a week.

The collagen scaffolds used for all cell culture experiments were punched out by disposable skin punches (Stiefel ® Biopsy punch) with the size of 8 mm.

The BMP-2 used here was purchased from Peprotech. The BMP-2 loading on aminopropylsilyl-modified NPSNPs was carried out as described in previous section. The integration of BMP-2-loaded NPSNPs into collagen scaffolds was performed overnight (≈ 12 h).

To investigate the three dimensional osteogenic differentiation of hASCs in collagen scaffolds four groups of samples were tested: 1) pure collagen scaffolds; 2) collagen scaffolds with integrated aminopropylsilyl-modified NPSNPs (2 mg); 3) collagen

scaffolds with integrated, BMP-2-loaded aminopropylsilyl-modified NPSNPs (2 mg of NPSNPs with 800 ng mg^{-1} of BMP-2) and 4) collagen scaffolds soaked in BMP-2 solution (800 ng). Each sample group was tested in triplicates.
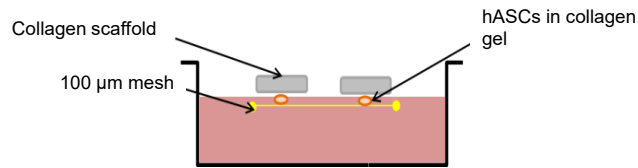
Figure 27: Schematic illustration of the experimental set up for osteogenic differentiation of hASCs in collagen gel in contact with collagen scaffolds.

3.3.26 Histochemical stainings

To investigate the cell viability live/dead staining was performed. To analyse the differentiation towards osteogenic lineage von Kossa, Alizarin Red S, Calcein and DAPI stainings were carried out. All histological stainings were performed according to the manufacturer's instructions.

For that, collagen samples were fixed with 4% paraformaldehyde, embedded in paraffin wax and cut into 6 μm thick slides. The middle slides of each sample were examined after staining under the Olympus CKX41 microscope using appropriate filters and objectives.

4 Results and discussion

4.1 Hydrolytic stability and reversible pore clogging of aminopropylsilyl-modified NPSNPs

Research on nanoporous silica nanoparticles (NPSNPs) as drug delivery systems have gained tremendous attention in the field of nanomedicine due to their unique textural and physicochemical properties [29, 31]. The presence of high surface areas and large pore volumes with tunable pore sizes allows nanoporous silica nanoparticles to encapsulate and deliver large quantities of various drugs, including antibiotics and anti-cancer therapeutics [266, 267]. Furthermore, tailoring the surface of the nanoporous silica nanoparticles with appropriate functional groups offers the opportunity to design customizable surface-drug interactions, resulting in controlled drug delivery [41, 268]. As the drug incorporation is highly dependent on the surface properties and the surface itself, more drugs can be loaded on particles with the higher quantity of functional groups covalently attached on the surface, higher specific surface areas and larger pore volumes [31]. However, it is questionable whether the surface modification really occurs (as commonly depicted in reaction schemes, e.g. Figure 29) between a surface silanol group and the modifying silane or whether self-condensation of the dissolved silane leads to the formation of organosilica moieties, which form in solution and deposit on the surface of the NPSNPs. Furthermore, NPSNPs may suffer from degradation and detachment of anchored functional groups upon exposure to aqueous environment accompanied by the reduction of porosity. On that account, maintaining highly porous particles with accessible pores throughout multiple modification steps and preparation of hydrolytically stable layers of functional groups on the surface of nanoporous silica nanoparticles are immediate challenges that need to be addressed if the high potential of these particles as drug reservoirs and carriers is to be realized.

Most studies on the degradation of mesoporous silica materials have focused on non-modified materials in aqueous systems [36, 37, 74]. The issue of hydrolytic stability of the anchored functional groups on the surface of NPSNPs as well as pore-clogging effects have not been addressed yet. Herein, we describe a simple method to investigate the effect of aqueous media on the stability of (3-aminopropyl)triethoxysilane (APTES) functionalities tethered on the surface of nanoporous silica nanoparticles; we observe pore clogging and present an innovative solution to regain the porosity of aminopropylsilyl-modified nanoporous silica nanoparticles through subsequent reaction with succinic anhydride in DMF.

4.1.1 Characterization of non-modified and aminopropylsilyl-modified NPSNPs before and after hydrolytic stability testing and of carboxy-modified NPSNPs

Firstly, spherical, uniform and monodisperse nanoporous silica nanoparticles with an average particle diameter of 40 – 60 nm were synthesized [55], and the existence of the disordered porous structure was confirmed using transmission electron microscopy (TEM) (Figure 28a). The obtained non-modified NPSNPs were highly porous with a calculated specific surface area of 1000 $m^2 g^{-1}$ (S_{BET}), an average pore width of approximately 3.2 nm (d_{NLDFT}) and an accessible pore volume of 0.83 $cm^3 g^{-1}$ (V_{total}) determined on the nitrogen adsorption-desorption isotherms (Figure 28b).

The presence of highly reactive silanol (−Si−OH) groups on the surface of NPSNPs allows for the attachment of different organosilane coupling reagents. In this study, the modification of silica materials with aminosilanes was carried out employing (3-aminopropyl)triethoxysilane (APTES) at 80 °C in toluene for 2 h.
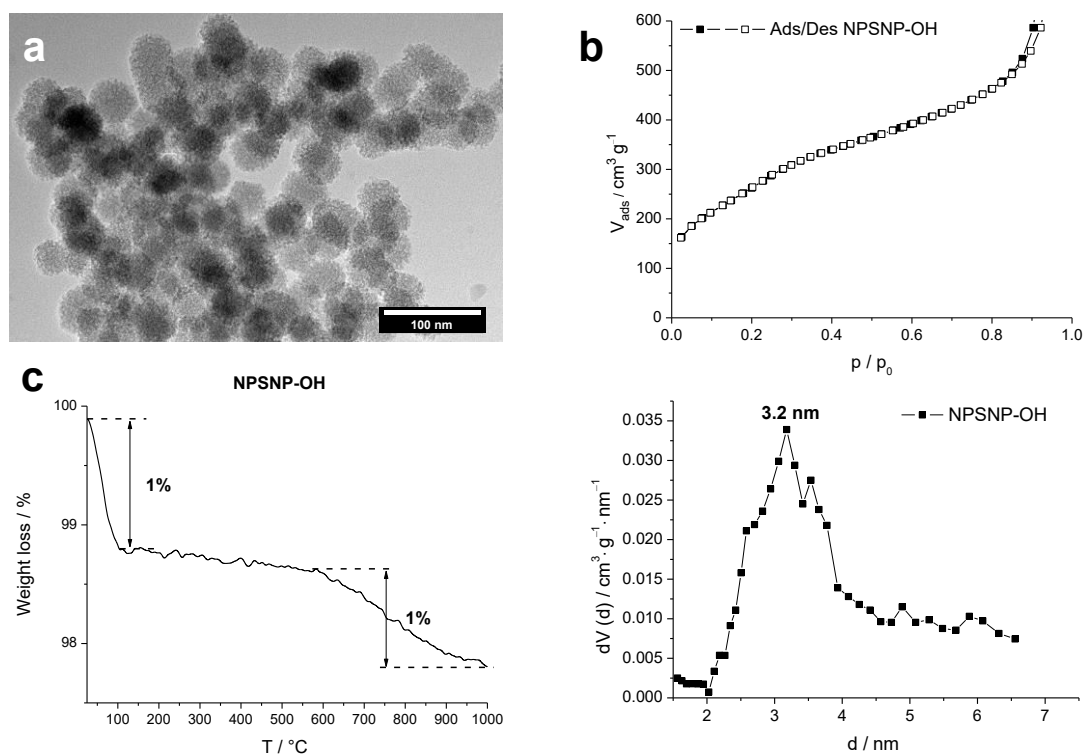
Figure 28: Characterization of non-modified nanoporous silica nanoparticles by (a) transmission electron microscopy; (b) nitrogen adsorption-desorption measurements: isotherms and pore size distribution according to the DFT theory; (c) thermogravimetric analysis.

Due to the potential application of surface-modified nanocarriers in an aqueous environment, the hydrolytic stability of the attached functional groups, as well as the porosity of the surface-modified nanoporous silica nanoparticles, are very important factors to know before proceeding with encapsulation of the therapeutic agents. To this end, the hydrolytic stability of the attached aminopropylsilyl groups on the surface of NPSNPs was examined by exposing the particles to ultrapure water at room temperature for 64 h. The applied method to investigate the hydrolytic stability of the aminopropylsilyl groups on the surface of NPSNPs and the synthesis of different surface-modified NPSNPs is demonstrated in Figure 29.
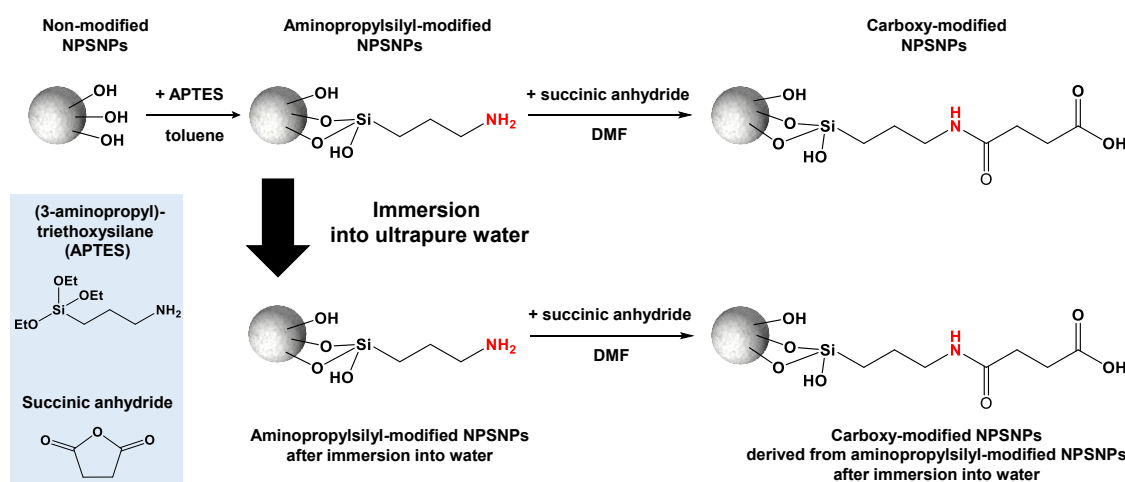
Figure 29: Schematic representation of the modification procedure. The modification of NPSNPs was carried out by the attachment of aminopropylsilyl groups through a reaction with (3-aminopropyl)triethoxysilane (APTES). Afterwards, carboxylic groups were anchored by a ring-opening reaction with succinic anhydride. In the case of aminopropylsilyl-modified NPSNPs, hydrolytic stability of the attached aminopropylsilyl groups was investigated by the immersion of the particles in an aqueous medium followed by the reaction with succinic anhydride in DMF.

The amount of detached aminopropylsilyl moieties upon water exposure was determined by thermogravimetric analysis (TGA) (see Table S1 in supporting information (SI)). As shown in Figure 30a, aminopropylsilyl-modified NPSNPs before water exposure (black curve) contained 3 wt.% more organic residues than those aminopropylsilyl-modified silica nanoparticles after water exposure (red curve): 13 wt.% vs. 10 wt.%, respectively. In contrast, non-modified NPSNPs showed no significant weight loss between 120 °C and 700 °C (Figure 28c). Knowing the original weight of the samples and assuming that all APTES molecules were hydrolysed, the amount of aminopropylsilyl groups added to the samples can be estimated. NPSNPs before and after water exposure had taken up hydrolysed and partly condensed aminopropylsilyl groups of 1.1 mmol g^{-1} and 0.8 mmol g^{-1}, respectively. As the initial amount of APTES in the reaction was about

1.1 mmol g^{-1}, obviously all of the APTES molecules were bound to the surface of NPSNPs.
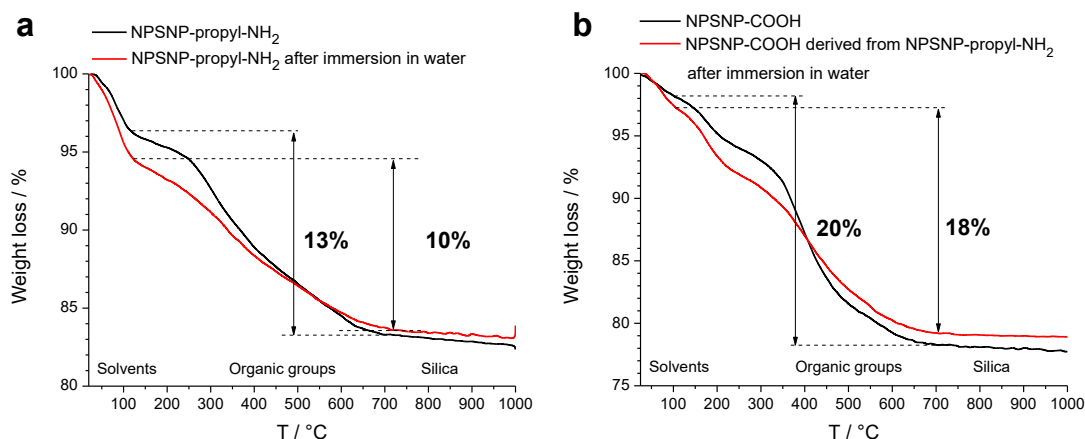
Figure 30: Thermogravimetric analysis. a) TGA curves for aminopropylsilyl-modified nanoporous silica nanoparticles before and after immersion in water. (b) TGA curves for carboxy-modified NPSNPs derived from as-prepared aminopropylsilyl-modified NPSNPs and from aminopropylsilyl-modified NPSNPs, which had been immersed in water.

In general, there are two models how APTES molecules can be bound on silica surfaces. On one hand, APTES molecules can form a liquid-like, non-oriented film that remodels to a covalently attached, ordered monolayer of aminopropylsilyl groups (Figure 31a). On the other hand, intermolecular condensation of hydrolysed APTES molecules in solution can occur resulting in the formation of small aminopropylsilyl oligomers [72] (Figure 31b). The formed small oligomers can be deposited on the surface of silica and grow into a thick and dense film, instead of generating a monolayer modification [269].

After the aminopropylsilyl-modified NPSNPs were immersed into an aqueous medium, about 30 % (0.3 mmol g^{-1}) of the initially tethered aminopropylsilyl groups were detached from the surface. The detachment of aminopropylsilyl entities can be associated with several reasons: the detachment of weakly bound (via hydrogen bond and electrostatic interactions) and small condensed aminopropylsilyl oligomers, which can be washed off upon immersion in water, and the catalysed hydrolysis of the siloxane (−Si−O−Si−) bonds of covalently grafted aminosilanes by a nucleophilic attack of the amine groups [270] (Figure 31c).

Figure 31: (a) Silanization of NPSNPs by partial hydrolysis of APTES and subsequent condensation on the silica surface [271]. (b) Intermolecular condensation of hydrolysed aminopropylsilyl molecules, resulting in oligomeric organosilica species, which can precipitate onto the surface of NPSNPs [72]. (c) A detachment of aminopropylsilyl groups from the surface of nanoporous silica nanoparticles caused by the catalytic hydrolysis of covalently attached aminopropylsilyl moieties via a nucleophilic attack of the amine groups due to water exposure and hydrolytically stable cyclic zwitterion-like species [75].

The persistence of hydrolytically stable aminopropylsilyl groups on the surface of silica gels was first observed by Zhmud [272] and then investigated by Etienne and Walcarius [75]. They proposed the formation of hydrolytically stable, cyclic zwitterion-like species between amine groups of covalently bound aminopropylsilyl moieties and residual surface silanol groups (Figure 31c). In such entities, siloxane bonds cannot be readily hydrolysed involving catalysis due to the absence of free electrons at the ammonium ion; these groups are stable in the aqueous medium. However, these authors demonstrated that only about one-third of the attached aminopropyl groups was hydrolytically stable. In contrast, we found that a higher proportion of hydrolytically stable aminopropylsilyl groups was formed on the surface of our NPSNPs since about 70% (0.8 mmol g^{-1}) of the initially attached aminopropylsilyl moieties remained on the surface of the NPSNPs upon water exposure. We assume that these stable species are probably similar to the aforementioned cyclic zwitterion-like species.

We hypothesize that the high amount presented in our study can be attributed to the high porosity of the nanoporous silica nanoparticles. Unlike the aminosilane moieties grafted on nonporous [273, 274] or low porous silica materials [75, 275], the aminosilane moieties reported here, especially those attached to the inner surface of highly porous silica nanoparticles, could not be readily washed off of the surface due to the steric hindrance.

To determine whether aminopropylsilyl-modified NPSNPs can be equipped with further functionalities, linkers with terminal carboxy (−COOH) groups were covalently attached on the surface of aminopropylsilyl-modified silica nanoparticles before and after the immersion into the water by a ring-opening reaction of succinic anhydride with amine groups (Figure 32).
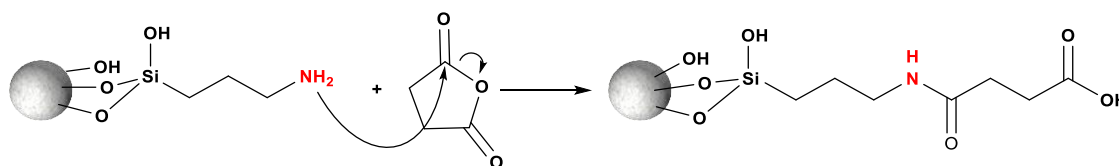
Figure 32: Schematic illustration of the modification of aminopropylsilyl-modified NPSNPs with succinic anhydride in DMF by a ring-opening reaction.

The success of this reaction has been previously shown for nonporous and porous aminopropylsilyl-modified silica nanoparticles [276, 277]. By comparing TGA graphs, shown in Figure 30a and b, significant differences in weight loss between 120 °C and 700 °C can be observed (Table S2, SI). Thus, after modification with succinic anhydride, the mass fraction of organic groups increased by 7 wt.% and 8 wt.% for carboxy-modified NPSNPs derived from as-prepared aminopropylsilyl-modified NPSNPs and from aminopropylsilyl-modified NPSNPs, which had been immersed in water, respectively. These results point to the successful covalent attachment of carboxylic functionalities on

the surface of aminopropylsilyl-modified NPSNPs, regardless of whether or not they were exposed to water. The amount of the newly attached carboxy functionalities can be estimated by TG measurement to be about 0.7 mmol g^{-1} and 0.8 mmol g^{-1} for the corresponding particle types.

Further evidence of successful functionalization was provided by pH-dependent zeta potential measurements (Figure 33). The titration curves from aminopropylsilyl-modified NPSNPs revealed different electrochemical behaviour before and after functionalization with succinic anhydride, pointing to the change of surface charge of NPSNPs. The surface of aminopropylsilyl-modified silica nanoparticles was strongly positive at acidic and neutral conditions and slightly negative at higher pH values. This is the result of the protonation of amine groups ($-NH_3^+$) and deprotonation of silanol groups ($-SiO^-$) at acidic and alkaline medium, respectively. In contrast, after reaction with the succinic anhydride, a negative surface charge was detected at neutral and alkaline conditions due to the presence of acidic carboxy groups, which can be readily deprotonated on the surface of NPSNPs. This zeta potential profile is therefore similar to the profile of the non-modified silica nanoparticles, which exhibit acidic silanol groups.
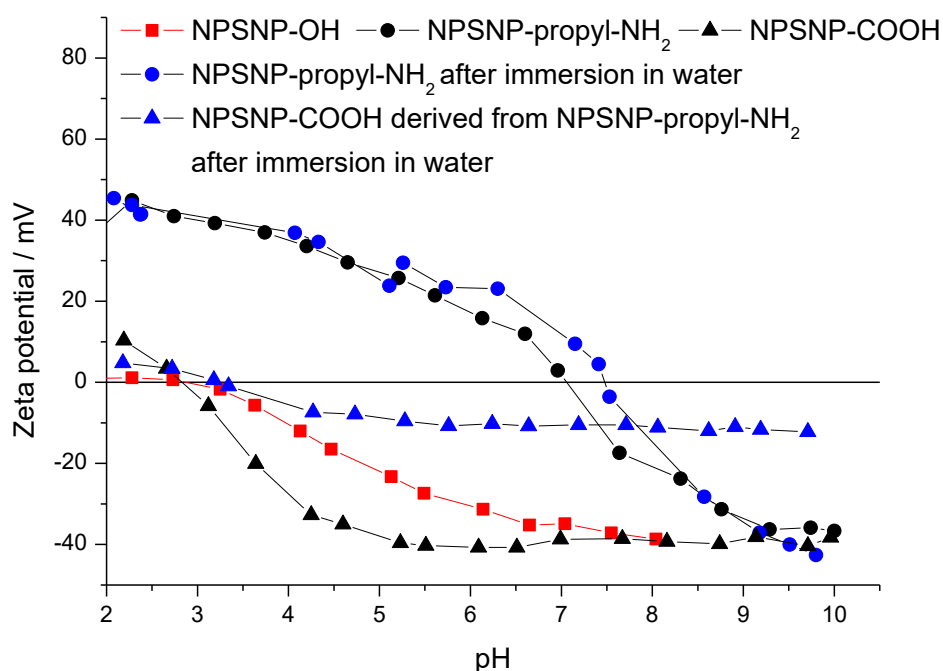
Figure 33: pH-dependent zeta potential curves from non-modified, aminopropylsilyl-modified NPSNPs before and after water exposure, and of carboxy-modified NPSNPs, derived from as-prepared and immersed aminopropylsilyl-modified NPSNPs.

After the exposure of the aminopropylsilyl-modified silica nanoparticles to water, the surface charge behaviour is almost the same throughout the entire pH range like before the exposure, notwithstanding the removal of ca. 30% of the functional groups from the

surface of aminopropylsilyl-modified silica nanoparticles as described previously. In contrast, when immersed aminopropylsilyl-modified silica nanoparticles were subsequently modified with succinic anhydride, the surface became less negatively charged than the surface of the carboxy-modified silica nanoparticles, which had not been exposed to water. This outcome cannot be clarified at this point.

As a result, it could be shown that through the simple reaction with the succinic anhydride, terminal amine functionalities on the surface of NPSNPs could be converted into carboxy moieties without applying higher temperatures or using catalysts [276].

4.1.2 Studies on clogging and re-opening of pores

Another important issue, which was addressed in the current study, was to identify the changes in porosity of the NPSNPs due to the aminopropylsilyl modification, the water exposure of the samples and the subsequent reaction with succinic anhydride. The sorption properties of differently surface-modified NPSNPs before and after water immersion were determined using nitrogen adsorption-desorption isotherms (Figure 34a and b) and compared with those of the non-modified NPSNPs (Figure 28b). The corresponding graphs reveal type IV isotherms according to the IUPAC classification [278], with narrow hysteresis loops between 0.2 - 0.4 and > 0.8 p/p_0, indicating the condensation of nitrogen in the nanopores and interparticle volumes, respectively.

After modification of the original NPSNPs with APTES, both specific surface area and pore volume were reduced by half (Table S3, SI). However, the average pore width remained invariable at 3.2 nm. Furthermore, a comparison of the values for specific surface areas and pore volumes of the aminopropylsilyl-modified NPSNPs before and after exposure to water revealed an additional decrease of the surface area from 442 $m^2 g^{-1}$ to 160 $m^2 g^{-1}$ and of the pore volumes from 0.45 $cm^3 g^{-1}$ to 0.21 $cm^3 g^{-1}$, respectively (Figure 34a and c).
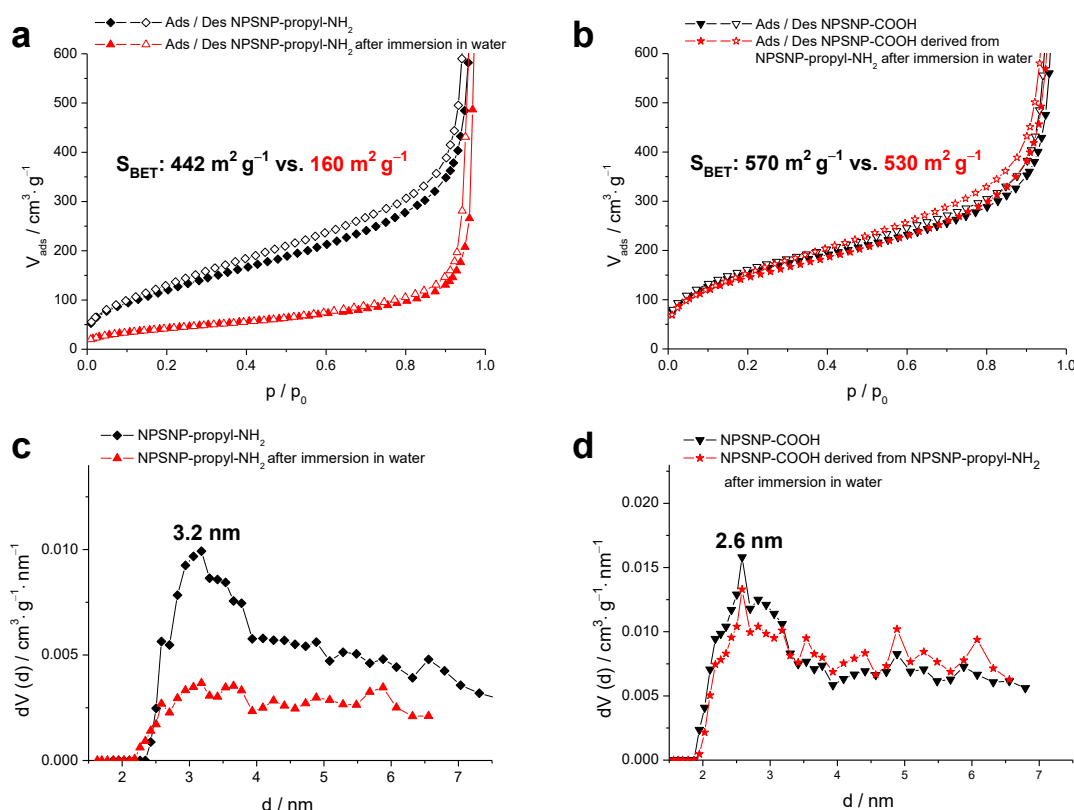
Figure 34: Nitrogen physisorption studies. (a, b) Adsorption-desorption isotherms and (c, d) pore size distributions according to the DFT theory. (a, c) Aminopropylsilyl-modified NPSNPs before and after water exposure; (b, d) carboxy-modified NPSNPs derived from as-prepared and immersed aminopropylsilyl-modified NPSNPs.

The most striking observation to emerge from a comparison of the isotherms illustrated in Figure 34 was the increase of the specific surface area and pore volume of the immersed aminopropylsilyl-modified NPSNPs after their subsequent modification with succinic anhydride. In fact, the surface area and the pore volume increased threefold from 160 $m^2 g^{-1}$ to a value of about 530 $m^2 g^{-1}$ and from 0.21 $cm^3 g^{-1}$ to 0.59 $cm^3 g^{-1}$, respectively. The values are comparable with those obtained from carboxy-modified NPSNPs without water exposure (Figure 34b; Table S3, SI). Of note, both types of carboxy-modified NPSNPs point to a narrow pore size distribution with a smaller average pore width of 2.6 nm compared to aminopropylsilyl-modified silica nanoparticles with an average pore width of 3.2 nm, providing strong evidence for a structure where the functional groups line the pore walls (Figure 34d).

To study the morphology of the investigated surface-modified NPSNPs and to shed additional light on their porosity characteristics, TEM analyses were performed. As shown in Figure 35b, the particle morphology of the immersed aminopropylsilyl-modified NPSNPs seems to remain intact; however, the mesostructure could not be clearly

observed. In comparison, in the TEM micrographs of the aminopropylsilyl-modified silica nanoparticles not subjected to the water exposure step, a disordered porous structure can be observed (Figure 35a). Furthermore, spherical nanoparticles with a mesoporous structure were evident for both types of carboxy-modified NPSNPs (Figure 35c and d). These results clearly affirm that the morphology and the porous system of aminopropylsilyl-modified nanoporous silica nanoparticles stayed intact even after extended water exposure at room temperature.
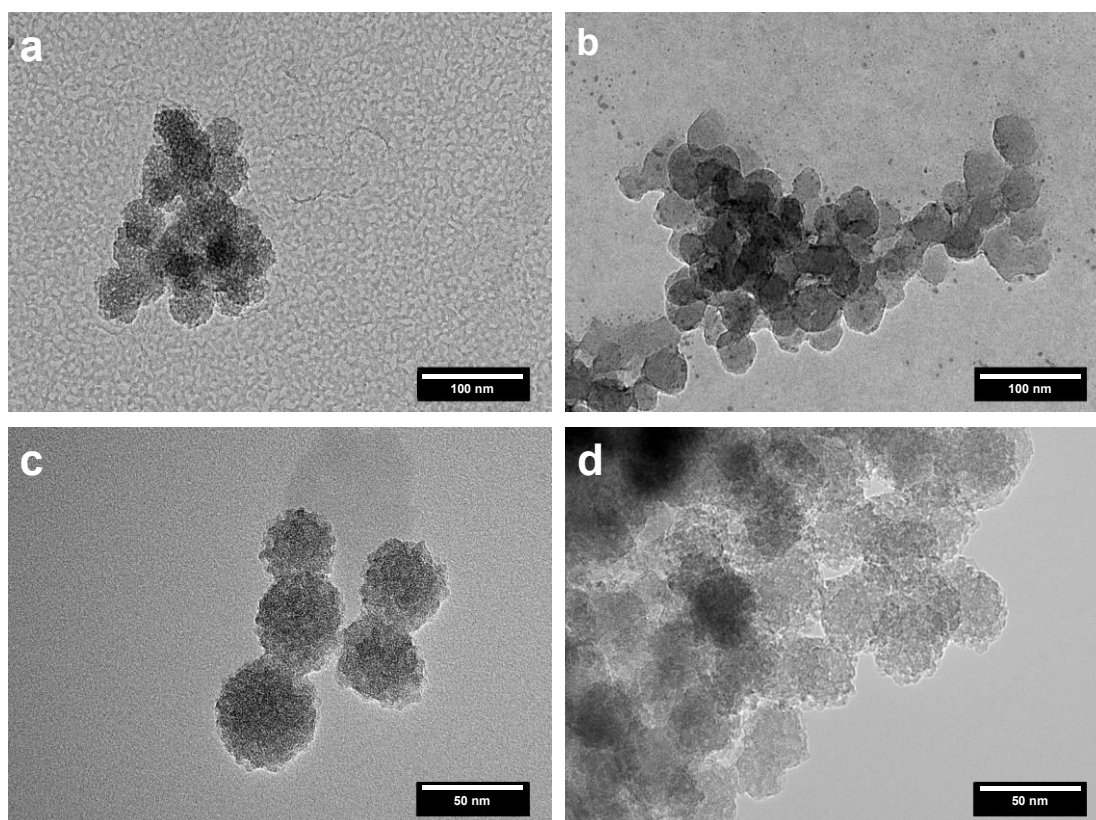
Figure 35: Transmission electron microscopy images of (a, b) aminopropylsilyl-modified NPSNPs before and after water exposure, respectively; (c, d) carboxy-modified NPSNPs derived from as-prepared aminopropylsilyl-modified NPSNPs and from such nanoparticles after they had been exposed to water. Note that mesopore structures are clearly visible in a), c) and d) but not in b).

In order to further clarify the mechanisms of pore clogging and reopening, we treated the immersed aminopropylsilyl-modified NPSNPs with the pure solvent DMF (without the addition of succinic anhydride) at 25 °C and at 155 °C. To prove whether the nanopores could be re-opened by these methods, nitrogen adsorption-desorption measurements and TEM analyses were performed. From the sorption isotherms shown in Figure 36a, specific surface areas of 229 $m^2 g^{-1}$ and 248 $m^2 g^{-1}$ were measured for the immersed NPSNPs after stirring in pure DMF at 25 °C and 155 °C, respectively. The corresponding values for the pore volume were around 0.29 $cm^3 g^{-1}$ in both cases (Figure 36b). Comparing these values with those of the aminopropylsilyl-modified NPSNPs directly

after the immersion (160 m^2 g^{-1} and 0.21 cm^3 g^{-1}), a slight increase in the surface area and the pore volume could be detected. These are only modest, in contrast to the values obtained when the pore re-opening was carried out with a combination of DMF and the reactive agent succinic anhydride. TEM images further confirm the low porosity of aminopropylsilyl-modified NPSNPs treated with pure DMF. The images presented in Figure 36c and d reveal partially degraded and highly interconnected silica nanoparticles.
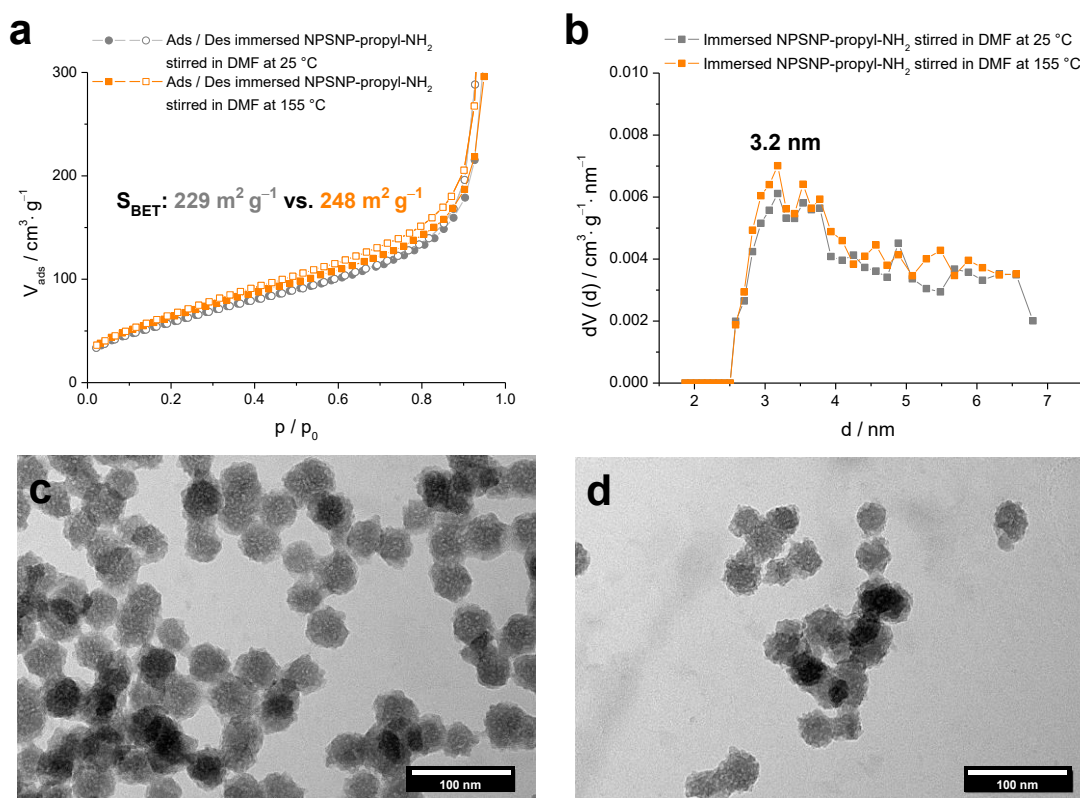
Figure 36: (a) Nitrogen adsorption-desorption isotherms and (b) pore size distributions of the immersed aminopropylsilyl-modified NPSNPs stirred in DMF at 25 °C and at 155 °C. (c) and (d) TEM images of the immersed aminopropylsilyl-modified NPSNPs stirred in DMF at 25 °C and at 155 °C, respectively.

From the results given above, it appears that the presence of succinic anhydride plays an important role in the ability to reopen clogged pores. We hypothesize the following model, as depicted in Figure 37. In this model, condensed aminoorganosilica oligomers, which have precipitated onto the surface of the NPSNPs to clog the pores are mainly bound by hydrogen bonds between silanol surface groups and the amino groups of the aminoorganosilica deposits. When these amino groups react with succinic acid, the resulting amide and carboxylic acid groups exert considerably weaker hydrogen bonds, allowing the deposits to detach from the surface, resulting in free pore entrances and higher porosity. Such a pore clogging-reopening effect, to the best of our knowledge, has important consequences for stability studies on nanoporous silica materials [74, 279].

When a loss of porosity is observed in such studies, this is not necessarily equivalent to the destruction of the mesostructure.
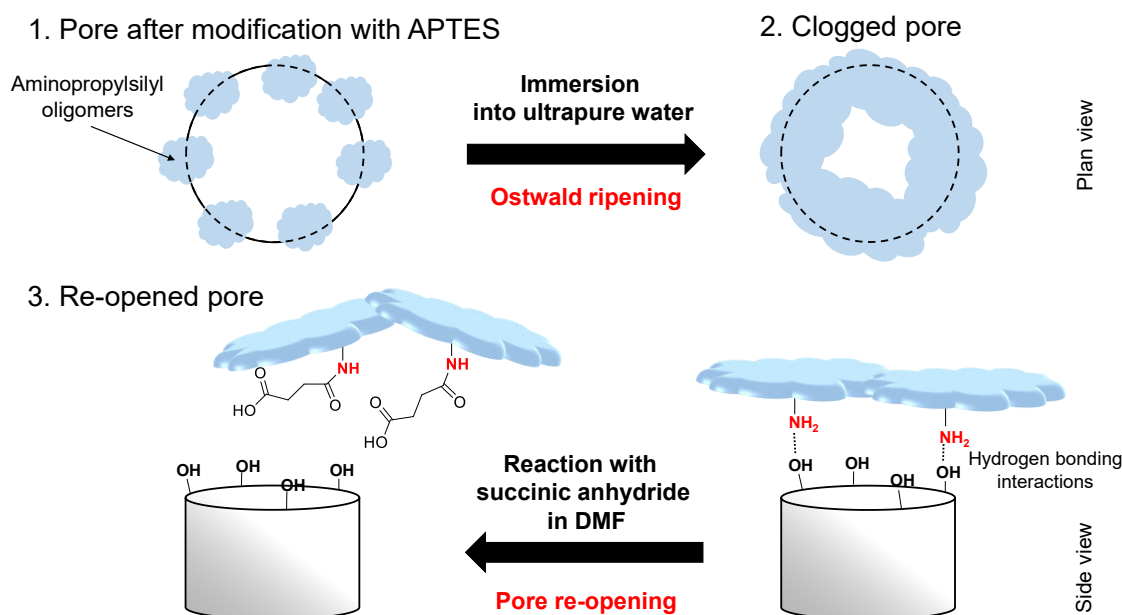
Figure 37: Models for pore clogging in aminopropylsilyl-modified NPSNPs after water exposure and for the re-opening of the pores after reaction with succinic anhydride in DMF.

In summary, hydrolytically highly stable aminopropylsilyl moieties on the surface of nanoporous silica nanoparticles were identified in the present study. Moreover, a possibility to reopen clogged nanopores and thus, to regain the porosity of aminopropylsilyl-modified nanoporous silica nanoparticles by subsequent functionalization with succinic anhydride in DMF was demonstrated. The results from this work not only provide unique insights into the hydrolytic stability of the aminopropylsilyl-modified nanoporous silica nanoparticles but also show that the reduction of the porosity is not necessarily equivalent to the destruction of the pore system. Furthermore, our results will be of importance for the construction of NPSNP-based drug delivery devices, which often rely on an aminopropylsilyl modification.

4.2   BMP-2-loaded nanoporous silica nanoparticles (NPSNPs)

Growth factor delivery is one of the powerful tools in tissue engineering. In this chapter, first, the influence of a variety of surface modifications of NPSNPs is investigated with regard to the binding capacity and the release kinetics of the growth factor bone morphogenetic protein 2 (BMP-2). In the second section, the differentiating action of BMP-2-loaded NPSNPs is tested in cell-culture studies. With regard to the future application for biomedical applications, the cytotoxicity of NPSNPs bearing different functional groups is investigated for two different cell lines.

4.2.1   General concept: modified NPSNPs for controlled loading and release of BMP-2

Nanoporous silica nanoparticles (NPSNPs) is a promising nanomaterial for the delivery of various therapeutics due to their unique properties such as the size, tunable surface chemistry, biocompatibility and -degradability [28-30]. Recently, NPSNPs have demonstrated a great potential for the loading and delivery of the growth factor BMP-2 to induce osteogenic differentiation *in vitro* [33, 34]. However, the mechanisms of how the surface chemistry of NPSNPs controls growth factor loading capacities and release kinetics is not yet fully understood. Therefore, in this study, the surface chemistry of NPSNPs have been tailored by various functional groups possessing different physicochemical properties such as the different hydrophobicity/hydrophilicity and surface charge, following by the BMP-2 adsorption on the surface of differently modified NPSNPs and release studies of BMP-2 from the NPSNPs. The understanding of the adsorption-desorption mechanisms of growth factors can lead to universal NPSNP-based platforms for adapted loadings and release profiles needed for different therapeutic applications.

4.2.2   Characterisation of NPSNPs

First, nanoporous silica nanoparticles were synthesized following the procedure described by Huo *et al*. [55]. In this procedure, the silica source tetraethylorthosilicate (TEOS) was added to an ethanol-water solution containing diethanolamine (DEA) as a complexing agent for silicate species and cetyltrimethylammonium bromide (CTAB) as a structure-directing agent to form the pores. The formation of nanoporous material occurs due to the condensation of hydrolysed TEOS molecules around the CTAB

micelles. However, in order to use the pores for possible drug loading and as CTAB surfactant is cytotoxic, it must be removed from the pores before using them for biomedical applications. Therefore, the prepared silica nanoparticles were calcined at 550 °C to burn out the organic CTAB and to obtain bare nanoporous silica nanoparticles. The analysis by transmission electron microscopy (TEM) reveals the presence of spherical, uniform and monodisperse silica nanoparticles with diameters of 40 – 60 nm and confirms the existence of the disordered porous structure (Figure 38a). The obtained non-modified NPSNPs were highly porous with a calculated specific surface area of 1100 $m^2 g^{-1}$ (S_{BET}), an average pore width of approximately 3.2 nm (d_{NLDFT}) and an accessible pore volume of 0.92 $cm^3 g^{-1}$ (V_{total}) determined from the N_2 adsorption-desorption isotherm (Figure 38b), which shows a type IV isotherm, according to the IUPAC classification [278], with inflections between 0.05 – 0.30 and > 0.8 p/p_0 indicating the condensation of nitrogen in the nanopores and interparticle volumes, respectively (Figure 38b).
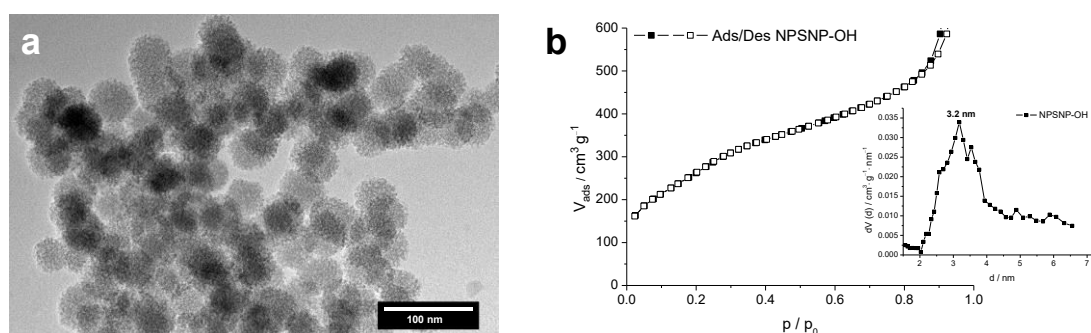
Figure 38: Characterization of non-modified nanoporous silica nanoparticles by means of (a) transmission electron microscopy; (b) nitrogen adsorption-desorption measurements: isotherms and pore size distribution according to the NLDFT theory.

The presence of reactive silanol groups on the surface of NPSNPs allows the reaction with different organosilane coupling reagents, given in Figure 39, to obtain NPSNPs with versatile surface chemistries, namely NPSNP-propyl-NH_2, NPSNP-methyl-NH-hexyl-NH_2, NPSNP-propyl-NH-hexyl-NH_2 and NPSNP-propyl-SH. NPSNPs bearing terminal sulfonic acid groups (NPSNP-propyl-SO_3H) were obtained by the reaction of NPSNP-propyl-SH with H_2O_2. Additionally, NPSNP-propyl could be prepared by the reaction of NPSNPs with trimethoxy(propyl)silane. However, these nanoparticles were too hydrophobic and could not be dispersed in aqueous solution and therefore, were omitted from this study.

(**3-aminopropyl**)triethoxysilane   (**3-mercaptopropyl**)trimethoxysilane

N-**(6-aminohexyl)aminomethyl**triethoxysilane   *N*-**(6-aminohexyl)aminopropyl**trimethoxysilane
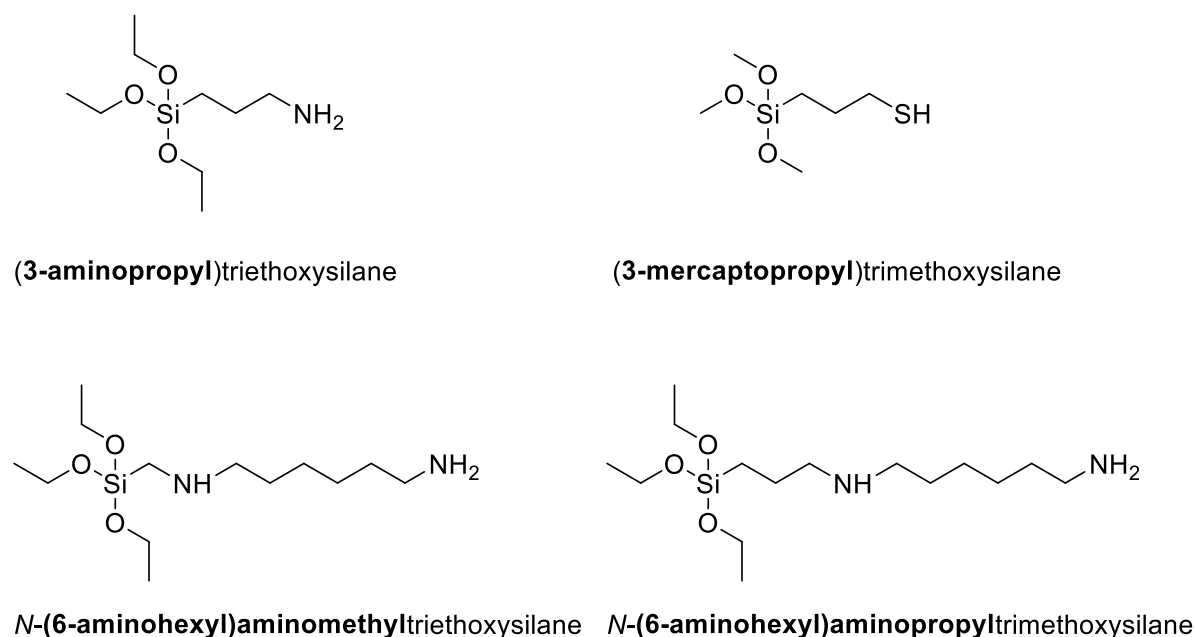
Figure 39: Different organosilanes used for the modification of NPSNPs.

The successful attachment of organic groups on the surface of NPSNPs after the modification described above was confirmed by thermogravimetric analysis (TGA). Figure 40 shows the weight loss curves of non-modified and modified NPSNPs. First, non-modified NPSNPs reveal a weight loss only of 1 wt. % between 25 °C and 120 °C correlating with the removal of solvent molecules, water and ethanol. Further, slight weight loss was detected between 120 °C and 600 °C indicating the absence of organic residues such as the structure-directing agent CTAB. About 1 wt.% of water was lost due to dehydroxylation of silanol groups starting at 600 °C. In comparison, the solvents used for synthesis and washing are removed from organosilane-modified NPSNPs samples between 25 °C up to 120 °C. Furthermore, TG curves of the organosilane-modified samples clearly exhibit the decomposition of grafted organic groups with the mass fraction of 13 wt.% to 20 wt.% between 150 °C and 700 °C. In all samples, about 1 wt.% of water was lost due to dehydroxylation of silanol groups starting between 600 °C and 700 °C.

Based on these results, the amount of the silanol and grafted organic groups on the surface of each type of NPSNPs were calculated. The affiliated values, summarized in Table 5, are ranging from 0.56 mmol g^{-1} for the silanol groups of non-modified NPSNPs to 0.87 mmol g^{-1} for the decomposed -propyl-SH groups. It can be also seen that the amount of all grafted functional group exceeded the amount of silanol groups pointing to a multilayer coverage by organosilanes on the nanoparticle surface. In addition, the quantitative amounts of the thiol and sulfonate groups could be assessed using C/S analysis (Table 5). The sulphur content of both NPSNP-propyl-SH and -propyl-SO$_3$H was

around 3% clearly indicating a successful grafting. In the other samples, no sulphur was detected.
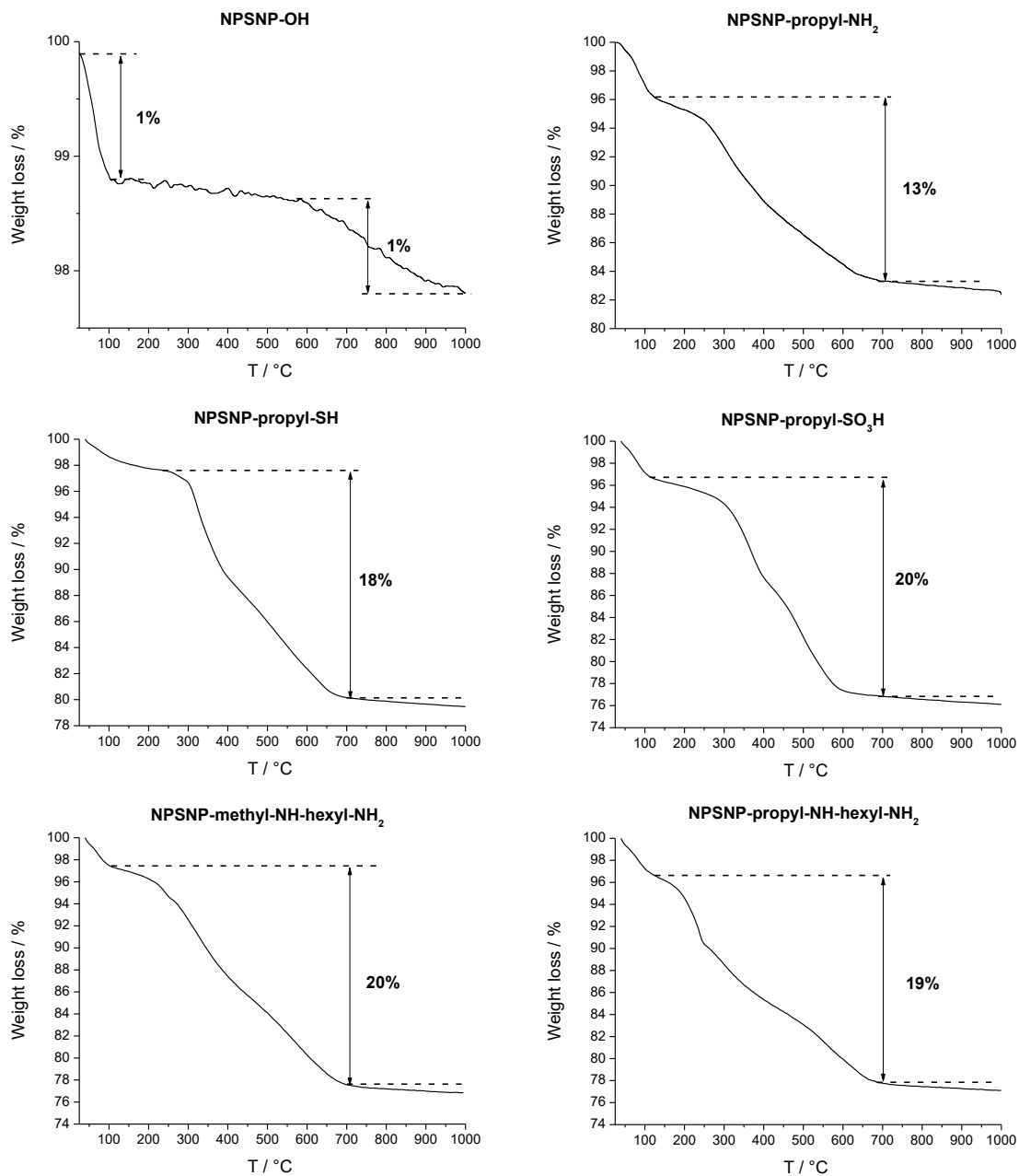
Figure 40: Thermogravimetric analysis curves of non-modified and differently modified NPSNPs.

Table 5: Physicochemical properties of the non-modified and differently modified NPSNPs determined by different types of methods.

Sample NPSNP-	n / mmol g^{-1} (a)	c_S / % (b)	S_{BET} / m^2 g^{-1} (c)	V_{total} / cm^{3}g^{-1} (d)	d_{Pore} / nm	ζ / mV (e)	r / nm (f)
OH	0.56	-	1100	0.92	3.2	−9.2 ± 0.1	70 ± 5
propyl-NH$_2$	0.62	-	442	0.45	3.2	27.6 ± 1.3	77 ± 9
propyl-SH	0.87	3.4	496	0.44	2.6	−15.1± 0.4	2268± 515
propyl-SO$_3$H	0.77	3.1	473	0.45	2.6	−24.4± 0.5	62 ± 29
methyl-NH-hexyl-NH$_2$	0.84	-	373	0.38	2.9	15.3 ± 0.8	110 ± 19
propyl-NH-hexyl-NH$_2$	0.62	-	343	0.37	2.9	29.4 ± 1.0	62 ± 12

(a) Functional groups content calculated from the TGA weight loss curves. (b) Sulphur content measured by C/S analysis. (c) Specific surface area determined by BET analysis of the nitrogen sorption isotherms ($0.05 \leq p/p_0 \leq 0.30$). (d) Total pore volume calculated via DFT analysis of the nitrogen adsorption isotherm ($p/p_0 \leq 0.90$). (e) Zeta potential in MES buffer at pH 5. (f) Hydrodynamic radius in MES buffer at pH 5 measured by DLS.

Figure 41 shows the FTIR spectra of all samples. All spectra exhibit two intensive bands at around 1220 cm^{-1} and 1085 cm^{-1}, corresponding to the asymmetric Si−O−Si covalent bond vibrations and indicating the presence of the silica network [280]. Furthermore, the band at 800 cm^{-1} belongs to the symmetric Si−O stretching mode. The Si−OH and SiO−H stretching modes of terminal silanol groups on the surface of the silica nanoparticles appear at 966 cm^{-1} and at around 3400 cm^{-1} [280]. The latter overlaps with the strong O−H stretching vibration of water molecules [280]. In addition, the band at 1647 cm^{-1} can be assigned to the deformation mode of the O−H groups of the water molecules or of the N−H groups of the modified silica nanoparticles [280]. Furthermore, several very weak bands corresponding to the C−H symmetric and asymmetric stretching vibrations (2980 - 2850 cm^{-1}) and asymmetric deformation vibrations (1490 - 1325 cm^{-1}) of the CH$_2$ groups in the alkyl chains can be observed [281].

The FTIR spectra of modified NPSNPs containing amino groups further revealed bands at 1560 cm^{-1} and 1475 cm^{-1} corresponding to N−H and -NH$_3^+$ deformation modes, respectively [282]. The bands at 3340 cm^{-1} and 3100 cm^{-1} of the amino groups could not be identified due to the overlap with the strong bands of the hydroxyl and silanol groups [283].

The S−H stretching vibration (2500 cm^{-1}) of the thiol group as well as the and S=O stretching vibration (1060 -1020 cm^{-1}) of the sulfonic acid group were not observed the corresponding FTIR spectra, probably due to the weak band intensity and an overlap with other stronger bands, respectively [284, 285]. For a better overview, all characteristic IR bands of all samples are given in Table S6 in supporting information (SI).
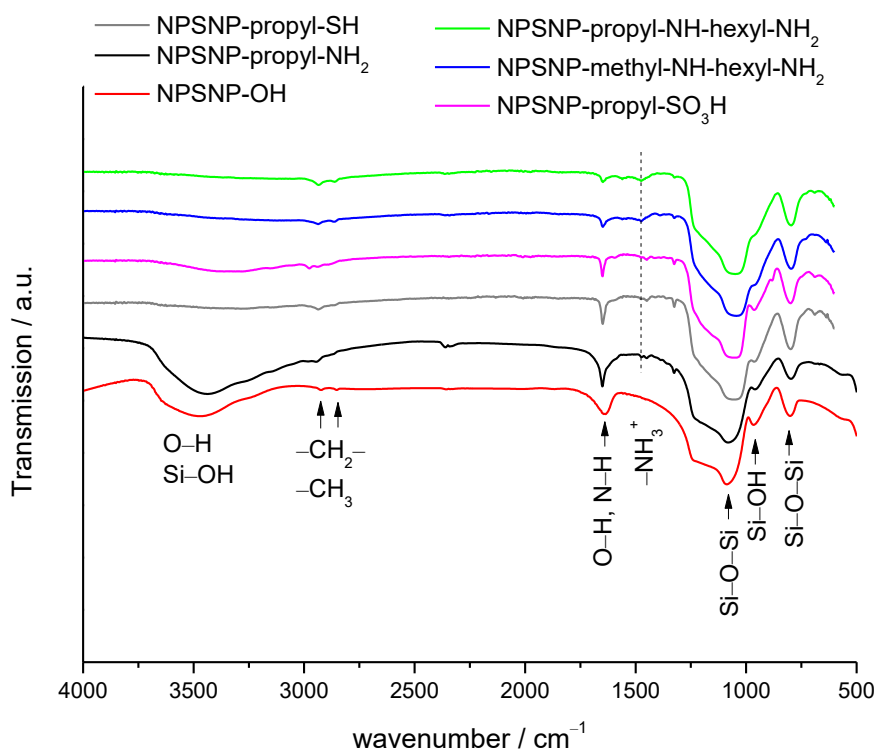
Figure 41: FTIR spectra of the non-modified and differently modified NPSNPs showing characteristic IR bands of silica and functional groups.

Nitrogen physisorption measurements were used to investigate the changes in porosity of the obtained modified nanoparticles. There is a strong indication that both the length and type of the functional group have an influence on the porosity of the modified NPSNPs. The calculated surface areas S_{BET} and the total pore volumes V_{total} of NPSNPs revealed the reduction of the porosity by half in case of NPSNPs consisting of the short-chained functional groups such as -propyl-NH$_2$, -propyl-SH and -propyl-SO$_3$H, and by one-third in case of NPSNPs with the long-chained functionalities, namely -methyl-NH-hexyl-NH$_2$ and -propyl-NH-hexyl-NH$_2$ (Table 5). However, the average pore width d_{Pore} of the NPSNP-propyl-NH$_2$ remained constant at 3.2 nm, while the pore widths of the

NPSNPs bearing -propyl-SH and -propyl-SO$_3$H moieties were calculated to be 2.6 nm. In contrast, the average pore widths of the long-chained NPSNPs were slightly larger (2.9 nm). The decrease of the pore widths after the modification of NPSNPs with different organosilanes points to the lining of the functional groups along the pore walls inside the nanopores.

The surface chemistry of NPSNPs is crucial for their interaction with the growth factors. Therefore, pH-dependent zeta potential measurements were used to assess the surface properties of non-modified and differently modified NPSNPs (Figure 42).
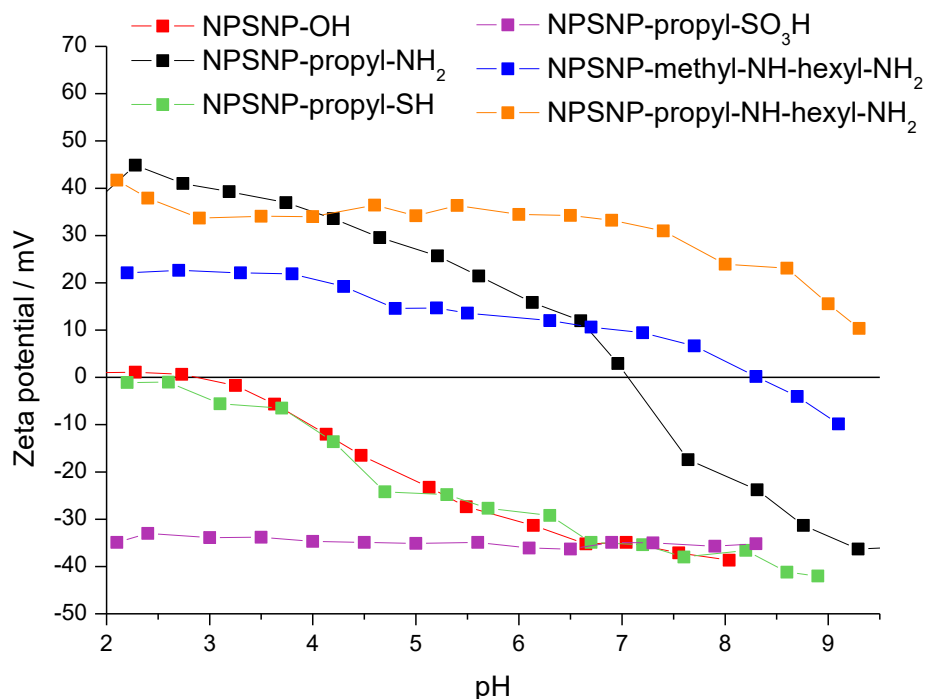
Figure 42: pH-dependent zeta potential curves of non-modified and differently modified NPSNPs showing different electrochemical behaviours.

Figure 42 illustrates three distinguishable electrochemical behaviours: a) modified NPSNPs bearing terminal amino groups, which show positive charge above pH 7 due to the protonation of -NH$_2$ groups; b) NPSNP-OH and -propyl-SH, which exhibit negative charge below pH 2 due to the deprotonation of silanol and thiol groups; c) NPSNP-propyl-SO$_3$H, which are strongly negatively charged over the entire pH range due to the deprotonation of strongly acidic sulfonic acid groups. It is noteworthy that zeta potential curves of NPSNPs bearing -methyl-NH-hexyl-NH$_2$ and -propyl-NH-hexyl-NH$_2$ groups are parallel to each other and keep a constant distance along the entire pH range. It seems that in case of NPSNP-propyl-NH-hexyl-NH$_2$ both amines can be deprotonated resulting in the higher zeta potential, while for NPSNP-methyl-NH-hexyl-NH$_2$ only the terminal amino groups are deprotonated. Taken together, a silica nanoparticle type with the most

suitable surface chemistry can be selected for the loading of growth factors when electrostatic interactions are considered.

4.2.3   Characterisation of the aggregation behaviour of BMP-2

Besides the surface chemistry of the NPSNPs, physicochemical properties of growth factors should be understood when designing growth factor delivery systems. For the present study, BMP-2 was chosen as the model growth factor with regard to its osteoinductive capability. BMP-2 is a homodimeric protein with an approximate molecular mass of 26 kDa, large hydrophobic areas and a modelled dimension of 7.0 x 3.5 x 3.0 nm [219]. For biomedical purposes, high quantities of recombinant human BMP-2, rhBMP-2, can be produced using mammalian cells such as Chinese Hamster Ovary (CHO) cells [286] or bacteria such as *Escherichia coli* (*E. coli*) [222, 287]. While the CHO-derived rhBMP-2 dimers are glycosylated, rhBMP-2 dimers expressed in *E. coli* lack this functionality. Based on that, rhBMP-2 from different sources exhibit different physicochemical properties. For example, the isoelectric point (pI), which has an influence on the solubility and the release kinetics of proteins, was slightly higher for CHO-derived rhBMP-2 (pI ≈ 9) than for *E. coli*-derived rhBMP-2 (pI ≈ 8.5) [221].

Several studies have analysed the stability, integrity and aggregation of CHO-derived rhBMP-2 at different pH values [288, 289]. Luca *et al*. demonstrated that CHO-derived rhBMP-2 dimers formed small aggregates (100 nm) at pH 4.5 and aggregated strongly (up to 2 µm) at pH 6.5 that was close to the pI of the rhBMP-2 [288]. However, Schwartz *et al*. showed that the aggregation was reversible when the pH was lowered down to 4.5 and 3 again and that dissolved, aggregated and re-dissolved rhBMP-2 did not reveal any conformational changes [289]. In addition, he also showed that BMP-2 aggregates were more stable against denaturation than dissolved BMP-2 dimers when stored at 5 °C and 25 °C for 6 months. A recent study compared the biological activities of CHO-derived rhBMP-2 purchased from two different providers [290]. The authors could show large differences in biological activities between seemingly identical CHO-derived rhBMP-2 both *in vitro* and *in vivo* due to their different aggregation behaviours at the same storage conditions and pH. However, less is still known about the behaviour of *E. coli*-derived rhBMP-2. Therefore, *E. coli*-derived rhBMP-2 from two different sources were analysed within the DFG research group FOR 2180, including our group. It was observed that the commercially available *E. coli*-derived rhBMP-2 purchased from Peprotech (Hamburg, Germany) was of lower quality according to the results from the gel electrophoresis, which showed that the sample mainly contained biologically inactive rhBMP-2 monomer instead of the functional dimer (Figure S3, SI). In comparison, *E. coli*-derived rhBMP-2 that was produced by our cooperation partners (Institut für Technische

Chemie, Leibniz Universität Hannover) within the DFG research group FOR 2180 [224], consisted of bioactive rhBMP-2 dimers. In addition, the in-house produced rhBMP-2 exhibited higher biological activity according to the results from the cell-based BRE-Luc assay than the purchased *E. coli*-derived rhBMP-2 (Figure S3, SI). In general, with regard to the routine clinical application of BMP-2 for bone regeneration, the use of *E. coli*-derived rhBMP-2 is more favourable due to its low-cost mass-production compared with the more costly production of CHO-derived thBMP-2.

In this study, the in-house produced rhBMP-2 expressed in *E. coli* (referred to as "BMP-2") was used to investigate its physicochemical properties at different pH. We believe that it is favourable to have a stable colloidal dispersion of BMP-2 dimers in order to achieve a homogeneous coverage of nanoparticles by BMP-2 dimers and to control the BMP-2 loading capacity.

To investigate the aggregation behaviour, dynamic light scattering (DLS) measurements were performed on BMP-2 that was dissolved in different buffers in the pH range of between 4 and 11 (Figure 43).

NaAc: sodium acetate

MES: 2-(*N*-morpholino)ethanesulfonic acid

MOPS: 2-(*N*-morpholino)propanesulfonic acid

PBS: Phosphate buffered saline with chloride

Soerensen: Phosphate buffer without chloride

TRIS: Tris(hydroxymethyl)aminomethan

CHES: *N*-cyclohexyl-2-aminoethanesulfonic acid

CAPS: *N*-cyclohexyl-2-aminopropanesulfonic acid
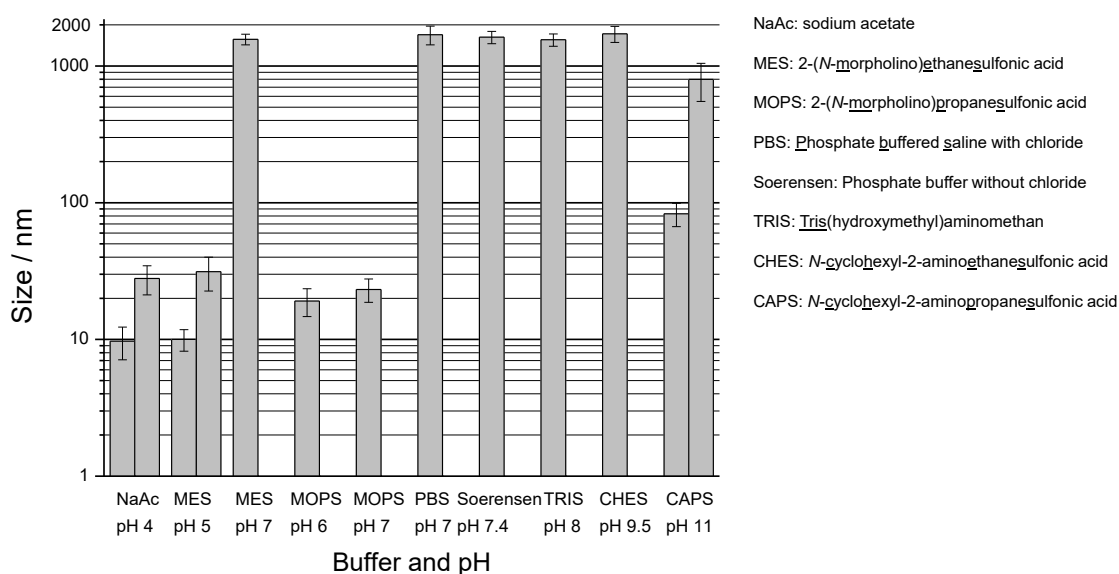
Figure 43: Results derived from DLS measurements of BMP-2 dissolved in different buffers at different pH values with a concentration of 25 µg ml^{-1}. Results are shown as means ± standard deviation of triple measurements for three representative samples.

It can be observed that BMP-2 aggregation is highly dependent on the pH. While BMP-2 dimers of around 10 nm and small aggregates of around 30 nm could be detected at pH values lower than 7, large BMP-2 aggregates of 1.5-1.7 µm were present at pH values higher than 7. At pH 11, BMP-2 aggregates of the size of 1 µm and 100 nm could be detected. The pH-dependent aggregation of BMP-2 is schematically illustrated in Figure 44.

This behaviour is typical for proteins [291] and depends on their pI and the hydrophobicity. When the pH of the buffer is significantly lower than the pI, protein molecules are positively charged and repel each other through electrostatic repulsion. At pH = pI ± 1, the electric charge of protein molecules is compensated, so that they are attracted to each other through hydrophobic forces resulting in aggregation and precipitation. When pH of the buffer is higher than pI, protein molecules become negatively charged and can repel each other again. In general, proteins are amphipathic species, which have both hydrophilic (charged) and hydrophobic regions. For hydrophobic proteins with a high pI like BMP-2 (pI ≈ 8.5), interactions between the hydrophobic regions of the molecules are favoured at physiological pH (7.4) due to the charge compensation on the surface of BMP-2. In addition, the aggregation of hydrophobic BMP-2 results in the increase of the entropy, which is energetically favoured [141, 142]. Therefore, BMP-2 is more prone to fast aggregation at pH near the pI and even above it.
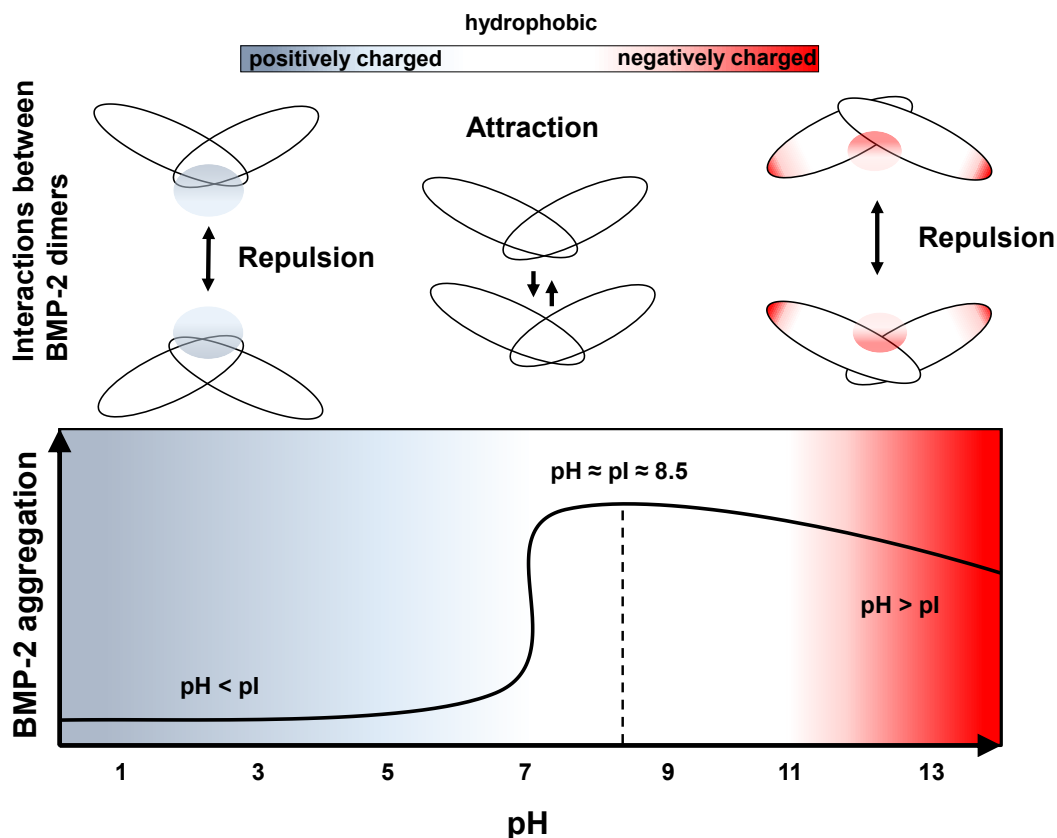
Figure 44: Schematic illustration of the pH-dependent aggregation of BMP-2 dimers showing interactions between them. The illustration of the surface potential of a BMP-2 dimer was adapted from [219].

Based on the results described above, BMP-2 was dissolved in 2-(*N*-morpholino)-ethanesulfonic acid (MES) buffer at pH 5. The colloidal stability of BMP-2 at different concentrations in MES buffer at pH 5 was verified using DLS measurements (Figure

45a). It can be seen that the mean size of BMP-2 aggregates is strongly dependent on the BMP-2 concentration. In fact, the lower the BMP-2 concentrations, the smaller the BMP-2 aggregate size. Thus, the BMP-2 solution at the concentration of 66 µg ml^{-1} contained mostly aggregates with the mean size of 35 ± 16 nm. When the BMP-2 concentration was reduced by half to 33 µg ml^{-1}, the mean size of BMP-2 aggregates dropped to 25 ± 11 nm. At the lowest concentration of about 16 µg ml^{-1}, the minimal concentration needed for DLS measurements, mostly BMP-2 dimers with the means size of 10 ± 2 nm were detected. In addition, zeta potential measurements were performed with BMP-2 dissolved in MES buffer at a concentration of 130 µg ml^{-1}, minimal for zeta potential measurements, showing highly positively charged BMP-2 species with the measured zeta potential of 42.8 ± 4.7 mV (Figure 45b). These results demonstrate successful stabilisation of individually solubilised BMP-2 dimers by simply exploiting electrostatic repulsion. Therefore, we suggest that in order to achieve homogeneous adsorption of BMP-2 on the surface of NPSNPs, BMP-2 should be dissolved in a buffer with maximal pH 5 and at low concentrations.

The results derived from DLS and zeta potential measurements represent an initial step towards the understanding of the physicochemical properties of *E. coli*-derived rhBMP-2.
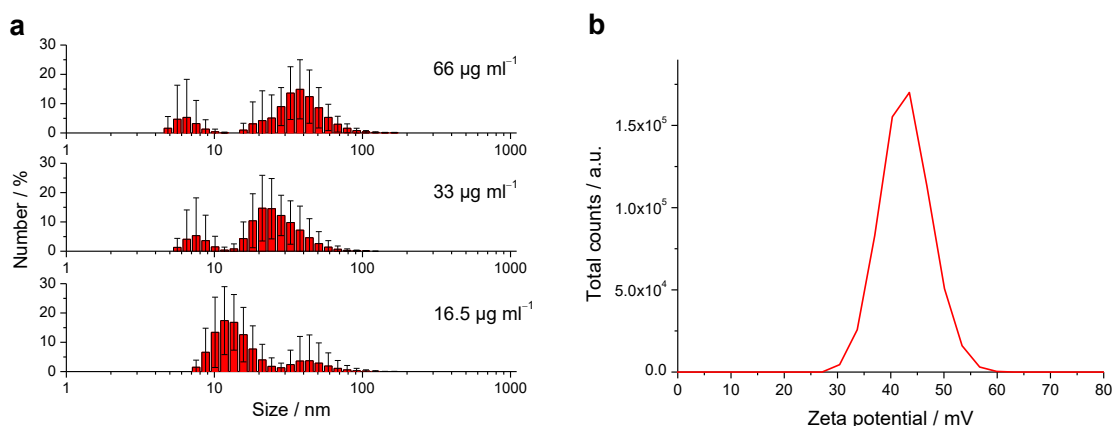
Figure 45: (a) Size distribution of BMP-2 at different concentrations and (b) zeta potential of BMP-2 molecules in MES buffer at pH 5 at the concentration of 130 µg ml^{-1}. Results are shown as means ± standard deviation of triple measurements for one representative sample.

4.2.4 Possible growth factor-NPSNP interactions

As the solution of BMP-2 in MES buffer at pH 5 provided favourable properties, zeta potential and DLS measurements were performed with all nanoparticle types also in MES buffer at pH 5, providing corresponding zeta potentials, apparent particle sizes and possible aggregation phenomena (Table 5). As expected, NPSNPs bearing terminal -OH, -SH and -SO$_3$H groups were negatively charged, while NPSNPs bearing terminal -

NH_2 groups showed positively charged surfaces. The particles sizes of all particle types, except NPSNP-propyl-SH, were in the range of between 60 nm and 110 nm, evidencing colloidally stable dispersions in MES buffer at pH 5. Only NPSNP-propyl-SH formed large aggregates in the range of between 2 µm and 3 µm. This could be due to the strong van der Waals interactions between the thiol groups.

After the assessment of the physicochemical properties of both NPSNPs, as the carrier material of choice, and the growth factor BMP-2, as its cargo, the possible growth factor-NPSNP interactions are discussed. Depending on the modification of the NPSNPs, BMP-2 could bind on their surface via electrostatic, hydrophobic and hydrogen bonding interactions or a combination of those (Figure 46). Both non-modified and differently modified NPSNPs could interact with growth factors through hydrogen bonds formed by hydroxyl and amino groups. Possibly, this way of interaction may not be favourable for the adsorption of BMP-2 due to the hydrophobic nature of large regions on the surface of BMP-2 dimers (see section 2.4.2 for more details). Instead, hydrophobic regions of BMP-2 molecules could interact with hydrophobic propyl and hexyl chains on the surface of NPSNPs. In addition, electrostatic interactions could play a role: positively charged BMP-2 might be attracted to NPSNPs bearing negatively charged -OH, -SH or $-SO_3H$ groups. In contrast, positively charged ammonium functionalities should be repellent to the equally charged BMP-2. In general, the non-covalent attachment of growth factors on biomaterial surfaces is a complicated process, which has not been fully understood yet (section 2.1.6). Therefore, adsorption mechanisms of growth factor BMP-2 on the surface of NPSNPs exhibiting versatile surface chemistries were assessed in this study.
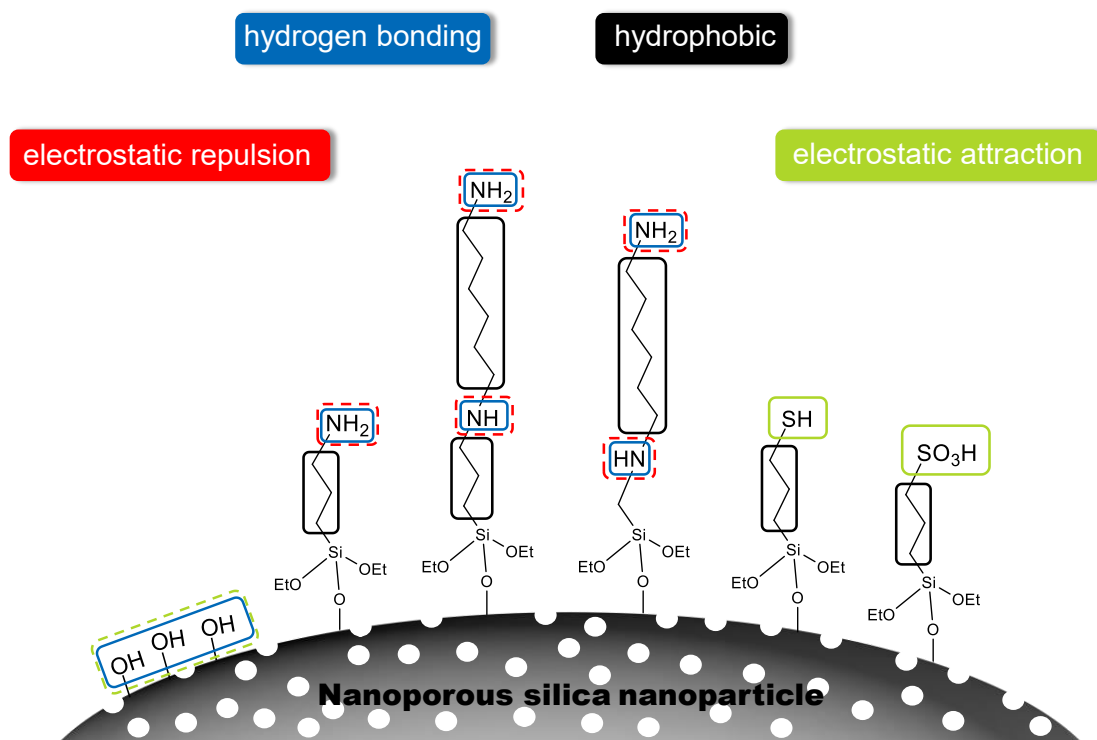
Figure 46: Schematic representation of possible interactions between the functional groups on the surface of NPSNPs and BMP-2.

4.2.5 Quantification of BMP-2 adsorbed on the surface of NPSNPs

To investigate the adsorption mechanisms of BMP-2 on the surface of non-modified and differently modified NPSNPs, a study of protein adsorption was conducted by soaking 5 mg of NPSNPs in the BMP-2 solution (5 µg ml^{-1} in 1 ml MES buffer at pH 5). The adsorbed BMP-2 amounts on the surface of each nanoparticles type was quantified by two different methods: by means of an antibody-based enzyme-linked immunosorbent assay (ELISA) and a cell-based assay based on the BMP-responsive element with luciferase transporter gene (BRE-Luc) (Figure 47). In case of ELISA, BMP-2 amounts in the supernatants were determined and subsequently subtracted from the initial BMP-2 amount resulting in an indirect quantification of adsorbed BMP-2. In contrast, adsorbed BMP-2 was quantified directly by a BRE-Luc assay by adding the BMP-2-loaded NPSNPs to the cells.

According to the results derived from ELISA measurements, non-modified NPSNPs adsorbed the least amount of BMP-2, namely around 37 ng mg^{-1}. This could be due to the weak interactions via hydrogen bonds between the silanol groups of the silica nanoparticles and BMP-2. Interestingly, all modified NPSNPs showed much higher

adsorbed amounts of BMP-2 in the range of between 700 ng mg^{-1} to 1100 ng mg^{-1} (Figure 47, left).
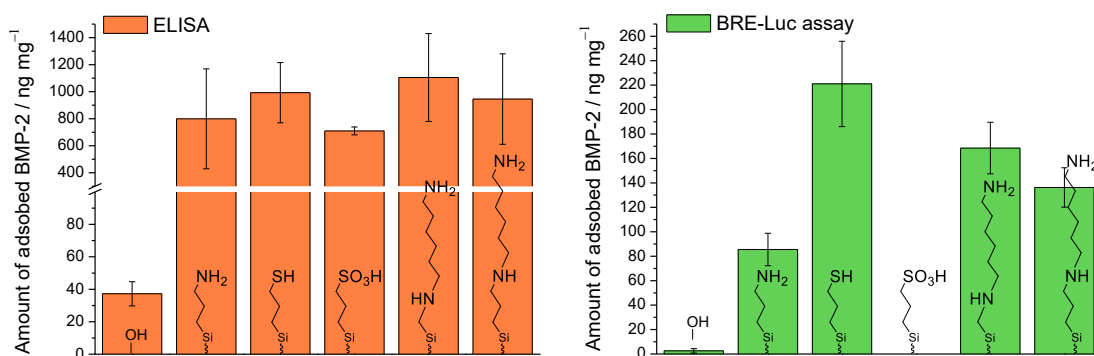
Figure 47: Quantification of BMP-2 that was adsorbed on the surface of non-modified and differently modified NPSNPs: indirect and direct by means of ELISA (left) and BRE-Luc assay (right), respectively. The data represent the mean ± standard deviation (n=3).

The ELISA results for NPSNP-OH and NPSNP-propyl-NH$_2$ are in line with our previous findings, demonstrating higher loading capacities of BMP-2 on the surface of silica surfaces equipped with the aminopropylsilyl functionalities [33, 105]. We proposed that on the one hand, propyl chains on the surface of modified silica interact with BMP-2 via hydrophobic interactions. On the other hand, positively charged amine groups could be electrostatically attracted to the negatively charged or polarized regions of BMP-2 dimers. The latter hypothesis will become clearer by looking at the crystal structure of the BMP-2 dimer reported by Scheufler *et al*. [219], presented earlier in section 2.4.2, in Figure 11. In his work, he described BMP-2 dimers exhibiting negatively charged regions on the fingertips and in the middle of the concave side of a BMP-2 dimer. This so-called cavity II was suggested to be the binding site for one of two BMP-2 receptors. Therefore, it is probable that positively charged ammonium groups of NPSNP-propyl-NH$_2$, as well as of NPSNP-methyl-NH-hexyl-NH$_2$ and -propyl-NH-hexyl-NH$_2$ tethered on the NPSNPs surface, interact with the negatively charged cavity II of the BMP-2 dimer, resulting in the electrostatic attraction. In addition, a positively charged cavity I on the convex side of a BMP-2 dimer was identified as a heparin binding site [219]. Heparin is a naturally occurring glycosaminoglycan, which consists of repeating disaccharide units bearing negatively charged sulphate groups and exhibits very high affinity to BMP-2 [292, 293]. It seems that similar to heparin, NPSNP-propyl-SO$_3$H from this study have adsorbed BMP-2 molecules by interacting with their positively charged cavity I region. The attraction can then be additionally strengthened by the hydrophobic interaction between the propyl chains of the NPSNPs and the hydrophobic areas on the surface of BMP-2. It can be hypothesized that a similar binding mechanism of BMP-2 is responsible for the high BMP-2 loading on the surface of negatively charged NPSNP-propyl-SH.

As such, the results derived from ELISA measurements offer compelling evidence for the binding mechanisms of BMP-2 on the surface of modified NPSNPs through hydrophobic interactions and electrostatic attraction, regardless of the charge of the functional groups, while hydrogen bonding interactions seemed to play only a minor role in BMP-2 adsorption (Figure 48).
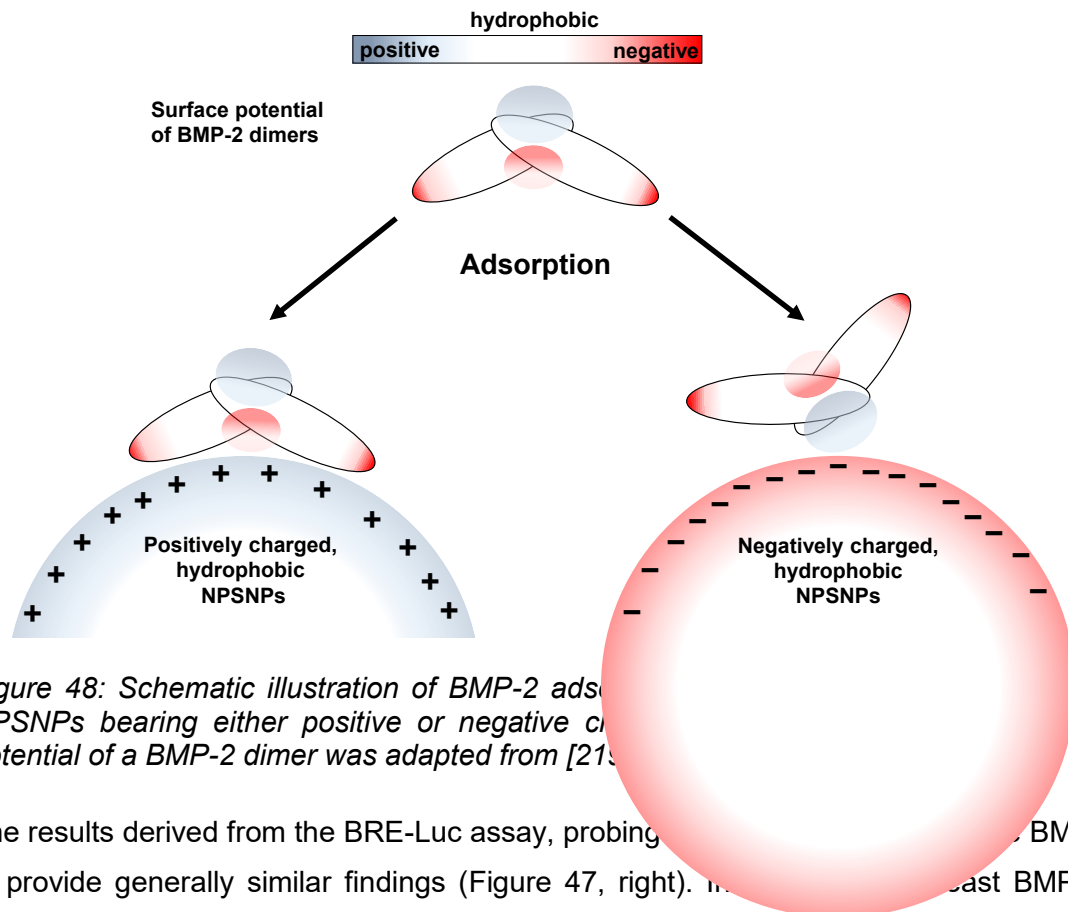
Figure 48: Schematic illustration of BMP-2 ads_____ _ic NPSNPs bearing either positive or negative c_____ ce potential of a BMP-2 dimer was adapted from [21___

The results derived from the BRE-Luc assay, probing_____ BMP-2, provide generally similar findings (Figure 47, right). In_____ast BMP-2 amount was also detected on the surface of non-modified NPSNPs (around 2.5 ng mg^{-1}), whereas the highest BMP-2 amount was measured on the surface of NPSNP-propyl-SH (221 ng mg^{-1}), closely followed by NPSNP-methyl-NH-hexyl-NH$_2$ (169 ng mg^{-1}) and NPSNP-propyl-NH-hexyl-NH$_2$ (136 ng mg^{-1}). Among NPSNPs bearing terminal amino groups, NPSNP-propyl-NH$_2$ adsorbed the least BMP-2, namely around 86 ng mg^{-1}. Unfortunately, no biologically active BMP-2 could be quantified on the surface of NPSNP-propyl-SO$_3$H by the BRE-Luc assay. On the one hand, BMP-2 might have been bound too strongly on the surface of NPSNPs, became biologically inactive and could not be detected by the cell receptors. On the other hand, NPSNP-propyl-SO$_3$H could have slowed down the metabolism of the BRE-Luc cells, so that the BMP-2 signal could not be transmitted to the cells. This issue will be discussed later in section 4.4.1.

The results derived from the BRE-Luc assay provide additional support for the previous hypothesis that more BMP-2 is bound on the surface of NPSNPs bearing hydrophobic

functionalities. In addition, it can be seen that more BMP-2 could be bound on the surface of NPSNPs bearing hydrophobic propyl chain with negatively charged thiol groups.

It is interesting to note that the values of BMP-2 amounts quantified by BRE-Luc assay are much lower than those quantified by ELISA. There are several possible explanations for this outcome. First, while BRE-Luc assay identifies only biologically active BMP-2 dimers, ELISA detects immunologically active species, including both biologically active, as well as partially denatured BMP-2, which still exhibits the recognition epitope. Second, as BMP-2-loaded NPSNPs were added directly to the cells for the BRE-Luc assay and the experiment was carried out for 24 h, probably not all BMP-2 could be released from the NPSNPs during this time and detected by the cells, resulting in lower quantified BMP-2 amounts. In contrast, BMP-2 detected by ELISA is dissolved in MES buffer and can be quantified entirely. Further, cell viability and metabolic activity of the cells used for the BRE-Luc assay could vary due to the exposure to differently modified NPSNPs, so that the nature of the particles influences the outcome of the test. This issue will be discussed later in detail in the chapter 4.4.

4.2.6 Effect of the surface chemistry of NPSNPs on BMP-2 binding and particle aggregation

To further prove the successful loading of BMP-2 on the surface of NPSNPs, the changes of particle sizes and surface charges before and after loading of different amounts of BMP-2 were examined by zeta potential and DLS measurements in MES buffer (Figure 49). Here, the concentration of the NPSNPs was fixed at 50 µg ml^{-1}, while the offered BMP-2 concentrations were increased from 0.05 µg ml^{-1} to 2.5 µg ml^{-1}. The studies for BMP-2 adsorption described previously were carried out at the BMP-2 concentration of 0.05 µg ml^{-1}.

The zeta potential of BMP-2-loaded NPSNPs bearing negatively charged groups in MES buffer, namely NPSNP-OH, -propyl-SH and -propyl-SO$_3$H (Table 5), shifted from negative to positive with increasing BMP-2 concentrations (Figure 49a, b and c, left). This was anticipated for NPSNP-propyl-SH and -propyl-SO$_3$H, because of their high loading capacity determined before by ELISA, but was surprising for NPSNP-OH due to their poor BMP-2 adsorption properties.

The reason for that is still not entirely clear, but could be explained by the rather low initial zeta potential of NPSNP-OH (around −9 mV) and relatively high zeta potential of BMP-2 in MES (around +43 mV). When BMP-2 is being adsorbed on the surface of these NPSNPs, small amounts of highly positive BMP-2 could probably compensate for the small negative surface charge of NPSNP-OH resulting in the zeta potential increase.
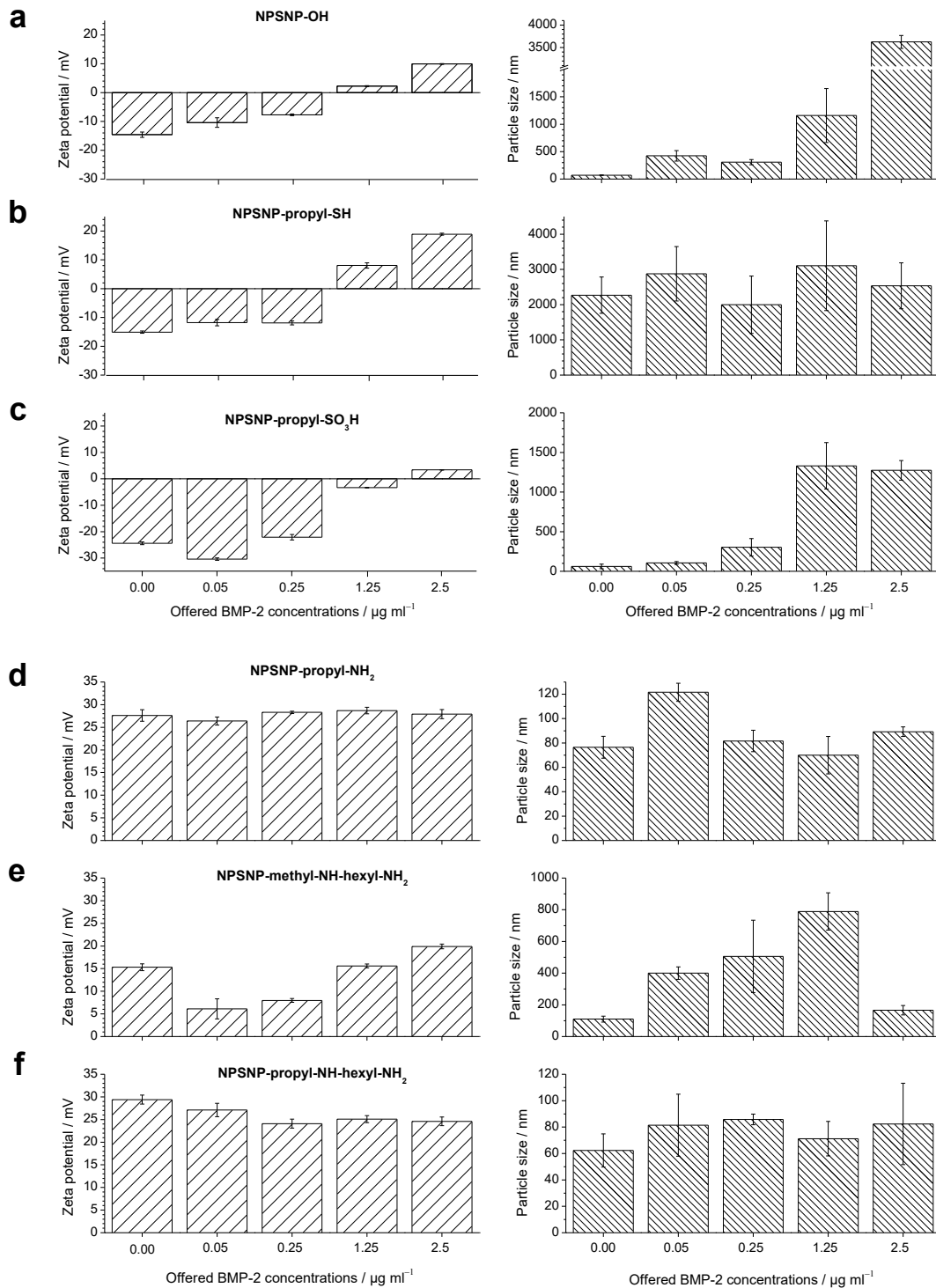
Figure 49: Zeta potentials (left column) and corresponding particle sizes (right column) of non-modified and differently modified NPSNPs as measured in MES buffer at pH 5 before and after loading of BMP-2, with various concentrations of the protein in the incubation solution. Results are shown as means ± standard deviation of triple measurements for one representative sample.

The particle sizes of NPSNP-OH and -propyl-SO₃H measured by DLS increased with increasing BMP-2 concentrations, correlating well with the respective zeta potential values (Figure 49a and c). In general, nanoparticle dispersions with a zeta potential

between +20 mV and −20 mV are considered colloidally unstable and tend to aggregate. Therefore, the increase of the particle size can be attributed to the aggregation of BMP-2-loaded NPSNPs, which becomes more pronounced at higher BMP-2 concentrations. By contrast, NPSNP-propyl-SH revealed large aggregates even before BMP-2 loading. This can be due to the attraction of hydrophobic propyl groups on the surface of the NPSNPs, the low zeta potential of around −15 mV and van der Waals interactions between thiol groups. With increasing BMP-2 concentration, the particle sizes varied between 2 μm and 4 μm (Figure 49b, right).

Only positive zeta potential values were observed for the three NPSNPs bearing positively charged terminal amine groups, regardless of the offered BMP-2 amounts for loading, since BMP-2 dimers were also positively charged (Figure 49d, e and f, left). According to DLS measurements, the particle sizes of the NPSNPs with propyl-NH_2 and propyl-NH-hexyl-NH_2 groups were slightly below or above 100 nm at all BMP-2 concentrations (Figure 49d and f, right). These results can be associated with the relatively high zeta potential values of above +25 mV, indicating the presence of stable colloidal dispersions. In contrast, the particle sizes of NPSNPs containing methyl-NH-hexyl-NH_2 functionalities increased with increasing BMP-2 concentration from 100 nm up to 800 nm, but then dropped to 200 nm at the highest BMP-2 concentration (Figure 49e, right). The zeta potential values of this particles were below +20 mV at every BMP-2 concentration, indicating an incipient instability of the particle dispersions.

Overall, it was demonstrated that zeta potential measurements offered an additional method to prove a successful loading of positively charged BMP-2 on the surface of negatively charged NPSNPs, in particular of NPSNP-OH, -propyl-SH and -propyl-SO_3H. However, this method was not suitable to observe BMP-2 adsorption on positively charged NPSNPs bearing terminal amino groups. In addition, DLS measurements of NPSNPs with all negatively charged and with positively charged methyl-NH-hexyl-NH_2 functional groups demonstrated the tendency for particle aggregation especially at high BMP-2 concentrations. However, when high BMP-2 amounts are needed to be adsorbed, NPSNPs with propyl-NH_2 and propyl-NH-hexyl-NH_2 groups would be suitable candidates due to the formation of colloidally stable nanoparticle dispersions at low and high BMP-2 concentrations.

4.2.7 Release kinetics of BMP-2

To learn about the release behaviour of BMP-2 from the different types of nanoparticles, release experiments were carried out with all previously BMP-2-loaded NPSNPs possessing different surface functionalities. Preliminary release experiments were performed at physiological conditions, pH 7.4 and 37 °C. However, very low amounts of released BMP-2 could be detected via ELISA due to the precipitation of BMP-2 under these conditions (Figure S4, SI). Therefore, MES buffer at pH 5 was chosen as the release medium to study the BMP-2 release behaviour due to the good colloidal stability of BMP-2 shown before. The amount of the released BMP-2 was measured at scheduled time points and quantified directly by means of ELISA.

According to the ELISA results, different released BMP-2 amounts were determined in MES buffer at pH 5 (Figure 50). While very small amounts of BMP-2 (up to 0.5 ng mg^{-1}) were released from NPSNPs bearing -propyl-SH, -propyl-SO$_3$H and -methyl-NH-hexyl-NH$_2$ functionalities, considerably higher BMP-2 amounts were released from NPSNPs bearing -propyl-NH$_2$ (75 ng mg^{-1}) and -propyl-NH-hexyl-NH$_2$ (35 ng mg^{-1}) moieties after a period of two weeks. The BMP-2 amount set free from the NPSNP-OH was around 6 ng mg^{-1}. The release kinetics of NPSNP-OH and NPSNP-propyl-NH$_2$ were similar showing a sustained release up to one week followed by no or slow release. The BMP-2 release rates up to one week could be determined by means of the linear regression to 0.9 ng mg^{-1} per day and 10.0 ng mg^{-1} per day for NPSNP-OH and NPSNP-propyl-NH$_2$, respectively (Figure S5, SI). In the second week, the release rates were 0.0 ng mg^{-1} per day and 1.0 ng mg^{-1} per day for NPSNP-OH and NPSNP-propyl-NH$_2$, respectively. In contrast, NPSNP-propyl-NH-hexyl-NH$_2$ revealed a sustained release of BMP-2 for the entire release period of two weeks with the BMP-2 release rate of around 2.7 ng mg^{-1} per day (Figure S5, SI).

The differences in released BMP-2 amounts and release kinetics could be explained by three main reasons. These are i) the binding strength between BMP-2 and distinct functional groups on the surface of NPSNPs, ii) colloidal stability of NPSNPs and iii) conformational changes of adsorbed BMP-2.
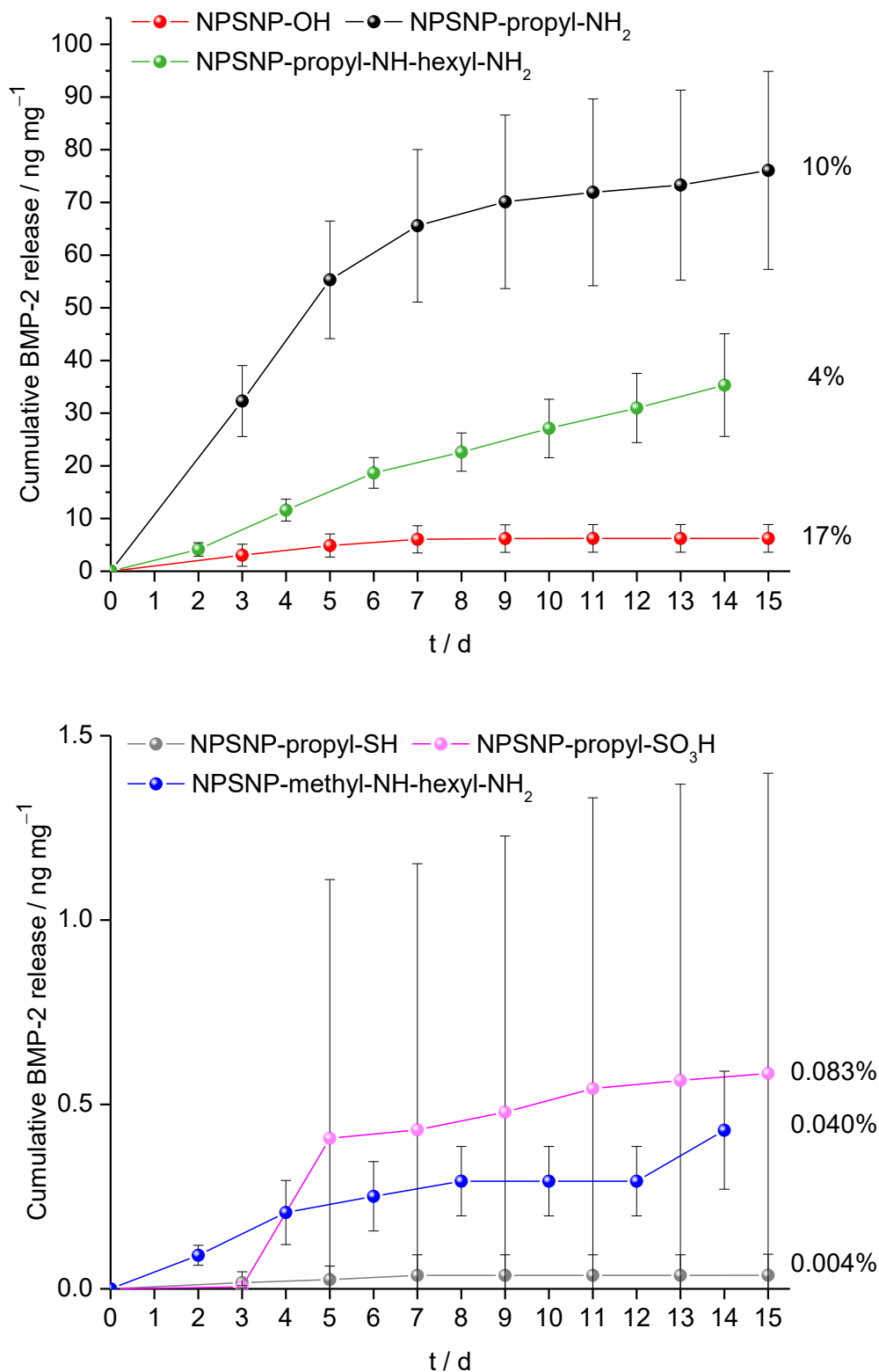
Figure 50: Release of BMP-2 from the surface of non-modified and differently modified NPSNPs in MES buffer at pH 5 and 37 °C as measured by ELISA. The data represent the mean ± standard deviation (n=3).

It can be hypothesized that the weak hydrogen bonding interactions between BMP-2 and silanol and amine groups on the surface of NPSNP-OH and NPSNP-NH$_2$ were probably responsible for the fast BMP-2 release within one week. Since more BMP-2 was adsorbed on the surface of NPSNP-propyl-NH$_2$ than on NPSNP-OH, 10 times more BMP-2 was released during the period of 2 weeks. In contrast, the very small amounts of BMP-2 released from NPSNP-propyl-SH, -SO$_3$H and -methyl-NH-hexyl-NH$_2$ may be attributed to the strong electrostatic or/and hydrophobic interactions between BMP-2 and the functional groups on the surface. In these cases, BMP-2 appears to be bound too strongly and therefore could be retained on the surface of the NPSNPs. In addition, it is also possible that BMP-2 underwent conformational changes due to the strong interactions and could not be recognized by the antibody used for BMP-2 quantification in an ELISA. For example, the thiol groups could have interacted with the cystine knots of BMP-2 dimers; this could have led to irreversible conformational changes of BMP-2. As a result, only small amounts of BMP-2 were detected by ELISA. Interestingly, only NPSNP-propyl-NH-hexyl-NH$_2$ revealed a sustained release of BMP-2 for the period of two weeks. Here, a beneficial synergistic effect of electrostatic repulsion of positively charged amine groups and BMP-2 molecules and hydrophobic interactions between hexyl chains and BMP-2 might have been responsible for the controlled BMP-2 release. Further investigations would be needed to determine exactly how different functional groups on the surface of NPSNPs affect the binding and the release kinetics of BMP-2. For example, computational approaches could provide further information into protein adsorption-desorption mechanisms at the molecular scale [145]. The adsorption-desorption mechanisms of one or several protein molecules on the surface of NPSNPs could be simulated with different degrees of exactness by different computational approaches. However, very large, detailed and precise simulations will result in the increase of the computational costs.

Further, we compare the DLS results shown in Figure 49 for the BMP-2 concentration of 0.05 µg ml^{-1} with the release profiles presented in Figure 50. The particle types that formed stable colloidal dispersions, namely NPSNP-propyl-NH$_2$ and NPSNP-propyl-NH-hexyl-NH$_2$, showed a significant release of BMP-2 according to the ELISA results (Figure 50). The released amount of BMP-2 decreased upon increasing aggregation of the nanoparticles, e.g. in case of the NPSNP-OH. The reason for that is probably the encapsulation of BMP-2 in the interparticle space which allowed for the reasonably fast detachment of BMP-2 only from the outer surface of the particle aggregates but hampered the release of the BMP-2 from the inside of such aggregates. This might be understood as a series of adsorption equilibria, where BMP-2 molecules which detach from occluded particle surfaces becomes re-adsorbed on adsorption sites on the

particles located nearer to the outer part of the aggregates. However, also the NPSNPs bearing -propyl-SO_3H and -methyl-NH-hexyl-NH_2 groups released only very small amounts of BMP-2 in spite of only slight aggregation at the lowest BMP-2 concentration of 0.05 µg ml^{-1}. As mentioned before, this could be attributed to the strong binding of the BMP-2 via electrostatic interactions with the sulfonic acid groups and hydrophobic interactions with -methyl-NH-hexyl-NH_2 groups. Furthermore, the inhibition of BMP-2 release from NPSNP-propyl-SH could have been caused by the entrapment of BMP-2 by particle aggregation or conformational changes of BMP-2, as discussed above.

As far as we know, it is the first time that the release of BMP-2 from NPSNPs can be controlled by tuning the nanoparticle surface with functionalities having different properties. In which manner BMP-2 should be released from a delivery system to result in successful bone healing is still a matter of debate. A generally accepted concept, in which a high initial release of BMP-2 should be followed by a sustained release of low doses of BMP-2 to induce bone regeneration, was proposed by several studies [294-296]. In contrast, more recent investigations show that a controlled release of low doses of BMP-2 without proceeding fast release could successfully promote new bone formation as well [297, 298]. In addition, some studies found out that the BMP-2 is not only active when being released, but also when it is retained at the scaffold [26], however, this issue remains under debate. Not only the release kinetics but also the released BMP-2 amounts are crucial for successful application of BMP-2-loaded NPSNPs. According to the literature [299], the minimal BMP-2 concentration needed to induce osteogenic differentiation of bone marrow-derived mesenchymal stem cells (BM-MSCs) is about 100 ng ml^{-1}. This was supported by the previously conducted study in our group [33]. Here, osteogenic differentiation of adipose tissue-derived MSCs was successfully promoted by using aminopropylsilyl-modified, BMP-2-loaded NPSNPs with a total BMP-2 concentration of about 110 ng ml^{-1} presented to the cells. In this work, the ability to induce the osteogenic differentiation of BM-MSCs was tested for BMP-2-loaded NPSNPs bearing -propyl-NH-hexyl-NH_2 functionalities with the total BMP-2 concentration of about 200 ng ml^{-1} and will be presented and discussed in the next chapter 4.3.

Apart from the fact that the reasons for the different release behaviours observed for differently modified NPSNPs cannot be fully clarified yet and need further investigations, we can conclude that we have been able to engineer different types of nanoporous silica nanoparticles featuring different release behaviours: fast initial, sustained and slow release (retention) of BMP-2. These can be used alone or in combination for bone tissue engineering. For this purpose, the BMP-2-loaded NPSNPs with the desired BMP-2 release kinetics can be integrated into an appropriate scaffold, e.g. collagen or poly(ε-

caprolactone) (PCL) scaffolds (see chapter 4.5), to provide osteoinductive properties to the scaffold materials.

4.3 Effect of BMP-2-loaded NPSNPs on early targeted gene induction in bone marrow-derived mesenchymal stem cells (BM-MSCs)

Primary bone marrow-derived mesenchymal stem cells (BM-MSCs) are promising candidates for tissue engineering [174]. They can differentiate into lineages of different tissues such as bone, cartilage, tendon, fat and muscle [172]. Bone morphogenetic protein 2 (BMP-2) has been shown to promote osteogenic differentiation of BM-MSCs *in vitro* and *in vivo* [210, 235, 300-302]. BMP-2-induced gene expression of various specific markers is one of the tools used to monitor the commitment and differentiation progress of BM-MSCs towards the osteogenic lineage [234]. Among these markers, the *inhibitor of differentiation* (*Id*) genes have been proposed to play a role in the control of mammalian cell growth, differentiation and tumorigenesis. The BMP-2-induced increase of *Id* gene expression may work as a molecular switch for osteoblastic differentiation by encoding certain negative transcription factors, which functionally block the differentiation of BM-MSCs into other cell lineages [303, 304].

In the present study, BM-MSCs were treated with either dissolved BMP-2 (200 ng) or BMP-2 that was adsorbed on the surface of NPSNPs bearing propyl-NH-hexyl-NH$_2$ groups (200 ng of BMP-2 adsorbed on the surface of 250 µg NPSNPs) for 2 h and 24 h. The NPSNP-propyl-NH-hexyl-NH$_2$ were chosen due to the sustained BMP-2 release behaviour (Figure 50), which was deemed favourable. The expression of two typical immediate responsive genes for osteogenesis, *Id1* and *Id3*, was analysed using quantitative real-time polymerase chain reaction (qRT-PCR) (Figure 51). The measurements were performed by LAURA BURMEISTER from the Klinik für Orthopädie im Annastift, Medizinische Hochschule Hannover, Germany.

The present study focused on the early responses of BM-MSCs associated with the duration and the way of BMP-2 treatment. Non-treated and NPSNP-treated BM-MSCs cultures displayed only a slight increase of *Id1* and *Id3* gene expressions after 2 h and a slight decrease of the gene expression after 24 h of cultivation compared with the control. In contrast, the exposure with BMP-2 induced a higher increase of *Id1* and *Id3* expression, which was dependent on both the duration of exposure and the way BMP-2 was administered to the cells. Thus, after the exposure for 2 h slightly higher gene expression was caused by 200 ng of BMP-2 adsorbed on the surface of 250 µg NPSNPs than by the same amount of dissolved BMP-2 for both *Id1* and *Id3*. However, after BMP-2

treatment for 24 h similar levels of *Id1* and *Id3* gene expression were observed for adsorbed and dissolved BMP-2.

Id 1

Id 3
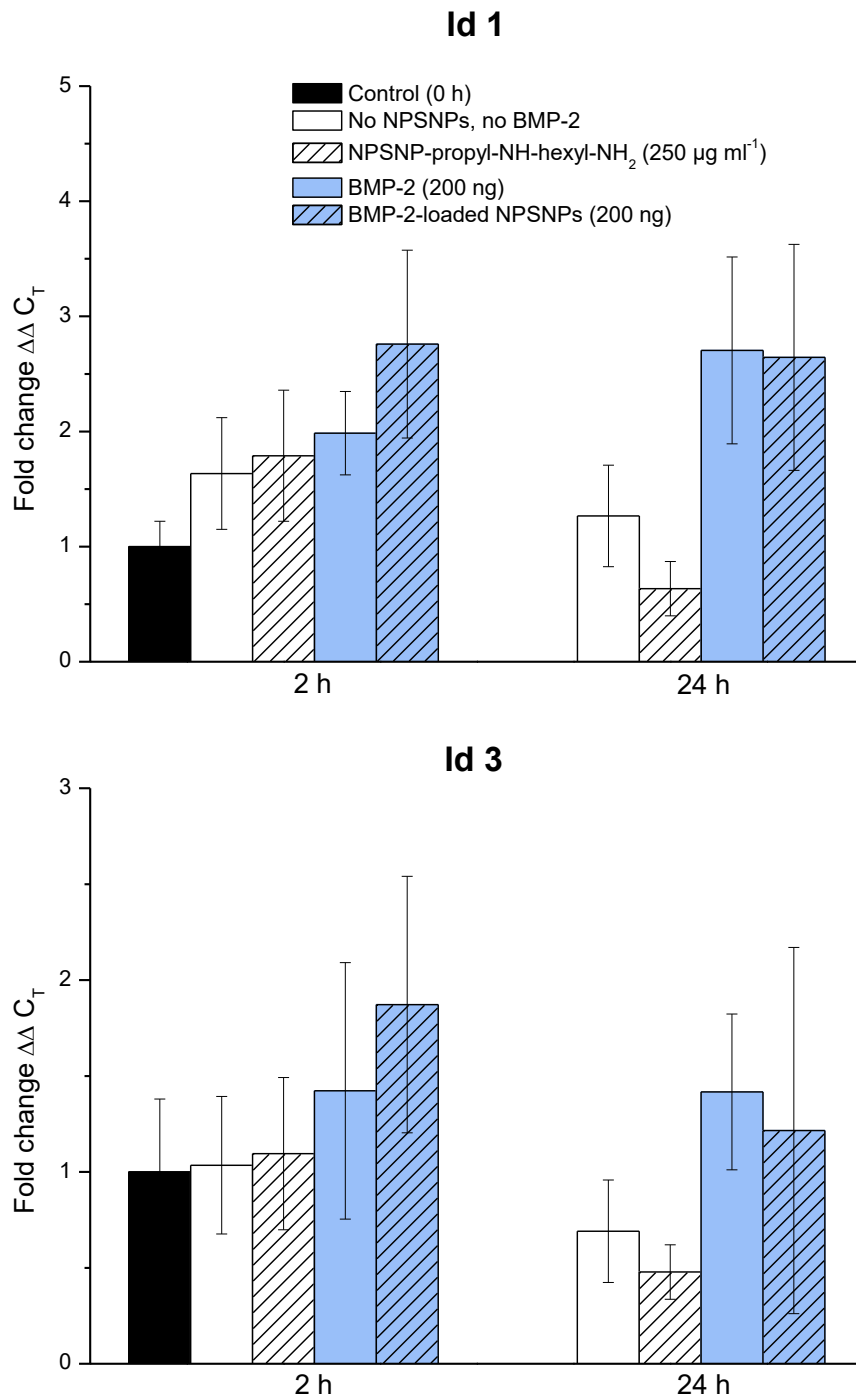
Figure 51: Expression of typical early genes for osteogenesis, Id1 and Id3, as measured by qRT-PCR upon BMP-2 treatment for 2 h and 24 h. Fold differences for each gene were calculated using a normalized C_T value for the housekeeping gene, Rps29, according to the manufacturer's instructions. The data represent the mean ± standard (triplicates of one independent experiment).

Previous studies have shown that a continuous BMP-2 exposure for at least 14 days is needed for maximal effect on mineralization of BM-MSCs [235, 302]. In addition, Neumann and Christel *et al*. reported a successful osteogenic differentiation of hASCs

upon the exposure with BMP-2-loaded NPSNPs (aminopropylsilyl modification) for up to 21 days [33]. Therefore, the duration of the BMP-2 exposure of 2 h and 24 h in this study was probably not sufficient to achieve mineral deposition on BM-MSCs. However, based on the results showing upregulated expression of *Id1* and *Id3*, it was demonstrated that short exposure times could already induce the commitment of BM-MSCs towards the osteogenic lineage. In addition, we found that the effect of BMP-2 adsorbed on the surface of NPSNPs on gene expression was slightly stronger than that of the dissolved BMP-2 after 2 h of exposure. We hypothesize that the physicochemical properties of BMP-2 and NPSNPs may be responsible for this outcome (Figure 52). It is known that BMP-2 tends to aggregate under physiological conditions. Therefore, when dissolved BMP-2 is added to the cell, rapid BMP-2 aggregate formation takes place. Thus, only BMP-2 molecules at the outer aggregate surface can be detected by the cells. In contrast, NPSNPs bearing propyl-NH-hexyl-NH$_2$ groups, used here, showed relatively high colloidal stability owing to the high zeta potential at physiological pH and were equally distributed over the cells (see Figure 42). Consequently, more BMP-2 could interact with the cell receptors resulting in higher levels of gene expression after 2 h. However, similar levels of gene expressions for dissolved and adsorbed BMP-2 were detected after 24 h probably due to the similar diffusion rates of BMP-2 from the aggregates and NPSNPs.
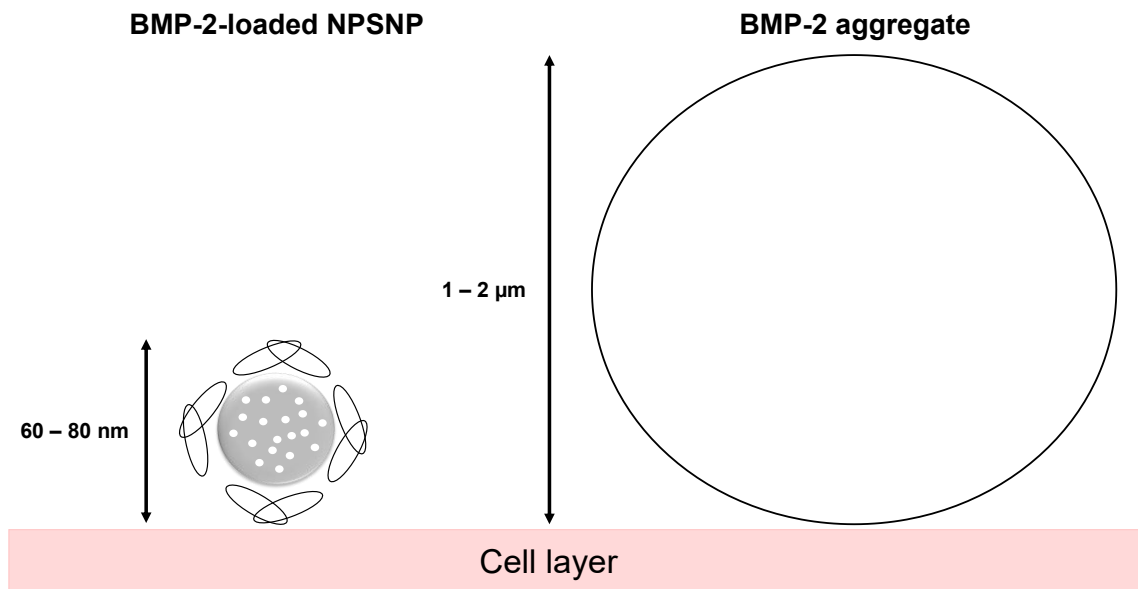
Figure 52: Availability of adsorbed BMP-2 on the surface of a NPSNP versus aggregated BMP-2.

In addition, higher levels of *Id1* genes were expressed in comparison to *Id3* after 2 and 24 h regardless of the way of BMP-2 administration. This fact is known from the literature

for BMP-9-induced expression of *Id1* and *3*, however, the reasons for that are unclear to this point [209, 236].

In conclusion, we could show that BMP-2 that was adsorbed on the surface of NPSNPs was slightly more effective in upregulating the expression of the early targeted *Id1* and *Id3* genes, which are typical for the osteogenic differentiation of BM-MSCs, than dissolved BMP-2. Although this is the result of only a single experiment, the findings suggest that the adsorption of BMP-2 on NPSNPs did not affect its biological functionality to promote osteogenesis of BM-MSCs. This study was the first step towards enhancing our understanding of how non-covalently adsorbed BMP-2 promotes osteogenic differentiation in MSCs. Future work will explore the synergistic effect of BMP-2 and dexamethasone on BM-MSCs. Further experiments with BMP-2 on dental pulp stem cells are planned to study the BMP-2-mediated odontogenesis.

4.4 Cytotoxicity investigations of non-modified and differently modified NPSNPs

4.4.1 Murine C2C12 BRE-Luc cells

The C2C12 cells belong to an immortalised mouse myoblast cell line and are often used to study the osteogenic differentiation upon the exposure to various BMPs. In this study, the murine cell line C2C12 BRE-Luc (BMP-Responsive-Element-Luciferase)-pGL3 was used to quantify BMP-2 on the surface of non-modified and differently modified NPSNPs by the so-called BRE-Luc assay (section 4.2.5). Therefore, the cytotoxicity of these NPSNPs towards the C2C12 BRE-Luc cells was examined. For that, a modified MTT (3-(4,5-dimethylthiazol-2-yl)-2,5-diphenyltetrazolium bromide) assay was used [305]. In this test, viable cells with active metabolism convert yellow water-soluble MTT into purple coloured insoluble formazan with an absorbance maximum of 570 nm. The absorbance is detected by the UV-Vis spectrophotometry. All measurements and light microscopic images were performed and taken by LAURA BURMEISTER from the Klinik für Orthopädie im Annastift, Medizinische Hochschule Hannover, Germany.

MTT assay results of the C2C12 BRE-Luc cells exposed to varying concentrations of non-modified and differently modified NPSNPs for 24 h (1 day) are shown in Figure 53.

Figure 53: Relative metabolic cell activity or viability of C2C12 BRE-Luc cells determined by the MTT assay (n=3), in the presence of varying concentrations of different types of NPSNPs after 24 h (1 day). The relative metabolic activity/viability of the cells in absence of NPSNPs was used as a control and set as 100%.

According to the ISO 10993:5-2009, the reduction of cell viability by more than 30% is considered a cytotoxic effect [306]. While the relative cell viability of the tested cells was only slightly affected by the presence of non-modified NPSNPs (NPSNP-OH) being above or slightly below 70% of the control for all concentrations, the relative cell viability decreased more strongly by contact with modified NPSNPs. Thus, the strongest reduction of the cell viability (less than 60%) was caused by NPSNP-propyl-SO$_3$H for all concentrations. Exposure to NPSNPs bearing terminal amine groups caused the decrease of the cell viability to less than 55% when concentration exceeded 100 µg ml^{-1}. Finally, NPSNP-propyl-SH were the least cytotoxic among all modified NPSNPs causing a reduction of the cell viability to around 55% above the concentration of 250 µg ml^{-1}. Taken together, all types of modified NPSNPs were slightly cytotoxic to the C2C12 BRE-Luc cells after 24 h of exposure at concentrations higher than 100 − 250 µg ml^{-1}.

Ideally, the amount of reduced MTT is proportional to the number of metabolic active viable cells and thus, to the cell viability. However, when the growth of viable cells becomes inhibited, e.g. when exposed to nanoparticles, metabolism of the cells may slow down resulting in a reduced metabolic activity of the cells [307]. Furthermore, stressed cells could also show an increased metabolic activity. Other factors such as

altered pH of the cell culture medium or removal of essential nutrients can additionally change the metabolic activity of the cells. In these cases, the cell viability results measured by the MTT assay are not directly proportional to the real number of viable cells, but to their metabolic activity. In particular, in case of NPSNPs, it was hard to distinguish between the reduction of the cell viability and the metabolic activity of viable cells.

To shed more light on this issue, light microscopy images of the C2C12 BRE-Luc cells upon exposure to varying concentrations of different types of NPSNPs for 24 h were taken to assess cell morphology (Figure 54). It can be seen that cell growth was inhibited for nearly all types of NPSNPs, especially at higher concentrations, due to the presence of nanoparticle aggregates covering the surface of the cells. As reported previously by Wittmaack, the supply of oxygen and nutrients to the cells, as well as the removal of the cell wastes, could have been inhibited by nanoparticle coverage causing cytotoxic effects [90]. Interestingly, NPSNP-propyl-SO$_3$H showed a different aggregation behaviour in the cell medium unlike all other types of NPSNPs. At high concentrations of 500 µg ml^{-1} and 1000 µg ml^{-1}, NPSNPs formed small nanoparticle aggregates and were equally distributed over the cells. We believe that the cell coverage together with the toxicity of the negatively charged sulfonic acid groups amplified the decrease of the relative metabolic cell activity/viability detected by the MTT assay.

NPSNP-OH

NPSNP-propyl-NH$_2$

NPSNP-propyl-SH

NPSNP-propyl-SO$_3$H

NPSNP-methyl-NH-hexyl-NH$_2$

NPSNP-propyl-NH-hexyl-NH$_2$
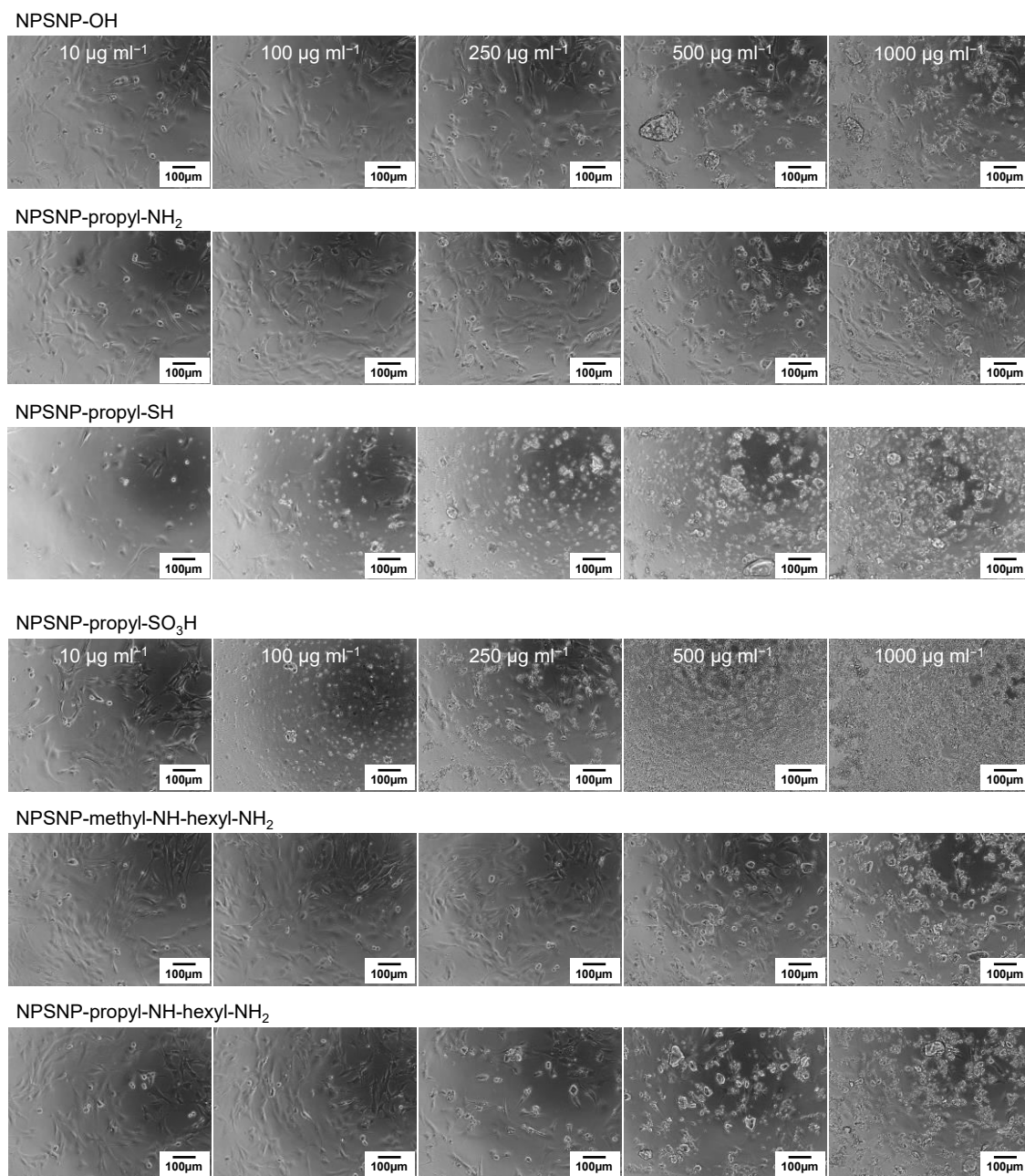
Figure 54: Light microscopy images of C2C12 BRE-Luc cells exposed to varying concentrations of different types of NPSNPs for 24 h (1 day). At the images, cell morphology and aggregation behaviours of NPSNPs in cell medium can be observed.

To verify whether NPSNPs showed chronic toxicity, MTT assays were performed after 3 days upon exposure of the C2C12 BRE-Luc cells to varying concentrations of different types of NPSNPs (Figure 55). The relative cell viability of the cells exposed to NPSNP-propyl-NH$_2$, -propyl-SH and -methyl-NH-hexyl-NH$_2$ for 3 days passed or reached towards 70% of the control, indicating a quick recovery of the cells from the initial cytotoxicity. The corresponding light microscopy images of the cells revealed confluent cell layers and thus, a successful cell proliferation (Figure 56). In contrast, NPSNP-propyl-SO$_3$H and NPSNP-propyl-NH-hexyl-NH$_2$ showed a persistent cytotoxicity at higher

concentrations (250-1000 µg ml^{-1}) after the exposure for 3 days (Figure 55). The corresponding light microscopy images showed no confluent cell layer at higher NPSNPs concentrations confirming reduced cell viability (Figure 56). According to the results of pH-dependent zeta potential measurements (Figure 42), these two types of NPSNPs revealed high colloidal stability at physiological pH. Thus, it seems that the cytotoxic effect of these NPSNPs is intensified by the presence of highly concentrated and colloidally stable NPSNPs, which were equally distributed over the cells and probably inhibited the cell proliferation, as already described above.
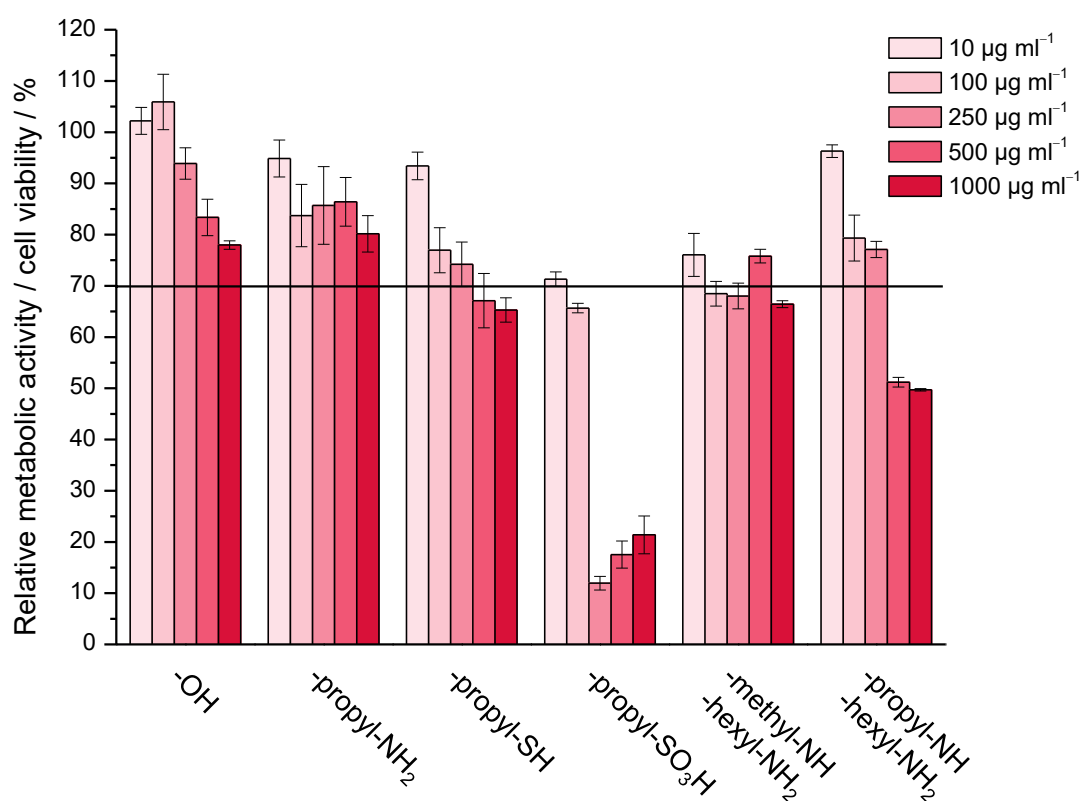
Figure 55: Relative metabolic cell activity or viability of C2C12 BRE-Luc cells determined by the MTT assay (n=3), in the presence of varying concentrations of different types of NPSNPs after 72 h (3 days). The relative metabolic activity/viability of the cells in absence of NPSNPs was used as a control and set as 100%.

NPSNP-OH

NPSNP-propyl-NH$_2$

NPSNP-propyl-SH

NPSNP-SO$_3$H

NPSNP-methyl-NH-hexyl-NH$_2$

NPSNP-propyl-NH-hexyl-NH$_2$
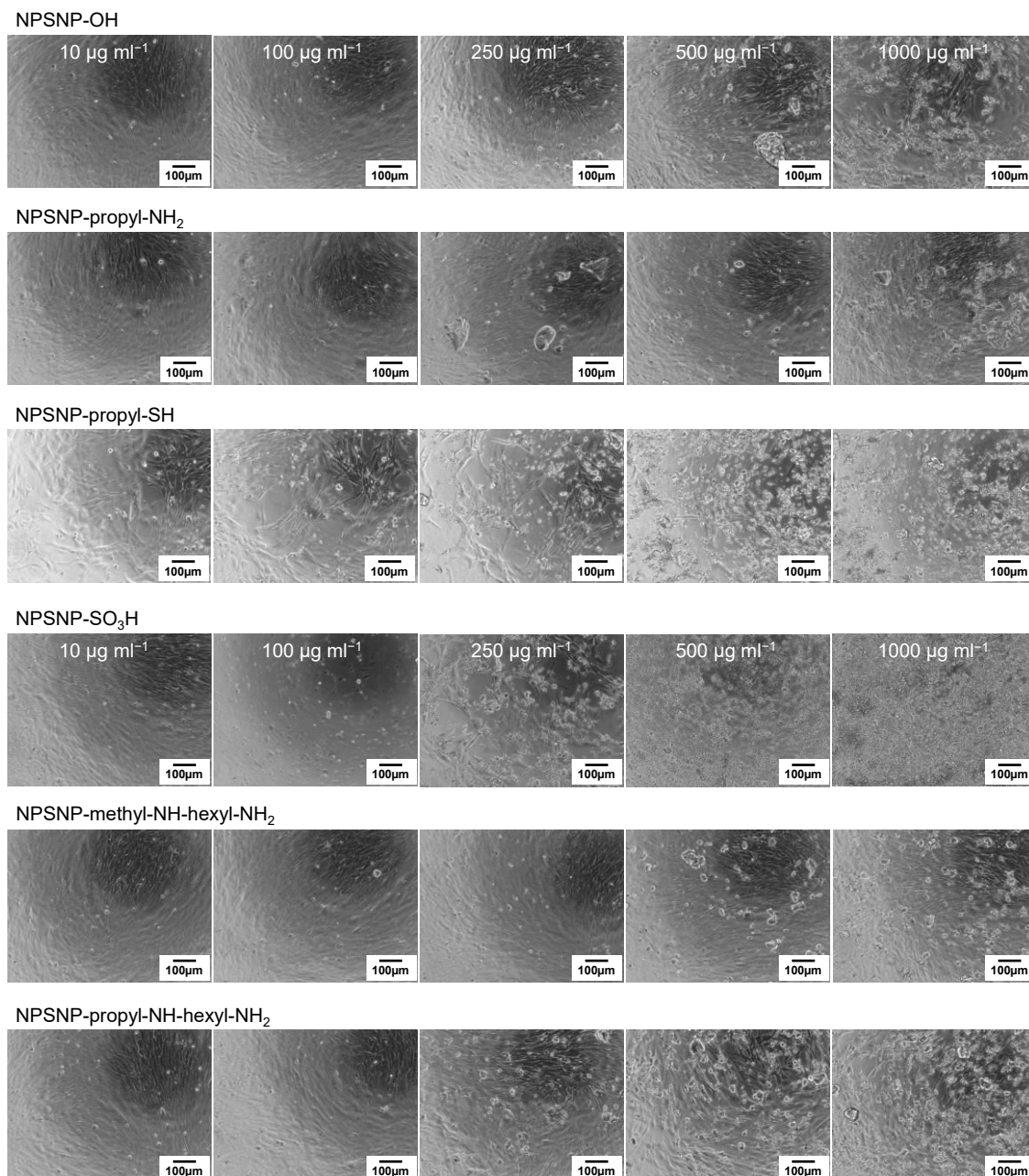
Figure 56: Light microscopy images of C2C12 BRE-Luc cells exposed to varying concentrations of different types of NPSNPs for 72 h (3 days). Confluent cell layer indicates quick recovery from the initial cytotoxicity.

Finally, relative cell viability results were derived from the MTT assays performed after 7 days of the exposure of the C2C12 BRE-Luc cells to varying concentrations of different types of NPSNPs (Figure 57). Besides a slight cytotoxic effect of the NPSNP-propyl-SO$_3$H and NPSNP-propyl-NH-hexyl-NH$_2$ at high concentrations, high relative metabolic cell activity/viability values above 70% of the control can be observed for all types of NPSNPs. The corresponding light microscopic images provided similar information compared to images after 3 days of exposure and therefore, are not shown here. In

conclusion, the results demonstrate a recovery of the C2C12 BRE-Luc cells from the initial cytotoxicity caused by differently modified NPSNPs within 7 days of cultivation.
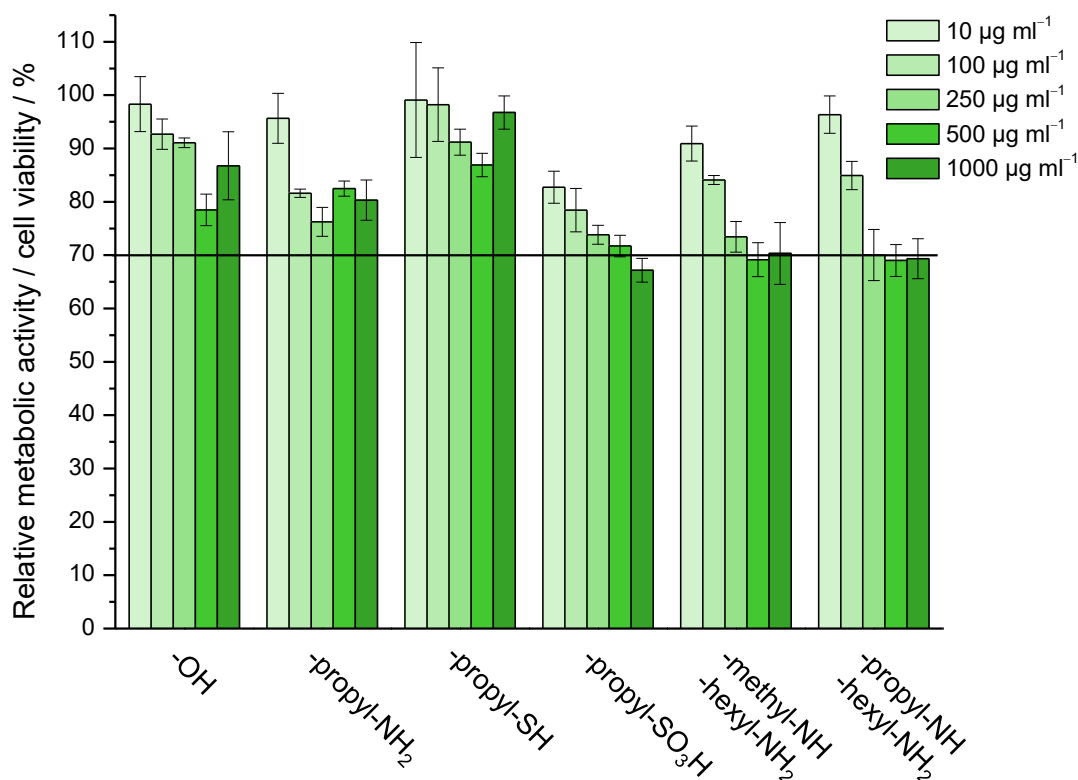
Figure 57: Relative metabolic cell activity or viability of C2C12 BRE-Luc cells determined by the MTT assay (n=3), in the presence of varying concentrations of different types of NPSNPs after 168 h (7 days). The relative metabolic activity/viability of the cells in absence of NPSNPs was used as a control and set as 100%.

In general, amorphous and porous silica nanoparticles are considered to exhibit low cytotoxicity *in vitro* [39]. This is in good agreement with our findings showing a low cytotoxic effect of non-modified NPSNPs on C2C12 BRE-Luc cells. However, the surface modification of NPSNPs is needed to change their physicochemical properties according to the desired biomedical application. In this study, the surface modification was carried out to achieve higher BMP-2 loading capacities on the surface of NPSNPs. Several studies have been conducted to study the cytotoxic effects of nanoparticles without or with further modifications on biological systems [308-310]. It is commonly accepted that positively charged nanoparticles cause cytotoxicity by cell membrane damage, while negatively charged nanoparticles cause intracellular damage [82, 83]. However, owing to the various reported synthesis and modification procedures of NPSNPs and various applied biological testing systems, it is not possible to compare the results derived from cytotoxicity investigations of the modified NPSNPs in our study with the literature [77]. In addition, the cytotoxicity of NPSNPs bearing methyl-NH-hexyl-NH$_2$ and propyl-NH-hexyl-NH$_2$ groups is reported for the first time in this study.

To sum up, cytotoxic effects of non-modified and differently modified NPSNPs on C2C12 BRE-Luc cells could be roughly assessed in this study. Whereas NPSNP-OH were not cytotoxic at any concentrations and any time, NPSNPs equipped with different functional groups showed a reduction of the relative cell viability of C2C12 BRE-Luc cells above the particle concentrations of 100 − 250 µg ml^{-1} after 24 h of exposure. Further, colloidally well-stabilized NPSNPs bearing strong positive or negative charge (NPSNP-propyl-NH-hexyl-NH$_2$ or NPSNP-propyl-SO$_3$H, respectively) showed a chronic cytotoxicity after 3 days of exposure, probably associated with the inhibition of the cell proliferation. However, after 7 days of the exposure, a quick recovery of C2C12 BRE-Luc cells from the cytotoxic effect caused by differently modified NPSNPs could be detected. Further studies will be needed to clarify the role of the functional groups and the surface chemistry on cytotoxicity of NPSNPs.

4.4.2 Human bone marrow-derived mesenchymal stem cells (BM-MSCs)

The MSCs used in this study were obtained from the human bone marrow of the femoral head. As multipotent cells, they can differentiate into lineages of different tissues such as bone, cartilage, tendon, fat and muscle [172], which makes them an attractive therapeutic tool for tissue engineering. With regard to the future application in bone tissue engineering, the cytotoxicity of different types of NPSNPs towards BM-MSCs was examined by a modified MTT assay [305]. In this assay, the relative metabolic cell activity/viability could be determined upon exposure of BM-MSCs to varying concentrations of NPSNPs for 1, 3 and 7 days. All measurements and light microscopic images were performed and taken by LAURA BURMEISTER from the Klinik für Orthopädie im Annastift, Medizinische Hochschule Hannover, Germany.

According to the ISO 10993:5-2009, a biomaterial causing a reduction of the relative metabolic cell activity/viability by more than 30% is considered as cytotoxic [306]. Similar to previous results, NPSNP-OH did not show cytotoxic effects towards BM-MSCs at any concentration and any time. Among modified NPSNPs, NPSNP-propyl-SH were the least cytotoxic after 24 h of exposure showing relative cell viabilities/metabolic activities over 70% of the control at concentrations between 10 and 500 µg ml^{-1} (Figure 58). Only at the highest concentration of 1000 µg ml^{-1}, a slight cytotoxic effect could be detected for NPSNP-propyl-SH. This effect was probably caused by the cell coverage through nanoparticles resulting in the inhibition of the supply of oxygen and nutrients to the cells, as well as the removal of the cell wastes [90]. In contrast, NPSNP-propyl-NH$_2$, -propyl-SO$_3$H, -methyl-NH-hexyl-NH$_2$ and -propyl-NH-hexyl-NH$_2$ can be considered non-cytotoxic only at the lowest concentration of 10 µg ml^{-1}. The exposure to higher particle

concentrations up to 1000 µg ml^{-1} for 24 h resulted in a concentration-dependent reduction of the relative metabolic cell activity/viability by more than 30% of the control.
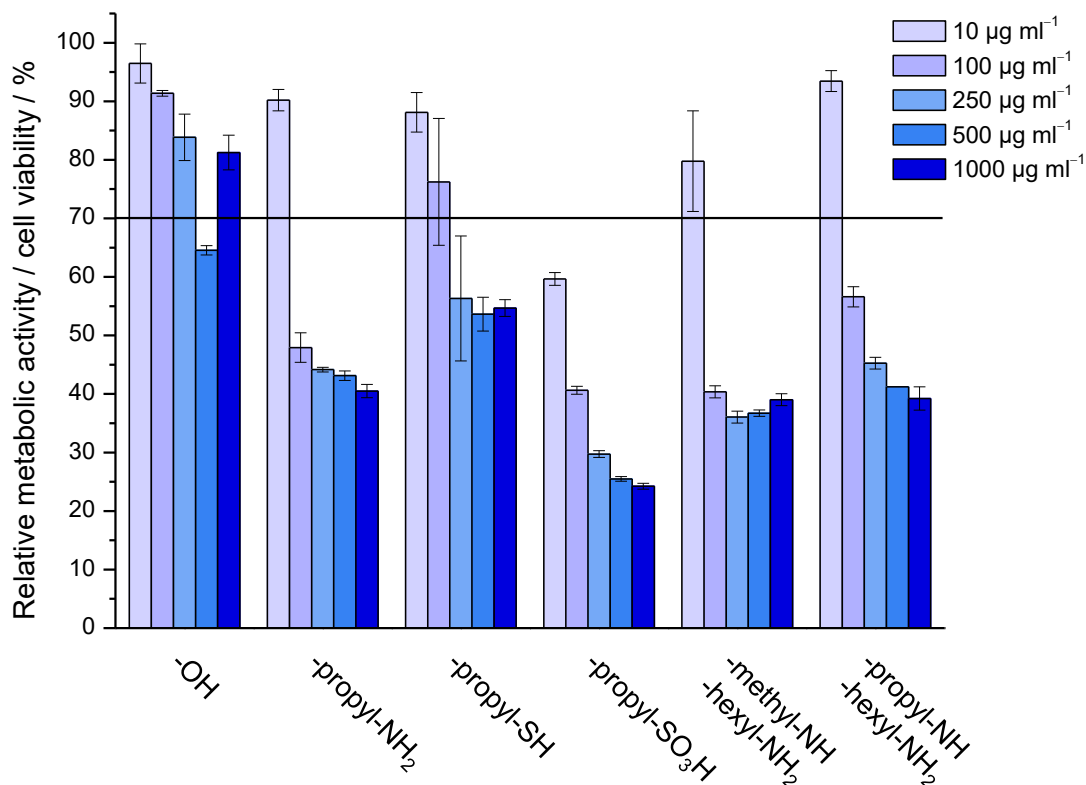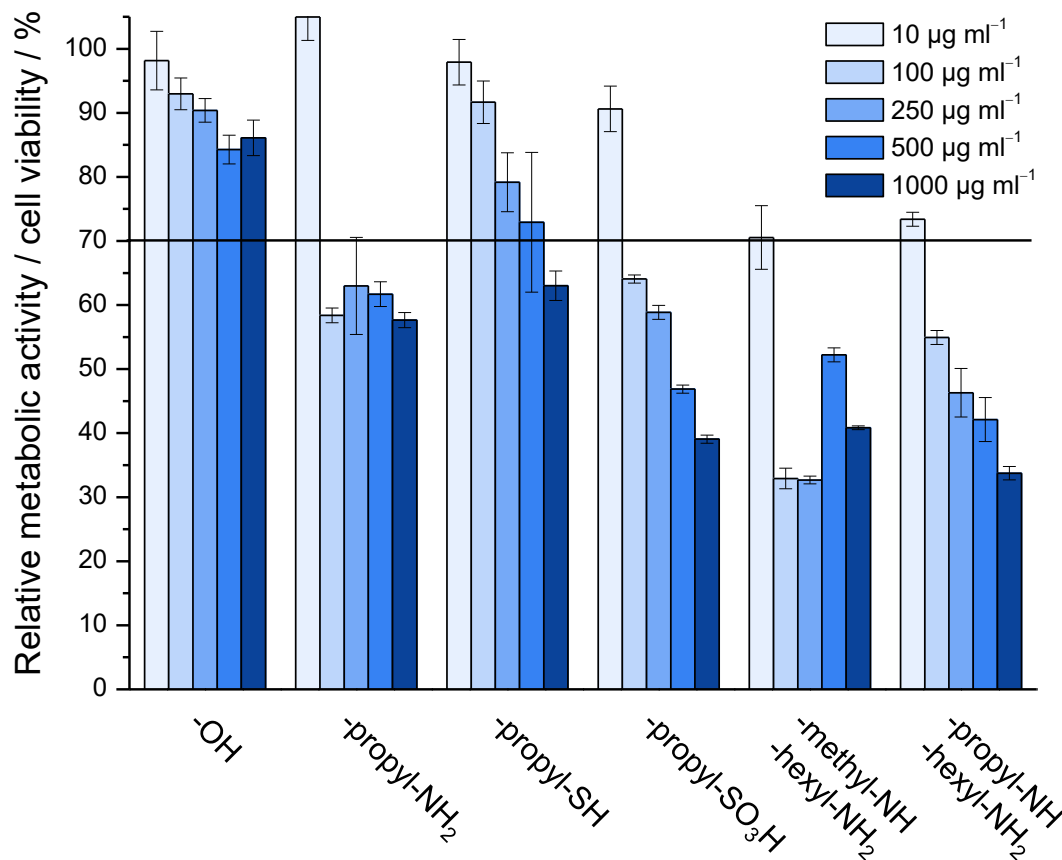

Figure 58: Relative metabolic cell activity or viability of BM-MSCs determined by the MTT assay (n=3), in the presence of varying concentrations of different types of NPSNPs after 24 h (1 day) of exposure. The relative metabolic activity of the cells in absence of NPSNPs was used as a control and set as 100%.

To examine whether NPSNPs cause chronic cytotoxicity, MTT assays were performed after 3 days upon exposure of the BM-MSCs to varying concentrations of different types of NPSNPs (Figure 59). It could be observed that BM-MSCs exposed to NPSNP-propyl-SH at all concentrations and NPSNP-propyl-SO$_3$H up to 250 µg ml^{-1} could quickly recover from the acute cytotoxicity caused during the first 24 h upon nanoparticle exposure. However, the NPSNP-propyl-NH$_2$ at all concentrations, the NPSNP-propyl-SO$_3$H above the concentration of 500 µg ml^{-1}, the NPSNP-methyl-NH-hexyl-NH$_2$ and -propyl-NH-hexyl-NH$_2$ above the concentration of 100 µg ml^{-1} still caused a reduction of the relative metabolic cell activity under 70% of the control.
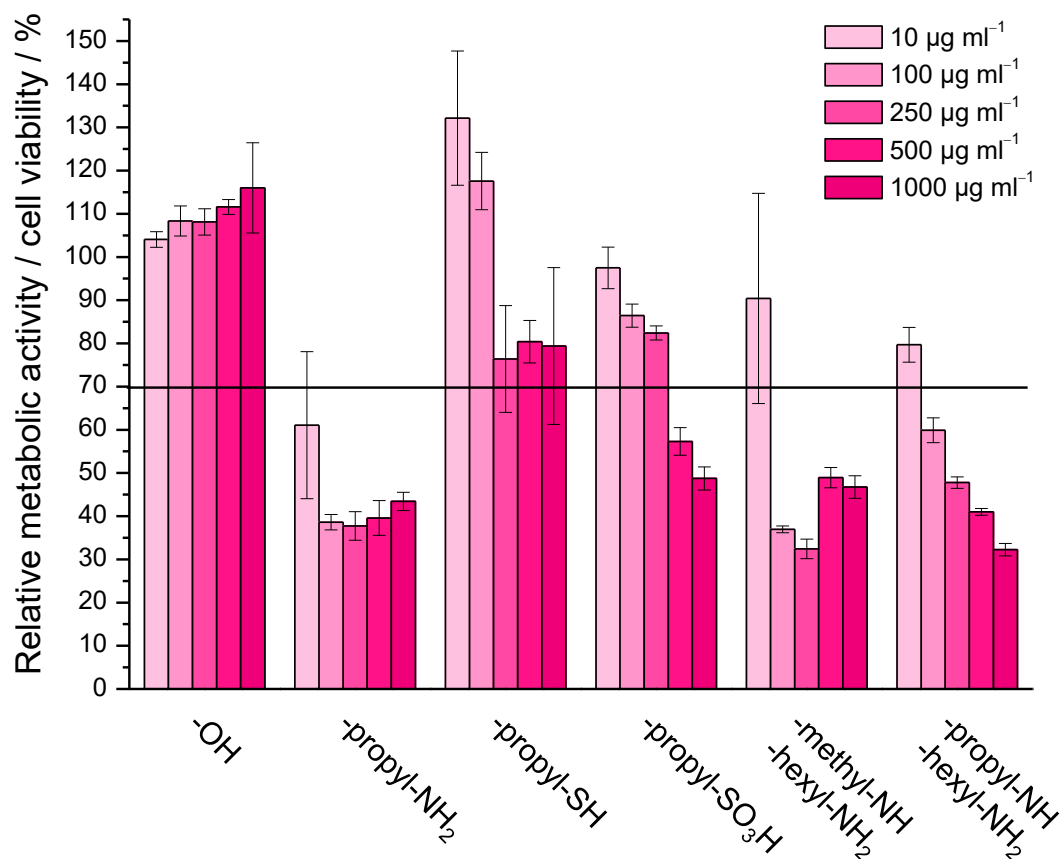
Figure 59: Relative metabolic cell activity or viability of BM-MSCs determined by the MTT assay (n=3), in the presence of varying concentrations of different types of NPSNPs after 72 h (3 days) of exposure. The relative metabolic activity of the cells in absence of NPSNPs was used as a control and set as 100%.

Interestingly, after the exposure of the NPSNP-propyl-SH and NPSNP-propyl-SO$_3$H for 7 days the measured values increased drastically up to 400% in comparison to the control sample (Figure 60). In this case, light microscopy images could provide more information (Figure 61). According to the images, no increased cell proliferation was observed upon exposure to NPSNP-propyl-SH and -propyl-SO$_3$H. Therefore, we believe that the MTT results show an increased relative metabolic activity of viable cells associated with cell stress rather than the actual cell viability. A slight increase towards 70% of the control could be detected for NPSNP-propyl-NH-hexyl-NH$_2$. In contrast, the cytotoxic effect of NPSNP-propyl-NH$_2$ and -methyl-NH-hexyl-NH$_2$ after the exposure for 7 days was similar to the previous results on day 3 indicating persistent reduction of the relative metabolic cell activity of the BM-MSCs.
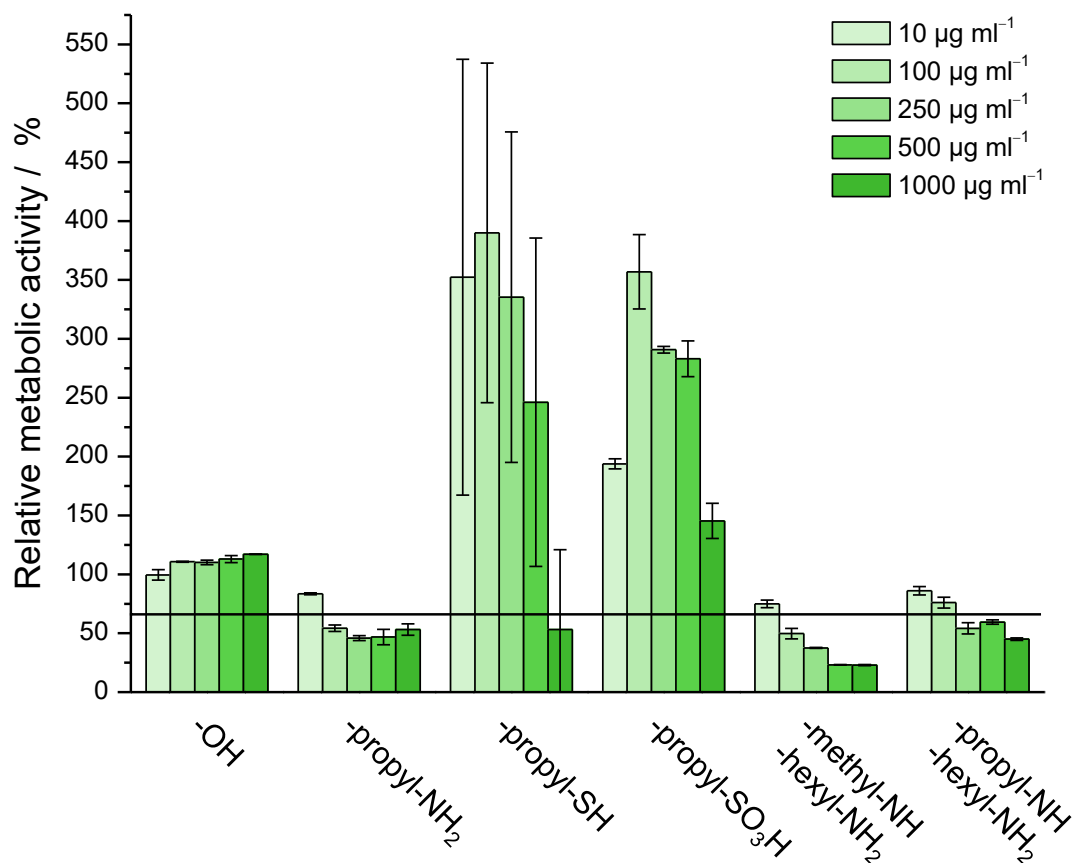
Figure 60: Relative metabolic activity of BM-MSCs determined by the MTT assay (n=3), in the presence of varying concentrations of different types of NPSNPs after 168 h (7 days) of exposure. The relative metabolic activity of the cells in absence of NPSNPs was used as a control and set as 100%.
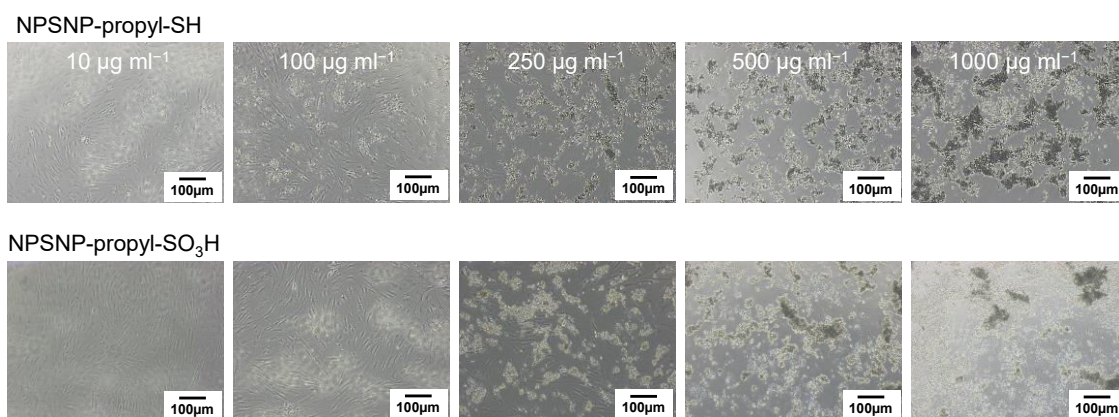
Figure 61: Light microscopy images of BM-MSCs exposed to varying concentrations of NPSNP-propyl-SH and -propyl-SO₃H for 72 h (3 days).

It is generally accepted that the effect of nanoparticles on the metabolic cell activity/viability is cell-dependent [311]. In this regard, primary cells such as mesenchymal stem cells are known to be more sensitive than other cell types. However, mechanisms of nanoparticle-cell interactions are not fully understood [82, 84, 312]. We believe that differently modified NPSNPs influence both the cell viability and metabolic

activity of the viable BM-MSCs in our study. However, a reduction of cell viabilities or metabolic activities of viable cells upon nanoparticle exposure does not have to indicate that NPSNPs cause a cytotoxic effect. The osteoinductive ability of silica nanoparticles, shown by Neumann and Christel *et al*. for hASCs [33] and Shi *et al*. [313], should be taken into account. Thus, the reduction of the cell proliferation and metabolic activity of BM-MSCs could have been caused by the incipient osteogenic differentiation due to the exposure to NPSNPs and not by the cytotoxicity of NPSNPs, in this study. To clarify this issue, further investigations of the differentiation of BM-MSCs due to the exposure of NPSNPs will be needed. Moreover, at high nanoparticle concentrations, the cytotoxic effect may have been caused by the NPSNPs coverage of the cells inhibiting the supply of oxygen and nutrients to the cells as well as the removal of the cell wastes [90]. This is not an issue when in future applications for bone tissue engineering the NPSNPs loaded with the osteogenic growth factor are attached on a three-dimensional scaffold (see chapter 4.5). The scaffolds implanted at the site of the bone defect should, in principle, attract stem cells from the surrounding bone tissue and induce their differentiation into osteoblasts.

4.5 Fabrication of nanocomposites for bone tissue engineering

Common bone tissue engineering approaches is based on three-dimensional scaffolds, which provide a friendly microenvironment for the attachment of cells and growth factors to restore form and functionality of damaged bone tissue [11-13]. In addition, the scaffold should enable cell ingrowth and vascularization of the newly formed tissue [8]. In this chapter, two different types of scaffolds are described. Although basically different in their structure and composition, both use BMP-2-loaded NPSNPs for controlled delivery of this growth factor. In the first approach, the basic structure of the scaffold consists of electrospun poly(ε-caprolactone) fibres; in the second, it is made up of a collagenous sponge.

It is of note that the conditions for BMP-2 loading on the surface of nanoporous silica nanoparticles (NPSNPs) were constantly improved during the entire period of the present work. A very important finding with regard to the loading of BMP-2 on NPSNPs was made in the last third of the working period, namely that BMP-2 derived from *E. coli* used in this work tends to aggregate at physiological conditions, e.g. when dissolved in phosphate buffered saline (PBS), at pH 7.4, and shows only low aggregation tendency at lower pH values, e.g. in 2-(*N*-morpholino)ethanesulfonic acid (MES) buffer at pH 5. For more information, see section 4.2.3. Therefore, some results presented and

discussed in the following chapter were derived from the experiments before this discovery, where PBS was used as medium for BMP-2 loading on NPSNPs and release from the scaffolds. Further, it was found that the BMP-2 quantification by means of enzyme-linked immunosorbent assay (ELISA) is not suitable for aggregated BMP-2. Instead, cell-based assay based on BMP-responsive element fused to luciferase reporter gene (BRE-Luc) is able to detect aggregated BMP-2 when it is still biologically active. However, the possibility to employ BRE-Luc assay provided by cooperation partner at the Hannover Medical School, in the work group of Prof. Dr. Andrea Hoffmann, occurred later during this work and thus could not be used for the majority of the experiments.

4.5.1 Bone tissue regeneration scaffolds based on electrospun poly(ε-caprolactone) and BMP-2-loaded nanoporous silica nanoparticles

Scaffolds made of poly(ε-caprolactone) (PCL) have gained attention for their use in bone regeneration in the last few years due to its good mechanical properties, biocompatibility and -degradability [197, 314, 315]. To provide a PCL scaffold with osteoinductive functionality, bone morphogenetic protein 2 (BMP-2) can be attached to it by means of tricalcium phosphate coating [316] or covalent attachment [25]. The former approach demonstrated fast and uncontrolled BMP-2 release. A fast burst release of the growth factor can cause uncontrolled bone formation and inflammation and is, therefore, not desired [259]. The latter approach resulted in a more controlled release of BMP-2, however, the covalent attachment of proteins to the scaffold is a complicated process that can lead to the loss of their bioactive properties due to harsh conditions sometimes required for satisfactory functionalization [317]. Herein, we report an optimised delivery system for controlled release of small BMP-2 amounts from the surface of differently modified nanoporous silica nanoparticles (NPSNPs) attached to the surface of modified electrospun PCL scaffolds. The modified PCL scaffolds decorated with BMP-2-loaded NPSNPs should be applied as one section of a graded implant for tendon-bone bridging in case of a rotator cuff rupture repair (for more details see section 2.3.3). The special focus of this work was placed on the regeneration of the bone site.

4.5.1.1   General concept

Biomaterials made of PCL show excellent properties as biomaterials such as biocompatibility and slow biodegradability. They can be easily processed into three-dimensional porous structures by electrospinning techniques. However, the hydrophobic and smooth surface of the electrospun PCL fibres is not beneficial for cell adhesion [318].

To make the surface of PCL fibres rough and hydrophilic and thus more attractive for the cell attachment they were coated with a chitosan-PCL graft copolymer to produce so called "shish-kebab" structures [35]. However, after the "shish-kebab" coating, the PCL surface became positively charged. Therefore, these PCL fibres were additionally coated with alginate to introduce a negative charge on the surface (hereafter referred to as "PCL_{SK-Alg}"). This surface modification was needed to enable electrostatic attraction of positively charged drug delivery systems, in our case of NPSNPs loaded with BMP-2. In addition to the direct attachment of drug delivery systems, the modification with chitosan graft copolymers or alginate leads to an improved biological performance. The cellular attachment can be significantly increased. PCL scaffolds used in this study were electrospun and modified by DOMINIC DE CASSAN from the Institut für Technische Chemie, Technische Universität Braunschweig, Germany.
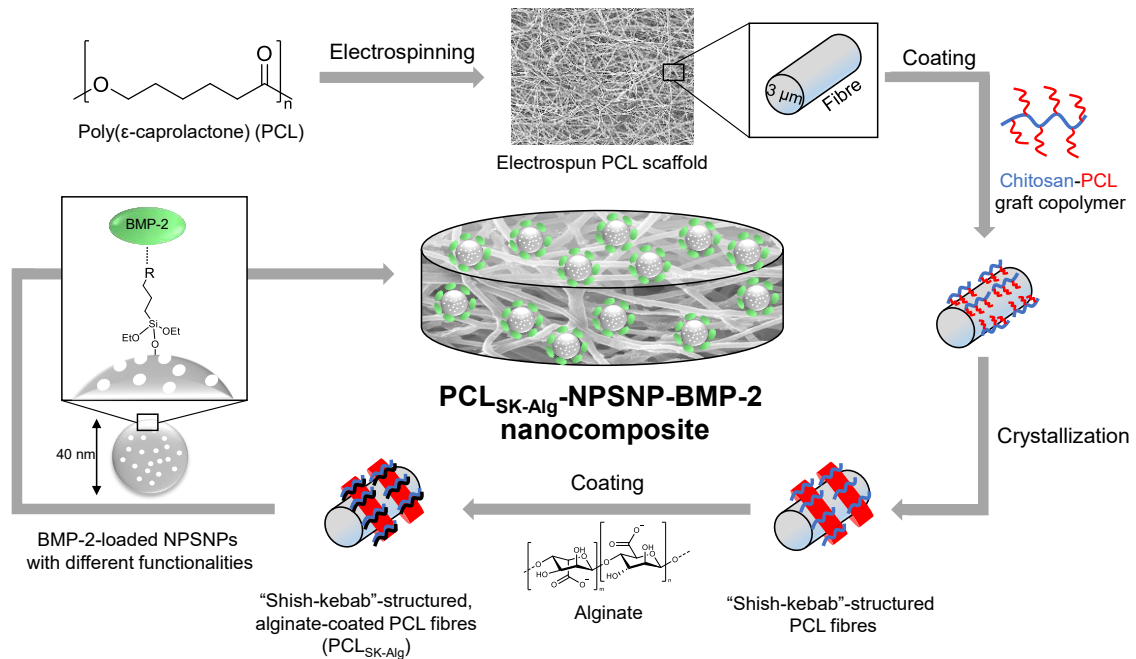
Figure 62: Schematic diagram illustrating the preparation of the PCL_{SK-Alg}-NPSNP-BMP-2 nanocomposites.

4.5.1.2   Morphology and porosity of the PCL_{SK-Alg} scaffolds

In a scaffold suitable for bone regeneration, pores are needed to enable the migration and proliferation of the mesenchymal stem cells and osteoblasts as well as the ingrowth of new blood vessels. Further, porous scaffolds allow for better connection between the scaffold and the existing bone tissue [319]. This is why pore size and porosity of the scaffolds play a crucial role in a successful bone tissue regeneration. Earlier studies

showed that the pore size should be about 100 μm to allow the generation of mineralized bone in dog femoral [163]. In contrast, later studies pointed to pore sizes of > 300 μm for enhanced bone formation and vascularization of the scaffold [164]. However, the mechanical properties of the scaffolds can be compromised by the large pore sizes due to the high void volume. For this reason, PCL scaffolds used in this study were highly porous (with a fibre diameter of about 3 μm and pore sizes in the range of 10-100 μm.

The morphology and the porosity of the "shish-kebab"-structured and alginate-coated PCL fibre mats was investigated by scanning electron microscopy (SEM) indicating rather smooth fibres (Figure 63). The total porosity of PCL_{SK-Alg} fibre mats is about 80%, as determined by a gravimetric method using the volume and the weight of the mats as well as the density of the PCL (for details see section 3.3.18). This simple and fast method served as a rough estimation of the porosity [265].
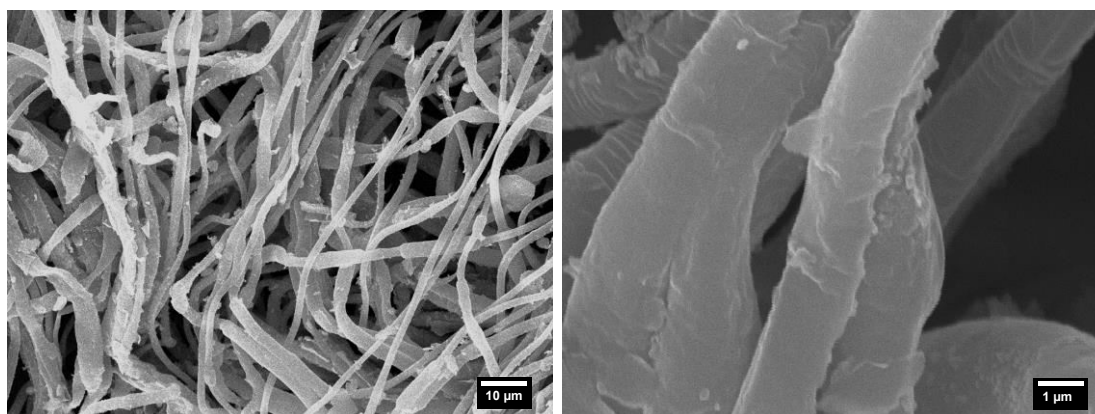
Figure 63: SEM images of "shish-kebab"-structured, alginate-coated PCL fibres.

4.5.1.3   Characterisation of PCL_{SK-Alg}-NPSNP nanocomposites

To introduce drug delivery vehicles on the PCL_{SK-Alg} scaffolds, NPSNPs were loaded on the surface of the PCL_{SK-Alg} fibres. Since the fibres were negatively charged, positively charged NPSNPs with three different functionalities, namely -propyl-NH_2, -methyl-NH-hexyl-NH_2 and -propyl-NH-hexyl-NH_2, were chosen to be electrostaticly attached to the fibres. Hereby, the scaffolds were simply immersed into a dispersion of the NPSNPs for 12 h. The unbound NPSNPs were washed off of the scaffolds with ultra-pure water.

The morphology of the as-prepared PCL_{SK-Alg}-NPSNP nanocomposites were analysed by SEM (Figure 64). SEM images illustrate a rough fibre surface indicative of the coverage of the fibre surface by NPSNPs. Furthermore, it seems that NPSNP-methyl-NH-hexyl-NH_2 formed multilayers on PCL_{SK-Alg} fibres demonstrating a strong electrostatic attraction between PCL_{SK-Alg} and NPSNPs.
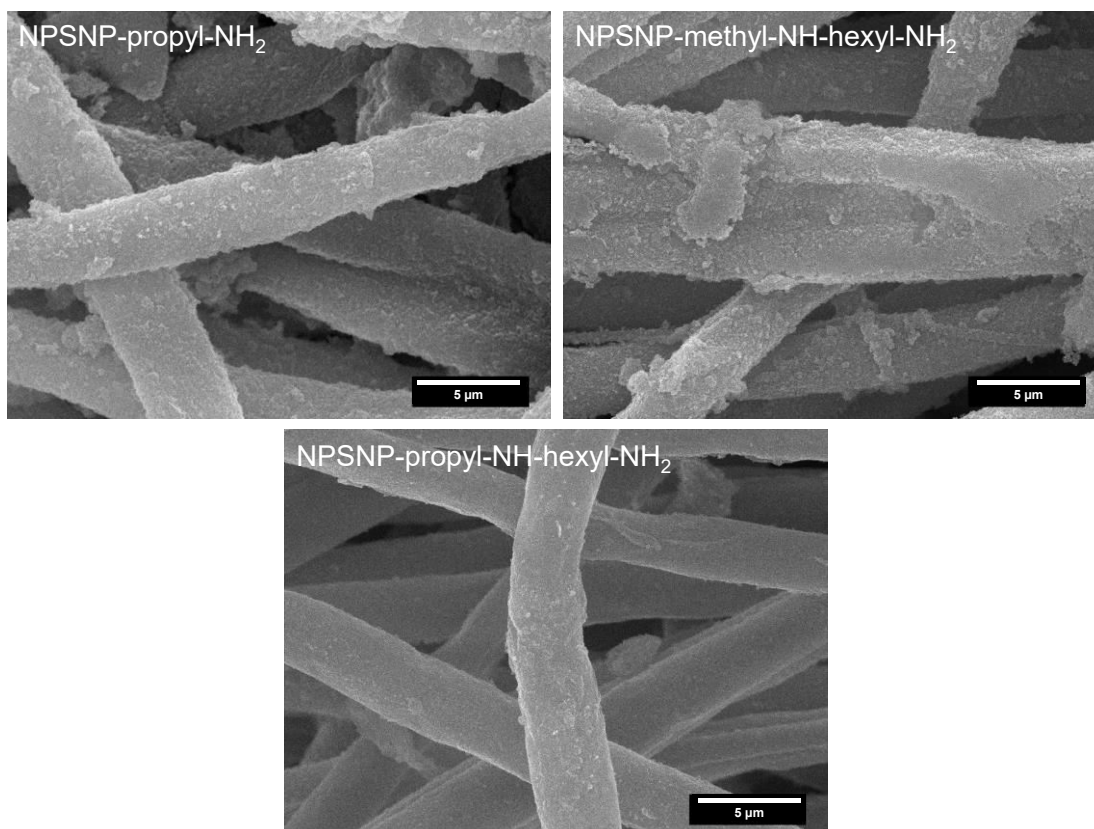
Figure 64: SEM images of "shish-kebab"-structured, alginate-coated PCL fibres decorated with BMP-2-loaded nanoporous silica nanoparticles. The NPSNPs were modified with different aminosilanes.

To further characterise the nanocomposites, Fourier transform infrared (FTIR) spectroscopy investigations were carried out. The corresponding FTIR spectra of the PCL_{SK-Alg} fibre mats before and after loading with NPSNPs are shown in Figure 65, data are given in Table 6. The characteristic band for poly(ε-caprolactone) is the carbonyl stretching mode at 1722 cm^{-1} and a symmetric C$-$O$-$C stretching mode between 1190 cm^{-1} and 1150 cm^{-1}. The strong carboxylate stretching modes of chitosan and alginate can be identified at 1590 cm^{-1} before loading the NPSNPs on the PCL_{SK-Alg} fibre mat (red curve). After loading with NPSNPs, this band became very weak, probably due to the interaction between negatively charged carboxylate groups of alginate coating with the positively charged amine groups on the surface of the NPSNPs. In addition, in the black spectrum, a strong asymmetric Si$-$O$-$Si stretching band can be identified, while in the other two spectra (blue and green) this band is less pronounced. The functional groups, in particular, amine groups, of the NPSNPs were hard to identify due to the very low intensity. It can be concluded that the IR spectra provided insights into a successful coating of the PCL fibres by alginate as well as the attachment of NPSNP-propyl-NH$_2$ on the surface of PCL_{SK-Alg} fibre mats.
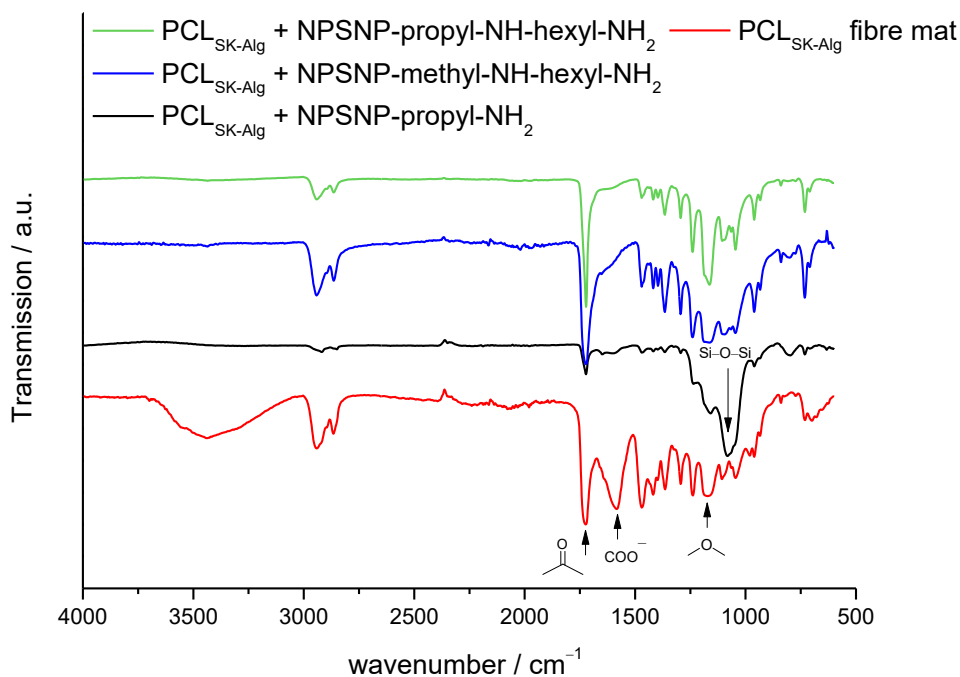
Figure 65: FTIR spectra of "shish-kebab"-structured, alginate-coated PCL fibres functionalized with BMP-2-loaded nanoporous silica nanoparticles.

Table 6: Characteristic IR bands of PCL [320], alginate [321], chitosan [322] and silica [323].

Position (cm⁻¹)	Vibrator	Abbreviation	Component
2935	Asymmetric CH$_2$ stretching	v_{as}(CH$_2$)	
2861	Symmetric CH$_2$ stretching	v_s(CH$_2$)	
1722	Carbonyl stretching	v(C=O)	PCL
1590	Asymmetric COO⁻ stretching	v_{as}(COO⁻)	Alginate,
	C−N stretching and N−H	v(C-N)	chitosan
	bending	δ(N-H)	
1468, 1417	Symmetric COO⁻ stretching	v_s(COO⁻)	Alginate, chitosan
1291	C−O and C−C stretching in the PCL crystalline phase	v_{Cr}	PCL
1239	Asymmetric C−O−C stretching	v_{as}(C−O−C)	PCL
1190-1150	Symmetric C−O−C stretching	v_s(C−O−C)	PCL
1120-1000	Asymmetric Si−O−Si stretching	v_{as}(Si−O−Si)	Silica

The amounts of loaded NPSNPs on the PCL_{SK-Alg} scaffolds were determined by means of thermogravimetric analysis (TGA). Since PCL_{SK-Alg} scaffolds consist of only organic materials, they should become completely oxidized in air. In contrast, the NPSNPs-loaded PCL_{SK-Alg} scaffolds should leave behind an inorganic residue which is related to the amount of loaded NPSNPs.

TGA curves of all samples highlighted two-step thermal degradation of PCL (Figure 66). According to the literature [324], ester pyrolysis reaction of the polyester chains takes place resulting in the release of H_2O, CO_2 and 5-hexenoic acid within the first step. At the second step, cyclic ε-caprolactone monomers are formed as a result of the depolymerisation process. Whereas the pure PCL_{SK-Alg} scaffold was oxidized completely as described above (Figure 66a), very low NPSNPs to PCL weight ratios of 1 wt.% and 0.5 wt.% could be determined for samples loaded with NPSNPs bearing propyl-NH_2 and propyl-NH-hexyl-NH_2 groups, respectively (Figure 66b and d). No inorganic residues were found after the decomposition of PCL_{SK-Alg}-silica nanocomposites loaded with NPSNP bearing methyl-NH-hexyl-NH_2 groups (Figure 66c). However, the SEM images in Figure 64 showed a successful loading of all types of NPSNPs on the surface of PCL_{SK-Alg} scaffolds. Therefore, it can be proposed that a PCL_{SK-Alg} scaffold can maximally load about 1 wt.% of NPSNPs. This value is very low and was not anticipated, since around 14 wt.% of NPSNPs could have been loaded into the scaffolds.

In general, the amounts of NPSNPs were too low to be determined precisely by TGA. Therefore, the data derived from this analysis should be interpreted with caution.
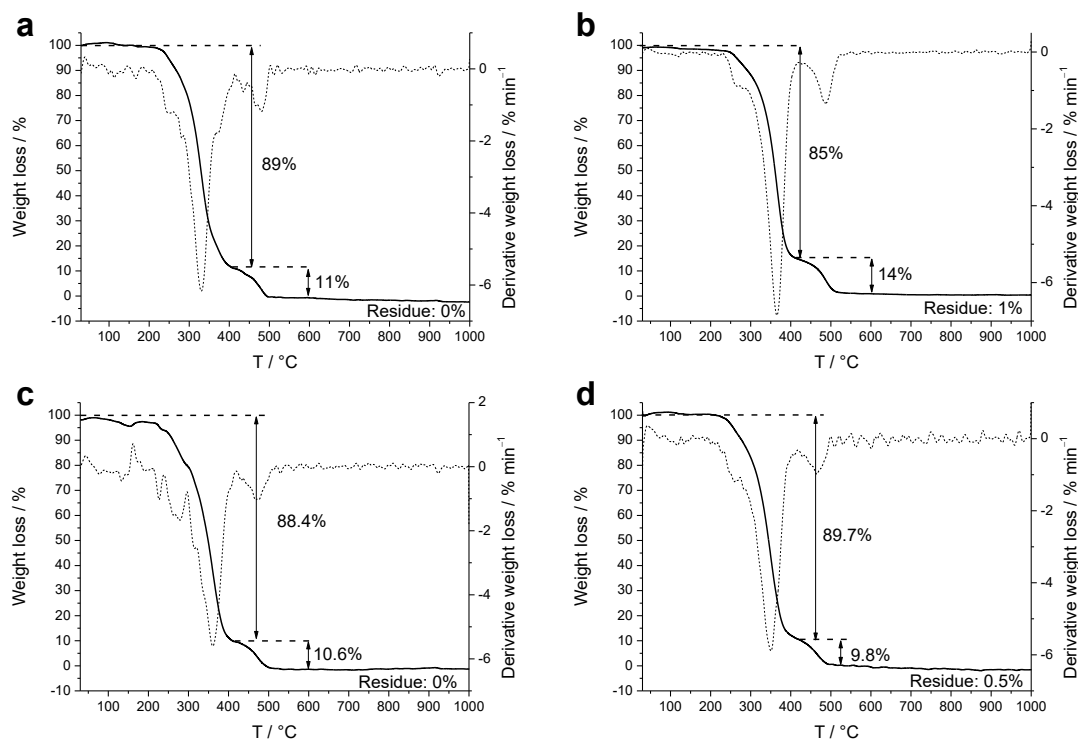
Figure 66: Thermogravimetric analysis curves derived from (a) "shish-kebab"-structured, alginate coated PCL fibre mat without NPSNPs and with differently modified NPSNPs bearing (b) propyl-NH₂, (c) methyl-NH-hexyl-NH₂ and (d) propyl-NH-hexyl-NH₂ groups.

4.5.1.4   BMP-2 loading capacity on NPSNPs and release from the PCL$_{SK-Alg}$-NPSNP-BMP-2 nanocomposites

The PCL$_{SK-Alg}$-NPSNP nanocomposites in this study were intended to be applied for the bone-tendon bridging in case of a rotator cuff rupture. The special focus of this work was placed on the bone tissue regeneration. Earlier studies have shown that silica-coated PCL scaffolds revealed enhanced cell viability and proliferation of pre-osteoblast cells as well as accelerated calcium deposition compared to the pure PCL scaffold [198, 325]. To provide additional osteoinductive function, BMP-2 molecules were adsorbed on the surface of differently modified NPSNPs before integration into the PCL$_{SK-Alg}$ scaffolds. By means of the different functional groups on the surface of NPSNPs we sought to control the loading capacity and the release behaviour of BMP-2.

First, the BMP-2 amounts in the supernatants were determined by ELISA and BRE-Luc assay after BMP-2 was loaded on NPSNPs in MES buffer (Figure 67a). Hereby, much lower BMP-2 concentrations were measured by ELISA than by BRE-Luc assay. This finding can be explained by the different measurement concepts of the assays. An ELISA can only detect molecularly dissolved BMP-2, as the responsible epitope may be masked in aggregated molecules; on the other hand, aggregated, but still biologically active, BMP-2 can be identified by a BRE-Luc assay, provided that there is an aggregation

equilibrium from which individual functional BMP-2 dimers can be attached to the extracellular receptor. The finding thus indicates that aggregation of BMP-2 takes place in the MES buffer solution used for the loading of BMP-2 on NPSNPs.

Therefore, the adsorbed BMP-2 amounts on the surface of the NPSNPs were determined by subtracting BMP-2 amounts, which were measured by the BRE-Luc assay in the supernatants, from the initially present BMP-2 amount of around 1000 ng mg^{-1} (Figure 67b). The results derived from BRE-Luc assay revealed different loading capacities dependent on the functional group of the NPSNPs. In fact, the NPSNPs bearing hydrophobic methyl-NH-hexyl-NH$_2$ and propyl-NH-hexyl-NH$_2$ groups seemed to adsorb more BMP-2, namely 916 ± 34 and 956 ± 3 ng mg^{-1}, respectively. The NPSNPs bearing less hydrophobic propyl-NH$_2$ groups adsorbed less BMP-2 (842 ± 23 ng mg^{-1}). As stated earlier, these results offer a compelling evidence for the binding mechanism of BMP-2 on the surface of the modified NPSNPs through hydrophobic interactions and electrostatic attraction (see the section 4.2.5 for a detailed discussion).
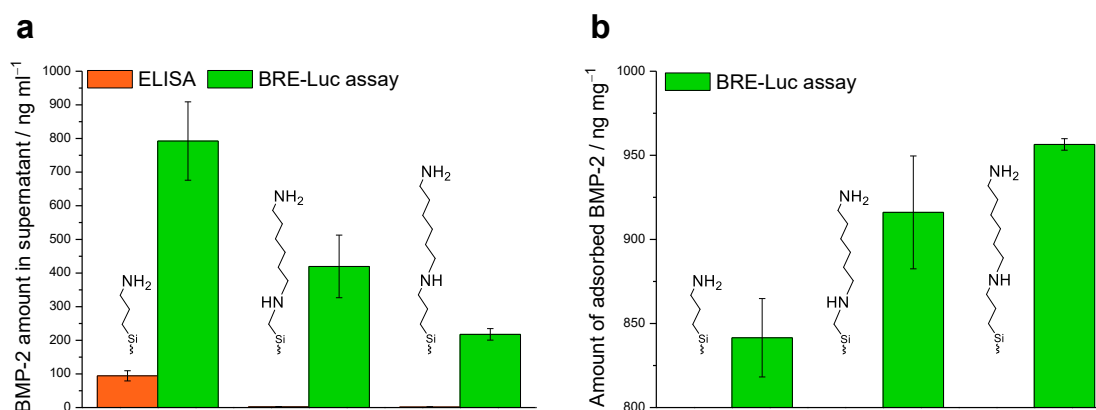
Figure 67: (a) Amounts of BMP-2 in the supernatant after the loading procedure and (b) of adsorbed BMP-2 on the surface of differently modified NPSNPs. The data represent the mean ± standard deviation (n=3).

To study the BMP-2 release behaviour from the PCL$_{SK-Alg}$ fibre mats, release experiments with the prepared PCL$_{SK-Alg}$-NPSNP-BMP-2 nanocomposites were carried out for the period of 5 weeks. Preliminary release experiments of BMP-2 were performed at physiological conditions in PBS, pH 7.4 and 37 °C. However, no released BMP-2 could be detected via ELISA. Through collaborations within the DFG research group "Graded implants", it was found out later that this was due to the precipitation of BMP 2 in PBS (for more details see section 4.2.3). Therefore, another medium was chosen for the release experiments consisting of PBS (pH 7.4), 0.1% bovine serum albumin (BSA) and 0.02% Tween 20 as stabilizing agents for BMP-2. This medium is a part of the ELISA kit (Peprotech) called "diluent", which should be used for the dilution of BMP-2 and prevent aggregation. The release temperature was kept at 37 °C. The amount of the released

BMP-2 was measured at scheduled time points and could be quantified directly by means of ELISA.

The results derived from ELISA measurements revealed similar release profiles for the differently modified NPSNPs, but with strongly different amounts (Figure 68). In general, BMP-2 amounts released from the PCL_{SK-Alg}-NPSNP-BMP-2 nanocomposites were rather small. The highest cumulative BMP-2 amount of about 8 ng ml^{-1} after a period of 5 weeks was released from the nanocomposites containing NPSNP-methy-NH-hexyl-NH$_2$, whereas smaller amounts of 4 ng ml^{-1} and 2 ng ml^{-1} were set free from the nanocomposites loaded with NPSNP-propyl-NH-hexyl-NH$_2$ and -propyl-NH$_2$ during the same time frame, respectively. These findings correlate well with the SEM images of the nanocomposites (Figure 64) showing multilayer coverage of PCL_{SK-Alg} fibres by NPSNP-methyl-NH-hexyl-NH$_2$ vs. monolayer formation by the two other nanoparticle types.
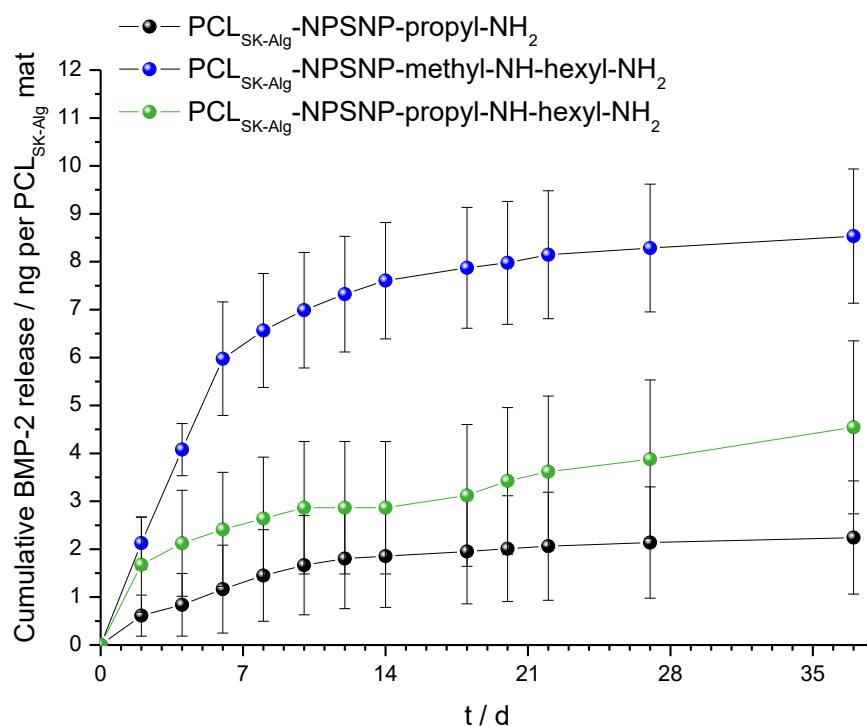
Figure 68: Release of BMP-2 from the surface of differently modified NPSNPs loaded on PCL$_{SK-Alg}$ scaffolds into PBS, 0.1% bovine serum albumin and 0.02% Tween 20 at pH 7.4 and 37 °C as measured by ELISA. The medium volume was 1 ml. The average weight of a PCL $_{SK-Alg}$ scaffold was around 14 mg. The data represent the mean ± standard deviation (n=3).

TG measurements shown before revealed that only low amounts of NPSNPs (up to 0.14 mg) could be loaded on the surface of PCL_{SK-Alg} resulting in a total BMP-2 amount of around 100 - 150 ng per PCL_{SK-Alg} scaffold (14 mg). However, the released BMP-2 amounts are considerably smaller, implying that from all samples only less than 5% of the initially loaded BMP-2 is released. On the one hand, BMP-2 could be bound too strongly on the surface of differently modified NPSNPs, preventing the release of BMP-2

into the medium. On the other hand, BMP-2 could have been released from the scaffold, but immediately aggregated and thus could not be detected by ELISA. Although a special medium based on PBS with stabilizing additives such as BSA and Tween 20 was chosen for the release experiments, the attempt to stabilize BMP-2 in this way might have failed. To shed more light on this issue, the released BMP-2 amounts were determined by the cell-based BRE-Luc assay, which can also detect aggregated BMP-2, when it is still biologically active. The detection limit of the BRE-Luc assay, however, is around 2 ng ml^{-1}, which makes it around 10000-fold less sensitive compared to ELISA (30 pg ml^{-1}). In fact, for all three particle types, no released BMP-2 could be detected by the BRE-Luc assay at any time (data not shown) since all released BMP-2 amounts detected by ELISA are at or below the detection limit of the BRE-Luc assay. Therefore, based on the results derived from the ELISA and BRE-Luc assays, we assume that small BMP-2 amounts were released from the PCL$_{SK-Alg}$-NPSNP-BMP-2 nanocomposites.

4.5.1.5   Degradation of PCL$_{SK-Alg}$-NPSNP nanocomposites during the release

To study their degradation behaviour, PCL $_{SK-Alg}$ fibre mats loaded with differently modified NPSNPs were immersed into the release medium ("diluent") for the period of 5 weeks. After 1, 2, 3 and 5 weeks of the immersion small pieces were cut out of the samples and the morphology of the silica coatings and PCL$_{SK-Alg}$ fibres were analysed by means of SEM. The SEM images made of scaffolds after degradation for 1, 2 and 3 weeks are given in supporting information (Figure S6-8). According to the SEM images, a detachment of the silica coating from the PCL$_{SK-Alg}$ fibres can be observed for all three samples.

After 5 weeks of immersion, it seems that only low amounts of silica nanoparticles with propyl-NH$_2$ groups are still attached on the surface of PCL$_{SK-Alg}$ fibres (Figure 69a). In contrast, the PCL$_{SK-Alg}$ scaffolds loaded with NPSNPs bearing methyl-NH-hexyl-NH$_2$ and propyl-NH-hexyl-NH$_2$ groups exhibit a homogeneous coverage of PCL$_{SK-Alg}$ fibres by silica nanoparticles (Figure 69b and c). The reason for that might be a strong interaction between the hydrophobic regions of PCL fibres and hexyl chains of the functional groups on the surface of the NPSNPs resulting in stronger attachment of the first silica nanoparticle layer.

In general, no degradation of PCL$_{SK-Alg}$ fibres during the period of 5 weeks of immersion into the release medium could be observed. Therefore, to study the degradation behaviour of the scaffolds, prolonged studies together with cell culture investigations of the PCL$_{SK-Alg}$-NPSNP nanocomposites should be conducted for an extended period of time.
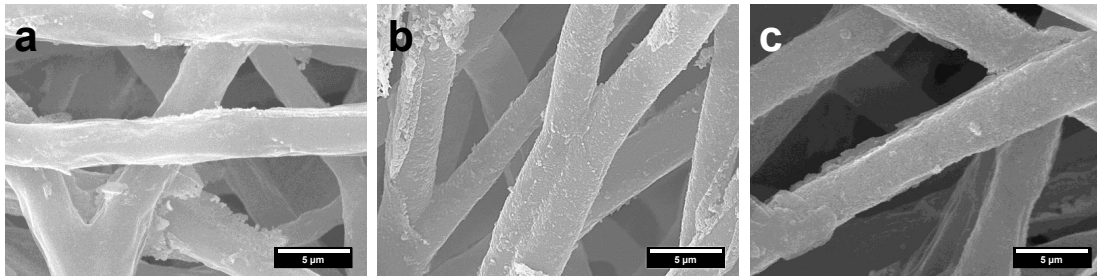
Figure 69: SEM images of PCL$_{SK-Alg}$ fibre mat loaded with NPSNPs bearing (a) -propyl-NH$_2$, (b) -methyl-NH-hexyl-NH$_2$ and (c) -propyl-NH-hexyl-NH$_2$ groups after 5 weeks of the immersion into the release medium (PBS, 0.1% BSA and 0.02% Tween 20) at 37 °C. Scale bar: 5 µm.

To sum up, this study was part of the first steps towards the fabrication of a graded implant for the treatment of a rotator cuff rupture. Hereby, nanocomposites made of three-dimensional, "shish kebab"-structured, alginate-coated PCL scaffolds and BMP-2-loaded nanoporous silica nanoparticles with different functional groups were successfully prepared. However, apparently, only low amounts of NPSNPs (1 wt.%) and BMP-2 (around 100 - 150 ng per scaffold) could be loaded on the PCL$_{SK-Alg}$ scaffolds. Even lower BMP-2 amounts (up to 8 ng ml^{-1}) were released from the surface of PCL$_{SK-Alg}$-NPSNP-BMP-2 nanocomposites in the period of 5 weeks. To verify whether this BMP-2 amount is enough to induce osteogenic differentiation of MSCs, cell culture investigations should follow. Moreover, future work will focus on optimisation of the loading and release amounts of BMP-2.

4.5.2   Bone tissue regeneration scaffolds based on collagen sponges and BMP-2-loaded nanoporous silica nanoparticles

Among natural scaffold materials, three-dimensional collagen scaffolds are the most prominent ones due to their inherent biological recognition through receptor-ligand interactions, biocompatibility and -degradability. In combination with osteoinductive bone morphogenetic protein 2 (BMP-2), a collagen scaffold-based medical product INFUSE® Bone Graft (Medtronic) was approved by the FDA for the interbody spinal fusion in 2002 as the first medical preparation employing a growth factor [27]. However, more recently, concerns have been raised regarding the use of this product due to severe side effects associated with supraphysiological doses of BMP-2, especially in other non-topical applications [16].

Here, we report a novel scaffold system with a built-in delivery system for the controlled release of small BMP-2 doses from the surface of nanoporous silica nanoparticles (NPSNPs) attached directly to the surface of collagen scaffolds for bone regeneration.

1. Integrate BMP-2-loaded NPSNPs in the collagen scaffold

≈ 4 mm

8 mm

Collagen scaffold

+

40 - 60 nm

BMP-2

NH₂   NH₂

EtO   EtO
  Si⁻OEt   Si⁻OEt
  O   O

BMP-2-loaded NPSNPs
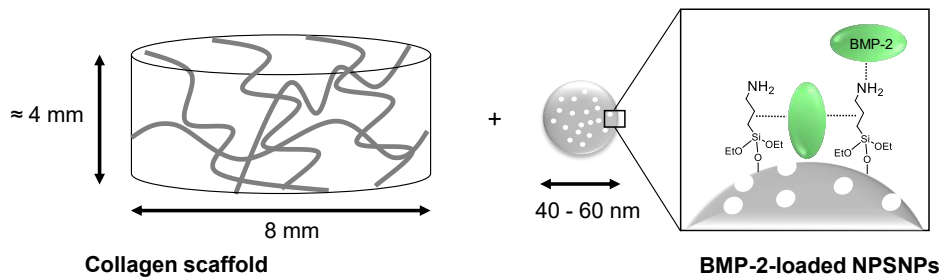
2. Seed hASCs on the nanocomposite

Human adipose tissue-derived mesenchymal stem cells (hASCs) seeded in a collagen gel

Collagen-NPSNP-BMP-2 nanocomposite
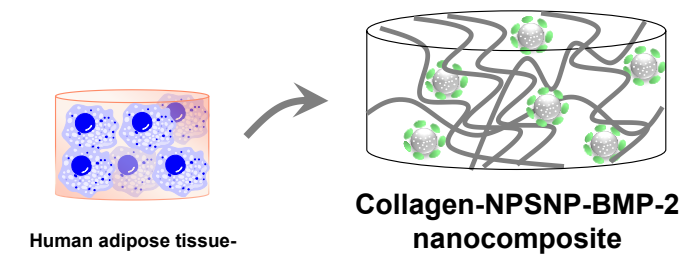
3. Cultivate for 2 to 4 weeks

Collagen gel with hASCs

Collagen scaffold with BMP-2-loaded NPSNPs
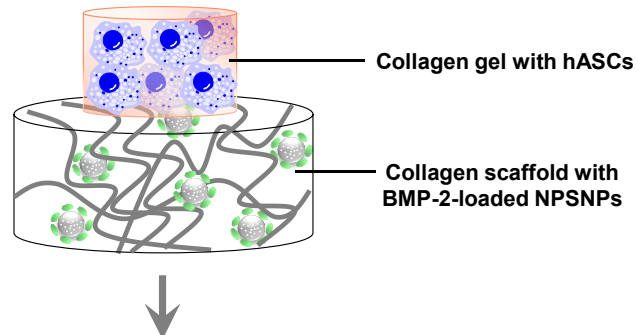
4. BMP-2 release, cell migration into the collagen scaffold, osteogenetic differentiation of hASCs
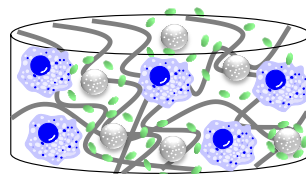
Tissue-engineered scaffold for bone regeneration

Figure 70: Schematic diagram illustrating four steps on the way to an engineered scaffold for bone regeneration based on collagen sponges, BMP-2-loaded NPSNPs and hASCs.

The present work is a continuation of the previous study conducted by Anne Neumann and Anne Christel *et al*. [33]. They demonstrated the successful osteogenic differentiation of adipose tissue-derived mesenchymal stem cells (ASCs) by using aminopropylsilyl-modified, BMP-2-loaded NPSNPs.

In this work, after the integration of BMP-2-loaded NPSNPs into the collagen scaffolds, we sought to evaluate the ability of the prepared collagen-NPSNP-BMP-2 nanocomposites to induce osteogenic differentiation of human ASCs (Figure 70). hASCs are derived from adipose tissue, which makes them an abundant and autologous cell source with relatively low donor site morbidity [175]. In addition, hASCs have demonstrated rapid osteogenic differentiation after stimulation with BMP-2, making them a promising option for bone tissue engineering [326, 327].

4.5.2.1   Characterisation of collagen-NPSNP nanocomposites

First, collagen-NPSNP nanocomposites were prepared and characterized, as previously described in [328]. A short summary of the results will be given below. The morphology of collagen scaffolds were investigated by SEM. The collagen scaffolds were highly porous with a pore size of about 100 µm (Figure 71a). After loading of non-modified NPSNPs, collagen fibres were completely covered with NPSNPs (Figure 71b). Corresponding IR spectra of collagen-NPSNP nanocomposites showed characteristic bands of silica after the loading into the collagen scaffold (Figure 71c). In addition, successful fabrication of collagen-NPSNP nanocomposites was verified by fluorescence microscopy (Figure 71d). For this purpose, fluorescent silica nanoparticles equipped with the fluorescent dye Alexa Fluor® 488 were loaded into collagen scaffolds resulting in strong fluorescence of the initially non-fluorescent collagen scaffold.
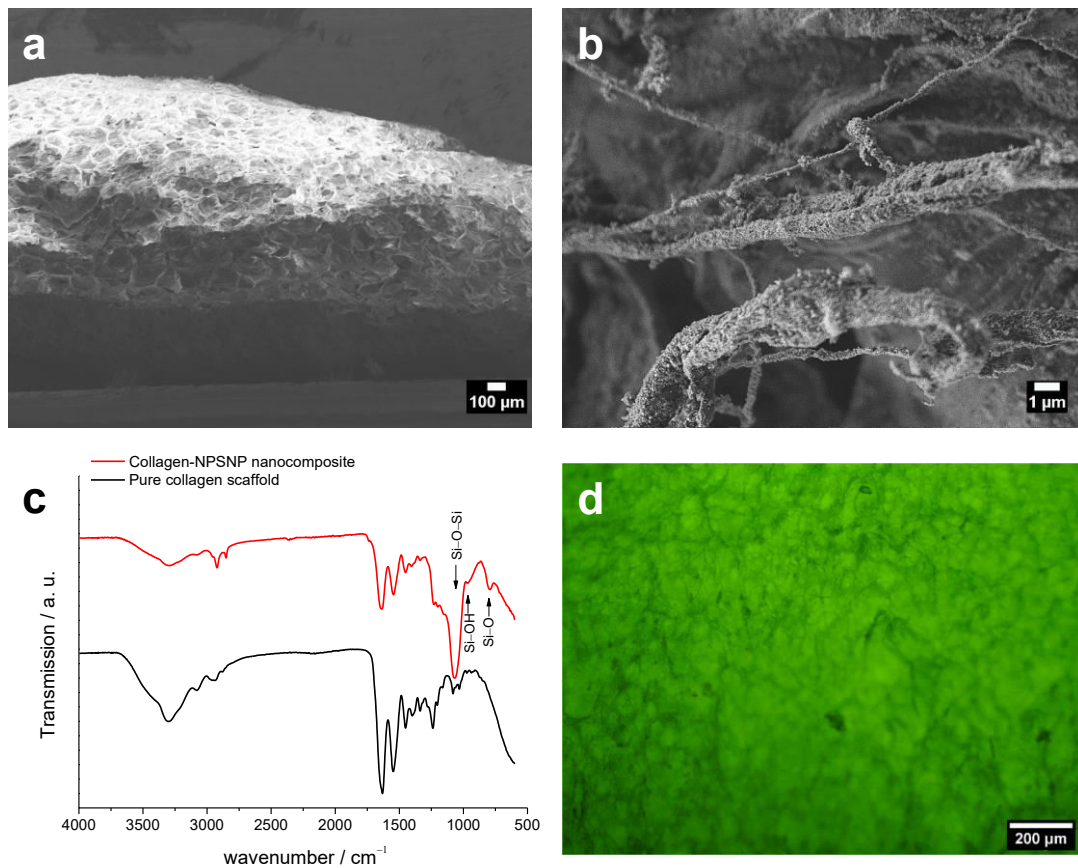
Figure 71: Characterization of collagen scaffolds. (a) Cross-section SEM image of a collagen scaffolds. (b) SEM image of a collagen-NPSNP nanocomposite. (c) IR spectra of a pure collagen scaffolds and a collagen-NPSNP nanocomposite. (d) Fluorescence microscopic image of the collagen-NPSNP nanocomposite loaded with fluorescent silica nanoparticles.

In the present work, one of the aims was to further characterize collagen-NPSNP nanocomposites in terms of the loading of NPSNPs into the collagen scaffolds as a function of exposure time. Since collagen scaffolds consist of organic materials only, they should become completely oxidized into water and carbon dioxide when being heated up to 1000 °C in air. In contrast, collagen-NPSNP nanocomposites should reveal inorganic residues that correspond to the amounts of loaded NPSNPs. The amounts of non-modified NPSNPs that were loaded into the collagen scaffolds in the periods of 1, 3, 19 and 24 h exposure time, were determined by TG measurements (Figure 72 and Table 7).

According to the TG measurements, NPSNPs amounts between 31 wt.% and 37 wt.% were integrated into collagen scaffolds. Based on the obtained results, collagen scaffolds could already incorporate around 33 wt.% of NPSNPs after 1 h of the immersion. The nanoparticle integration into the collagen scaffolds seems to be completed after 1 h. This result points to a high affinity of NPSNPs towards collagen.

These findings should be considered for the incorporation of BMP-2-loaded NPSNPs into the collagen sponges. To prevent BMP-2 from the premature release, the integration time of the NPNSPs into the scaffold should be kept as short as possible, in our case 1 h would be enough.
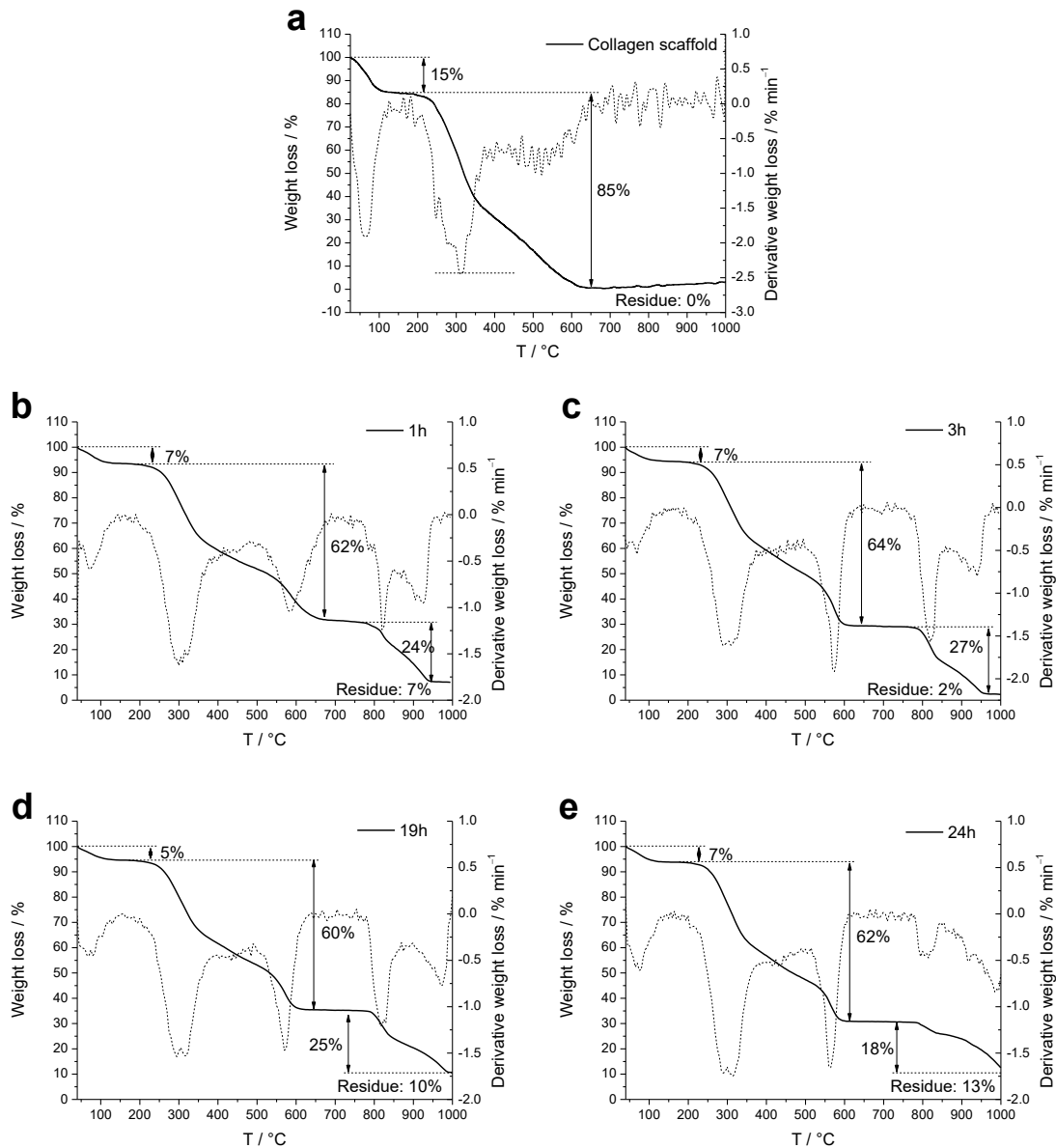
Figure 72: Thermogravimetric analysis curves derived from (a) pure collagen scaffold and non-modified NPSNPs loaded into the collagen scaffolds in the period of 1, 3, 19 and 24 h.

Table 7: Evaluation of thermogravimetric analysis data. Normalized amounts of NPSNPs loaded into collagen scaffolds for different periods of time.

Samples	Integrated NPSNPs / wt.%
Pure Collagen	0
Coll-NPSNP_1h	33
Coll-NPSNP_3h	31
Coll-NPSNP_19h	37
Coll-NPSNP_24h	33

4.5.2.2   BMP-2 loading capacity on NPSNPs and release from collagen-NPSNP-BMP-2 nanocomposites

Since one of the aims was to engineer composites suitable for bone regeneration, BMP-2 molecules were immobilized on the surface of NPSNPs to provide osteoinductive properties to osteoconductive collagen-NPSNP nanocomposites.

BMP-2 loading on the surface of non-modified and aminopropylsilyl-modified NPSNPs took place in PBS with 0.1% BSA in this study. Only very small amounts of BMP-2 could be measured in the supernatants by ELISA indicating a high loading of BMP-2 on NPSNPs (Figure S9, SI). However, as stated earlier, BMP-2 molecules tend to aggregate under the given conditions (see section 4.2.3). Therefore, the conclusions derived from ELISA measurements should be treated with caution.

After BMP-2 was loaded on the surface of the non-modified and aminopropylsilyl-modified NPSNPs, nanoparticles (5 mg) were integrated into collagen scaffolds (20 mg, 1.8 cm x 3.6 cm) by an immersion process. To study BMP-2 release behaviour from the collagen scaffolds, release experiments with the prepared collagen-NPSNP-BMP-2 nanocomposites were conducted for the period of 5 weeks. The release experiments took place in PBS with 0.1% bovine serum albumin (BSA) and at 37 °C to mimic the physiological conditions. BSA was added in order to prevent BMP-2 aggregation [329]. The amount of the released BMP-2 was measured at scheduled time points and quantified directly by means of ELISA.

BMP-2 release was lower with around 35 ng being released from a collagen scaffold containing non-modified NPSNPs compared to the released BMP-2 amount from scaffolds loaded with aminopropylsilyl-modified NPSNPs of around 75 ng for the period of 5 weeks (Figure 73). The released BMP-2 amounts were rather low. One of the reasons may be the precipitation of BMP-2 in PBS making it not possible to detect via ELISA. In addition, it is also possible that some BMP-2 was released prematurely from

the surface of NPSNPs while being loaded into the collagen scaffold (24 h). BMP-2 may have also been precipitated during this time.

The aim of this study was to slow down and inhibit the burst release of BMP-2 typically shown by BMP-2-loaded collagen scaffolds by delivering BMP-2 in a controlled manner from the surface of NPSNPs integrated into the collagen scaffold. The BMP-2 release from collagen-based scaffolds without NPSNPs usually undergoes a three-stage process: i) an initial burst release (some hours) followed by ii) a sustained release (up to 14 days) and iii) a release plateau [330]. The release profile can be fitted by a bi exponential model (first-order kinetics). Although in some cases like wound treatment, initial burst release with high drug release rates is desired, in case of growth factor delivery a high initial burst release will be economically and therapeutically wasteful and will shorten the total release time [331]. In addition, minimizing the burst release of BMP-2 can help to reduce undesired side effects [259]. Moreover, a positive correlation between the BMP-2 retention at the scaffold and the osteoconductive activity *in vivo* have been previously demonstrated [221].
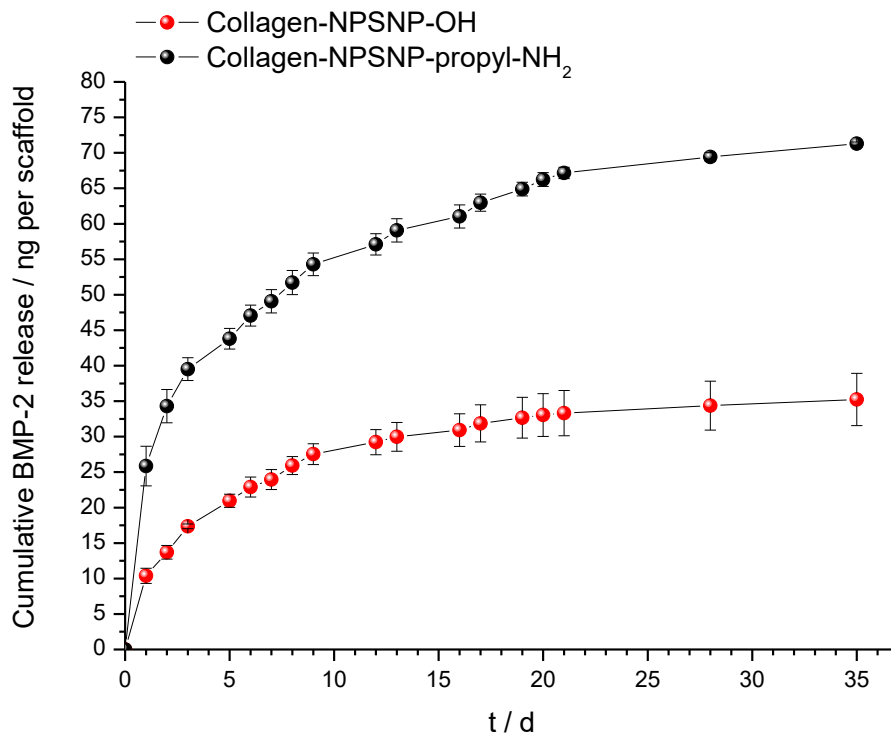
Figure 73: Release of BMP-2 from collagen-NPSNP-BMP-2 nanocomposites with two different nanoparticles types: non-modified and aminopropylsilyl-modified NPSNPs, as measured by ELISA. Release medium is 2 ml of PBS containing 0.1% bovine serum albumin at pH 7.4 and 37 °C. The average weight of a collagen scaffold was around 20 mg. The data represent the mean ± standard deviation (n=3).

In this study, the release kinetics of two different types of collagen-NPSNP-BMP-2 nanocomposites were similar showing a i) strong release during the first 3 days, followed by ii) a sustained release of smaller BMP-2 amounts up to day 21 and from there iii) a

period, in which almost no BMP-2 was released (Figure 73). Subsequently, BMP-2 release profiles were fitted by the first-order release kinetics equations (Figure S9, SI) and compared with those from the *in vivo* BMP-2 release study using only collagen scaffolds [330]. As a result, the strong release of 25% of the initial BMP-2 amount was slowed down from 3 h for collagen-BMP-2 scaffolds to up to 1.4 days and 15 h for collagen nanocomposites containing non- and aminopropylsilyl-modified NPSNPs, respectively (Table 8). In addition, the first and the second $t_{1/2}$ values, referred to as the time at which 50% and 75% of the initially loaded BMP-2 is released, could be significantly delayed for collagen-NPSNP-BMP-2 composites in comparison to collagen-BMP-2 scaffolds (Table 8).

Table 8: Comparison of the released BMP-2 amounts fitted by the first-order release kinetics equation from a collage-BMP-2 scaffold from ref. [330] and the present study.

Released BMP-2 amount / %	Collagen-BMP-2 scaffold	Collagen-NPSNP-BMP-2 nanocomposites	
		NPSNP-OH	NPSNP-propyl-NH$_2$
$t_{1/4}$	3 h	1.4 days	15 h
First $t_{1/2}$	≈ 1 day	3 days	2.3 days
Second $t_{1/2}$	5.9 days	9.4 days	8.8 days

In conclusion, by the loading of BMP-2 on the surface of non-modified and aminopropylsilyl-modified NPSNPs and subsequent integration into collagen scaffolds, it was possible to control the release of BMP-2.

Despite promising results in terms of the BMP-2 release kinetics, the BMP-2 loading procedure should be optimized by using another buffer to prevent BMP-2 aggregation. Thus, after conducting the above described experiment, it was found that BMP-2 tends to aggregate under physiological conditions (PBS). In contrast, BMP-2 forms stable dispersions at lower pH, e.g. at pH 5 in MES buffer (see section 4.2.3). Therefore, future experiments should be conducted by employing MES buffer for loading of BMP-2.

4.5.2.3   BMP-2 release profiles of PCL$_{SK-Alg}$- and collagen-NPSNP-BMP-2 nanocomposites in comparison

To compare the BMP-2 release profiles of PCL$_{SK-Alg}$- and collagen-NPSNP-BMP-2 nanocomposites, the data were modified and now refer to ng of the released BMP-2 per 10 mg of the corresponding scaffold (Figure 74).
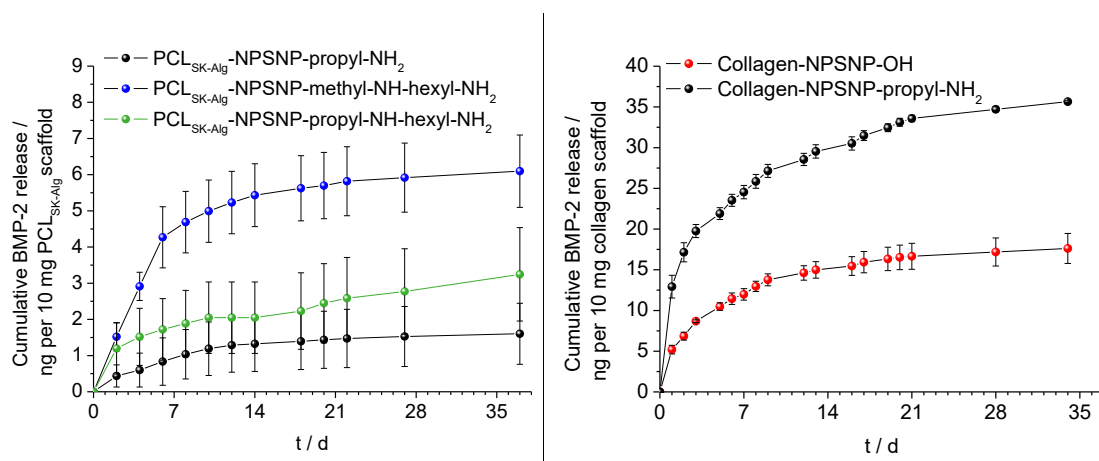
Figure 74: BMP-2 release profiles of PCL$_{SK-Alg}$ and collagen-NPSNP-BMP-2 nanocomposites in comparison. The released BMP-2 amounts refer to ng per 10 mg of the respective scaffold.

In case of PCL$_{SK-Alg}$-NPSNP-BMP-2 nanocomposites, low BMP-2 amounts (up to ≈ 6 ng per 10 mg scaffold) were released in the period of 5 weeks. In the same period, 3- to 20-times more BMP-2 was released from the collagen-NPSNP-BMP-2 nanocomposites. This can be explained by the strong difference in nanoparticle amounts integrated into the scaffolds as shown previously in Figure 66 and Figure 72: 1 wt.% vs. 33 wt.% for PCL$_{SK-Alg}$ and collagen scaffolds, respectively. The reason behind the strong differences in loading capacities may have several explanations. On the one hand, it could be seen on the SEM images that the collagen fibres are thinner (about 1 μm) than the electrospun fibres of PCL scaffolds (around 3 μm). Since the lateral surface of a cylinder (outer fibre surface) is directly proportional to the cylinder radius (fibre radius), 3-times higher amount of the NPSNPs could be theoretically attached on the surface of the collagen fibres compared to the PCL fibres. On the other hand, the pore sizes of the collagen scaffolds are 10-times larger than the pore sizes of the PCL scaffolds (100 μm vs. 10 μm). Therefore, large NPSNP-BMP-2 aggregates could easily diffuse into the collagen scaffolds through the large pore entrances resulting in higher loading capacity (Figure S12, SI).

The effective BMP-2 concentrations and release kinetics necessary for the induction of osteogenic differentiation are still a matter of debate. According to the literature [299], the minimal BMP-2 concentration needed to induce osteogenic differentiation of bone

marrow mesenchymal stem cells (BM-MSCs) is about 100 ng ml^{-1}. This finding can be supported by the previously conducted study in our group [33]. Herein, osteogenic differentiation of adipose tissue-derived MSCs was successfully promoted by using aminopropylsilyl-modified, BMP-2-loaded NPSNPs with a total BMP-2 concentration of about 110 ng ml^{-1} presented to the cells. However, the BMP-2 release from NPSNPs was not measured in the previous study.

However, opposing findings were reported for other growth factors, which were bound to a matrix, showing their bioactivity not only when being released, but also when bound on the scaffold by interacting with receptors on the surface of adjacent cells [332]. Subsequent studies with conjugated BMP-2 on different biomaterials have demonstrated that BMP-2 stays bioactive and promotes cell proliferation and differentiation [333-335]. Consequently, our BMP-2 delivery approach may provide a universal way to reduce BMP-2 dosage by remaining on the surface of the scaffold, interacting with the cells and thus facilitating the osteogenesis.

To further explore this issue, cell culture investigations are required to evaluate the PCL$_{SK-Alg}$- and collagen-NPSNP-BMP-2 nanocomposites regarding their biological activity and the ability to induce osteogenic differentiation of MSCs when bound on the scaffold.

While such investigation are currently in planning for PCL$_{SK-Alg}$-NPSNP-BMP-2 nanocomposites, they have been already conducted for collagen-NPSNP-BMP-2 nanocomposites within this study and are presented in the next chapter.

4.5.3 Cell culture investigations of collagen-NPSNP-BMP-2 scaffolds for bone regeneration

Cell culture experiments were performed by VINCENT COGER from the Kerstin Reimers Labor für Regenerationsbiologie, Klinik für Plastische, Ästhetische, Hand- und Wiederherstellungschirurgie, Medizinische Hochschule Hannover, Germany.

The induction of osteogenic differentiation of mesenchymal stem cells by bone morphogenetic proteins (BMPs) is one of the promising approaches in the field of bone tissue engineering [27]. Several studies, also by our group, have shown that adipose tissue-derived mesenchymal stem cells (hASCs) are able to differentiate towards bone tissue in the presence of BMP-2 [33, 176, 177, 326, 336, 337]. In the current study, we sought to evaluate the ability of collagen-NPSNP-BMP-2 nanocomposites to promote osteogenic differentiation of hASCs in a three-dimensional collagen scaffold. Therefore, collagen-NPSNP-BMP-2 nanocomposites with 8 mm in diameter containing 2 mg of aminopropylsilyl-modified NPSNPs with 800 ng of BMP-2 per 1 mg were cultivated together with hASCs for 2 or 4 weeks. As controls, the same experiments were carried

out with pure collagen scaffolds, collagen scaffolds with NPSNPs not carrying BMP-2
and collagen scaffolds containing a comparable amount of BMP-2.

After 4 weeks, cell viability was determined using live/dead viability assay, in which live
cells appear green and dead cells are red. According to the images in Figure 75a, the
majority of the cells was viable for all samples. In addition, hASCs were evenly distributed
throughout the entire collagen scaffold (Figure 75b). These results reveal that regardless
of the presence of NPSNPs and BMP-2, collagen scaffolds offer a cell-friendly
environment for hASCs. This is probably due to the scaffold pore size of about 100 µm,
which allows for the cell ingrowth, migration and proliferation [338].
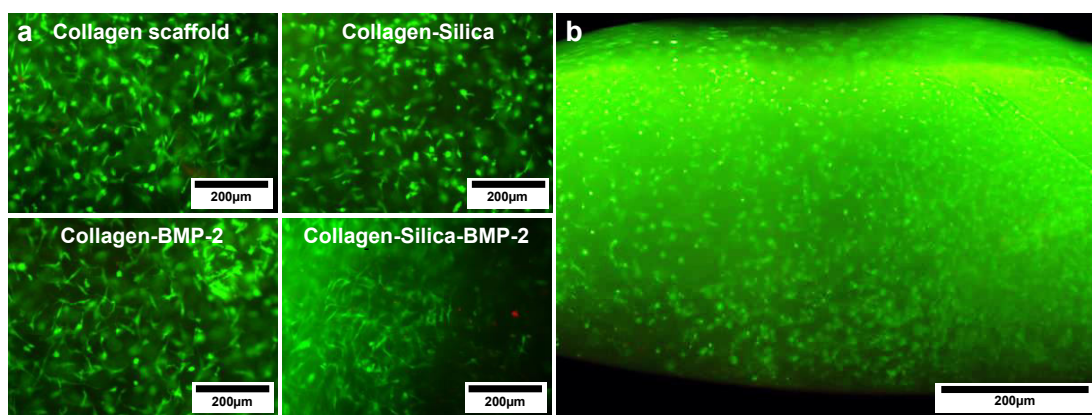
*Figure 75: Results derived from live/dead viability assay of adipose tissue-derived
mesenchymal stem cells (hASCs) seeded on (a) 4 different collagen scaffold samples
and (b) a cross-section of the pure collagen scaffolds after 4 weeks of cultivation.*

The progress of osteogenic differentiation of the hASCs inside the collagen-NPSNP-
BMP-2 nanocomposites samples after 2 weeks of cultivation was analysed by Alizarin
Red S, von Kossa and Calcein stainings (Figure 76a, b and c, respectively). In case of
successful osteogenetic differentiation, samples stained with Alizarin Red, von Kossa
and Calcein should show intensive red, brownish and green colour, respectively.
Together with Calcein staining, samples were treated with DAPI reagent colouring cell
nuclei into blue (Figure 76c).

Based on the affiliated images, no osteogenic differentiation of hASCs after 2 weeks of
cultivation could be observed for all samples and staining methods.
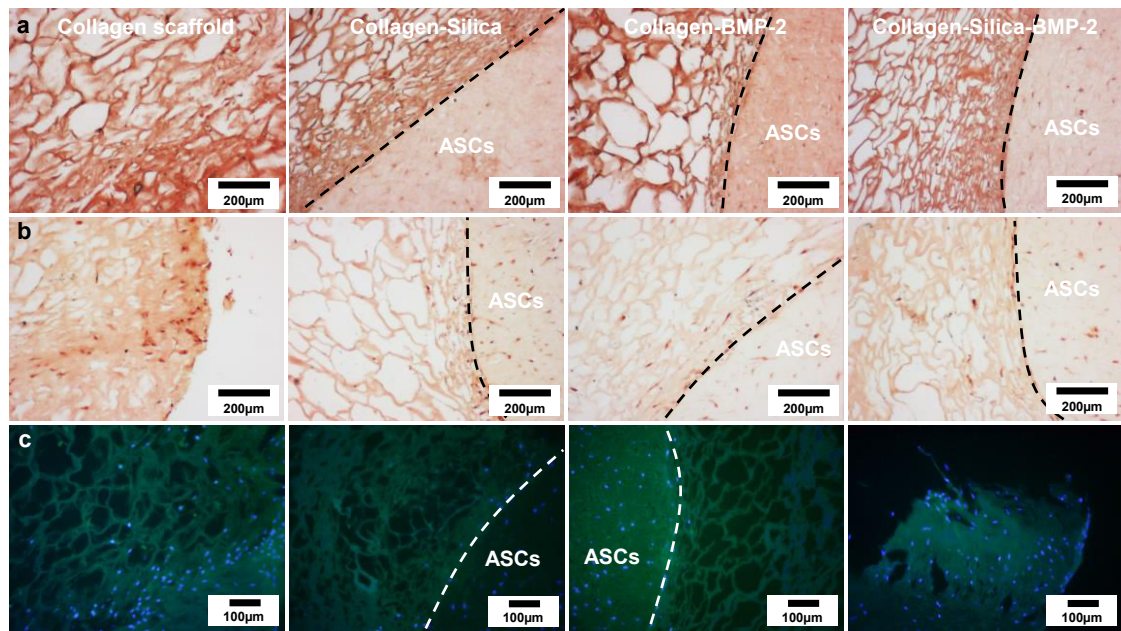
Figure 76: (a) Alizarin red S, (b) von Kossa and (c) Calcein with DAPI staining of hASCs seeded on collagen scaffolds after 2 weeks of cultivation without dexamethasone. The dashed line indicates the border between the collagen gel and the collagen scaffold, for details see Figure 70.

There are several possible reasons leading to this outcome. In contrast to bone marrow mesenchymal stem cells (BM-MSCs), the effect of BMP-2 on osteogenic differentiation of hASCs is yet to be fully understood. Besides osteoinductive BMPs, in particular BMP-2, -4, -6, -7 and -9 [165], several other growth factors such as insulin-like growth factor (IGF)-1, fibroblast growth factor (FGF)-2, vascular endothelial growth factor (VEGF) and transforming growth factor beta (TGF-β) are present within the extracellular matrix of bones. Therefore, it appears possible that for the osteogenic differentiation of hASCs not only one of the growth factors, e.g. BMP-2, has to be applied, but a combination of the different factors [177]. However, the approach of using a combination of several growth factors might be too complicated and too expensive. As a convenient alternative, the osteoinductive steroid drug dexamethasone could be used in combination with BMP-2 to enhance the osteogenic differentiation of hASCs [339-341]. Therefore, future experiments will be performed with the addition of dexamethasone to support the osteogenic differentiation of hASCs.

In addition, the BMP-2 source might play an important role. Thus, recombinant human (rh) BMP-2 can be produced using mammalian cells such as Chinese Hamster Ovary (CHO) cells [286] or bacteria such as *Escherichia coli* (*E. coli*) [222, 287]. While the CHO-derived rhBMP-2 dimer is glycosylated, rh-BMP-2 expressed in *E. coli* lacks this functionality. Based on that, rhBMP-2 from different sources exhibit different physicochemical properties. For example, the isoelectric point (pI), which has an influence on the solubility and release kinetics of proteins, was slightly bigger for CHO

rhBMP-2 (pI ≈ 9), than for *E. coli* rhBMP-2 (pI ≈ 8.5).[221] Another study compared the biological activity of CHO derived rhBMP-2 purchased from two different providers [290]. The authors could show large differences in activity between seemingly identical CHO-derived rhBMP-2 both *in vitro* and *in vivo*. To evaluate the osteogenic differentiation in this study, commercially available *E. coli* derived BMP-2 from Peprotech (Hamburg, BMP-2) was used. However, in later studies, it could be demonstrated that the purchased *E. coli* rhBMP-2 was of lower quality according to the results from gel electrophoresis, which showed that the sample mainly contained the BMP-2 monomer instead of the functional dimer; correspondingly, it exhibited lower biological activity according to the results from BRE-Luc assay when compared to rhBMP-2 from *E. coli* produced by our cooperation partners (Institut für Technische Chemie, Leibniz Universität Hannover) (Figure S3, SI).

In addition, the BMP-2 loading was performed using PBS. However, at later time points, it was detected that BMP-2 forms large (1 - 2 µm) aggregates and precipitates in this buffer (see section 4.2.3).

Therefore, next experiments on the osteogenic differentiation of hASCs will be performed with the in-house produced *E. coli*-derived rhBMP-2 and an appropriate buffer, e.g. MES buffer, and are currently in progress. In addition, for ongoing experiments the cultivation time of hASCs on different collagen scaffold samples will be increased to 4 weeks to give the cells enough time for differentiation [336].

In summary, in this study a potentially osteoinductive nanocomposite for bone tissue regeneration based on three-dimensional collagen scaffolds and nanoporous silica nanoparticles loaded with the osteoinductive growth factor BMP-2 could be produced. By using NPSNPs with and without additional functional groups it was possible to control the BMP-2 release. However, first cell culture investigations with the collagen-NPSNP-BMP-2 nanocomposites seeded with adipose tissue-derived mesenchymal stem cells have not shown the desired osteoinductive capability. Research into solving this issue is already in progress.

5   Summary and outlook

The main aim of this work was the development of a universal delivery platform by using nanoporous silica nanoparticles (NPSNPs) for applications in the field of tissue engineering and regenerative medicine. For this purpose, the osteoinductive growth factor bone morphogenetic protein 2 (BMP-2) was loaded on the surface of NPSNPs. By tailoring the surface chemistry of the NPSNPs, the loading capacity and the release of BMP-2 should be engineered. With regard to the possible use for bone regeneration and for the treatment of rotator cuff ruptures, first steps were undertaken towards the fabrication of engineered implants by the integration of BMP-2-loaded NPSNPs into two different types of scaffolds made up of collagen and electrospun poly(ε-caprolactone) fibres, respectively. This approach should enable the delivery of low doses of BMP-2 in a controlled manner and induce osteogenic differentiation of mesenchymal stem cells leading to the regeneration of the damaged tissue.

First, spherical, uniform, monodisperse and highly porous NPSNPs with a particle diameter of 40 - 60 nm and a measured specific surface area of 1000 $m^2 g^{-1}$ were synthesised by a modified sol-gel process using the structure-directing agent (SDA) cetyltrimethylammonium bromide (CTAB) that was removed after the nanoparticle synthesis by calcination to open the nanopores. All further experiments were performed using this starting material.

Due to the potential application of surface-modified NPSNPs as delivery systems for therapeutic applications, the hydrolytic stability of the attached functional groups, as well as the porosity of the NPSNPs, were examined upon exposure to ultrapure water (chapter 4.1). For this purpose, aminopropylsilyl groups were successfully introduced on the surface of NPSNPs by post-synthetic grafting employing (3-aminopropyl)-triethoxysilane (APTES). It was shown that about 70% of the initially anchored aminopropylsilyl groups were hydrolytically stable and remained on the surface of NPSNPs upon water exposure for 64 h. While the particle morphology remained intact, a significant reduction in porosity of the aminopropylsilyl-modified NPSNPs was observed. It was proposed that the nanopores were clogged by aminopropylsilyl oligomers deposited on the surface of NPSNPs. However, the lost porosity could be recovered during the subsequent functionalization of the aminopropylsilyl-modified NPSNPs with succinic anhydride in dimethylformamide (DMF). In this process, the presence of the succinic anhydride seems to play a decisive role in the ability to reopen the clogged pores. Therefore, we hypothesize that the condensed aminoorganosilica oligomers, which have precipitated on the surface of the NPSNPs, were probably mainly

bound by hydrogen bonds between silanol surface groups and the amino groups of the oligomers. After the reaction with succinic anhydride, amino groups were converted into amide groups which exert considerably weaker hydrogen bonding interactions. Consequently, the pore-clogging aminoorganosilica oligomers were detached from the surface, resulting in free pore entrances and higher porosity. This hypothesis could be verified in the future by employing other organic acid anhydrides like acetic or benzoic acid anhydrides instead of succinic anhydride, which should react in a similar way with the amino groups of the aminoorganosilica oligomers and convert them into amide groups.

To sum up, the findings derived from this part of the work not only provide unique insights into the hydrolytic stability of aminopropylsilyl-modified NPSNPs, which are commonly used for biomedical applications and are important for the construction of NPSNP-based drug delivery devices, but also show that the reduction of the porosity due to the water exposure is not necessarily equivalent to the destruction of the pore system.

The main aim of the second part of the thesis was to develop a strategy to control the binding capacity and the release of the osteoinductive BMP-2 by exploiting NPSNPs with versatile surface chemistries (chapter 4.2). It was assumed that in order to achieve a homogeneous BMP-2 coverage on the surface of NPSNP, it is favourable to have a stable colloidal solution of BMP-2 dimers. For this purpose, the aggregation behaviour of BMP-2 in dependence of pH and concentration was determined by dynamic light scattering (DLS) and zeta potential measurements in different buffers. In general, the pH-dependent aggregation behaviour strongly depends on the isoelectric point (pI) and the hydrophobicity of the protein. For hydrophobic proteins with a high pI like BMP-2 (pI ≈ 8.5), interactions between the hydrophobic regions of the molecules are favoured at physiological pH (7.4). Therefore, BMP-2 was more prone to fast aggregation at pH values near its pI, i.e. at pH 7 and above, showing large BMP-2 aggregates with diameters of 1.5 − 1.7 µm. In contrast, at pH values below 7, equally charged BMP-2 dimers repel each other due to the electrostatic repulsion resulting in a stable colloidal solution of BMP-2. As a result, the best conditions to load BMP-2 on the surface of NPSNPs were identified to be at pH 5 using the 2-(N-morpholino)ethanesulfonic acid (MES) buffer showing highly positively charged BMP-2 dimers of around 10 nm and small aggregates of around 30 nm. Further, it was shown that the BMP-2 concentration played a crucial role in the formation of BMP-2 aggregates in MES buffer at pH 5. Naturally, the lower the BMP-2 concentrations were, the smaller were the BMP-2 aggregates.

The characterization of BMP-2 in different buffers and at different concentrations by DLS and zeta potential measurements represents a major initial step towards the understanding of the physicochemical properties of BMP-2. The approach used here can be adapted to other biomolecules used for biomedical applications. Further research is

being undertaken within the DFG research group FOR 2180 "Graded implants for tendon-bone junction" with the focus on the pH-dependent solubility, stability and biological activity of BMP-2.

As next, mechanisms of how the surface chemistry of NPSNPs controls the BMP-2 loading capacity and the release behaviour were extensively studied. Besides non-modified (NPSNP-OH) and aminopropylsilyl-modified NPSNPs (NPSNP-propyl-NH$_2$) that have already been used in the first part of the work, NPSNPs were equipped with four other functional groups, namely -propyl-SH, -propyl-SO$_3$H, -methyl-NH-hexyl-NH$_2$ and -propyl-NH-hexyl-NH$_2$ providing different physicochemical properties, e.g. hydrophobicity/hydrophilicity and surface charge, to the NPSNPs. To identify the loading capacities of BMP-2 on the surface of non-modified and all types of modified NPSNPs, adsorbed BMP-2 amounts were quantified by means of an antibody-based enzyme-linked immunosorbent assay (ELISA) and a cell-based assay containing the BMP-responsive element fused to the luciferase reporter gene (BRE-Luc). Following important findings can be drawn from both methods. Non-modified NPSNPs adsorbed the least amount of BMP-2, namely around 37 ng mg^{-1} (ELISA) and 2.5 ng mg^{-1} (BRE-Luc assay), whereas much higher BMP-2 amounts were adsorbed on the surface of modified NPSNPs, namely between 700 ng mg^{-1} and 1000 ng mg^{-1} (ELISA) and between 140 ng mg^{-1} and 220 ng mg^{-1} (BRE-Luc assay). Therefore, we hypothesize that the presence of hydrophobic functionalities on the surface of the NPSNPs is the major factor controlling the BMP-2 loading capacity. In addition, it was demonstrated that BMP-2 was adsorbed on the surface of modified NPSNPs bearing both positively (-NH$_2$) and negatively charged (-SH and -SO$_3$H) terminal functional group probably due to the presence of both negatively and positively charged regions on the surface of BMP-2.

Furthermore, zeta potential measurements of NPSNPs that were loaded with increasing BMP-2 amounts offer an additional method to prove the successful loading of positively charged BMP-2 (in MES buffer, at pH 5) on the surface of negatively charged NPSNPs, in particular, of NPSNP-OH, -propyl-SH and -propyl-SO$_3$H. However, this method was not suitable to observe BMP-2 adsorption on positively charged NPSNPs with terminal amino groups. DLS measurements of NPSNPs bearing -propyl-NH$_2$ and -propyl-NH-hexyl-NH$_2$ groups showed a formation of colloidally stable nanoparticle dispersions at low and high BMP-2 concentrations. In contrast, NPSNPs bearing negatively charged functional groups (-OH, -SH and -SO$_3$H), as well as the positively charged NPSNP-methyl-NH-hexyl-NH$_2$, demonstrated the tendency for particle aggregation, especially at high BMP-2 concentrations. During the aggregation, it is very likely that some BMP-2 was trapped in the interparticle space of the aggregates and thus, would not be available

for the cells. Therefore, only NPSNPs bearing -propyl-NH_2 and -propyl-NH-hexyl-NH_2 groups will be suitable candidates for future biomedical applications.

After the determination of the binding mechanisms of BMP-2, the BMP-2 release behaviour from the surface of differently modified NPSNPs was evaluated based on the results derived from the ELISA measurements. Depending on the modification of NPSNPs, three different types of BMP-2 release behaviours were identified. However, the observed release behaviour could not be fully clarified. 1) NPSNP-OH and NPSNP-propyl-NH_2 revealed a fast initial release within the first week followed by a sustained release within the second week. The weak hydrogen bonding interactions between BMP-2 and silanol and amino groups on the surface of NPSNP-OH and NPSNP-propyl-NH_2 could be responsible for this fast BMP-2 release. 2) Only NPSNP-propyl-NH-hexyl-NH_2 revealed a sustained release of BMP-2 for the entire period of two weeks. Here, a beneficial synergistic effect of electrostatic repulsion of positively charged amino groups and BMP-2 molecules and hydrophobic interactions between hexyl chains and BMP-2 might have been responsible for the controlled BMP-2 release. 3) The very small amounts of BMP-2 released from NPSNPs bearing -propyl-SH, -SO_3H and -methyl-NH-hexyl-NH_2 moieties could be attributed to the strong electrostatic or/and hydrophobic interactions between BMP-2 and the functional groups on the surface. In these cases, BMP-2 seemed to be bound too strongly and therefore was retained on the surface of the NPSNPs. The strong binding could have also led to irreversible conformational changes of BMP-2. As a result, BMP-2 could not be recognized by the antibody-based ELISA and therefore, only small amounts of BMP-2 were detected.

In general, very low released amounts of BMP-2 (less than 10%) were detected for modified NPSNPs if compared to the initially loaded BMP-2 amounts (up to 1000 ng mg^{-1} for modified NPSNPs). One of the reasons could be the precipitation of BMP-2 during the release procedure. However, an ELISA can only detect molecularly dissolved BMP-2, as the responsible epitope may be masked in aggregated molecules. For the future experiments, aggregated but still biologically active BMP-2 should be quantified by the cell-based BRE-Luc assay.

Further investigations would be needed to determine exactly how different functional groups on the surface of NPSNPs affect the binding and the release kinetics of BMP-2. For example, computational approaches could provide further information into protein adsorption-desorption mechanisms at the molecular scale. These mechanisms could be simulated with different degrees of exactness by the different computational approach. However, very large, detailed and precise simulations will result in the increase of the computational costs.

With regard to the future biomedical applications of BMP-2-loaded NPSNPs for bone regeneration, the release kinetics of BMP-2 should be studied at physiological

conditions. Because of the fast precipitation of BMP-2 under these conditions, released BMP-2 amounts should also be quantified by the BRE-Luc assay. Moreover, to increase the amount of the released BMP-2, more BMP-2 can be loaded on the surface of modified NPSNPs. Knowing the external surface area of the NPSNPs (around 200 $m^2 g^{-1}$) and the dimension of one BMP-2 dimer (7.5 nm x 3.5 nm), around 26 µg of BMP-2 dimers are needed to cover 100% of the surface of 1 mg of NPSNPs by BMP-2 dimer monolayer. In the present study, up to 1 µg mg^{-1} were adsorbed on the surface of modified NPSNP corresponding to the surface coverage of less than 4%. Therefore, in future studies much more BMP-2 could be adsorbed on the surface of modified NPSNPs to achieve higher BMP-2 release amounts. However, it should be kept in mind that the use of more BMP-2 will lead to increased costs to produce BMP-2-loaded NPSNPs and could cause severe side effects when employed for bone regeneration.

In general, it would be possible to modify the surface of NPSNPs by numerous commercially available organosilanes possessing versatile physicochemical properties that can be chosen according to the needs. Therefore, the application of NPSNPs with versatile surface chemistries could provide a universal solution for engineering nanoparticles with desired loading capacity and release kinetics for any biomolecules. For example, besides BMP-2, transcription factor Smad8 Linker region + Mad Homology Region 2 (Smad8 (L+MH2) and transforming growth factor (TGF)-β3 should be loaded on NPSNPs and integrated into a scaffold within the research group "Graded implants for tendon-bone junction" to re-establish the tendon-bone junction as a novel therapy to restore the functionality of the rotator cuff after a rupture. The approach described above can be useful in combination with other methods to study the binding capacities and the release behaviours of these biomolecules when loaded on the surface of modified NPSNPs.

To study the potential of BMP-2-loaded NPSNPs for bone regeneration, BMP-2-mediated early targeted gene expression of *inhibitor of differentiation 1* and *3* (*Id1 and Id3*) genes was used to monitor the commitment of human bone marrow-derived mesenchymal stem cell (BM-MSCs) towards the osteogenic lineage (chapter 4.3). In this study, the effect of dissolved BMP-2 and BMP-2 adsorbed on the surface of NPSNP-propyl-NH-hexyl-NH_2 were compared with each other. It was demonstrated that BMP-2-loaded NPSNPs were slightly more effective in upregulating early targeted *Id1* and *Id3* gene expression after the short exposure of 2 h than dissolved BMP-2. It was hypothesized that BMP-2 adsorbed on NPSNPs could intensively interact with the cell receptors due to the even distribution of the nanoparticles over the cells. In contrast, free BMP-2, known for strong aggregation at physiological conditions, would be in contact only with the limited number of cells. However, similar levels of gene expressions for

dissolved and adsorbed BMP-2 were detected after 24 h probably due to the similar diffusion rates of BMP-2 from the aggregates and NPSNPs. These results provide first insights into the understanding of how non-covalently adsorbed BMP-2 promotes osteogenic differentiation in BM-MSCs. However, for a deeper understanding of the involved processes, further experiments are needed. In addition, the effect of adsorbed BMP-2 on the osteo- or odontogenic differentiation of dental pulp stem cells will be in focus of future research.

With regard to the future application in tissue engineering, a modified MTT assay was used to assess the cytotoxicity of non-modified and all five types of modified NPSNPs towards murine cell line C2C12 BRE-Luc (BMP-Responsive-Element-Luciferase)-pGL3 and BM-MSCs by the exposure to various concentrations of NPSNPs for 1, 3 and 7 days (chapter 4.4). Additionally, cell morphology and proliferation were examined by the light microscopy. Following findings can be drawn from these studies. NPSNP-OH were not cytotoxic at any concentrations, any time and for any cell line. Moreover, all types of modified NPSNPs were not cytotoxic towards both cell lines up to the nanoparticle concentration of 10 µg ml^{-1} throughout 7 days of the exposure. However, above this concentration, all types of modified NPSNPs showed a strong reduction of the metabolic activity of viable C2C12 BRE-Luc cells, in particular, after 24 h of the exposure. It is noteworthy that the colloidally stable NPSNP-propyl-NH-hexyl-NH$_2$ and NPSNP-propyl-SO$_3$H at high concentrations, which were evenly distributed over the cells, showed the strongest reduction of the metabolic activity of viable C2C12 BRE-Luc cells after 3 days of the exposure. It was proposed that at high nanoparticle concentrations and even distribution over the cells, the reduction was caused by the NPSNPs coverage of the cells inhibiting the supply of oxygen and nutrients, as well as the removal of the cell wastes. After 7 days of the exposure to differently modified NPSNPs, a quick recovery of C2C12 BRE-Luc cells from the initial cytotoxic effect could be observed.

As primary cells, BM-MSCs were more sensitive towards exposure to high concentrations of modified NPSNPs. Thus, a strong reduction of the metabolic activity of viable BM-MSCs could be demonstrated throughout the period of 7 days. Especially, NPSNPs bearing terminal amino groups showed a strong effect above the nanoparticle concentration of 10 µg ml^{-1}. These effects were probably caused by the coverage of the cells with NPSNPs preventing the cell from growth and regular metabolic activity. In addition, the reduction of the cell proliferation and metabolic activity of BM-MSCs could have been caused by the incipient osteogenic differentiation due to the exposure to NPSNPs, which are known to induce the differentiation towards the osteogenic lineage on their own. However, further studies will be needed to clarify this issue and the exact role of each functional groups on the NPSNP-induced reduction of the metabolic activity of BM-MSCs.

The development of optimised implants for tissue regeneration enabling the delivery of low doses of the BMP-2 in a controlled manner by using NPSNPs was also in focus of this thesis (chapter 4.5). To this aim, first steps have been done towards the fabrication of a graded implant for the treatment of a rotator cuff rupture within the DFG research group FOR 2180 "Graded implants for tendon-bone junction". Here, nanocomposites made of three-dimensional, "shish kebab"-structured, alginate-coated PCL scaffolds and BMP-2-loaded NPSNPs with different functional groups were successfully prepared by the electrostatic attraction. However, apparently, only low amounts of NPSNPs (1 wt.%) and BMP-2 (around 100 -150 ng per scaffold) could be loaded on the PCL_{SK-Alg} scaffolds. Even lower BMP-2 amounts (up to 8 ng ml^{-1}) were released from the surface of PCL_{SK-Alg}-NPSNP-BMP-2 nanocomposites in PBS containing (pH 7.4), 0.1% bovine serum albumin (BSA) and 0.02% Tween 20 within the period of 5 weeks. The PBS buffer was chosen to mimic the physiological conditions, whereas the BSA and the surfactant Tween 20 were supposed to prevent BMP-2 aggregation. However, this approach was not successful. Therefore, future work needs to focus on the optimisation of the medium to mimic BMP-2 release under physiological conditions. Moreover, research should be undertaken to improve the integration of the BMP-2-loaded NPSNPs into the PCL_{SK-Alg} scaffolds. After that, first cell culture investigations should be performed to evaluate the PCL_{SK-Alg}-NPSNP-BMP-2 nanocomposites regarding their ability to induce osteogenic differentiation in mesenchymal stem cells.

In comparison to PCL-based scaffolds, higher amounts of NPSNPs were integrated into collagen scaffolds ($\approx$ 33 wt.%). Consequently, much higher BMP-2 amounts, namely 35 ng ml^{-1} for NPSNP-OH and 75 ng ml^{-1} NPSNP-propyl-NH$_2$, were released within a period of 5 weeks. The BMP-2 release followed first-order kinetics in both cases and the release curves could be fitted by using logarithmic equations. After the comparison with BMP-2 release data from the literature, it could be shown that the fast initial release of BMP-2, typically shown by BMP-2-loaded collagen scaffolds, was slowed down by using NPSNPs as delivery carriers for BMP-2.

Unfortunately, BMP-2 amounts released from the collagen-NPSNP-BMP-2 nanocomposites were not sufficient to promote osteogenic differentiation of human adipose-derived stem cells (hASCs) after 2 weeks of cultivation, as confirmed by Alizarin Red S, von Kossa and Calcein stainings. Nevertheless, live/dead cell viability assay of the collagen scaffolds with or without BMP-2-loaded NPSNPs showed a good distribution of viable stem cells across entire collagen scaffolds after the cultivation for 4 weeks. As such, collagen scaffolds offered a cell-friendly environment and were, in principle, suitable for cell attachment and proliferation.

In these studies, commercially available *E. coli*-derived BMP-2 was used. However, in later studies, it could be demonstrated that the purchased *E. coli*-derived BMP-2 was of lower quality and exhibited lower biological activity when compared to the *E. coli*-derived BMP-2 produced by the cooperation partners within the DFG research group FOR 2180. Moreover, BMP-2 loading on NPSNPs was performed using PBS. However, at later time points, it was detected that BMP-2 forms large (1 - 2 µm) aggregates and precipitates in this buffer. Therefore, next experiments on the osteogenic differentiation of hASCs will be performed using the in-house produced *E. coli*-derived BMP-2 and an appropriate buffer, e.g. MES buffer, and are currently in progress. In addition, osteoinductive drug dexamethasone could be incorporated into the nanopores of NPSNPs and used in combination with BMP-2 to support the osteogenic differentiation of hASCs. Besides BMP-2, several other growth factors such as insulin-like growth factor (IGF)-1, fibroblast growth factor (FGF)-2, vascular endothelial growth factor (VEGF) and transforming growth factor beta (TGF-β), which are present within the extracellular matrix of bones, could also increase the chance of the osteogenic differentiation of hASCs when applied in combination with BMP-2.

6 References

[1] J.A. Buckwalter, M.J. Glimcher, R.R. Cooper, R. Recker, Bone biology. II: Formation, form, modeling, remodeling, and regulation of cell function, Instr. Course Lect., 45 (1996) 387-399.
[2] D.J. Hadjidakis, Androulakis, II, Bone remodeling, Ann. N. Y. Acad. Sci., 1092 (2006) 385-396.
[3] F. Loi, L.A. Cordova, J. Pajarinen, T.H. Lin, Z. Yao, S.B. Goodman, Inflammation, fracture and bone repair, Bone, 86 (2016) 119-130.
[4] A.S. Brydone, D. Meek, S. Maclaine, Bone grafting, orthopaedic biomaterials, and the clinical need for bone engineering, Proc. Inst. Mech. Eng. H, 224 (2010) 1329-1343.
[5] C. Laurencin, Y. Khan, S.F. El-Amin, Bone graft substitutes, Expert Rev. Med. Devices, 3 (2006) 49-57.
[6] P.J. Yang, J.S. Temenoff, Engineering Orthopedic Tissue Interfaces, Tissue Eng. Part B, Rev., 15 (2009) 127-141.
[7] M. Benjamin, H. Toumi, J.R. Ralphs, G. Bydder, T.M. Best, S. Milz, Where tendons and ligaments meet bone: attachment sites ('entheses') in relation to exercise and/or mechanical load, J. Anat., 208 (2006) 471-490.
[8] A. Chainani, D. Little, Current Status of Tissue-Engineered Scaffolds for Rotator Cuff Repair, Tech. Orthop. (Rockville, Md.), 31 (2016) 91-97.
[9] L.M. Galatz, C.M. Ball, S.A. Teefey, W.D. Middleton, K. Yamaguchi, The outcome and repair integrity of completely arthroscopically repaired large and massive rotator cuff tears, J. Bone Joint Surg. Am., 86-a (2004) 219-224.
[10] L.M. Cross, A. Thakur, N.A. Jalili, M. Detamore, A.K. Gaharwar, Nanoengineered biomaterials for repair and regeneration of orthopedic tissue interfaces, Acta Biomater., 42 (2016) 2-17.
[11] S.J. Hollister, Porous scaffold design for tissue engineering, Nat Mater, 4 (2005) 518-524.
[12] R. Chen, J. Wang, C. Liu, Biomaterials Act as Enhancers of Growth Factors in Bone Regeneration, Adv. Funct. Mater., 26 (2016) 8810-8823.
[13] S. Bose, M. Roy, A. Bandyopadhyay, Recent advances in bone tissue engineering scaffolds, Trends Biotechnol., 30 (2012) 546-554.
[14] B.L. Banik, G.S. Lewis, J.L. Brown, Multiscale Poly-(ε-caprolactone) Scaffold Mimicking Nonlinearity in Tendon Tissue Mechanics, Regen. Eng. Transl. Med., 2 (2016) 1-9.
[15] M. Geiger, R.H. Li, W. Friess, Collagen sponges for bone regeneration with rhBMP-2, Adv. Drug. Deliv. Rev, 55 (2003) 1613-1629.
[16] R. Chen, J. Wang, C. Liu, Biomaterials Act as Enhancers of Growth Factors in Bone Regeneration, Adv. Funct. Mater., n/a-n/a.
[17] X. Wang, E. Wenk, X. Zhang, L. Meinel, G. Vunjak-Novakovic, D.L. Kaplan, Growth factor gradients via microsphere delivery in biopolymer scaffolds for osteochondral tissue engineering, J. Control. Release, 134 (2009) 81-90.
[18] T. Suciati, D. Howard, J. Barry, N.M. Everitt, K.M. Shakesheff, F.R. Rose, Zonal release of proteins within tissue engineering scaffolds, J. Mater. Sci. Mater. Med., 17 (2006) 1049-1056.
[19] C. Erisken, D.M. Kalyon, H. Wang, Functionally graded electrospun polycaprolactone and beta-tricalcium phosphate nanocomposites for tissue engineering applications, Biomaterials, 29 (2008) 4065-4073.
[20] X. Li, J. Xie, J. Lipner, X. Yuan, S. Thomopoulos, Y. Xia, Nanofiber scaffolds with gradations in mineral content for mimicking the tendon-to-bone insertion site, Nano Lett., 9 (2009) 2763-2768.
[21] J. Kim, A. Sharma, B. Runge, H. Waters, B. Doll, S. McBride, P. Alvarez, M. Dadsetan, M.J. Yaszemski, J.O. Hollinger, Osteoblast growth and bone-healing response to three-dimensional poly(ε-caprolactone fumarate) scaffolds, J. Tissue Eng. Regen. Med., 6 (2012) 404-413.
[22] M. Mehta, K. Schmidt-Bleek, G.N. Duda, D.J. Mooney, Biomaterial delivery of morphogens to mimic the natural healing cascade in bone, Adv. Drug. Del. Rev., 64 (2012) 1257-1276.
[23] V. Mouriño, A.R. Boccaccini, Bone tissue engineering therapeutics: controlled drug delivery in three-dimensional scaffolds, J. R. Soc. Interface, 7 (2010) 209-227.
[24] J.L. Moreau, H.H.K. Xu, Mesenchymal stem cell proliferation and differentiation on an injectable calcium phosphate - chitosan composite scaffold, Biomaterials, 30 (2009) 2675-2682.
[25] H. Zhang, F. Migneco, C.Y. Lin, S.J. Hollister, Chemically-conjugated bone morphogenetic protein-2 on three-dimensional polycaprolactone scaffolds stimulates osteogenic activity in bone marrow stromal cells, Tissue Eng. Part A, 16 (2010) 3441-3448.

[26] J.D. Boerckel, Y.M. Kolambkar, K.M. Dupont, B.A. Uhrig, E.A. Phelps, H.Y. Stevens, A.J. García, R.E. Guldberg, Effects of protein dose and delivery system on BMP-mediated bone regeneration, Biomaterials, 32 (2011) 5241-5251.

[27] P.C. Bessa, M. Casal, R.L. Reis, Bone morphogenetic proteins in tissue engineering: the road from the laboratory to the clinic, part I (basic concepts), J. Tissue Eng. Regen. Med., 2 (2008) 1-13.

[28] K. Möller, T. Bein, Talented Mesoporous Silica Nanoparticles, Chem. Mater., 29 (2017) 371-388.

[29] S. Simovic, N. Ghouchi-Eskandar, A.M. Sinn, D. Losic, C.A. Prestidge, Silica materials in drug delivery applications, Curr. Drug. Discov. Technol, 8 (2011) 269-276.

[30] V. Mamaeva, C. Sahlgren, M. Linden, Mesoporous silica nanoparticles in medicine--recent advances, Adv. Drug. Deliv. Rev, 65 (2013) 689-702.

[31] M. Vallet-Regi, F. Balas, D. Arcos, Mesoporous materials for drug delivery, Angew. Chem. Int. Ed. Engl., 46 (2007) 7548-7558.

[32] P. Yang, S. Gai, J. Lin, Functionalized mesoporous silica materials for controlled drug delivery, Chem. Soc. Rev., 41 (2012) 3679-3698.

[33] A. Neumann, A. Christel, C. Kasper, P. Behrens, BMP2-loaded nanoporous silica nanoparticles promote osteogenic differentiation of human mesenchymal stem cells, RSC Advances, 3 (2013) 24222-24230.

[34] Q. Gan, J. Zhu, Y. Yuan, H. Liu, J. Qian, Y. Li, C. Liu, A dual-delivery system of pH-responsive chitosan-functionalized mesoporous silica nanoparticles bearing BMP-2 and dexamethasone for enhanced bone regeneration, J. Mater. Chem. B, 3 (2015) 2056-2066.

[35] X. Jing, H.-Y. Mi, X.-C. Wang, X.-F. Peng, L.-S. Turng, Shish-Kebab-Structured Poly(ε-Caprolactone) Nanofibers Hierarchically Decorated with Chitosan–Poly(ε-Caprolactone) Copolymers for Bone Tissue Engineering, ACS Appl. Mater. Interfaces, 7 (2015) 6955-6965.

[36] Q. He, J. Shi, M. Zhu, Y. Chen, F. Chen, The three-stage in vitro degradation behavior of mesoporous silica in simulated body fluid, Microporous Mesoporous Mater., 131 (2010) 314-320.

[37] H. Yamada, C. Urata, Y. Aoyama, S. Osada, Y. Yamauchi, K. Kuroda, Preparation of Colloidal Mesoporous Silica Nanoparticles with Different Diameters and Their Unique Degradation Behavior in Static Aqueous Systems, Chem. Mater., 24 (2012) 1462-1471.

[38] V. Cauda, C. Argyo, T. Bein, Impact of different PEGylation patterns on the long-term bio-stability of colloidal mesoporous silica nanoparticles, J. Mater. Chem., 20 (2010) 8693-8699.

[39] F. Tang, L. Li, D. Chen, Mesoporous silica nanoparticles: synthesis, biocompatibility and drug delivery, Adv. Mater., 24 (2012) 1504-1534.

[40] I.I. Slowing, B.G. Trewyn, S. Giri, V.S.Y. Lin, Mesoporous Silica Nanoparticles for Drug Delivery and Biosensing Applications, Adv. Funct. Mater., 17 (2007) 1225-1236.

[41] S. Baek, R.K. Singh, D. Khanal, K.D. Patel, E.J. Lee, K.W. Leong, W. Chrzanowski, H.W. Kim, Smart multifunctional drug delivery towards anticancer therapy harmonized in mesoporous nanoparticles, Nanoscale, 7 (2015) 14191-14216.

[42] J.M. Rosenholm, C. Sahlgren, M. Linden, Towards multifunctional, targeted drug delivery systems using mesoporous silica nanoparticles--opportunities & challenges, Nanoscale, 2 (2010) 1870-1883.

[43] D.A. J. Rouquerol, C. W. Fairbridge, D. H. Everett, J. M. Haynes, N. Pernicone, J. D. F. Ramsay, K. S. W. Sing and K. K. Unger, Recommendations for the characterization of porous solids (Technical Report), Pure Appl. Chem., 66 (1994) 1739-1758.

[44] J.S. Beck, J.C. Vartuli, W.J. Roth, M.E. Leonowicz, C.T. Kresge, K.D. Schmitt, C.T.W. Chu, D.H. Olson, E.W. Sheppard, S.B. McCullen, J.B. Higgins, J.L. Schlenker, A new family of mesoporous molecular sieves prepared with liquid crystal templates, J. Am. Chem. Soc., 114 (1992) 10834-10843.

[45] Y.F. S. Inagaki, A. Okada, C. Kato, K Kuroda, Manufacture of layer-form silica-metal oxide porous intercalation compounds useful as adsorbents and catalysts, Toyota Central Research and Development Laboratories, Inc., Japan, 1992.

[46] M. Vallet-Regi, A. Rámila, R.P. del Real, J. Pérez-Pariente, A New Property of MCM-41: Drug Delivery System, Chem. Mater., 13 (2001) 308-311.

[47] Q. Cai, W.-Y. Lin, F.-S. Xiao, W.-Q. Pang, X.-H. Chen, B.-S. Zou, The preparation of highly ordered MCM-41 with extremely low surfactant concentration, Microporous Mesoporous Mater., 32 (1999) 1-15.

[48] Y. Wan, D. Zhao, On the controllable soft-templating approach to mesoporous silicates, Chem. Rev., 107 (2007) 2821-2860.

[49] F. Hoffmann, M. Cornelius, J. Morell, M. Fröba, Silica-Based Mesoporous Organic–Inorganic Hybrid Materials, Angew. Chem. Int. Ed., 45 (2006) 3216-3251.

[50] S.-H. Wu, C.-Y. Mou, H.-P. Lin, Synthesis of mesoporous silica nanoparticles, Chem. Soc. Rev., 42 (2013) 3862-3875.

[51] I.I. Slowing, J.L. Vivero-Escoto, B.G. Trewyn, V.S.Y. Lin, Mesoporous silica nanoparticles: structural design and applications, J. Mater. Chem., 20 (2010) 7924-7937.

[52] H.-P. Lin, C.-Y. Mou, Structural and Morphological Control of Cationic Surfactant-Templated Mesoporous Silica, Acc. Chem. Res., 35 (2002) 927-935.

[53] C.E. Fowler, D. Khushalani, B. Lebeau, S. Mann, Nanoscale materials with mesostructured interiors, Adv. Mater., 13 (2001) 649-652.

[54] C.-Y. Lai, B.G. Trewyn, D.M. Jeftinija, K. Jeftinija, S. Xu, S. Jeftinija, V.S.Y. Lin, A Mesoporous Silica Nanosphere-Based Carrier System with Chemically Removable CdS Nanoparticle Caps for Stimuli-Responsive Controlled Release of Neurotransmitters and Drug Molecules, J. Am. Chem. Soc., 125 (2003) 4451-4459.

[55] Z.-A. Qiao, L. Zhang, M. Guo, Y. Liu, Q. Huo, Synthesis of Mesoporous Silica Nanoparticles via Controlled Hydrolysis and Condensation of Silicon Alkoxide, Chem. Mater., 21 (2009) 3823-3829.

[56] K. Suzuki, K. Ikari, H. Imai, Synthesis of Silica Nanoparticles Having a Well-Ordered Mesostructure Using a Double Surfactant System, J. Am. Chem. Soc., 126 (2004) 462-463.

[57] Y.-S. Lin, C.L. Haynes, Synthesis and Characterization of Biocompatible and Size-Tunable Multifunctional Porous Silica Nanoparticles, Chem. Mater., 21 (2009) 3979-3986.

[58] K. Möller, J. Kobler, T. Bein, Colloidal Suspensions of Nanometer-Sized Mesoporous Silica, Adv. Funct. Mater., 17 (2007) 605-612.

[59] M. Grün, I. Lauer, K.K. Unger, The synthesis of micrometer- and submicrometer-size spheres of ordered mesoporous oxide MCM-41, Adv. Mater., 9 (1997) 254-257.

[60] S. Huh, J.W. Wiench, J.-C. Yoo, M. Pruski, V.S.Y. Lin, Organic Functionalization and Morphology Control of Mesoporous Silicas via a Co-Condensation Synthesis Method, Chem. Mater., 15 (2003) 4247-4256.

[61] T. Delclos, C. Aimé, E. Pouget, A. Brizard, I. Huc, M.-H. Delville, R. Oda, Individualized Silica Nanohelices and Nanotubes: Tuning Inorganic Nanostructures Using Lipidic Self-Assemblies, Nano Lett., 8 (2008) 1929-1935.

[62] L.-P. Yang, P. Zou, C.-Y. Pan, Preparation of hierarchical worm-like silica nanotubes, J. Mater. Chem., 19 (2009) 1843-1849.

[63] S.-Y. Chen, C.-Y. Tang, W.-T. Chuang, J.-J. Lee, Y.-L. Tsai, J.C.C. Chan, C.-Y. Lin, Y.-C. Liu, S. Cheng, A Facile Route to Synthesizing Functionalized Mesoporous SBA-15 Materials with Platelet Morphology and Short Mesochannels, Chem. Mater., 20 (2008) 3906-3916.

[64] A.B. Fuertes, P. Valle-Vigon, M. Sevilla, Synthesis of colloidal silica nanoparticles of a tunable mesopore size and their application to the adsorption of biomolecules, J. Colloid Interface Sci., 349 (2010) 173-180.

[65] M.H. Kim, H.K. Na, Y.K. Kim, S.R. Ryoo, H.S. Cho, K.E. Lee, H. Jeon, R. Ryoo, D.H. Min, Facile synthesis of monodispersed mesoporous silica nanoparticles with ultralarge pores and their application in gene delivery, ACS Nano, 5 (2011) 3568-3576.

[66] Y. Han, J.Y. Ying, Generalized Fluorocarbon-Surfactant-Mediated Synthesis of Nanoparticles with Various Mesoporous Structures, Angew. Chem. Int. Ed., 44 (2005) 288-292.

[67] J. Hu, M. Chen, X. Fang, L. Wu, Fabrication and application of inorganic hollow spheres, Chem. Soc. Rev., 40 (2011) 5472-5491.

[68] S.L. Burkett, S.D. Sims, S. Mann, Synthesis of hybrid inorganic-organic mesoporous silica by co-condensation of siloxane and organosiloxane precursors, Chem. Commun., (1996) 1367-1368.

[69] D.J. Macquarrie, Direct preparation of organically modified MCM-type materials. Preparation and characterisation of aminopropyl-MCM and 2-cyanoethyl-MCM, Chem. Commun., (1996) 1961-1962.

[70] M.H. Lim, C.F. Blanford, A. Stein, Synthesis and Characterization of a Reactive Vinyl-Functionalized MCM-41: Probing the Internal Pore Structure by a Bromination Reaction, J. Am. Chem. Soc., 119 (1997) 4090-4091.

[71] F. de Juan, E. Ruiz-Hitzky, Selective functionalization of mesoporous silica, Adv. Mater., 12 (2000) 430-+.

[72] T. Vallant, H. Brunner, U. Mayer, H. Hoffmann, T. Leitner, R. Resch, G. Friedbacher, Formation of Self-Assembled Octadecylsiloxane Monolayers on Mica and Silicon Surfaces Studied by Atomic Force Microscopy and Infrared Spectroscopy, J. Phys. Chem. B, 102 (1998) 7190-7197.

[73] R. Mortera, S. Fiorilli, E. Garrone, E. Verné, B. Onida, Pores occlusion in MCM-41 spheres immersed in SBF and the effect on ibuprofen delivery kinetics: A quantitative model, Chem. Eng. J., 156 (2010) 184-192.

[74] V. Cauda, A. Schlossbauer, T. Bein, Bio-degradation study of colloidal mesoporous silica nanoparticles: Effect of surface functionalization with organo-silanes and poly(ethylene glycol), Microporous Mesoporous Mater., 132 (2010) 60-71.

[75] M. Etienne, A. Walcarius, Analytical investigation of the chemical reactivity and stability of aminopropyl-grafted silica in aqueous medium, Talanta, 59 (2003) 1173-1188.

[76] E. Asenath Smith, W. Chen, How To Prevent the Loss of Surface Functionality Derived from Aminosilanes, Langmuir, 24 (2008) 12405-12409.

[77] H.F. Krug, Nanosafety Research—Are We on the Right Track?, Angew. Chem. Int. Ed., 53 (2014) 12304-12319.

[78] www.nanoobjects.info/en/.

[79] www.nanoobjects.info/files/methodik/DaNa_criteria_checklist_2016tox_en.pdf.

[80] T.J. Brunner, P. Wick, P. Manser, P. Spohn, R.N. Grass, L.K. Limbach, A. Bruinink, W.J. Stark, In Vitro Cytotoxicity of Oxide Nanoparticles: Comparison to Asbestos, Silica, and the Effect of Particle Solubility, Environ. Sci. Technol., 40 (2006) 4374-4381.

[81] K. Peters, R.E. Unger, C.J. Kirkpatrick, A.M. Gatti, E. Monari, Effects of nano-scaled particles on endothelial cell function in vitro: Studies on viability, proliferation and inflammation, J. Mater. Sci. Mater. Med., 15 (2004) 321-325.

[82] A.E. Nel, L. Madler, D. Velegol, T. Xia, E.M.V. Hoek, P. Somasundaran, F. Klaessig, V. Castranova, M. Thompson, Understanding biophysicochemical interactions at the nano-bio interface, Nat. Mater., 8 (2009) 543-557.

[83] E. Fröhlich, The role of surface charge in cellular uptake and cytotoxicity of medical nanoparticles, Int. J. Nanomedicine, 7 (2012) 5577-5591.

[84] A. Verma, F. Stellacci, Effect of surface properties on nanoparticle-cell interactions, Small, 6 (2010) 12-21.

[85] I.I. Slowing, C.-W. Wu, J.L. Vivero-Escoto, V.S.Y. Lin, Mesoporous Silica Nanoparticles for Reducing Hemolytic Activity Towards Mammalian Red Blood Cells, Small, 5 (2009) 57-62.

[86] M.A. Maurer-Jones, Y.S. Lin, C.L. Haynes, Functional assessment of metal oxide nanoparticle toxicity in immune cells, ACS Nano, 4 (2010) 3363-3373.

[87] Y.-S. Lin, C.L. Haynes, Impacts of Mesoporous Silica Nanoparticle Size, Pore Ordering, and Pore Integrity on Hemolytic Activity, J. Am. Chem. Soc., 132 (2010) 4834-4842.

[88] Z. Tao, M.P. Morrow, T. Asefa, K.K. Sharma, C. Duncan, A. Anan, H.S. Penefsky, J. Goodisman, A.-K. Souid, Mesoporous Silica Nanoparticles Inhibit Cellular Respiration, Nano Lett., 8 (2008) 1517-1526.

[89] H.J. Eom, J. Choi, Oxidative stress of silica nanoparticles in human bronchial epithelial cell, Beas-2B, Toxicol. In Vitro, 23 (2009) 1326-1332.

[90] K. Wittmaack, Excessive Delivery of Nanostructured Matter to Submersed Cells Caused by Rapid Gravitational Settling, ACS Nano, 5 (2011) 3766-3778.

[91] K. Wittmaack, Novel Dose Metric for Apparent Cytotoxicity Effects Generated by in Vitro Cell Exposure to Silica Nanoparticles, Chem. Res. Toxicol., 24 (2011) 150-158.

[92] J.-S. Chang, K.L.B. Chang, D.-F. Hwang, Z.-L. Kong, In Vitro Cytotoxicitiy of Silica Nanoparticles at High Concentrations Strongly Depends on the Metabolic Activity Type of the Cell Line, Environ. Sci. Technol., 41 (2007) 2064-2068.

[93] J. Blechinger, A.T. Bauer, A.A. Torrano, C. Gorzelanny, C. Bräuchle, S.W. Schneider, Uptake Kinetics and Nanotoxicity of Silica Nanoparticles Are Cell Type Dependent, Small, 9 (2013) 3970-3980.

[94] Y. Shi, M.L. Miller, A.J. Di Pasqua, Biocompatibility of Mesoporous Silica Nanoparticles?, Comments Inorg. Chem., 36 (2016) 61-80.

[95] J.E. Lee, N. Lee, T. Kim, J. Kim, T. Hyeon, Multifunctional Mesoporous Silica Nanocomposite Nanoparticles for Theranostic Applications, Acc. Chem. Res., 44 (2011) 893-902.

[96] A.L. Doadrio, E.M.B. Sousa, J.C. Doadrio, J. Pérez Pariente, I. Izquierdo-Barba, M. Vallet-Regí, Mesoporous SBA-15 HPLC evaluation for controlled gentamicin drug delivery, J. Control. Release, 97 (2004) 125-132.

[97] I. Izquierdo-Barba, A. Martinez, A.L. Doadrio, J. Perez-Pariente, M. Vallet-Regi, Release evaluation of drugs from ordered three-dimensional silica structures, Eur. J. Pharm. Sci., 26 (2005) 365-373.

[98] W. Zeng, X.-F. Qian, Y.-B. Zhang, J. Yin, Z.-K. Zhu, Organic modified mesoporous MCM-41 through solvothermal process as drug delivery system, Mater. Res. Bull., 40 (2005) 766-772.

[99] V.S.Y. Lin, C.-Y. Lai, J. Huang, S.-A. Song, S. Xu, Molecular Recognition Inside of Multifunctionalized Mesoporous Silicas: Toward Selective Fluorescence Detection of Dopamine and Glucosamine, J. Am. Chem. Soc., 123 (2001) 11510-11511.

[100] S.W. Song, K. Hidajat, S. Kawi, Functionalized SBA-15 Materials as Carriers for Controlled Drug Delivery: Influence of Surface Properties on Matrix−Drug Interactions, Langmuir, 21 (2005) 9568-9575.

[101] N. Ehlert, M. Badar, A. Christel, S.J. Lohmeier, T. Luessenhop, M. Stieve, T. Lenarz, P.P. Mueller, P. Behrens, Mesoporous silica coatings for controlled release of the antibiotic ciprofloxacin from implants, J. Mater. Chem., 21 (2011) 752-760.

[102] Q. Tang, Y. Xu, D. Wu, Y. Sun, Hydrophobicity-controlled Drug Delivery System from Organic Modified Mesoporous Silica, Chem. Lett., 35 (2006) 474-475.

[103] S.W. Song, K. Hidajat, S. Kawi, Functionalized SBA-15 materials as carriers for controlled drug delivery: influence of surface properties on matrix-drug interactions, Langmuir, 21 (2005) 9568-9575.

[104] I.I. Slowing, B.G. Trewyn, V.S.Y. Lin, Mesoporous Silica Nanoparticles for Intracellular Delivery of Membrane-Impermeable Proteins, J. Am. Chem. Soc., 129 (2007) 8845-8849.

[105] N. Ehlert, A. Hoffmann, T. Luessenhop, G. Gross, P.P. Mueller, M. Stieve, T. Lenarz, P. Behrens, Amino-modified silica surfaces efficiently immobilize bone morphogenetic protein 2 (BMP2) for medical purposes, Acta Biomater., 7 (2011) 1772-1779.

[106] K.A. Whitehead, R. Langer, D.G. Anderson, Knocking down barriers: advances in siRNA delivery, Nat. Rev. Drug Discov., 8 (2009) 129-138.

[107] H.J. Kim, A. Kim, K. Miyata, K. Kataoka, Recent progress in development of siRNA delivery vehicles for cancer therapy, Adv. Drug. Del. Rev., 104 (2016) 61-77.

[108] J. Wang, P. Mi, G. Lin, Y.X.J. Wáng, G. Liu, X. Chen, Imaging-guided delivery of RNAi for anticancer treatment, Adv. Drug. Del. Rev., 104 (2016) 44-60.

[109] D. Lin, Q. Cheng, Q. Jiang, Y. Huang, Z. Yang, S. Han, Y. Zhao, S. Guo, Z. Liang, A. Dong, Intracellular cleavable poly(2-dimethylaminoethyl methacrylate) functionalized mesoporous silica nanoparticles for efficient siRNA delivery in vitro and in vivo, Nanoscale, 5 (2013) 4291-4301.

[110] S.B. Hartono, M. Yu, W. Gu, J. Yang, E. Strounina, X. Wang, S. Qiao, C. Yu, Synthesis of multi-functional large pore mesoporous silica nanoparticles as gene carriers, Nanotechnology, 25 (2014) 055701.

[111] J. Shen, H.C. Kim, H. Su, F. Wang, J. Wolfram, D. Kirui, J. Mai, C. Mu, L.N. Ji, Z.W. Mao, H. Shen, Cyclodextrin and polyethylenimine functionalized mesoporous silica nanoparticles for delivery of siRNA cancer therapeutics, Theranostics, 4 (2014) 487-497.

[112] J. Finlay, C.M. Roberts, J. Dong, J.I. Zink, F. Tamanoi, C.A. Glackin, Mesoporous silica nanoparticle delivery of chemically modified siRNA against TWIST1 leads to reduced tumor burden, Nanomedicine, 11 (2015) 1657-1666.

[113] W. Ngamcherdtrakul, J. Morry, S. Gu, D.J. Castro, S.M. Goodyear, T. Sangvanich, M.M. Reda, R. Lee, S.A. Mihelic, B.L. Beckman, Z. Hu, J.W. Gray, W. Yantasee, Cationic Polymer Modified Mesoporous Silica Nanoparticles for Targeted SiRNA Delivery to HER2+ Breast Cancer, Adv. Funct. Mater., 25 (2015) 2646-2659.

[114] S.H. Lee, Y.Y. Kang, H.-E. Jang, H. Mok, Current preclinical small interfering RNA (siRNA)-based conjugate systems for RNA therapeutics, Adv. Drug. Del. Rev., 104 (2016) 78-92.

[115] C.H. Lee, S.H. Cheng, I.P. Huang, J.S. Souris, C.S. Yang, C.Y. Mou, L.W. Lo, Intracellular pH-responsive mesoporous silica nanoparticles for the controlled release of anticancer chemotherapeutics, Angew. Chem. Int. Ed. Engl., 49 (2010) 8214-8219.

[116] X.F. Zhang, S. Mansouri, L. Clime, H.Q. Ly, L.H. Yahia, T. Veres, Fe3O4-silica core-shell nanoporous particles for high-capacity pH-triggered drug delivery, J. Mater. Chem., 22 (2012) 14450-14457.

[117] A. Schlossbauer, C. Dohmen, D. Schaffert, E. Wagner, T. Bein, pH-Responsive Release of Acetal-Linked Melittin from SBA-15 Mesoporous Silica, Angew. Chem. Int. Ed., 50 (2011) 6828-6830.

[118] H.J. Kim, H. Matsuda, H. Zhou, I. Honma, Ultrasound-Triggered Smart Drug Release from a Poly(dimethylsiloxane)– Mesoporous Silica Composite, Adv. Mater., 18 (2006) 3083-3088.

[119] T.M. Guardado-Alvarez, L. Sudha Devi, M.M. Russell, B.J. Schwartz, J.I. Zink, Activation of Snap-Top Capped Mesoporous Silica Nanocontainers Using Two Near-Infrared Photons, J. Am. Chem. Soc., 135 (2013) 14000-14003.

[120] J. Chen, M. Liu, C. Chen, H. Gong, C. Gao, Synthesis and characterization of silica nanoparticles with well-defined thermoresponsive PNIPAM via a combination of RAFT and click chemistry, ACS Appl. Mater. Interfaces, 3 (2011) 3215-3223.

[121] A. Li, J. Zhang, Y. Xu, J. Liu, S. Feng, Thermoresponsive copolymer/SiO2 nanoparticles with dual functions of thermally controlled drug release and simultaneous carrier decomposition, Chemistry (Easton), 20 (2014) 12945-12953.

[122] R. Liu, Y. Zhang, P. Feng, Multiresponsive Supramolecular Nanogated Ensembles, J. Am. Chem. Soc., 131 (2009) 15128-15129.

[123] E. Aznar, M.D. Marcos, R. Martinez-Manez, F. Sancenon, J. Soto, P. Amoros, C. Guillem, pH- and photo-switched release of guest molecules from mesoporous silica supports, J. Am. Chem. Soc., 131 (2009) 6833-6843.

[124] E. Aznar, M. Oroval, L. Pascual, J.R. Murguía, R. Martínez-Máñez, F. Sancenón, Gated Materials for On-Command Release of Guest Molecules, Chem. Rev., 116 (2016) 561-718.

[125] H. Fullriede, P. Abendroth, N. Ehlert, K. Doll, J. Schäske, A. Winkel, N. Stumpp Sascha, M. Stiesch, P. Behrens, pH-responsive release of chlorhexidine from modified nanoporous silica nanoparticles for dental applications, BioNanoMaterials2016, pp. 59.

[126] A. Baeza, E. Guisasola, E. Ruiz-Hernández, M. Vallet-Regí, Magnetically Triggered Multidrug Release by Hybrid Mesoporous Silica Nanoparticles, Chem. Mater., 24 (2012) 517-524.

[127] W. Guo, C. Yang, H. Lin, F. Qu, P(EO-co-LLA) functionalized Fe3O4@mSiO2 nanocomposites for thermo/pH responsive drug controlled release and hyperthermia, Dalton Trans, 43 (2014) 18056-18065.

[128] Y. Song, Y. Li, Q. Xu, Z. Liu, Mesoporous silica nanoparticles for stimuli-responsive controlled drug delivery: advances, challenges, and outlook, Int. J. Nanomedicine, 12 (2017) 87-110.

[129] X. Wang, H. Chen, Y. Zheng, M. Ma, Y. Chen, K. Zhang, D. Zeng, J. Shi, Au-nanoparticle coated mesoporous silica nanocapsule-based multifunctional platform for ultrasound mediated imaging, cytoclasis and tumor ablation, Biomaterials, 34 (2013) 2057-2068.

[130] J.L. Vivero-Escoto, I.I. Slowing, C.-W. Wu, V.S.Y. Lin, Photoinduced Intracellular Controlled Release Drug Delivery in Human Cells by Gold-Capped Mesoporous Silica Nanosphere, J. Am. Chem. Soc., 131 (2009) 3462-3463.

[131] C. Eggeling, J. Widengren, R. Rigler, C.A.M. Seidel, Photobleaching of Fluorescent Dyes under Conditions Used for Single-Molecule Detection: Evidence of Two-Step Photolysis, Anal. Chem., 70 (1998) 2651-2659.

[132] S. Veeranarayanan, A.C. Poulose, M.S. Mohamed, Y. Nagaoka, S. Iwai, Y. Nakagame, S. Kashiwada, Y. Yoshida, T. Maekawa, D.S. Kumar, Synthesis and application of luminescent single CdS quantum dot encapsulated silica nanoparticles directed for precision optical bioimaging, Int. J. Nanomedicine, 7 (2012) 3769-3786.

[133] B.-H. Jun, D.W. Hwang, H.S. Jung, J. Jang, H. Kim, H. Kang, T. Kang, S. Kyeong, H. Lee, D.H. Jeong, K.W. Kang, H. Youn, D.S. Lee, Y.-S. Lee, Ultrasensitive, Biocompatible, Quantum-Dot-Embedded Silica Nanoparticles for Bioimaging, Adv. Funct. Mater., 22 (2012) 1843-1849.

[134] X. Kang, Z. Cheng, C. Li, D. Yang, M. Shang, P.a. Ma, G. Li, N. Liu, J. Lin, Core–Shell Structured Up-Conversion Luminescent and Mesoporous NaYF4:Yb3+/Er3+@nSiO2@mSiO2 Nanospheres as Carriers for Drug Delivery, J. Phys. Chem. C, 115 (2011) 15801-15811.

[135] C. Mi, J. Zhang, H. Gao, X. Wu, M. Wang, Y. Wu, Y. Di, Z. Xu, C. Mao, S. Xu, Multifunctional nanocomposites of superparamagnetic (Fe3O4) and NIR-responsive rare earth-doped up-conversion fluorescent (NaYF4 : Yb,Er) nanoparticles and their applications in biolabeling and fluorescent imaging of cancer cells, Nanoscale, 2 (2010) 1141-1148.

[136] A.S. Hoffman, J.A. Hubbell, Chapter I.2.17 - Surface-Immobilized Biomolecules, Biomaterials Science (Third Edition), Academic Press2013, pp. 339-349.

[137] M.E. Aubin-Tam, K. Hamad-Schifferli, Structure and function of nanoparticle–protein conjugates, Biomedical Materials, 3 (2008) 034001.

[138] B. Teste, J. Vial, S. Descroix, T. Georgelin, J.M. Siaugue, J. Petr, A. Varenne, M.C. Hennion, A chemometric approach for optimizing protein covalent immobilization on magnetic core-shell nanoparticles in view of an alternative immunoassay, Talanta, 81 (2010) 1703-1710.

[139] S.L. Hirsh, M.M.M. Bilek, N.J. Nosworthy, A. Kondyurin, C.G. dos Remedios, D.R. McKenzie, A Comparison of Covalent Immobilization and Physical Adsorption of a Cellulase Enzyme Mixture, Langmuir, 26 (2010) 14380-14388.

[140] K.C. Dee, D.A. Puleo, R. Bizios, Protein-Surface Interactions, An Introduction To Tissue-Biomaterial Interactions, John Wiley & Sons, Inc.2003, pp. 37-52.

[141] D.R. Schmidt, H. Waldeck, W.J. Kao, Protein Adsorption to Biomaterials, in: D.A. Puleo, R. Bizios (Eds.) Biological Interactions on Materials Surfaces: Understanding and Controlling Protein, Cell, and Tissue Responses, Springer US, New York, NY, 2009, pp. 1-18.

[142] T.A. Horbett, J.L. Brash, Proteins at Interfaces: Current Issues and Future Prospects, Proteins at Interfaces, ACS, (1987), pp. 1-33.

[143] V. Puddu, C.C. Perry, Peptide Adsorption on Silica Nanoparticles: Evidence of Hydrophobic Interactions, ACS Nano, 6 (2012) 6356-6363.

[144] K.D. Jandt, Evolutions, Revolutions and Trends in Biomaterials Science – A Perspective, Adv. Eng. Mater., 9 (2007) 1035-1050.

[145] M. Rabe, D. Verdes, S. Seeger, Understanding protein adsorption phenomena at solid surfaces, Adv. Colloid Interface Sci., 162 (2011) 87-106.

[146] R. Marsell, T.A. Einhorn, The biology of fracture healing, Injury, 42 (2011) 551-555.

[147] L. Claes, S. Recknagel, A. Ignatius, Fracture healing under healthy and inflammatory conditions, Nat. Rev. Rheumatol., 8 (2012) 133-143.

[148] M.M. Martino, P.S. Briquez, K. Maruyama, J.A. Hubbell, Extracellular matrix-inspired growth factor delivery systems for bone regeneration, Adv. Drug. Del. Rev., 94 (2015) 41-52.

[149] H. Schell, G.N. Duda, A. Peters, S. Tsitsilonis, K.A. Johnson, K. Schmidt-Bleek, The haematoma and its role in bone healing, J. Exp. Orthop., 4 (2017) 5.

[150] Z.S. Al-Aql, A.S. Alagl, D.T. Graves, L.C. Gerstenfeld, T.A. Einhorn, Molecular Mechanisms Controlling Bone Formation during Fracture Healing and Distraction Osteogenesis, J. Dent. Res., 87 (2008) 107-118.

[151] P. Pelissier, F. Villars, S. Mathoulin-Pelissier, R. Bareille, M.H. Lafage-Proust, J. Vilamitjana-Amedee, Influences of vascularization and osteogenic cells on heterotopic bone formation within a madreporic ceramic in rats, Plast. Reconstr. Surg., 111 (2003) 1932-1941.

[152] F.W. Rhinelander, Tibial blood supply in relation to fracture healing, Clin. Orthop. Relat. Res., (1974) 34-81.

[153] L. Claes, K. Eckert-Hubner, P. Augat, The effect of mechanical stability on local vascularization and tissue differentiation in callus healing, J. Orthop. Res., 20 (2002) 1099-1105.

[154] L.C. Gerstenfeld, D.M. Cullinane, G.L. Barnes, D.T. Graves, T.A. Einhorn, Fracture healing as a post-natal developmental process: Molecular, spatial, and temporal aspects of its regulation, J. Cell. Biochem., 88 (2003) 873-884.

[155] A. Schindeler, M.M. McDonald, P. Bokko, D.G. Little, Bone remodeling during fracture repair: The cellular picture, Semin. Cell Dev. Biol., 19 (2008) 459-466.

[156] M.R. Newman, D.S.W. Benoit, Local and targeted drug delivery for bone regeneration, Curr. Opin. Biotechnol., 40 (2016) 125-132.

[157] A. Oryan, S. Alidadi, A. Moshiri, N. Maffulli, Bone regenerative medicine: classic options, novel strategies, and future directions, J. Orthop. Surg. Res., 9 (2014) 18.

[158] M. Orciani, M. Fini, R. Di Primio, M. Mattioli-Belmonte, Biofabrication and Bone Tissue Regeneration: Cell Source, Approaches, and Challenges, Front Bioeng. Biotechnol., 5 (2017) 17.

[159] P.V. Giannoudis, T.A. Einhorn, D. Marsh, Fracture healing: the diamond concept, Injury, 38 Suppl 4 (2007) S3-6.

[160] J.L. Brown, S.G. Kumbar, C.T. Laurencin, Chapter II.6.7 - Bone Tissue Engineering A2 - Ratner, Buddy D, in: A.S. Hoffman, F.J. Schoen, J.E. Lemons (Eds.) Biomaterials Science (Third Edition), Academic Press2013, pp. 1194-1214.

[161] P.M. Mountziaris, P.P. Spicer, F.K. Kasper, A.G. Mikos, Harnessing and modulating inflammation in strategies for bone regeneration, Tissue Eng. Part B Rev., 17 (2011) 393-402.

[162] D. Sarkar, W. Zhao, S. Schaefer, J.A. Ankrum, G.S.L. Teo, M.N. Pereira, L. Ferreira, J.M. Karp, Chapter II.6.2 - Overview of Tissue Engineering Concepts and Applications A2 - Ratner, Buddy D, in: A.S. Hoffman, F.J. Schoen, J.E. Lemons (Eds.) Biomaterials Science (Third Edition), Academic Press2013, pp. 1122-1137.

[163] S.F. Hulbert, F.A. Young, R.S. Mathews, J.J. Klawitter, C.D. Talbert, F.H. Stelling, Potential of ceramic materials as permanently implantable skeletal prostheses, J. Biomed. Mater. Res., 4 (1970) 433-456.

[164] Y. Kuboki, Q. Jin, H. Takita, Geometry of carriers controlling phenotypic expression in BMP-induced osteogenesis and chondrogenesis, J. Bone Joint Surg. Am., 83-A Suppl 1 (2001) S105-115.

[165] J.A. Jadlowiec, A.B. Celil, J.O. Hollinger, Bone tissue engineering: recent advances and promising therapeutic agents, Expert Opin. Biol. Ther., 3 (2003) 409-423.

[166] W. Friess, Collagen--biomaterial for drug delivery, Eur. J. Pharm. Biopharm., 45 (1998) 113-136.

[167] J. Glowacki, S. Mizuno, Collagen scaffolds for tissue engineering, Biopolymers, 89 (2008) 338-344.

[168] S. Govender, C. Csimma, H.K. Genant, A. Valentin-Opran, Y. Amit, R. Arbel, H. Aro, D. Atar, M. Bishay, M.G. Borner, P. Chiron, P. Choong, J. Cinats, B. Courtenay, R. Feibel, B. Geulette, C. Gravel, N. Haas, M. Raschke, E. Hammacher, D. van der Velde, P. Hardy, M. Holt, C. Josten, R.L. Ketterl, B. Lindeque, G. Lob, H. Mathevon, G. McCoy, D. Marsh, R. Miller, E. Munting, S. Oevre, L. Nordsletten, A. Patel, A. Pohl, W. Rennie, P. Reynders, P.M. Rommens, J. Rondia, W.C. Rossouw, P.J. Daneel, S. Ruff, A. Ruter, S. Santavirta, T.A. Schildhauer, C. Gekle, R. Schnettler, D. Segal, H. Seiler, R.B. Snowdowne, J. Stapert, G. Taglang, R. Verdonk, L. Vogels, A. Weckbach, A. Wentzensen, T. Wisniewski, Recombinant human bone morphogenetic protein-2 for treatment of open tibial fractures: a prospective, controlled, randomized study of four hundred and fifty patients, J. Bone Joint Surg. Am., 84-a (2002) 2123-2134.

[169] G.E. Friedlaender, C.R. Perry, J.D. Cole, S.D. Cook, G. Cierny, G.F. Muschler, G.A. Zych, J.H. Calhoun, A.J. LaForte, S. Yin, Osteogenic protein-1 (bone morphogenetic protein-7) in the treatment of tibial nonunions, J. Bone Joint Surg. Am., 83-A Suppl 1 (2001) S151-158.

[170] U.G.K. Wegst, H. Bai, E. Saiz, A.P. Tomsia, R.O. Ritchie, Bioinspired structural materials, Nat. Mater., 14 (2015) 23-36.

[171] A. Vats, N.S. Tolley, J.M. Polak, L.D. Buttery, Stem cells: sources and applications, Clin. Otolaryngol. Allied Sci., 27 (2002) 227-232.

[172] M. Owen, Marrow stromal stem cells, J. Cell Sci. Suppl., 10 (1988) 63-76.

[173] A.J. Friedenstein, S. Piatetzky, II, K.V. Petrakova, Osteogenesis in transplants of bone marrow cells, J. Embryol. Exp. Morphol., 16 (1966) 381-390.

[174] M.F. Pittenger, A.M. Mackay, S.C. Beck, R.K. Jaiswal, R. Douglas, J.D. Mosca, M.A. Moorman, D.W. Simonetti, S. Craig, D.R. Marshak, Multilineage Potential of Adult Human Mesenchymal Stem Cells, Science, 284 (1999) 143-147.

[175] P.A. Zuk, M. Zhu, H. Mizuno, J. Huang, J.W. Futrell, A.J. Katz, P. Benhaim, H.P. Lorenz, M.H. Hedrick, Multilineage cells from human adipose tissue: implications for cell-based therapies, Tissue Eng., 7 (2001) 211-228.

[176] N.J. Panetta, D.M. Gupta, J.K. Lee, D.C. Wan, G.W. Commons, M.T. Longaker, Human adipose-derived stromal cells respond to and elaborate bone morphogenetic protein-2 during in vitro osteogenic differentiation, Plast. Reconstr. Surg., 125 (2010) 483-493.

[177] B.E. Grottkau, Y. Lin, Osteogenesis of Adipose-Derived Stem Cells, 1 (2013) 133.

[178] S.-H. Park, A. Tofighi, X. Wang, M. Strunk, T. Ricketts, J. Chang, D.L. Kaplan, Calcium Phosphate Combination Biomaterials as Human Mesenchymal Stem Cell (hMSC) Delivery Vehicles for Bone Repair, J. Biomed. Mater. Res. Part B, Appl. Biomater., 97 (2011) 235-244.

[179] J. Kim, I.S. Kim, T.H. Cho, K.B. Lee, S.J. Hwang, G. Tae, I. Noh, S.H. Lee, Y. Park, K. Sun, Bone regeneration using hyaluronic acid-based hydrogel with bone morphogenic protein-2 and human mesenchymal stem cells, Biomaterials, 28 (2007) 1830-1837.

[180] A. Terella, P. Mariner, N. Brown, K. Anseth, S.-O. Streubel, Repair of a Calvarial Defect with Biofactor and Stem Cell Embedded Poly (ethylene glycol) Scaffold, Archives of facial plastic surgery : official publication for the American Academy of Facial Plastic and Reconstructive Surgery, Inc. and the International Federation of Facial Plastic Surgery Societies, 12 (2010) 166-171.

[181] S. Kumar, C. Wan, G. Ramaswamy, T.L. Clemens, S. Ponnazhagan, Mesenchymal stem cells expressing osteogenic and angiogenic factors synergistically enhance bone formation in a mouse model of segmental bone defect, Mol. Ther., 18 (2010) 1026-1034.

[182] H. Peng, V. Wright, A. Usas, B. Gearhart, H.C. Shen, J. Cummins, J. Huard, Synergistic enhancement of bone formation and healing by stem cell-expressed VEGF and bone morphogenetic protein-4, J. Clin. Invest., 110 (2002) 751-759.

[183] T.N. Vo, F.K. Kasper, A.G. Mikos, Strategies for controlled delivery of growth factors and cells for bone regeneration, Adv. Drug. Del. Rev., 64 (2012) 1292-1309.

[184] W.J. King, P.H. Krebsbach, Growth factor delivery: How surface interactions modulate release in vitro and in vivo, Adv. Drug. Del. Rev., 64 (2012) 1239-1256.

[185] K. Lee, E.A. Silva, D.J. Mooney, Growth factor delivery-based tissue engineering: general approaches and a review of recent developments, J. R. Soc. Interface, 8 (2011) 153-170.

[186] A. Weiler, S. Scheffler, M. Apreleva, Healing of Ligament and Tendon to Bone, in: W.R. Walsh (Ed.) Repair and Regeneration of Ligaments, Tendons, and Joint Capsule, Humana Press, Totowa, NJ, 2006, pp. 201-231.

[187] M. Benjamin, S. Qin, J.R. Ralphs, Fibrocartilage associated with human tendons and their pulleys, J. Anat., 187 (1995) 625-633.

[188] D.L.J. Bunker, V. Ilie, V. Ilie, S. Nicklin, Tendon to bone healing and its implications for surgery, Muscles, Ligaments Tendons J.l, 4 (2014) 343-350.

[189] M. O'Brien, Anatomy of Tendons, in: N. Maffulli, P. Renström, W.B. Leadbetter (Eds.) Tendon Injuries: Basic Science and Clinical Medicine, Springer London, London, 2005, pp. 3-13.

[190] http://www.synthasome.com/tendon-repair.php.

[191] F.R. Noyes, J.L. DeLucas, P.J. Torvik, Biomechanics of anterior cruciate ligament failure: an analysis of strain-rate sensitivity and mechanisms of failure in primates, J. Bone Joint Surg. Am., 56 (1974) 236-253.

[192] M.W.N. Wong, L. Qin, J.K.O. Tai, S.K.M. Lee, K.S. Leung, K.M. Chan, Engineered allogeneic chondrocyte pellet for reconstruction of fibrocartilage zone at bone–tendon junction—A preliminary histological observation, J. Biomed. Mater. Res. Part B: Appl. Biomater., 70B (2004) 362-367.

[193] G. Wei, Q. Jin, W.V. Giannobile, P.X. Ma, Nano-fibrous scaffold for controlled delivery of recombinant human PDGF-BB, J. Control. Release, 112 (2006) 103-110.

[194] J.E. Phillips, K.L. Burns, J.M. Le Doux, R.E. Guldberg, A.J. García, Engineering graded tissue interfaces, Proc. Natl. Acad. Sci., 105 (2008) 12170-12175.

[195] www.gradierte-implantate.de/fragestellung.

[196] M. Treiser, S. Abramson, R. Langer, J. Kohn, Chapter I.2.6 - Degradable and Resorbable Biomaterials A2 - Ratner, Buddy D, in: A.S. Hoffman, F.J. Schoen, J.E. Lemons (Eds.) Biomaterials Science (Third Edition), Academic Press2013, pp. 179-195.

[197] P.N. Bahareh Azimi, Mohamad Rabiee, Shahram Arbab, Poly (ε-caprolactone) Fiber: An Overview, J. Eng. Fiber. Fabr., 9 (2014) 74-90.

[198] H. Lee, H. Hwang, Y. Kim, H. Jeon, G. Kim, Physical and bioactive properties of multi-layered PCL/silica composite scaffolds for bone tissue regeneration, Chem. Eng. J., 250 (2014) 399-408.

[199] Q.P. Pham, U. Sharma, A.G. Mikos, Electrospun poly(epsilon-caprolactone) microfiber and multilayer nanofiber/microfiber scaffolds: characterization of scaffolds and measurement of cellular infiltration, Biomacromolecules, 7 (2006) 2796-2805.

[200] H. Zhang, S. Hollister, Comparison of bone marrow stromal cell behaviors on poly(caprolactone) with or without surface modification: studies on cell adhesion, survival and proliferation, J. Biomater. Sci. Polym. Ed., 20 (2009) 1975-1993.

[201] W.-J. Li, R. Tuli, X. Huang, P. Laquerriere, R.S. Tuan, Multilineage differentiation of human mesenchymal stem cells in a three-dimensional nanofibrous scaffold, Biomaterials, 26 (2005) 5158-5166.

[202] A.A. Sawyer, S.J. Song, E. Susanto, P. Chuan, C.X. Lam, M.A. Woodruff, D.W. Hutmacher, S.M. Cool, The stimulation of healing within a rat calvarial defect by mPCL-TCP/collagen scaffolds loaded with rhBMP-2, Biomaterials, 30 (2009) 2479-2488.

[203] J.H. Bae, H.R. Song, H.J. Kim, H.C. Lim, J.H. Park, Y. Liu, S.H. Teoh, Discontinuous release of bone morphogenetic protein-2 loaded within interconnected pores of honeycomb-like polycaprolactone scaffold promotes bone healing in a large bone defect of rabbit ulna, Tissue Eng. Part A, 17 (2011) 2389-2397.

[204] S.A. Abbah, C.X. Lam, A.K. Ramruttun, J.C. Goh, H.K. Wong, Fusion performance of low-dose recombinant human bone morphogenetic protein 2 and bone marrow-derived multipotent stromal cells in biodegradable scaffolds: a comparative study in a large animal model of anterior lumbar interbody fusion, Spine (Phila Pa 1976), 36 (2011) 1752-1759.

[205] M.R. Urist, Bone: formation by autoinduction, Science, 150 (1965) 893-899.

[206] M.R. Urist, B.S. Strates, Bone morphogenetic protein, J. Dent. Res., 50 (1971) 1392-1406.

[207] E.A. Wang, V. Rosen, P. Cordes, R.M. Hewick, M.J. Kriz, D.P. Luxenberg, B.S. Sibley, J.M. Wozney, Purification and characterization of other distinct bone-inducing factors, Proc. Natl. Acad. Sci. U. S. A., 85 (1988) 9484-9488.

[208] J.M. Wozney, V. Rosen, Bone morphogenetic protein and bone morphogenetic protein gene family in bone formation and repair, Clin. Orthop. Relat. Res., (1998) 26-37.

[209] H.H. Luu, W.-X. Song, X. Luo, D. Manning, J. Luo, Z.-L. Deng, K.A. Sharff, A.G. Montag, R.C. Haydon, T.-C. He, Distinct roles of bone morphogenetic proteins in osteogenic differentiation of mesenchymal stem cells, J. Orthop. Res., 25 (2007) 665-677.

[210] H. Yamagiwa, N. Endo, K. Tokunaga, T. Hayami, H. Hatano, H.E. Takahashi, In vivo bone-forming capacity of human bone marrow-derived stromal cells is stimulated by recombinant human bone morphogenetic protein-2, J. Bone Miner. Metab., 19 (2001) 20-28.

[211] S. Scarfi, Use of bone morphogenetic proteins in mesenchymal stem cell stimulation of cartilage and bone repair, World J. Stem Cells, 8 (2016) 1-12.

[212] K. Bessho, Y. Konishi, S. Kaihara, K. Fujimura, Y. Okubo, T. Iizuka, Bone induction by Escherichia coli -derived recombinant human bone morphogenetic protein-2 compared with Chinese hamster ovary cell-derived recombinant human bone morphogenetic protein-2, Br. J. Oral Maxillofac. Surg., 38 (2000) 645-649.

[213] N.R. Kubler, J.F. Reuther, G. Faller, T. Kirchner, R. Ruppert, W. Sebald, Inductive properties of recombinant human BMP-2 produced in a bacterial expression system, Int. J. Oral Maxillofac. Surg., 27 (1998) 305-309.

[214] M. Nakashima, A.H. Reddi, The application of bone morphogenetic proteins to dental tissue engineering, Nat. Biotechnol., 21 (2003) 1025-1032.

[215] H. Seeherman, J.M. Wozney, Delivery of bone morphogenetic proteins for orthopedic tissue regeneration, Cytokine Growth Factor Rev., 16 (2005) 329-345.

[216] K. Schmidt-Bleek, B.M. Willie, P. Schwabe, P. Seemann, G.N. Duda, BMPs in bone regeneration: Less is more effective, a paradigm-shift, Cytokine Growth Factor Rev., 27 (2016) 141-148.

[217] D.O. Wagner, C. Sieber, R. Bhushan, J.H. Börgermann, D. Graf, P. Knaus, BMPs: from bone to body morphogenetic proteins, 2010, pp. mr1.

[218] T.K. Sampath, J.E. Coughlin, R.M. Whetstone, D. Banach, C. Corbett, R.J. Ridge, E. Ozkaynak, H. Oppermann, D.C. Rueger, Bovine osteogenic protein is composed of dimers of OP-

1 and BMP-2A, two members of the transforming growth factor-beta superfamily, J. Biol. Chem., 265 (1990) 13198-13205.

[219] C. Scheufler, W. Sebald, M. Hulsmeyer, Crystal structure of human bone morphogenetic protein-2 at 2.7 A resolution, J. Mol. Biol., 287 (1999) 103-115.

[220] S. Daopin, K.A. Piez, Y. Ogawa, D.R. Davies, Crystal structure of transforming growth factor-beta 2: an unusual fold for the superfamily, Science, 257 (1992) 369-373.

[221] H. Uludag, D. D'Augusta, J. Golden, J. Li, G. Timony, R. Riedel, J.M. Wozney, Implantation of recombinant human bone morphogenetic proteins with biomaterial carriers: A correlation between protein pharmacokinetics and osteoinduction in the rat ectopic model, J. Biomed. Mater. Res., 50 (2000) 227-238.

[222] L.F. Vallejo, M. Brokelmann, S. Marten, S. Trappe, J. Cabrera-Crespo, A. Hoffmann, G. Gross, H.A. Weich, U. Rinas, Renaturation and purification of bone morphogenetic protein-2 produced as inclusion bodies in high-cell-density cultures of recombinant Escherichia coli, J. Biotechnol., 94 (2002) 185-194.

[223] J. Lee, E.N. Lee, J. Yoon, S.M. Chung, H. Prasad, C. Susin, U.M. Wikesjo, Comparative study of Chinese hamster ovary cell versus Escherichia coli-derived bone morphogenetic protein-2 using the critical-size supraalveolar peri-implant defect model, J. Periodontol., 84 (2013) 415-422.

[224] L.F. Vallejo, M. Brokelmann, S. Marten, S. Trappe, J. Cabrera-Crespo, A. Hoffmann, G. Gross, H.A. Weich, U. Rinas, Renaturation and purification of bone morphogenetic protein-2 produced as inclusion bodies in high-cell-density cultures of recombinant Escherichia coli, J. Biotechnol., 94 (2002) 185-194.

[225] Y. Shi, J. Massague, Mechanisms of TGF-beta signaling from cell membrane to the nucleus, Cell, 113 (2003) 685-700.

[226] C.H. Heldin, K. Miyazono, P. ten Dijke, TGF-beta signalling from cell membrane to nucleus through SMAD proteins, Nature, 390 (1997) 465-471.

[227] F. Liu, A. Hata, J.C. Baker, J. Doody, J. Carcamo, R.M. Harland, J. Massague, A human Mad protein acting as a BMP-regulated transcriptional activator, Nature, 381 (1996) 620-623.

[228] W. Balemans, W. Van Hul, Extracellular Regulation of BMP Signaling in Vertebrates: A Cocktail of Modulators, Dev. Biol., 250 (2002) 231-250.

[229] M. Okamoto, J. Murai, H. Yoshikawa, N. Tsumaki, Bone Morphogenetic Proteins in Bone Stimulate Osteoclasts and Osteoblasts During Bone Development, J. Bone Miner. Res., 21 (2006) 1022-1033.

[230] S. Piccolo, Y. Sasai, B. Lu, E.M. De Robertis, Dorsoventral Patterning in Xenopus: Inhibition of Ventral Signals by Direct Binding of Chordin to BMP-4, Cell, 86 (1996) 589-598.

[231] F. Itoh, H. Asao, K. Sugamura, C.-H. Heldin, P. ten Dijke, S. Itoh, Promoting bone morphogenetic protein signaling through negative regulation of inhibitory Smads, The EMBO Journal, 20 (2001) 4132-4142.

[232] D. Onichtchouk, Y.-G. Chen, R. Dosch, V. Gawantka, H. Delius, J. Massague, C. Niehrs, Silencing of TGF-[beta] signalling by the pseudoreceptor BAMBI, Nature, 401 (1999) 480-485.

[233] C. Sieber, J. Kopf, C. Hiepen, P. Knaus, Recent advances in BMP receptor signaling, Cytokine Growth Factor Rev., 20 (2009) 343-355.

[234] J.E. Aubin, Advances in the osteoblast lineage, Biochem. Cell Biol., 76 (1998) 899-910.

[235] I.S. Kim, Y.M. Song, T.H. Cho, Y.D. Park, K.B. Lee, I. Noh, F. Weber, S.J. Hwang, In vitro response of primary human bone marrow stromal cells to recombinant human bone morphogenic protein-2 in the early and late stages of osteoblast differentiation, Dev. Growth Differ., 50 (2008) 553-564.

[236] J.D. Lamplot, J. Qin, G. Nan, J. Wang, X. Liu, L. Yin, J. Tomal, R. Li, W. Shui, H. Zhang, S.H. Kim, W. Zhang, J. Zhang, Y. Kong, S. Denduluri, M.R. Rogers, A. Pratt, R.C. Haydon, H.H. Luu, J. Angeles, L.L. Shi, T.-C. He, BMP9 signaling in stem cell differentiation and osteogenesis, Am. J. Stem Cells, 2 (2013) 1-21.

[237] K.W.H. Lo, B.D. Ulery, K.M. Ashe, C.T. Laurencin, Studies of bone morphogenetic protein-based surgical repair, Adv. Drug. Del. Rev., 64 (2012) 1277-1291.

[238] A.C. Carreira, F.H. Lojudice, E. Halcsik, R.D. Navarro, M.C. Sogayar, J.M. Granjeiro, Bone Morphogenetic Proteins, J. Dent. Res., 93 (2014) 335-345.

[239] V. Agrawal, M. Sinha, A review on carrier systems for bone morphogenetic protein-2, J. Biomed. Mater. Res. Part B Appl. Biomater., (2016) n/a-n/a.

[240] H. Begam, S.K. Nandi, B. Kundu, A. Chanda, Strategies for delivering bone morphogenetic protein for bone healing, Mater. Sci. Eng. C, 70, Part 1 (2017) 856-869.

[241] E. Gruskin, B.A. Doll, F.W. Futrell, J.P. Schmitz, J.O. Hollinger, Demineralized bone matrix in bone repair: History and use, Adv. Drug. Del. Rev., 64 (2012) 1063-1077.

[242] A. El-Ghannam, Bone reconstruction: from bioceramics to tissue engineering, Expert Rev. Med. Devices, 2 (2005) 87-101.

[243] C.B. Kong, J.H. Lee, H.R. Baek, C.K. Lee, B.S. Chang, Posterolateral lumbar fusion using Escherichia coli-derived rhBMP-2/hydroxyapatite in the mini pig, Spine J, 14 (2014) 2959-2967.

[244] M.H. Pelletier, R.A. Oliver, C. Christou, Y. Yu, N. Bertollo, H. Irie, W.R. Walsh, Lumbar spinal fusion with beta-TCP granules and variable Escherichia coli-derived rhBMP-2 dose, Spine J., 14 (2014) 1758-1768.

[245] S.D. Boden, G.J. Martin, Jr., M.A. Morone, J.L. Ugbo, P.A. Moskovitz, Posterolateral lumbar intertransverse process spine arthrodesis with recombinant human bone morphogenetic protein 2/hydroxyapatite-tricalcium phosphate after laminectomy in the nonhuman primate, Spine (Phila Pa 1976), 24 (1999) 1179-1185.

[246] B.P. Hecht, J.S. Fischgrund, H.N. Herkowitz, L. Penman, J.M. Toth, A. Shirkhoda, The use of recombinant human bone morphogenetic protein 2 (rhBMP-2) to promote spinal fusion in a nonhuman primate anterior interbody fusion model, Spine (Phila Pa 1976), 24 (1999) 629-636.

[247] M. Yamamoto, Y. Takahashi, Y. Tabata, Enhanced bone regeneration at a segmental bone defect by controlled release of bone morphogenetic protein-2 from a biodegradable hydrogel, Tissue Eng., 12 (2006) 1305-1311.

[248] D.R. Hunt, S.A. Jovanovic, U.M. Wikesjo, J.M. Wozney, G.W. Bernard, Hyaluronan supports recombinant human bone morphogenetic protein-2 induced bone reconstruction of advanced alveolar ridge defects in dogs. A pilot study, J. Periodontol., 72 (2001) 651-658.

[249] Y.M. Kolambkar, K.M. Dupont, J.D. Boerckel, N. Huebsch, D.J. Mooney, D.W. Hutmacher, R.E. Guldberg, An Alginate-based Hybrid System for Growth Factor Delivery in the Functional Repair of Large Bone Defects, Biomaterials, 32 (2011) 65-74.

[250] S.J. Stephan, S.S. Tholpady, B. Gross, C.E. Petrie-Aronin, E.A. Botchway, L.S. Nair, R.C. Ogle, S.S. Park, Injectable tissue-engineered bone repair of a rat calvarial defect, Laryngoscope, 120 (2010) 895-901.

[251] W. Zhang, X. Wang, S. Wang, J. Zhao, L. Xu, C. Zhu, D. Zeng, J. Chen, Z. Zhang, D.L. Kaplan, X. Jiang, The use of injectable sonication-induced silk hydrogel for VEGF(165) and BMP-2 delivery for elevation of the maxillary sinus floor, Biomaterials, 32 (2011) 9415-9424.

[252] Y.I. Chung, K.M. Ahn, S.H. Jeon, S.Y. Lee, J.H. Lee, G. Tae, Enhanced bone regeneration with BMP-2 loaded functional nanoparticle-hydrogel complex, J. Control. Release, 121 (2007) 91-99.

[253] J. Takahashi, N. Saito, S. Ebara, T. Kinoshita, H. Itoh, T. Okada, K. Nozaki, K. Takaoka, Anterior thoracic spinal fusion in dogs by injection of recombinant human bone morphogenetic protein-2 and a synthetic polymer, J. Spinal Disord. Tech., 16 (2003) 137-143.

[254] F.E. Weber, G. Eyrich, K.W. Gratz, F.E. Maly, H.F. Sailer, Slow and continuous application of human recombinant bone morphogenetic protein via biodegradable poly(lactide-co-glycolide) foamspheres, Int. J. Oral Maxillofac. Surg., 31 (2002) 60-65.

[255] T. Akamaru, D. Suh, S.D. Boden, H.S. Kim, A. Minamide, J. Louis-Ugbo, Simple carrier matrix modifications can enhance delivery of recombinant human bone morphogenetic protein-2 for posterolateral spine fusion, Spine (Phila Pa 1976), 28 (2003) 429-434.

[256] K.A. Hussein, I.E. Zakhary, D. Hailat, R. Elrefai, M. Sharawy, M.E. Elsalanty, Delayed versus immediate reconstruction of mandibular segmental defects using recombinant human bone morphogenetic protein 2/absorbable collagen sponge, J. Oral Maxillofac. Surg., 71 (2013) 1107-1118.

[257] E.J. Carragee, E.L. Hurwitz, B.K. Weiner, A critical review of recombinant human bone morphogenetic protein-2 trials in spinal surgery: emerging safety concerns and lessons learned, Spine J., 11 (2011) 471-491.

[258] A.W. Ritting, E.W. Weber, M.C. Lee, Exaggerated inflammatory response and bony resorption from BMP-2 use in a pediatric forearm nonunion, J. Hand Surg. Am., 37 (2012) 316-321.

[259] K.S. Cahill, J.H. Chi, A. Day, E.B. Claus, Prevalence, complications, and hospital charges associated with use of bone-morphogenetic proteins in spinal fusion procedures, JAMA, 302 (2009) 58-66.

[260] E.J. Woo, Adverse events after recombinant human BMP2 in nonspinal orthopaedic procedures, Clin. Orthop. Relat. Res., 471 (2013) 1707-1711.

[261] J.G. DeVine, J.R. Dettori, J.C. France, E. Brodt, R.A. McGuire, The use of rhBMP in spine surgery: is there a cancer risk?, © AOSpine International, Stettbachstrasse 6 8600 Dübendorf, Switzerland, 2012.

[262] J.M. Wozney, V. Rosen, A.J. Celeste, L.M. Mitsock, M.J. Whitters, R.W. Kriz, R.M. Hewick, E.A. Wang, Novel regulators of bone formation: molecular clones and activities, Science, 242 (1988) 1528-1534.

[263] D. Logeart-Avramoglou, M. Bourguignon, K. Oudina, P. Ten Dijke, H. Petite, An assay for the determination of biologically active bone morphogenetic proteins using cells transfected with an inhibitor of differentiation promoter-luciferase construct, Anal. Biochem., 349 (2006) 78-86.

[264] X.S. Zhao, G.Q. Lu, Modification of MCM-41 by Surface Silylation with Trimethylchlorosilane and Adsorption Study, J. Phys. Chem. B, 102 (1998) 1556-1561.

[265] Q.L. Loh, C. Choong, Three-Dimensional Scaffolds for Tissue Engineering Applications: Role of Porosity and Pore Size, Tissue Eng. Part B, Rev., 19 (2013) 485-502.

[266] B. Ahn, J. Park, K. Singha, H. Park, W.J. Kim, Mesoporous silica nanoparticle-based cisplatin prodrug delivery and anticancer effect under reductive cellular environment, J. Mater. Chem. B, 1 (2013) 2829-2836.

[267] J. Lu, M. Liong, J.I. Zink, F. Tamanoi, Mesoporous silica nanoparticles as a delivery system for hydrophobic anticancer drugs, Small, 3 (2007) 1341-1346.

[268] B. Ruhle, P. Saint-Cricq, J.I. Zink, Externally Controlled Nanomachines on Mesoporous Silica Nanoparticles for Biomedical Applications, Chemphyschem, 17 (2016) 1769-1779.

[269] A.V. Krasnoslobodtsev, S.N. Smirnov, Effect of Water on Silanization of Silica by Trimethoxysilanes, Langmuir, 18 (2002) 3181-3184.

[270] A.A. Golub, A.I. Zubenko, B.V. Zhmud, gamma-APTES modified silica gels: The structure of the surface layer, J. Colloid Interface Sci., 179 (1996) 482-487.

[271] K.C. Vrancken, P. Van Der Voort, I. Gillis-D'Hamers, E.F. Vansant, P. Grobet, Influence of water in the reaction of [gamma]-aminopropyltriethoxysilane with silica gel. A Fourier-transform infrared and cross-polarisation magic-angle-spinning nuclear magnetic resonance study, J. Chem. Soc., Faraday Trans., 88 (1992) 3197-3200.

[272] B.V. Zhmud, A.A. Golub, Thermodynamic and kinetic study on protolytic reactions at the surface of porous matrices, Colloid. Surf. A Physicochem. Eng. Asp., 105 (1995) 173-180.

[273] E.A. Smith, W. Chen, Langmuir, 24 (2008) 12405.

[274] M. Zhu, M.Z. Lerum, W. Chen, How To Prepare Reproducible, Homogeneous, and Hydrolytically Stable Aminosilane-Derived Layers on Silica, Langmuir, 28 (2012) 416-423.

[275] F. Cuoq, A. Masion, J. Labille, J. Rose, F. Ziarelli, B. Prelot, J.-Y. Bottero, Preparation of amino-functionalized silica in aqueous conditions, Appl. Surf. Sci., 266 (2013) 155-160.

[276] Y. An, M. Chen, Q. Xue, W. Liu, Preparation and self-assembly of carboxylic acid-functionalized silica, J. Colloid Interface Sci., 311 (2007) 507-513.

[277] Q. Yang, S. Wang, P. Fan, L. Wang, Y. Di, K. Lin, F.-S. Xiao, pH-Responsive Carrier System Based on Carboxylic Acid Modified Mesoporous Silica and Polyelectrolyte for Drug Delivery, Chem. Mater., 17 (2005) 5999-6003.

[278] K.S.W. Sing, D.H. Everett, R.A.W. Haul, L. Moscou, R.A. Pierotti, J. Rouquerol, T. Siemieniewska, Reporting Physisorption Data for Gas Solid Systems with Special Reference to the Determination of Surface-Area and Porosity (Recommendations 1984), Pure Appl. Chem., 57 (1985) 603-619.

[279] I. Izquierdo-Barba, M. Colilla, M. Manzano, M. Vallet-Regí, In vitro stability of SBA-15 under physiological conditions, Microporous Mesoporous Mater., 132 (2010) 442-452.

[280] C.J. Brinker, G.W. Scherer, Sol-gel science: the physica and chemistry of sol-gel processing Academic Press Inc. 1990.

[281] D. Lin-Vien, N.B. Colthup, W.G. Fateley, J.G. Grasselli, CHAPTER 6 - Alkenes, The Handbook of Infrared and Raman Characteristic Frequencies of Organic Molecules, Academic Press, San Diego, 1991, pp. 73-94.

[282] D. Lin-Vien, N.B. Colthup, W.G. Fateley, J.G. Grasselli, CHAPTER 10 - Compounds Containing –NH2, –NHR, and –NR2 Groups, The Handbook of Infrared and Raman Characteristic Frequencies of Organic Molecules, Academic Press, San Diego, 1991, pp. 155-178.

[283] M. Colilla, I. Izquierdo-Barba, S. Sánchez-Salcedo, J.L.G. Fierro, J.L. Hueso, M. Vallet-Regí, Synthesis and Characterization of Zwitterionic SBA-15 Nanostructured Materials, Chem. Mater., 22 (2010) 6459-6466.

[284] D. Lin-Vien, N.B. Colthup, W.G. Fateley, J.G. Grasselli, CHAPTER 14 - Organic Sulfur Compounds, The Handbook of Infrared and Raman Characteristic Frequencies of Organic Molecules, Academic Press, San Diego, 1991, pp. 225-250.

[285] B.H. Stuart, Organic Molecules, Infrared Spectroscopy: Fundamentals and Applications, John Wiley & Sons, Ltd2005, pp. 71-93.

[286] D.I. Israel, J. Nove, K.M. Kerns, I.K. Moutsatsos, R.J. Kaufman, Expression and characterization of bone morphogenetic protein-2 in Chinese hamster ovary cells, Growth Factors, 7 (1992) 139-150.

[287] Z. Li, W. Kessler, J. van den Heuvel, U. Rinas, Simple defined autoinduction medium for high-level recombinant protein production using T7-based Escherichia coli expression systems, Appl. Microbiol. Biotechnol., 91 (2011) 1203.

[288] L. Luca, M.A.H. Capelle, G. Machaidze, T. Arvinte, O. Jordan, R. Gurny, Physical instability, aggregation and conformational changes of recombinant human bone morphogenetic protein-2 (rhBMP-2), Int. J. Pharm., 391 (2010) 48-54.

[289] D. Schwartz, S. Sofia, W. Friess, Integrity and stability studies of precipitated rhBMP-2 microparticles with a focus on ATR-FTIR measurements, Eur. J. Pharm. Biopharm., 63 (2006) 241-248.

[290] M. Kisiel, M. Ventura, O.P. Oommen, A. George, X.F. Walboomers, J. Hilborn, O.P. Varghese, Critical assessment of rhBMP-2 mediated bone induction: An in vitro and in vivo evaluation, J. Control. Release, 162 (2012) 646-653.

[291] M. Cicerone, J. Giri, Z.e. Shaked, C. Roberts, Protein stability — An underappreciated but critical need for drug delivery systems, Adv. Drug. Del. Rev., 93 (2015) 1.

[292] T. Toida, H. Yoshida, H. Toyoda, I. Koshiishi, T. Imanari, R.E. Hileman, J.R. Fromm, R.J. Linhardt, Structural differences and the presence of unsubstituted amino groups in heparan sulphates from different tissues and species, Biochem. J, 322 (1997) 499-506.

[293] R. Ruppert, E. Hoffmann, W. Sebald, Human Bone Morphogenetic Protein 2 Contains a Heparin-Binding Site which Modifies Its Biological Activity, Eur. J. Biochem., 237 (1996) 295-302.

[294] B. Li, T. Yoshii, A.E. Hafeman, J.S. Nyman, J.C. Wenke, S.A. Guelcher, The effects of rhBMP-2 released from biodegradable polyurethane/microsphere composite scaffolds on new bone formation in rat femora, Biomaterials, 30 (2009) 6768-6779.

[295] K.V. Brown, B. Li, T. Guda, D.S. Perrien, S.A. Guelcher, J.C. Wenke, Improving bone formation in a rat femur segmental defect by controlling bone morphogenetic protein-2 release, Tissue Eng. Part A, 17 (2011) 1735-1746.

[296] F.C.J. van de Watering, J.J.J.P. van den Beucken, S.P. van der Woning, A. Briest, A. Eek, H. Qureshi, L. Winnubst, O.C. Boerman, J.A. Jansen, Non-glycosylated BMP-2 can induce ectopic bone formation at lower concentrations compared to glycosylated BMP-2, J. Control. Release, 159 (2012) 69-77.

[297] E. Quinlan, E.M. Thompson, A. Matsiko, F.J. O'Brien, A. López-Noriega, Long-term controlled delivery of rhBMP-2 from collagen-hydroxyapatite scaffolds for superior bone tissue regeneration, J. Control. Release, 207 (2015) 112-119.

[298] B.-B. Seo, H. Choi, J.-T. Koh, S.-C. Song, Sustained BMP-2 delivery and injectable bone regeneration using thermosensitive polymeric nanoparticle hydrogel bearing dual interactions with BMP-2, J. Control. Release, 209 (2015) 67-76.

[299] E.A. Wang, D.I. Israel, S. Kelly, D.P. Luxenberg, Bone Morphogenetic Protein-2 Causes Commitment and Differentiation in C3HI0T1/2 and 3T3 Cells, Growth Factors, 9 (1993) 57-71.

[300] D.J. Rickard, T.A. Sullivan, B.J. Shenker, P.S. Leboy, I. Kazhdan, Induction of Rapid Osteoblast Differentiation in Rat Bone Marrow Stromal Cell Cultures by Dexamethasone and BMP-2, Dev. Biol., 161 (1994) 218-228.

[301] V. Karageorgiou, L. Meinel, S. Hofmann, A. Malhotra, V. Volloch, D. Kaplan, Bone morphogenetic protein-2 decorated silk fibroin films induce osteogenic differentiation of human bone marrow stromal cells, J. Biomed. Mater. Res. Part A, 71A (2004) 528-537.

[302] D.A. Puleo, Dependence of mesenchymal cell responses on duration of exposure to bone morphogenetic protein-2 in vitro, J. Cell. Physiol., 173 (1997) 93-101.

[303] T. Katagiri, M. Imada, T. Yanai, T. Suda, N. Takahashi, R. Kamijo, Identification of a BMP-responsive element in Id1, the gene for inhibition of myogenesis, Genes Cells, 7 (2002) 949-960.

[304] A. Hollnagel, V. Oehlmann, J. Heymer, U. Ruther, A. Nordheim, Id genes are direct targets of bone morphogenetic protein induction in embryonic stem cells, J. Biol. Chem., 274 (1999) 19838-19845.

[305] T. Mosmann, Rapid colorimetric assay for cellular growth and survival: Application to proliferation and cytotoxicity assays, J. Immunol. Methods, 65 (1983) 55-63.

[306] D.E.I. 10993:5-2009, Biological evaluation of medical devices - Part 5: Tests for in vitro cytotoxicity, 2009.

[307] T.L. Riss, R.A. Moravec, A.L. Niles, S. Duellman, H.A. Benink, T.J. Worzella, L. Minor, Cell Viability Assays, in: G.S. Sittampalam, N.P. Coussens, K. Brimacombe, A. Grossman, M. Arkin, D. Auld, C. Austin, J. Baell, B. Bejcek, T.D.Y. Chung, J.L. Dahlin, V. Devanaryan, T.L. Foley, M. Glicksman, M.D. Hall, J.V. Hass, J. Inglese, P.W. Iversen, S.D. Kahl, S.C. Kales, M. Lal-Nag, Z. Li, J. McGee, O. McManus, T. Riss, O.J. Trask, Jr., J.R. Weidner, M. Xia, X. Xu (Eds.) Assay Guidance Manual, Bethesda (MD), 2004.

[308] A.J. Di Pasqua, K.K. Sharma, Y.-L. Shi, B.B. Toms, W. Ouellette, J.C. Dabrowiak, T. Asefa, Cytotoxicity of mesoporous silica nanomaterials, J. Inorg. Biochem., 102 (2008) 1416-1423.

[309] B. Chang, J. Guo, C. Liu, J. Qian, W. Yang, Surface functionalization of magnetic mesoporous silica nanoparticles for controlled drug release, J. Mater. Chem., 20 (2010) 9941-9947.

[310] T. Asefa, Z. Tao, Biocompatibility of mesoporous silica nanoparticles, Chem. Res. Toxicol., 25 (2012) 2265-2284.

[311] J.S. Chang, K.L. Chang, D.F. Hwang, Z.L. Kong, In vitro cytotoxicitiy of silica nanoparticles at high concentrations strongly depends on the metabolic activity type of the cell line, Environ. Sci. Technol., 41 (2007) 2064-2068.

[312] B. Fadeel, A.E. Garcia-Bennett, Better safe than sorry: Understanding the toxicological properties of inorganic nanoparticles manufactured for biomedical applications, Adv. Drug. Deliv. Rev., 62 (2010) 362-374.

[313] M. Shi, Y. Zhou, J. Shao, Z. Chen, B. Song, J. Chang, C. Wu, Y. Xiao, Stimulation of osteogenesis and angiogenesis of hBMSCs by delivering Si ions and functional drug from mesoporous silica nanospheres, Acta Biomater., 21 (2015) 178-189.

[314] E. García-Gareta, M.J. Coathup, G.W. Blunn, Osteoinduction of bone grafting materials for bone repair and regeneration, Bone, 81 (2015) 112-121.

[315] W. Cui, Y. Zhou, J. Chang, Electrospun nanofibrous materials for tissue engineering and drug delivery, Sci. Tech. Adv. Mater., 11 (2010) 014108.

[316] B. Rai, S.H. Teoh, D.W. Hutmacher, T. Cao, K.H. Ho, Novel PCL-based honeycomb scaffolds as drug delivery systems for rhBMP-2, Biomaterials, 26 (2005) 3739-3748.

[317] M. Tallawi, E. Rosellini, N. Barbani, M.G. Cascone, R. Rai, G. Saint-Pierre, A.R. Boccaccini, Strategies for the chemical and biological functionalization of scaffolds for cardiac tissue engineering: a review, J. R. Soc. Interface, 12 (2015) 20150254.

[318] H. Yuan, K. Kurashina, J.D. de Bruijn, Y. Li, K. de Groot, X. Zhang, A preliminary study on osteoinduction of two kinds of calcium phosphate ceramics, Biomaterials, 20 (1999) 1799-1806.

[319] V. Karageorgiou, D. Kaplan, Porosity of 3D biomaterial scaffolds and osteogenesis, Biomaterials, 26 (2005) 5474-5491.

[320] M.M. Coleman, J. Zarian, Fourier-transform infrared studies of polymer blends. II. Poly(ϵ-caprolactone)–poly(vinyl chloride) system, J. Polym. Sci. Polym. Phys. Ed., 17 (1979) 837-850.

[321] C.G. van Hoogmoed, H.J. Busscher, P. de Vos, Fourier transform infrared spectroscopy studies of alginate–PLL capsules with varying compositions, J. Biomed. Mater. Res. Part A, 67A (2003) 172-178.

[322] Z. Li, H.R. Ramay, K.D. Hauch, D. Xiao, M. Zhang, Chitosan–alginate hybrid scaffolds for bone tissue engineering, Biomaterials, 26 (2005) 3919-3928.

[323] P. Innocenzi, Infrared spectroscopy of sol–gel derived silica-based films: a spectra-microstructure overview, J. Non-Cryst. Solids, 316 (2003) 309-319.

[324] O. Persenaire, M. Alexandre, P. Degée, P. Dubois, Mechanisms and Kinetics of Thermal Degradation of Poly(ε-caprolactone), Biomacromolecules, 2 (2001) 288-294.

[325] S.-H. Rhee, J.-Y. Choi, H.-M. Kim, Preparation of a bioactive and degradable poly(ε-caprolactone)/silica hybrid through a sol–gel method, Biomaterials, 23 (2002) 4915-4921.

[326] M. Knippenberg, M.N. Helder, B. Zandieh Doulabi, P.I.J.M. Wuisman, J. Klein-Nulend, Osteogenesis versus chondrogenesis by BMP-2 and BMP-7 in adipose stem cells, Biochem. Biophys. Res. Commun., 342 (2006) 902-908.

[327] I. Song, B.-S. Kim, C.-S. Kim, G.-I. Im, Effects of BMP-2 and vitamin D3 on the osteogenic differentiation of adipose stem cells, Biochem. Biophys. Res. Commun., 408 (2011) 126-131.

[328] A. Satalov, Composites made of polymers, silica nanoparticles and bioactive molecules for biomedical applications Leibniz Universität Hannover2013.

[329] T.E. Finn, A.C. Nunez, M. Sunde, S.B. Easterbrook-Smith, Serum Albumin Prevents Protein Aggregation and Amyloid Formation and Retains Chaperone-like Activity in the Presence of Physiological Ligands, J. Biol. Chem., 287 (2012) 21530-21540.

[330] H. Uludag, D. D'Augusta, R. Palmer, G. Timony, J. Wozney, Characterization of rhBMP-2 pharmacokinetics implanted with biomaterial carriers in the rat ectopic model, J. Biomed. Mater. Res., 46 (1999) 193-202.

[331] X. Huang, C.S. Brazel, On the importance and mechanisms of burst release in matrix-controlled drug delivery systems, J. Control. Release, 73 (2001) 121-136.

[332] J. Massague, Transforming growth factor-alpha. A model for membrane-anchored growth factors, J. Biol. Chem., 265 (1990) 21393-21396.

[333] H.W. Liu, C.H. Chen, C.L. Tsai, G.H. Hsiue, Targeted delivery system for juxtacrine signaling growth factor based on rhBMP-2-mediated carrier-protein conjugation, Bone, 39 (2006) 825-836.

[334] N.A. Gharibjanian, W.C. Chua, S. Dhar, T. Scholz, T.Y. Shibuya, G.R. Evans, J.W. Calvert, Release kinetics of polymer-bound bone morphogenetic protein-2 and its effects on the osteogenic expression of MC3T3-E1 osteoprecursor cells, Plast. Reconstr. Surg., 123 (2009) 1169-1177.

[335] Y.J. Park, K.H. Kim, J.Y. Lee, Y. Ku, S.J. Lee, B.M. Min, C.P. Chung, Immobilization of bone morphogenetic protein-2 on a nanofibrous chitosan membrane for enhanced guided bone regeneration, Biotechnol. Appl. Biochem., 43 (2006) 17-24.

[336] J.E. Samorezov, E.B. Headley, C.R. Everett, E. Alsberg, Sustained presentation of BMP-2 enhances osteogenic differentiation of human adipose-derived stem cells in gelatin hydrogels, J. Biomed. Mater. Res. Part A, 104 (2016) 1387-1397.

[337] J.C. Rivera, C.A. Strohbach, J.C. Wenke, C.R. Rathbone, Beyond osteogenesis: an in vitro comparison of the potentials of six bone morphogenetic proteins, Front. Pharmacol., 4 (2013) 125.

[338] B.J. Lawrence, S.V. Madihally, Cell colonization in degradable 3D porous matrices, Cell Adh. Migr., 2 (2008) 9-16.

[339] B.A. Bunnell, M. Flaat, C. Gagliardi, B. Patel, C. Ripoll, Adipose-derived stem cells: Isolation, expansion and differentiation, Methods, 45 (2008) 115-120.

[340] L. Li, G. Zhou, Y. Wang, G. Yang, S. Ding, S. Zhou, Controlled dual delivery of BMP-2 and dexamethasone by nanoparticle-embedded electrospun nanofibers for the efficient repair of critical-sized rat calvarial defect, Biomaterials, 37 (2015) 218-229.

[341] N.J. London, A. Chiang, J.A. Haller, The dexamethasone drug delivery system: indications and evidence, Adv. Ther., 28 (2011) 351-366.

[342] C.H. Suelter, M. DeLuca, How to prevent losses of protein by adsorption to glass and plastic, Anal. Biochem., 135 (1983) 112-119.

[343] M. Goebel-Stengel, A. Stengel, Y. Tache, J.R. Reeve, Jr., The importance of using the optimal plasticware and glassware in studies involving peptides, Anal. Biochem., 414 (2011) 38-46.

[344] S. De Carlo, J.R. Harris, Negative staining and cryo-negative staining of macromolecules and viruses for TEM, Micron, 42 (2011) 117-131.

[345] J.R. Harris, Negative staining of thinly spread biological samples, Methods Mol. Biol., 369 (2007) 107-142.

7   Supporting information

Table S1: Summary of the weight loss of the aminopropylsilyl-modified nanoporous silica nanoparticles before and after water exposure obtained from thermogravimetric analyses.

Temperature range / °C	Weight loss with and without solvent / %				Components
	NPSNP-propyl-NH$_2$		NPSNP-propyl-NH$_2$ after immersion		
25 – 120	4	**-**	7	**-**	Solvent
120 – 800	13	**14**	10	**12**	Organic groups
Residues	83	**86**	83	**88**	Silica

Table S2: Summary of the weight loss of the carboxy-modified nanoporous silica nanoparticles before and after water exposure obtained from thermogravimetric analyses.

Temperature range / °C	Weight loss with and without solvent / %				Components
	NPSNP-COOH		NPSNP-COOH derived from immersed NPSNP-propyl-NH$_2$		
25 – 120	2	**-**	3	**-**	Solvent
120 – 250	4	**-**	5	**-**	DMF
250 – 750	16	**17**	13	**14**	Organic groups
Residues	78	**83**	79	**86**	Silica

Table S3: Characterization of the porosity of non-modified and surface-modified nanoporous silica nanoparticles.

Samples	Specific surface area S_{BET} (m² g⁻¹) (a)	Average pore width d_{Pore} (nm) (b)	Total pore volume V_{total} (cm³ g⁻¹) (c)
NPSNP-OH	1000	3.2	0.83
NPSNP-propyl-NH₂	442	3.2	0.45
NPSNP-COOH	570	2.6	0.55
NPSNP-propyl-NH₂ after immersion	160	3.2	0.21
NPSNP-COOH derived from immersed NPSNP-propyl-NH₂	233	3.2	0.27
Immersed NPSNP-propyl-NH₂ stirred in DMF, 12h, 25 °C	229	3.2	0.28
Immersed NPSNP-propyl-NH₂ stirred in DMF, 1h, 155 °C	248	3.2	0.29

(a) Determined by BET analysis of the nitrogen sorption isotherms ($0.05 \leq p/p^0 \leq 0.30$).
(b) Calculated via DFT analysis of the nitrogen adsorption isotherm ($p/p^0 \leq 0.90$).

Table S4: Summary of the weight loss of the aminopropylsilyl-modified nanoporous silica nanoparticles after water exposure stirred in DMF for 12 h at 25°C and for 1 h at 155 °C obtained from thermogravimetric analyses.

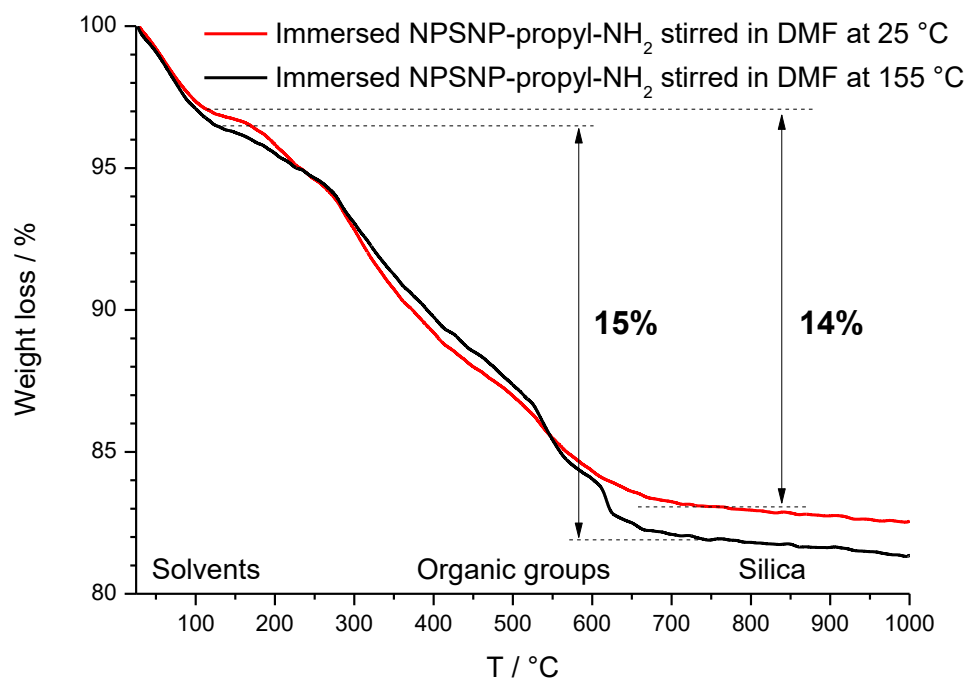| Temperature range / °C	Weight loss with and without solvent / %				Components
	Immersed NPSNP-propyl-NH₂ stirred in DMF, 1h, 155 °C		Immersed NPSNPs-propyl-NH₂ stirred in DMF, 12h, rt		
25 – 120	3	-	4	-	Solvent
120 – 250	2	-	1	-	DMF
250 – 750	12	**13**	13	**14**	Organic groups
Residues	83	**87**	82	**86**	Silica

Figure S 1: Thermogravimetric analysis curves for aminopropylsilyl-modified nanoporous silica nanoparticles after water exposure stirred in DMF for 1 h at 155 °C and for 12 h at 25 °C.

Table S 4: Summary of the weight loss of the NPSNP-OH, -propyl-NH₂ and -propyl-SH obtained from thermogravimetric analyses.

| Temperature range / °C	Weight loss with and without solvent / %			Decomposition
	NPSNP-OH	NPSNP-propyl-NH$_2$	NPSNP-propyl-SH	
25−120 °C	1	4	2	Solvents
120−700 °C	–	14	18	Organic groups
700−1000 °C	1	–	–	Dehydroxylation
–	98	83	80	Residues

Table S 5: Summary of the weight loss of NPSNP-propyl-SO$_3$H, -methyl-NH-hexyl-NH$_2$- and -propyl-NH-hexyl-NH$_2$ obtained from thermogravimetric analyses.

Temperature range / °C	Weight loss with and without solvent / %			Decomposition
	NPSNP-propyl-SO$_3$H	NPSNP-methyl-NH-hexyl-NH$_2$	NPSNP-propyl-NH-hexyl-NH$_2$	
25−200 °C	4	3	4	Solvents
200−700 °C	20	20	19	Organic groups
700−1000 °C	-	−	−	Dehydroxylation
−	76	77	77	Residues

Table S 6: Characteristic IR bands of non-modified and differently modified NPSNPs.

| Position (cm⁻¹)	Vibrator	Abbreviation
3000 - 3700	O−H, Si−OH stretching	$v(\text{OH})$
2976	Asymmetric CH$_3$ stretching	$v_{as}(\text{CH}_3)$
2935	Asymmetric CH$_2$ stretching	$v_{as}(\text{CH}_2)$
2854	Symmetric CH$_3$ stretching	$v_s(\text{CH}_3)$
1647	N−H, O−H deformation	$\delta(\text{OH})$, $\delta(\text{NH})$
1560	N−H deformation	$\delta(\text{NH})$
1475	−NH$_3^+$ deformation	$\delta(\text{NH}_3^+)$
1490 - 1325	Asymmetric CH$_2$ deformation	$\delta_{as}(\text{CH}_2)$
1085	Asymmetric Si−O−Si stretching	$v_{as}(\text{Si−O−Si})$
1041	COH deformation	$\delta(\text{COH})$
966	Si−OH and SiO−H stretching	$v(\text{Si−OH})$ and $v(\text{SiO−H})$
800	Symmetric Si−O−Si stretching	$v_s(\text{Si−O−Si})$
688	Symmetric SiO$_4$ stretching	$v_s(\text{SiO}_4)$
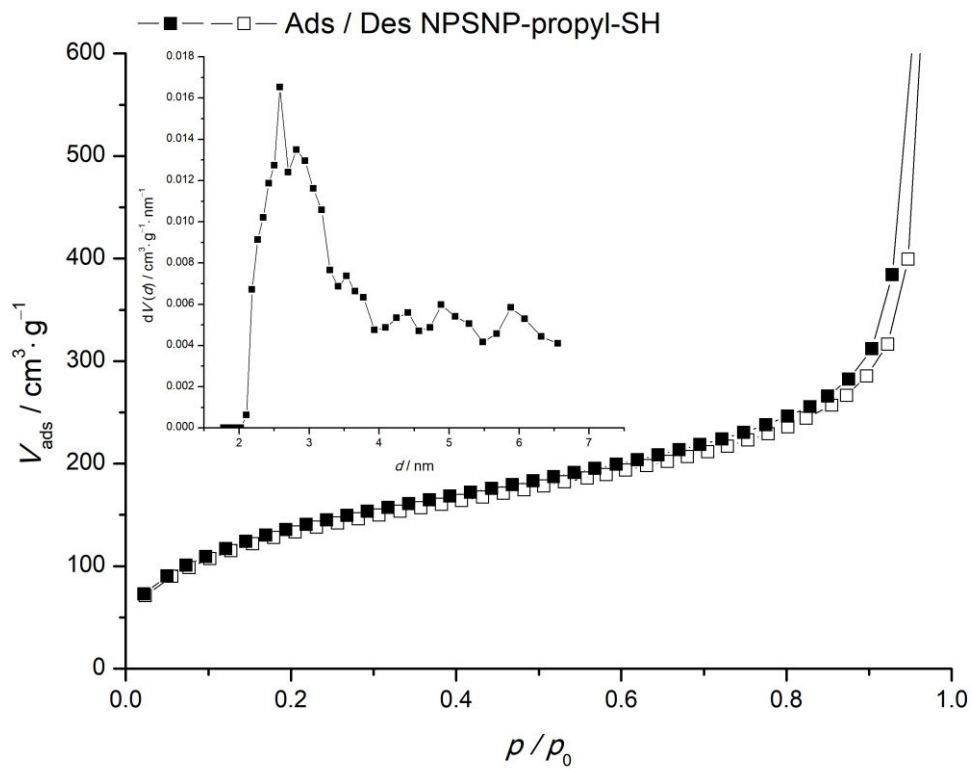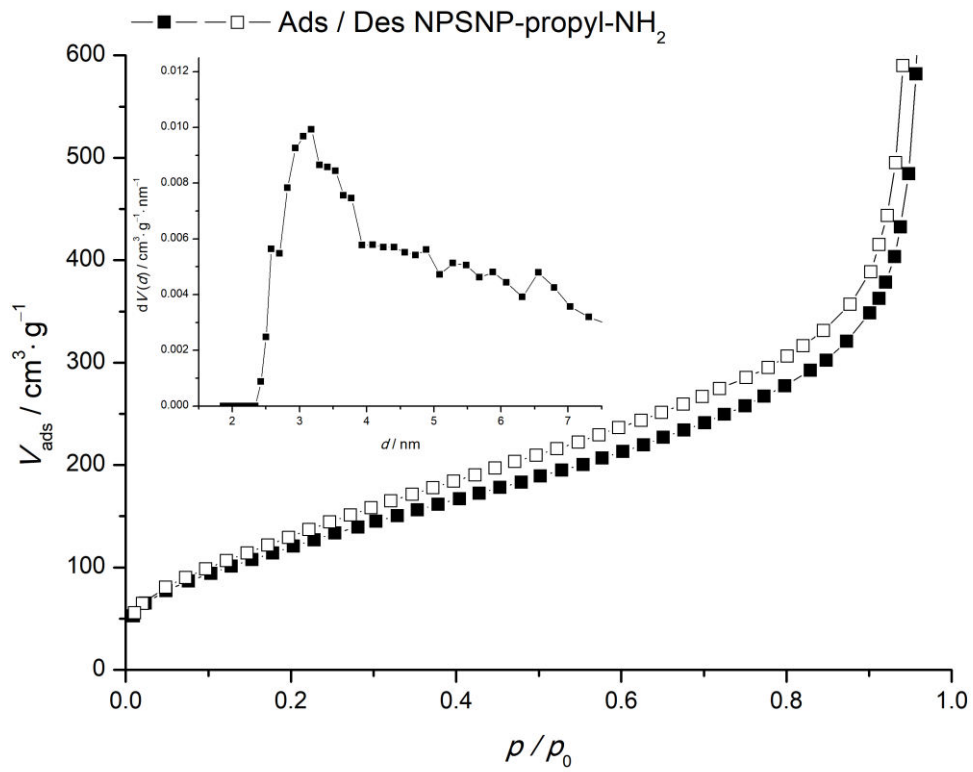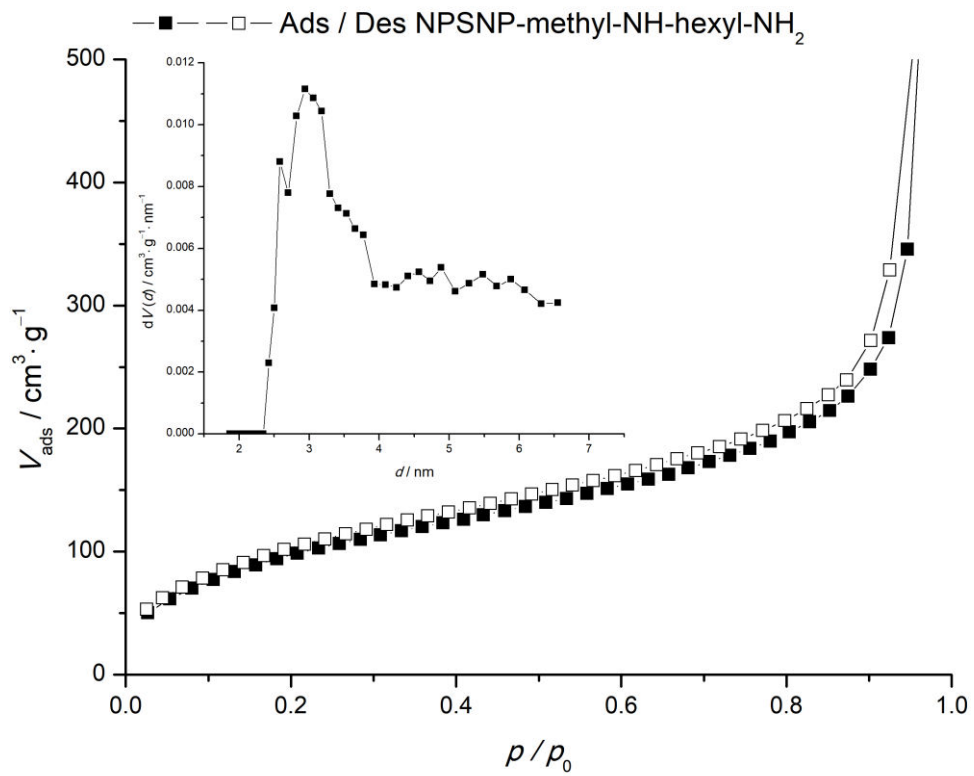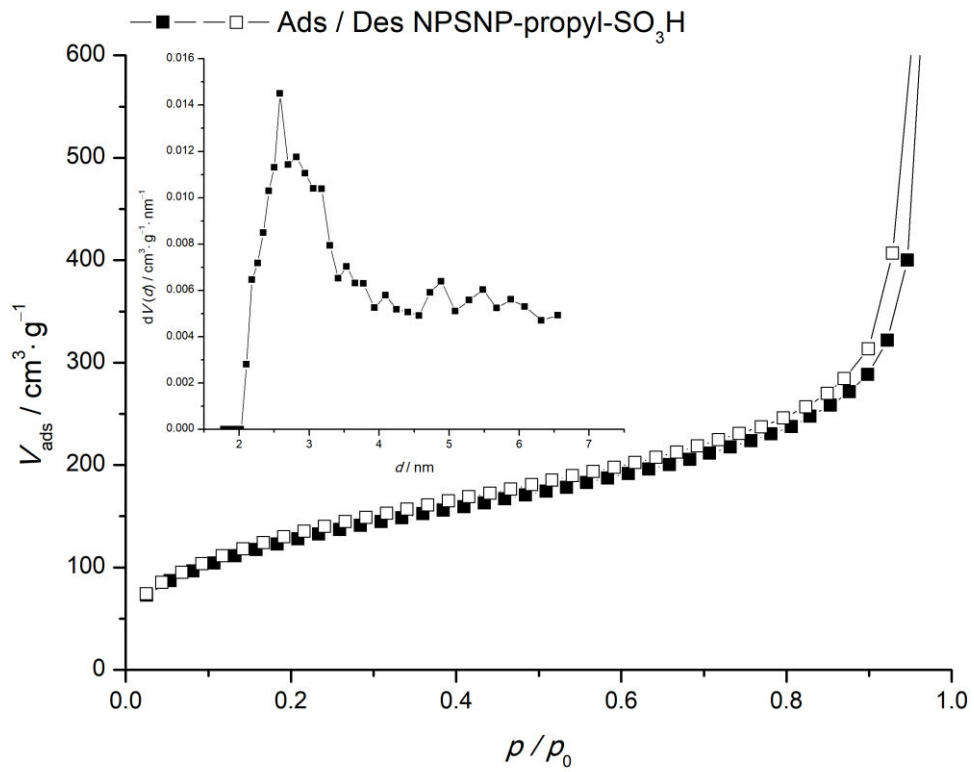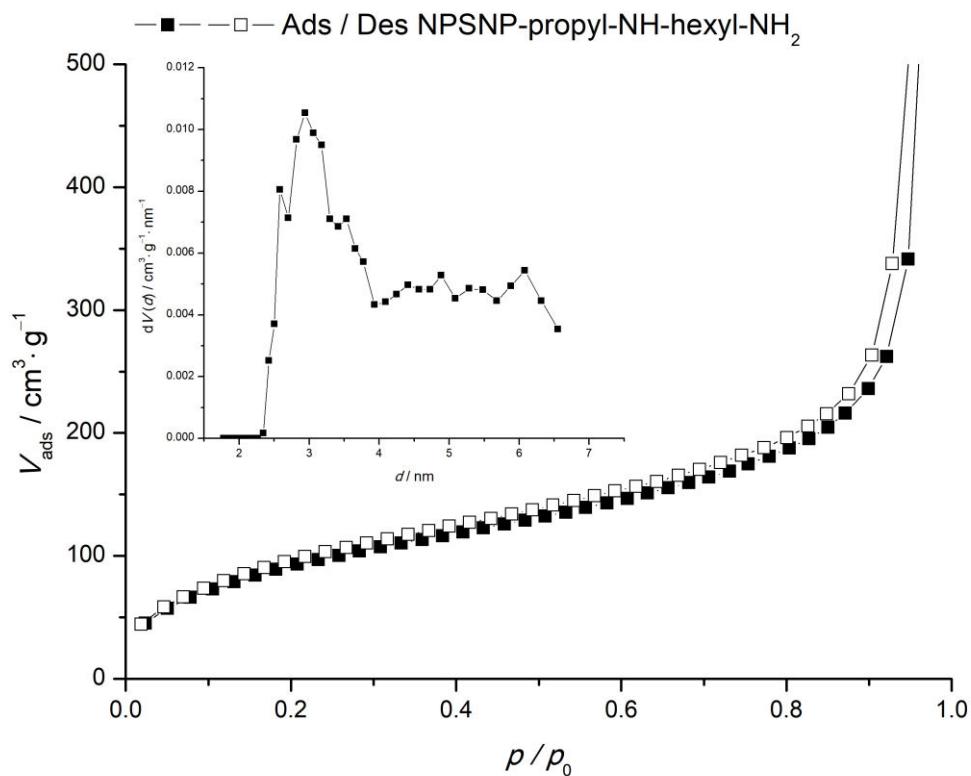
Figure S 2: Nitrogen adsorption-desorption isotherms and correlating pore size distributions according to the DFT theory of differently modified nanoporous silica nanoparticles.
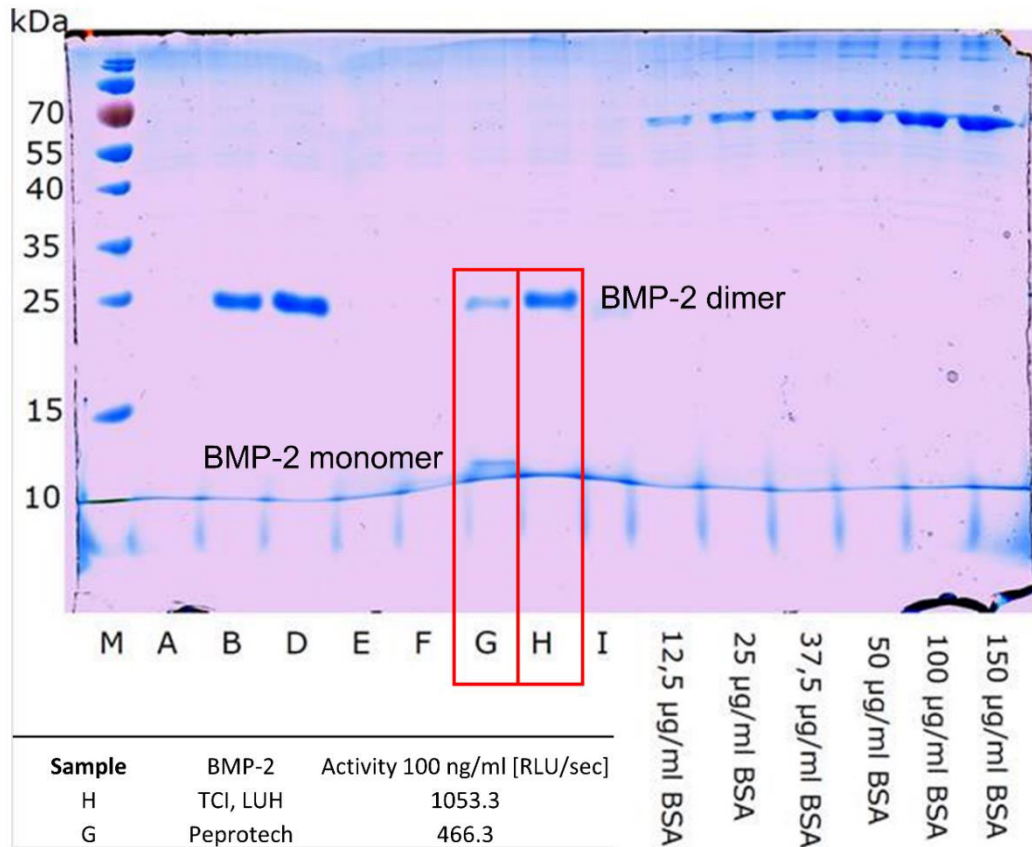
Figure S 3: Results from gel electrophoresis and BRE-Luc assay of E. coli-derived rhBMP-2 purchased from Peprotech (Hamburg, Germany) and provided by the Institut für Technische Chemie, Leibniz Universität Hannover.
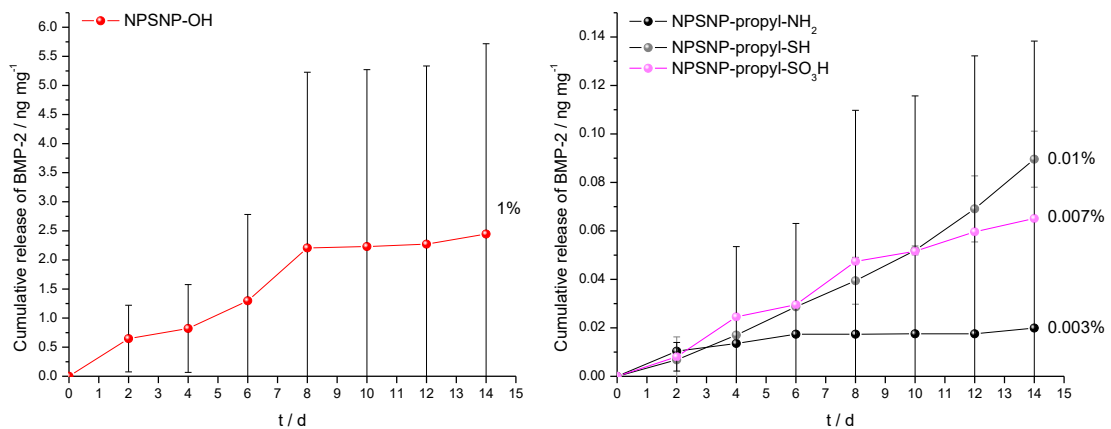

Figure S 4: In vitro release profiles of BMP-2 from the surface of non-modified and differently modified NPSNPs in Soerensen buffer at pH 7.4 and 37 °C as measured by ELISA. The data represent the mean ± standard deviation (n=3).
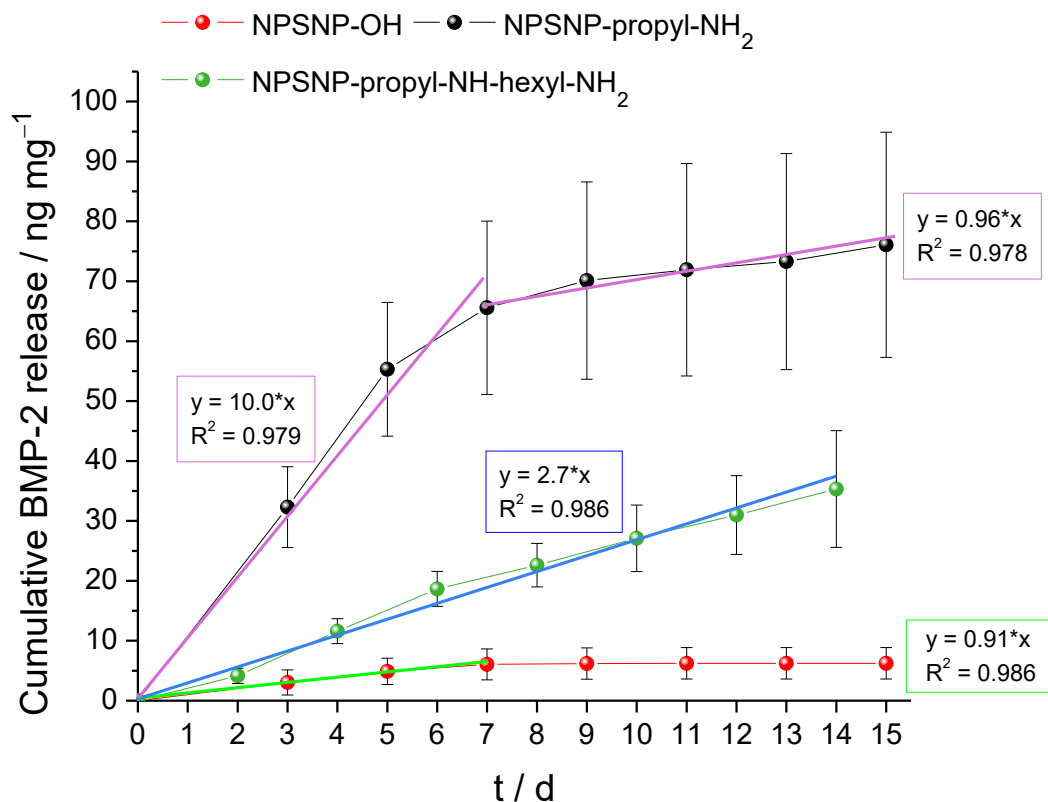
Figure S 5: Release of BMP-2 from NPSNP-OH, -propyl-NH$_2$ and -propyl-NH-hexyl-NH$_2$ as measured by ELISA and fitted by zero-order release kinetics equations.

Table S 7: Measured weight and thickness of the PCL$_{SK-Alg}$ scaffolds with the diameter of 15 mm to roughly estimate the porosity of the scaffolds.

Nr.	Weight / mg	Thickness / mm
1	13.3	0.30
2	13.9	0.34
3	14.5	0.44
4	13.5	0.35
5	14.3	0.40
6	13.5	0.37
7	13.5	0.28
8	13.8	0.33
9	14.7	0.46
10	14.2	0.31
11	13.1	0.42
12	13.5	0.35
13	14.6	0.36

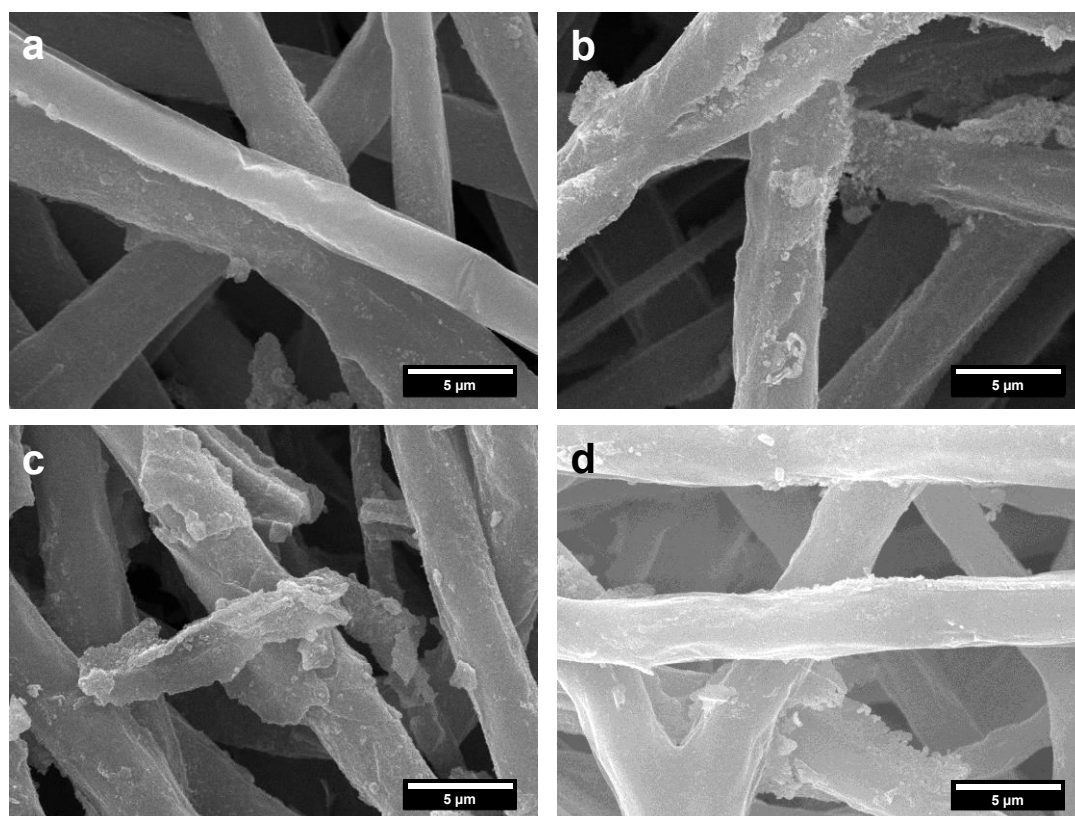| Nr.	Weight / mg	Thickness / mm
14	14.7	0.41
15	13.2	0.25
16	14.3	0.39
17	14.3	0.32
18	12.5	0.29
19	14.1	0.30
20	13.3	0.32
Average	13.84	0.35
Standard deviation	0.61	0.06

Figure S 6: SEM images of PCL$_{SK-Alg}$ fibre mat loaded with NPSNPs bearing propyl-NH$_2$ groups after (a) one week, (b) two weeks, (c) three and (d) five weeks of the immersion into the release medium (PBS, 0.1% BSA and 0.02% Tween 20) at 37 °C.
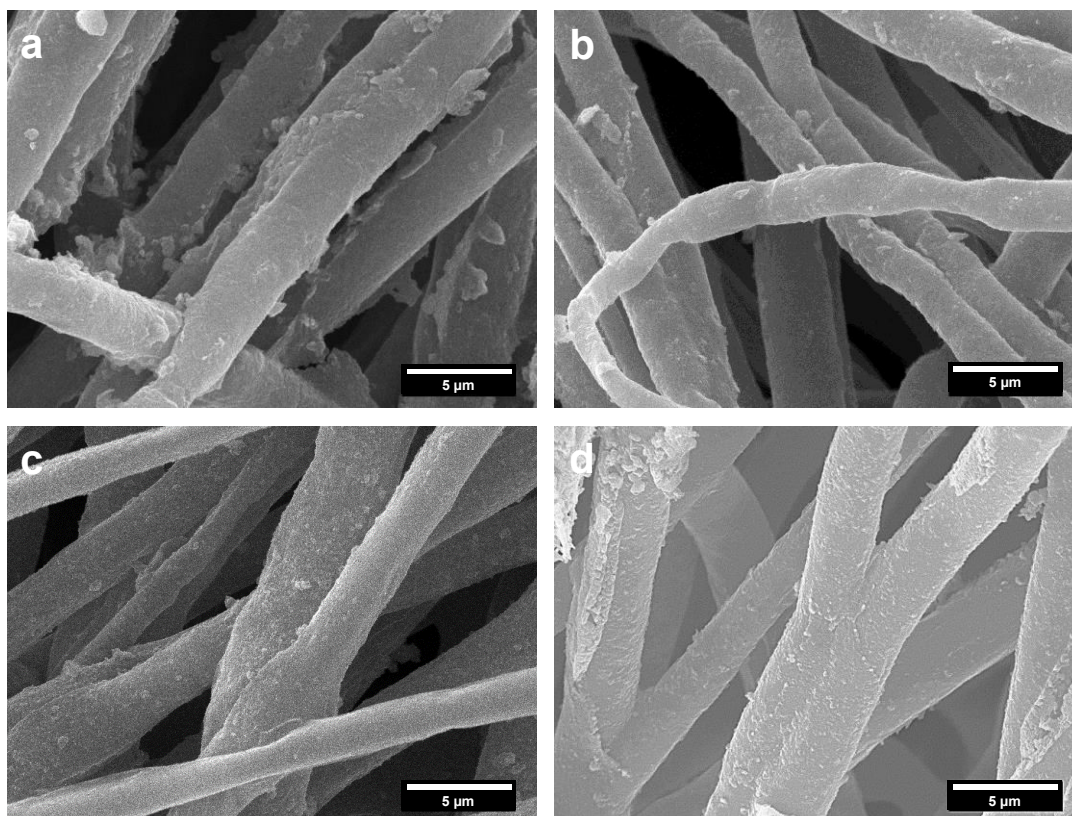
Figure S 7: SEM images of PCL$_{SK-Alg}$ fibre mat loaded with NPSNPs bearing methyl-NH-hexyl-NH$_2$ groups after (a) one week, (b) two weeks, (c) three and (d) five weeks of the immersion into the release medium (PBS, 0.1% BSA and 0.02% Tween 20) at 37 °C.
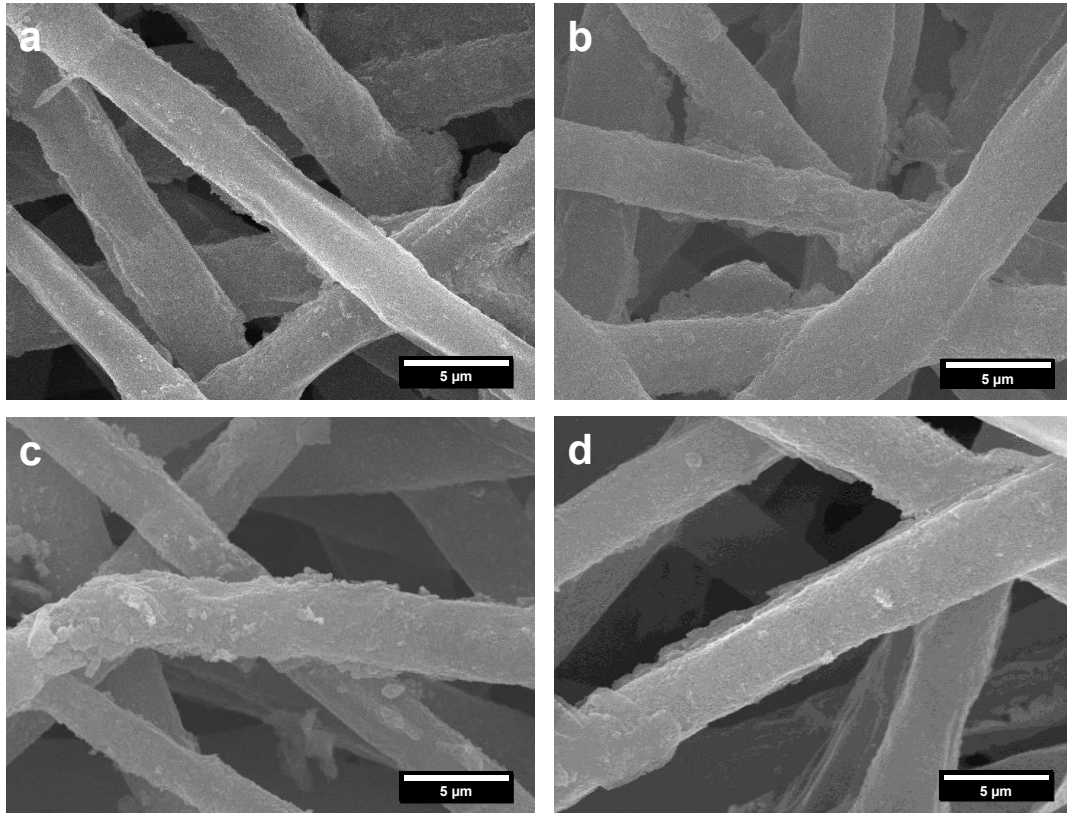
Figure S 8: SEM images of PCL$_{SK-Alg}$ fibre mat loaded with NPSNPs bearing propyl-NH-hexyl-NH$_2$ groups after (a) one week, (b) two weeks, (c) three and (d) five weeks of the immersion into the release medium (PBS, 0.1% BSA and 0.02% Tween 20) at 37 °C.
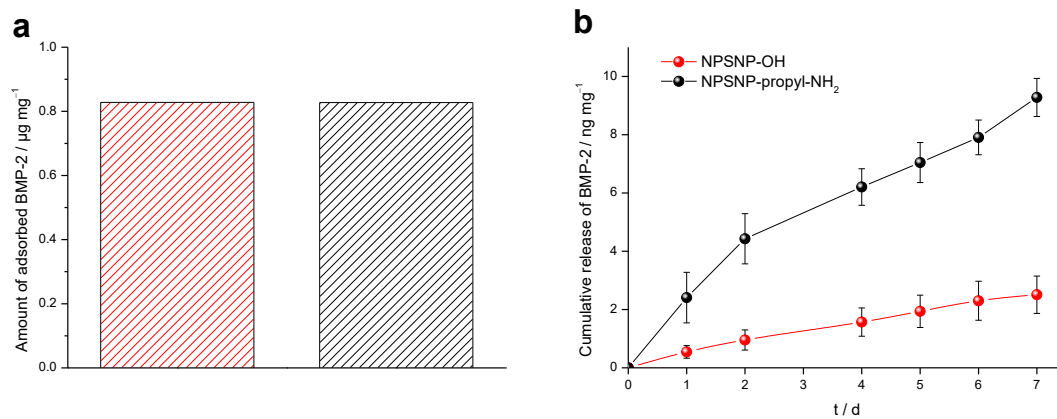

Figure S 9: (a) Amounts of adsobed BMP-2 on the surface of non-modified (red) and aminopropylsilyl-modified (black) NPSNPs and (b) BMP-2 release from NPSNPs derived from the ELISA measurements. As medium PBS and 0.1 % BSA were used. The data represent the mean ± SD (n=3).
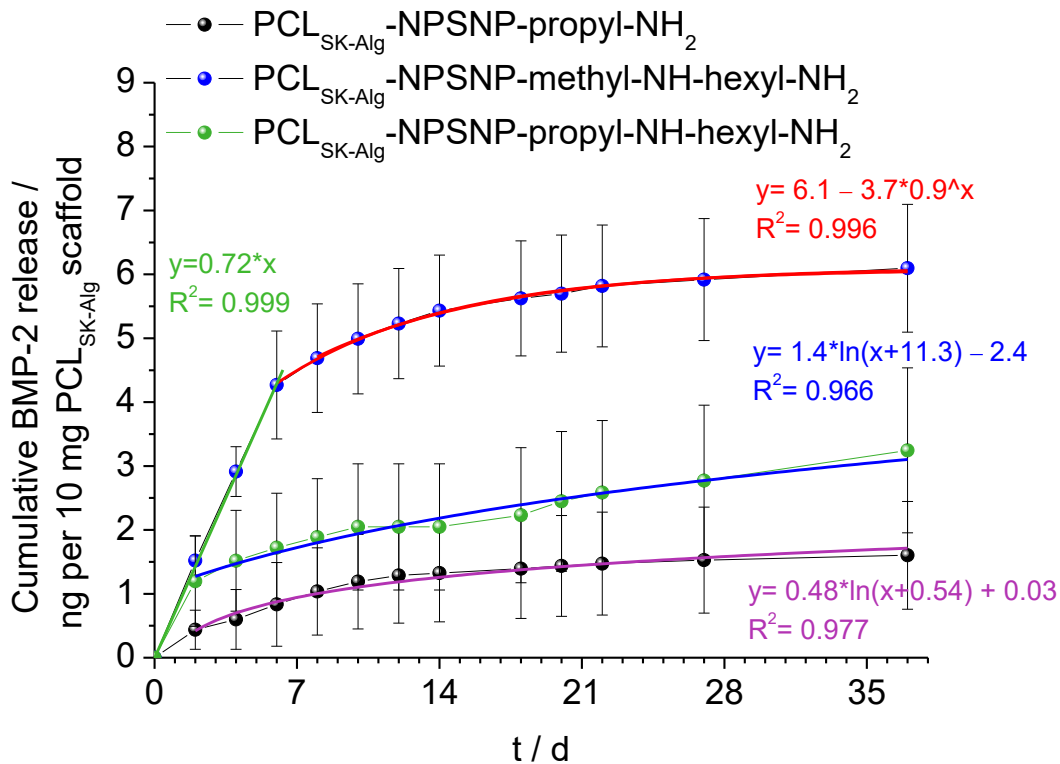
Figure S 10: Release of BMP-2 from the surface of differently modified NPSNPs loaded on PCL$_{SK-Alg}$ scaffolds into PBS, 0.1% bovine serum albumin and 0.02% Tween 20 at pH 7.4 and 37 °C as measured by ELISA. Release profiles from NPSNP-propyl-NH$_2$ and -propyl-NH-hexyl-NH$_2$ were fitted by first-order release kinetics equations. Release curve from NPSNP-methyl-NH-hexyl-NH2 were fitted first by the linear curve followed by fitting the data with an exponential equation.
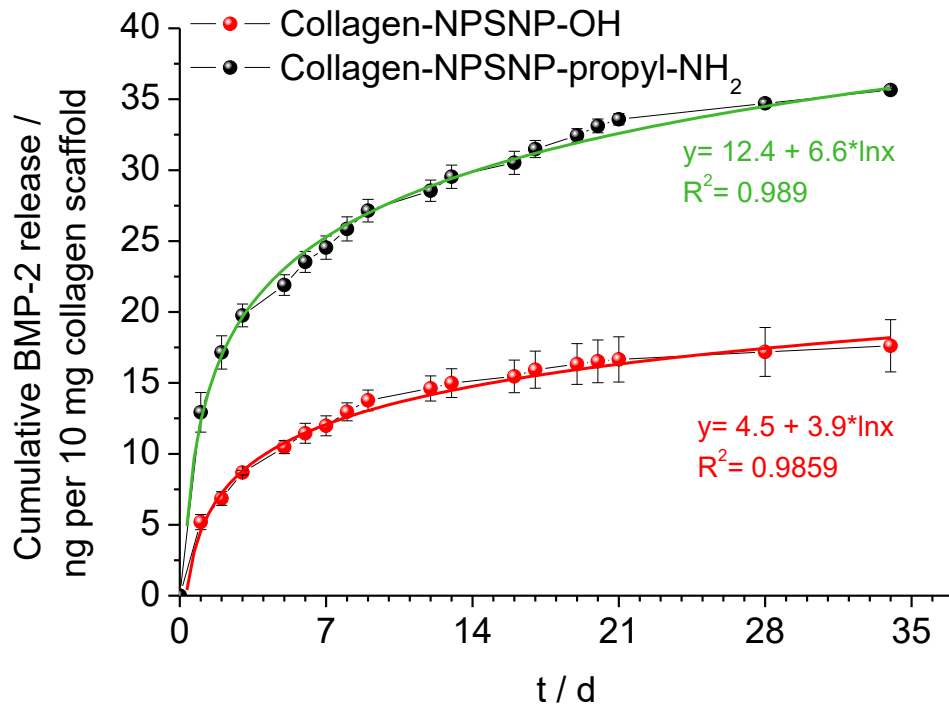
Figure S 11: Release of BMP-2 from collagen-NPSNP-BMP-2 nanocomposites with two different nanoparticles types: non-modified and aminopropylsilyl-modified NPSNPs, as measured by ELISA and fitted by first-order release kinetics equations. Release medium is 2 ml of PBS containing 0.1% bovine serum albumin at pH 7.4 and 37 °C.

Table S 8: Comparison of the released BMP-2 amounts from the PCL_{SK-Alg}- and collagen-NPSNP-BMP-2 nanocomposites derived from the fitting.

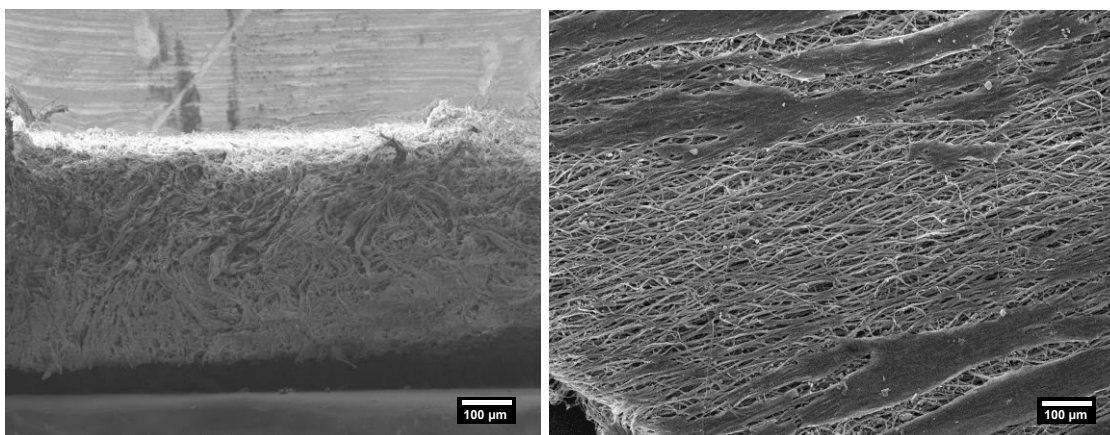| Days	PCL_{SK-Alg}-NPSNP-BMP-2 nanocomposites			Collagen-NPSNP-BMP-2 nanocomposites	
	NPSNP-propyl-NH_2	NPSNP-methyl-NH-hexyl-NH_2	NPSNP-propyl-NH-hexyl-NH_2	NPSNP-OH	NPSNP-propyl-NH_2
$t_{1/4}$	-	2.1 days	-	1.4 days	15 h
First $t_{1/2}$	5.0 days	4.2 days	5.7 days	3 days	2.3 days
Second $t_{1/2}$	12.4 days	7.4 days	18.9 days	9.4 days	8.8 days

Figure S 12: Collagen scaffold (left) and PCL fibre mat after loading with NPSNP-OH and NPSNP-methyl-NH-hexyl-NH$_2$ for 12 h.

8   Appendix

Appendix A Adsorption of BSA and BMP-2 on glass and plastic surfaces

A1 General concept

Proteins in aqueous solution readily adsorb to the most surfaces due to their amphiphilic nature. When the quantification of proteins is needed, protein adsorption to surfaces may lead to inaccurate results of the protein amounts [342]. The addition of bovine serum albumin (BSA) is commonly used to prevent adsorption of the quantified protein. However, for some quantification methods, this approach is not feasible [343].

In this work, bone morphogenetic protein 2 (BMP-2) was adsorbed on the surface of nanoporous silica nanoparticles (NPSNPs). Despite the addition of BSA, BMP-2 could not be accurately quantified. Therefore, we sought to verify whether BMP-2 and BSA were adsorbed on commonly used surfaces such as glass and plastic (polypropylene).

A2 Materials and methods

BMP-2 (Peprotech, Hamburg, Germany) was dissolved in phosphate buffered saline (PBS), pH 7.4 (Sigma Aldrich Chemie GmbH, Munich, Germany) to the final concentration of 5 µg ml^{-1}. In addition, 0.1% and 1% BSA solutions were prepared using PBS, pH 7.4. Glass slides for microscopy, 1x1 cm glass platelets and plastic vessels made of polypropylene were purchased from VWR International GmbH (Darmstadt, Germany).

To investigate the protein adsorption on the surface of glass and plastic, plastic vessels were filled with appropriate protein solutions (BMP-2 or BSA), and the glass slide was placed into the protein solution, as illustrated in Figure A 1. Subsequently, samples were placed into the refrigerator at 4 ° for 24 h. After that, the protein solution was removed, the plastic vessels and glass slides were rinsed with ultrapure water and dried under the nitrogen gas.

Static contact angle measurements were performed on the plastic vessel bottoms and glass slides using a Surftens universal contact angle goniometer (OEG, Frankfurt/Oder, Germany) with water as the probing liquid. On every sample, the contact angle was measured at three different positions.
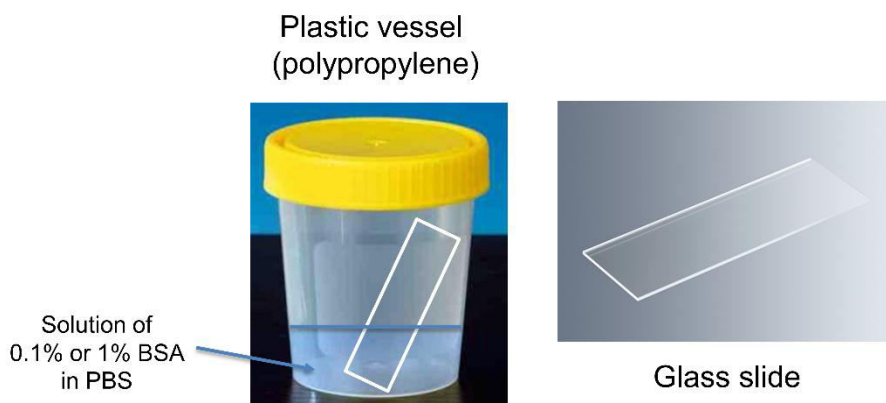
Plastic vessel
(polypropylene)

Solution of
0.1% or 1% BSA
in PBS

Glass slide

Figure A 1: Set up of the experiments.

A3 Results and discussion

To assess protein adsorption on the surface of glass and plastic, BSA was chosen as the model protein. The measured water contact angles on glass and plastic surfaces after immersion into 0.1% and 1% BSA solutions in PBS are demonstrated in Figure A 2. It can be seen that pure glass surfaces revealed a contact angle of about 13 ° evidencing a strongly hydrophilic surface. After the immersion into BSA solutions, the contact angle of the glass increased drastically up to 70 ° and 67 ° for 0.1% and 1% solution, respectively. These results offer compelling evidence for the adsorption of BSA on glass surfaces regardless of the BSA concentration.

In contrast, the water contact angle on the surface of pure plastic was about 78 ° demonstrating hydrophobic properties. After the immersion into the 0.1% BSA solution, no difference in contact angles could be detected pointing to no or very small adsorption of BSA. In case of the immersion into the 1% BSA solution, two different contact angles at 83 ° and 65 ° could be measured indicating a heterogeneous distribution of BSA molecules on the plastic surface.
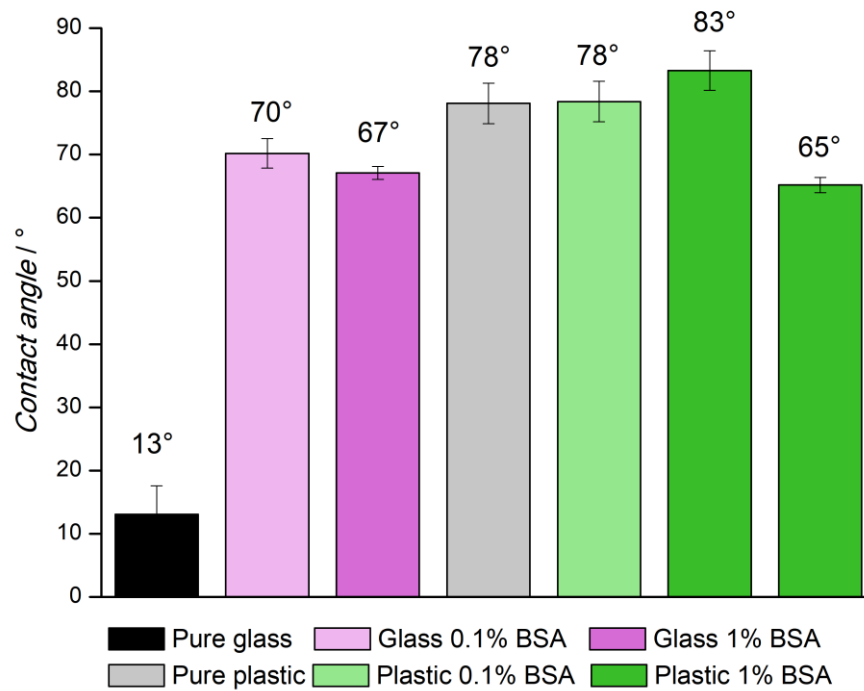
Figure A 2: Water contact angles on glass and plastic surfaces before and after the immersion into 0.1% or 1% BSA in PBS. Results are represented as mean ± standard deviation of triple measurements.

Next, the adsorption of BMP-2 molecules on glass and plastic surfaces was investigated by the contact angle measurements of water (Figure A 3). The contact angle of the glass used in these experiments was around 37 ° indicating a hydrophilic surface. When the glass slides were immersed in PBS only, the water contact angle changed slightly to 35 °. After the immersion into the BMP-2 solution in PBS, the contact angle increased up to 54 ° offering an indisputable evidence of BMP-2 adsorption on the glass surface. In case of the plastic surface, contradictory results were obtained. As shown previously for BSA adsorption, two contact angles were measured here as well, namely 69 ° and 80 °. Therefore, it cannot be ruled out that BMP-2 was adsorbed on the plastic surface.
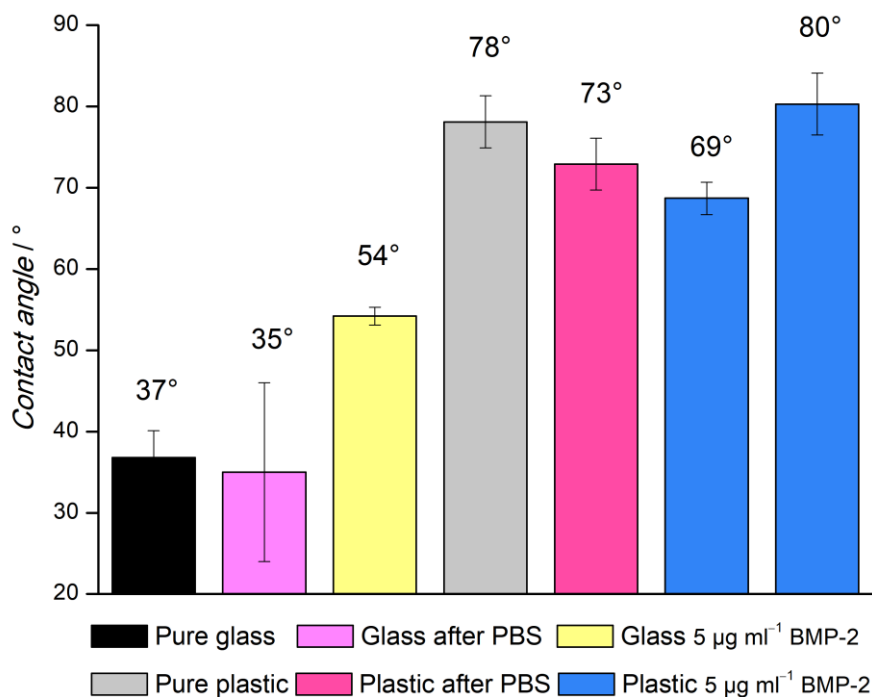
Figure A 3: Water contact angles on glass and plastic surfaces before and after the immersion in PBS or in PBS containing BMP-2 (5 µg ml^{-1}). Results are represented as mean ± standard deviation of triple measurements.

In conclusion, an easy method to verify protein adsorption on glass and plastic surfaces was demonstrated. The results of this study suggest that both BSA and BMP-2 were adsorbed on a glass surface. However, our study was not successful in proving whether BSA and BMP-2 were adsorbed on the plastic surface. Future work will concentrate on that.

Appendix B TEM investigations of BMP-2 and BMP-2-loaded NPSNPs

B1 General concept

Negative staining is a widely used technique to study viruses, purified enzyme, soluble protein molecules, isolated cell organelles etc., by transmission electron microscopy (TEM). The principle of the negative staining is based on that a thin layer of biological material is surrounded, permeated, supported and embedded by a dried thin amorphous layer of heavy metal-containing salt. This layer generates differential electron scattering due to the density differences between the electron-transparent biological material and the electron-opaque stain layer [344].

The most commonly used negative stains are ammonium molybdate, sodium/potassium phosphotungstate and uranyl acetate/formate. These negative stains commonly used as 1 wt.% or 2 wt.% in aqueous solutions. However, uranyl acetate/formate solutions are toxic and radioactive and therefore, were not used in the present study. A protective carbohydrate such as trehalose can be added to the negative stain solution creating a thicker layer of the stain and protecting biological sample during the drying process. For preliminary TEM assessments of biological materials air-drying is often used.

B2 Materials and methods

Ammonium molybdate, 99.98%; phosphotungstic acid, reagent grade; trehalose, for molecular biology; were purchased from Sigma-Aldrich Chemie GmbH (Munich, Germany) and used without further purification.

Cu grids with continuous carbon film and anti-adhesive forceps to hold the Cu grids were purchased from Plano GmbH (Wetzlar, Germany).

For visualization of soluble BMP-2 molecules and BMP-2 on the surface of non-modified NPSNPs, single-droplet negative staining technique was used according to [345]. Transmission electron microscopy (TEM) images were taken using TEM Tecnai G2 F20 TMP from FEI (Oregon, USA) operating at 200 kV.

B2.1 Applied protocol

Following aqueous negative staining solutions were prepared and used to stain BMP-2and BMP-2-loaded NPSNPs:

-5 wt.% ammonium molybdate / phosphotungstic acid with 0.1 wt.% and 1 wt.% trehalose

-2 wt.% and 1 wt.% ammonium molybdate / phosphotungstic acid

Before applying the sample to the Cu grids, the grids were not glow discharged, as recommended. Instead, they were placed into a convection oven at 70 °C for 12 h to remove adsorbed water.

A The non-modified NPSNPs with adsorbed BMP-2 (40 ng mg^{-1}) were dispersed in a MES buffer at pH 5.

B 2 µl of dispersed sample were placed on the shiny site of the Cu grid. The sample was allowed to stay there for 1 minute. The droplet was removed by touching the edge of the grid to a filter paper edge.

C On a piece of PARAFILM® M, 2 droplets of water and one droplet of the staining solution (20 µl) were placed.

D The grid with previously adsorbed sample was washed subsequently with these 2 water droplet by touching them with the site of the grid, where the sample was applied.

E The excessed water was removed each time by blotting the grid on the filter paper.

F At the last step, the grid touched the droplet with the appropriate staining solution for about 20 s. After that, the grid was blot on the filter paper to remove the excess of the solution.

G The grid was allowed to dry on the air for about 5 mins, before it was stored in a small plastic container for TEM grids.

H TEM images were taken next day.

B3 Results and discussion

B3.1 Negative staining of BMP-2

BMP-2 samples (concentration 5 µg ml^{-1}, in MES buffer at pH 5) were stained with 2 wt.% phosphotungstic acid. In Figure B 1, the best TEM images are presented probably showing a BMP-2 aggregate. The white spots might show BMP-2 dimers. However, the images should be interpreted with caution. To this point, no TEM images of BMP-2 molecules have been reported yet. In general, the chosen BMP-2 concentration was probably too low for this experiment.
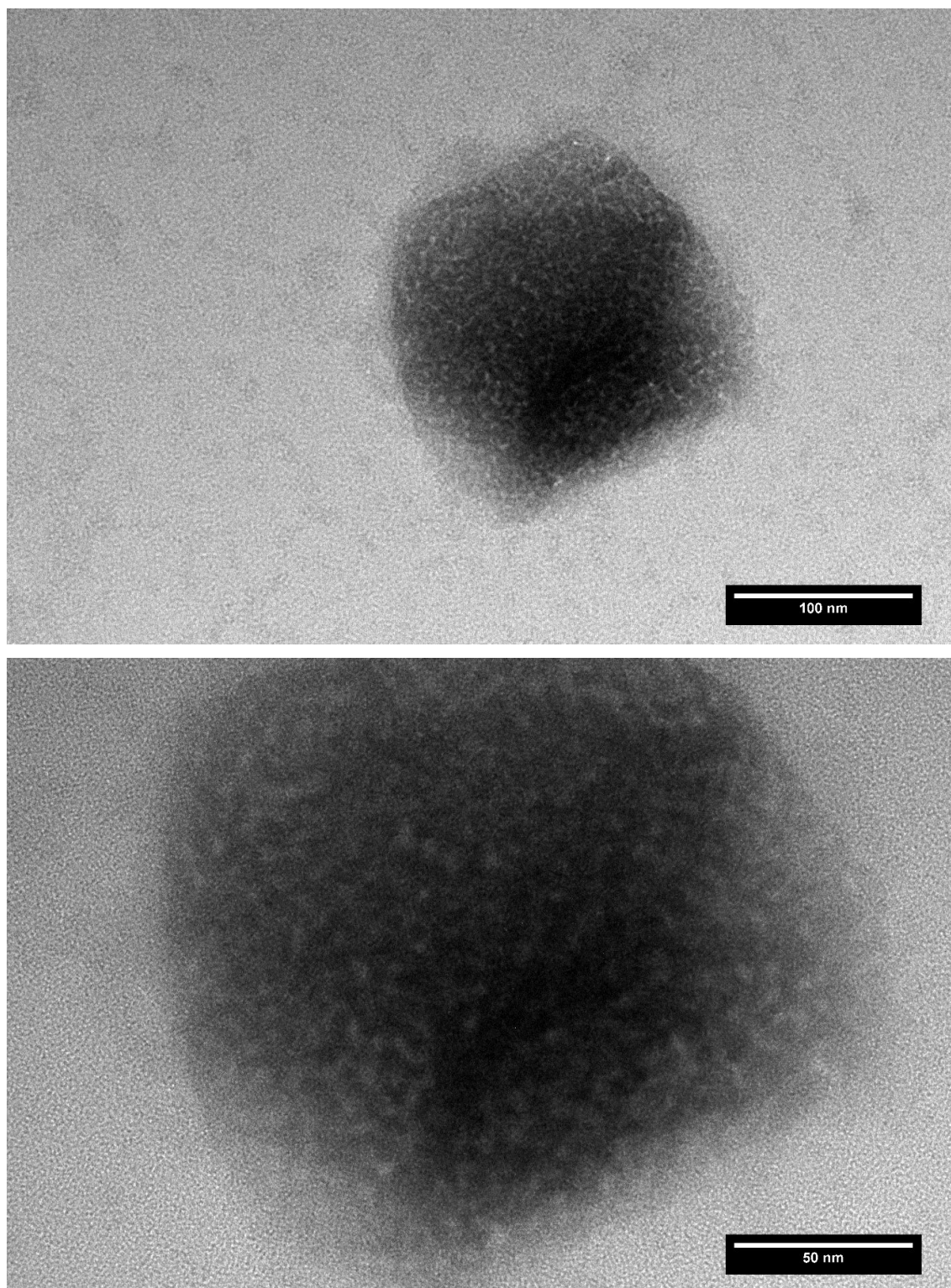
Figure B 1: TEM images of BMP-2 stained with 2 wt.% phosphotungstic acid.

B3.2 Negative staining of BMP-2-loaded NPSNPs with ammonium molybdate

On TEM image of BMP-2-loaded NPSNPs stained with 5 wt.% ammonium molybdate with 1 wt.% trehalose, no white spots of BMP-2 were observed (Figure B 2).
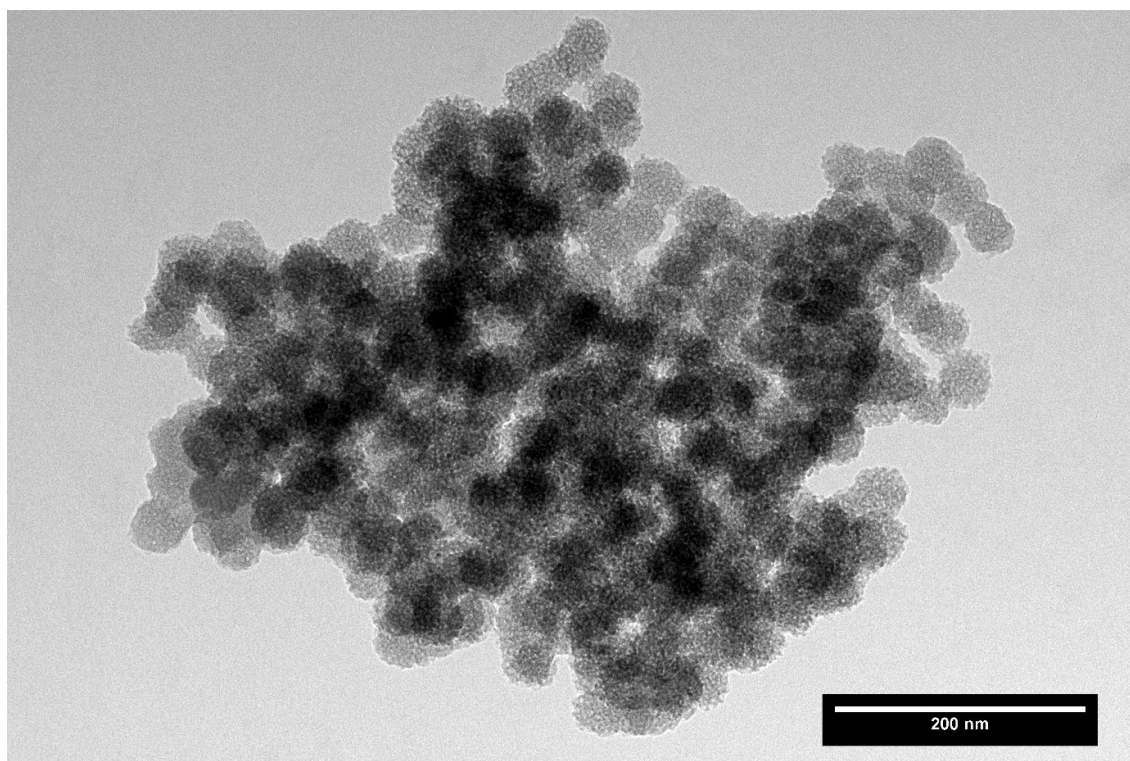
Figure B 2: TEM image of BMP-2 loaded on non-modified NPSNPs stained with 5 wt.% ammonium molybdate with 1 wt.% trehalose.

On the TEM image of BMP-2-loaded NPSNPs stained with 5 wt.% ammonium molybdate with 0.1 wt.% trehalose, white spots on the surface of the particles could be observed (Figure B 3). These might be BMP-2 dimers. However, in this sample the electron beam was burning away organic residues and thus, the focused spot on the sample became black very fast.
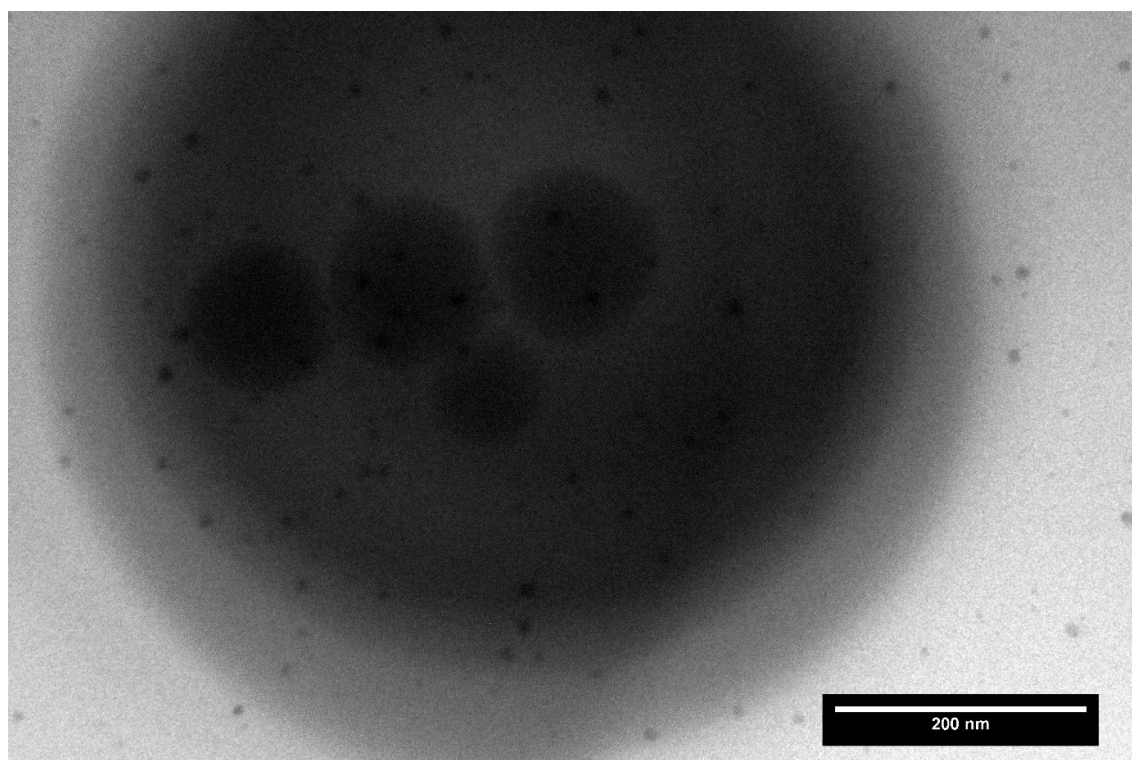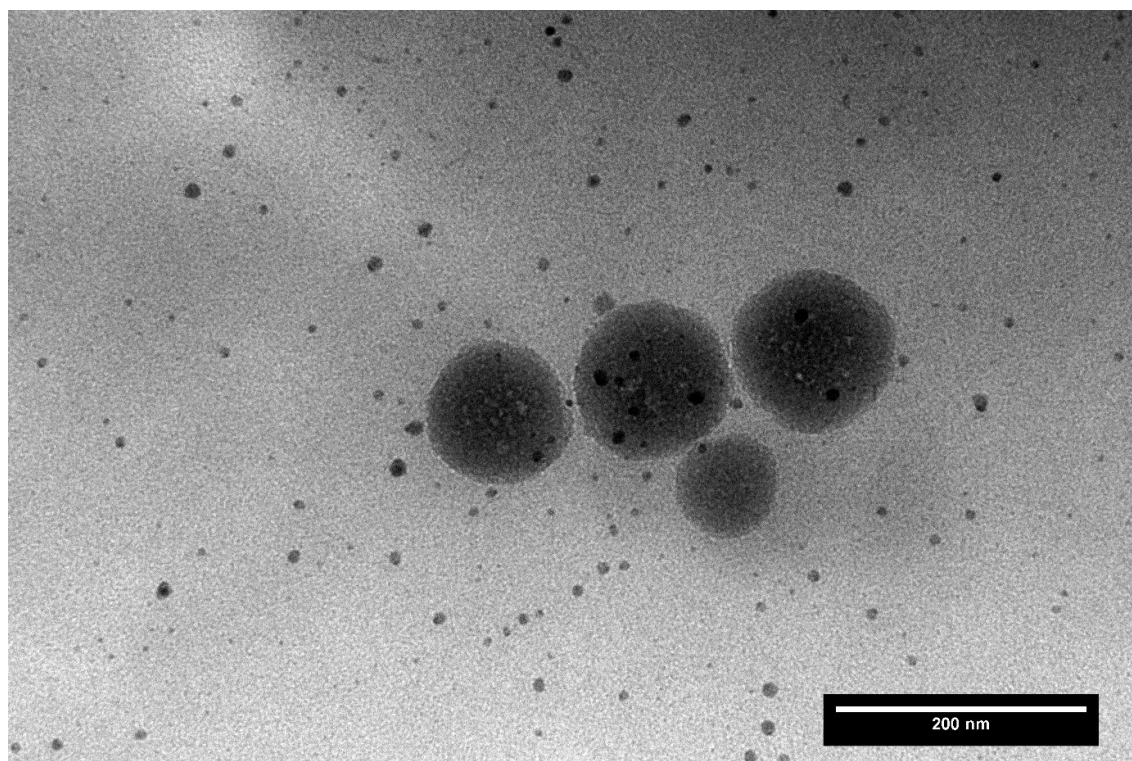
Figure B 3: TEM image of BMP-2 loaded on non-modified NPSNPs stained with 5 wt.% ammonium molybdate with 0.1 wt.% trehalose.

Samples of BMP-2 loaded on non-modified NPSNPs stained with 2 wt.% and 1 wt.% ammonium molybdate were of low contrast (Figure B 4).
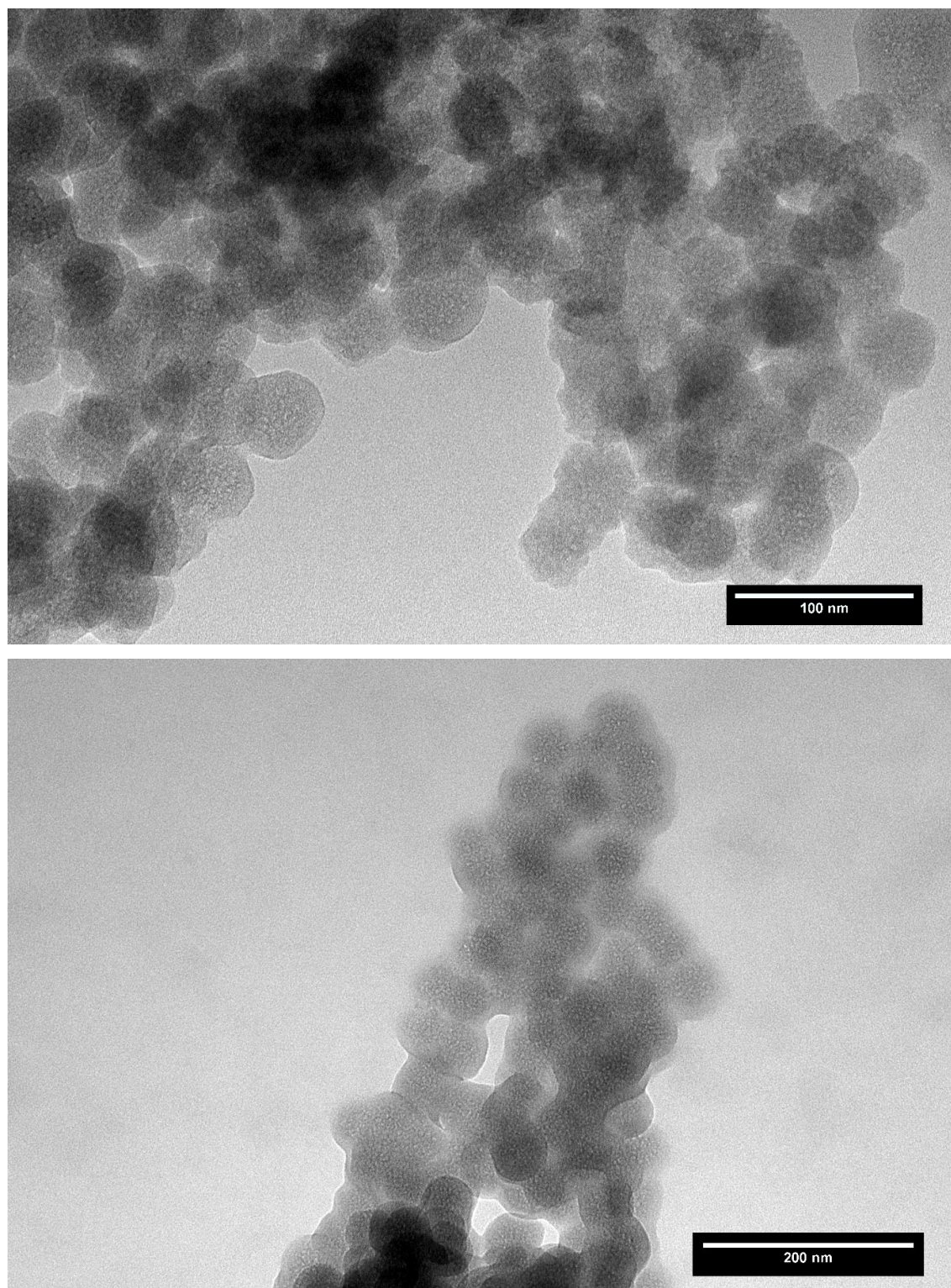
Figure B 4: TEM image of BMP-2 loaded on non-modified NPSNPs stained with 2 wt.% (upper image) and 1 wt.% (lower image) ammonium molybdate.

B3.3 Negative staining of BMP-2-loaded NPSNPs with phosphotungstic acid

TEM images with the high contrast could be obtained by staining BMP-2-loaded NPSNPs with phosphotungstic acid (Figure B 5 and 6). In addition, on the surface of the silica nanoparticles white spots could be observed (Figure B 6, lower image). These spots can

be an indication of either the adsorbed BMP-2 or the nanopores of silica nanoparticles. Unfortunately, this could not be clarified at this point.
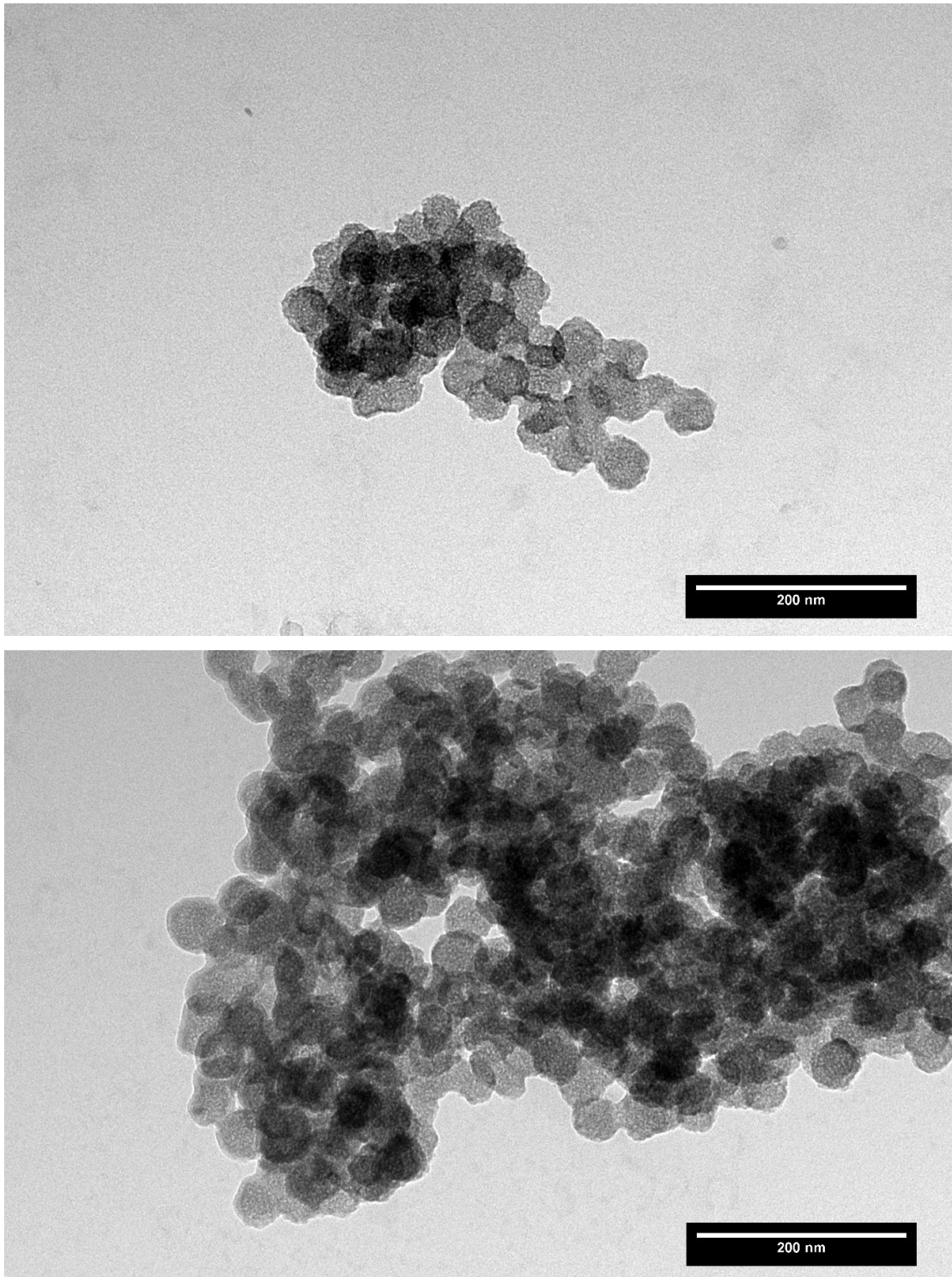

Figure B 5: TEM image of BMP-2 loaded on non-modified NPSNPs stained with 5 wt.% phosphotungstic acid with 1 wt.% (upper image) and 0.1 wt.% (lower image) trehalose.
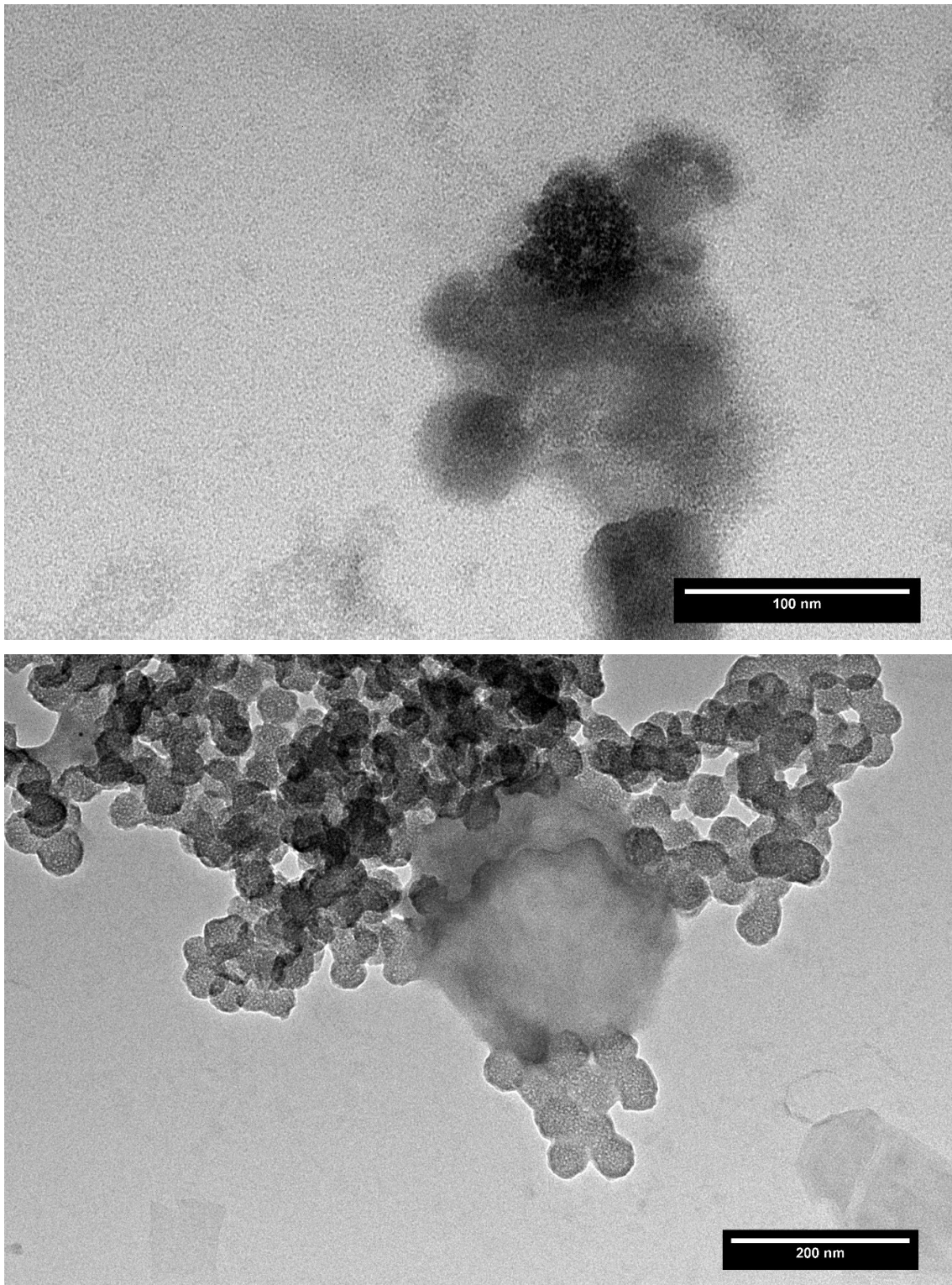
Figure B 6: TEM image of BMP-2 loaded on non-modified NPSNPs stained with 2 wt.% (upper image) and 1 wt.% (lower image) phosphotungstic acid.

Taken together, it can be stated that the TEM images of BMP-2 containing samples stained with phosphotungstic acid with or without trehalose provided images with higher contrast than those stained with ammonium molybdate. However, BMP-2 molecules could not be clearly seen on the surface of nanoporous silica nanoparticles. In addition, BMP-2 can be easily mistaken with the nanopores of NPSNPs appearing as white spots.

The conditions to obtain best-quality, high-resolution TEM images were not optimal and need to be enhanced. For example, instead of air-drying the samples after application on TEM grid, they can be frozen in liquid nitrogen and analysed by cryo-TEM under low electron dose conditions. In addition, in this preliminary study, no reference samples (NPSNPs without BMP-2) were analysed by TEM. Further studies, which take this into account, will need to be performed.

Appendix C Labelling of BMP-2 with a fluorescent dye

C1 General concept

In this study, we sought an alternative method for BMP-2 quantification. By means of BMP-2 labelling with a fluorescent dye, BMP-2 amounts that were adsorbed on the surface of non-modified NPSNPs and subsequently released into the medium were determined by using fluorescence spectrometry.

C2 Materials and methods

First, BMP-2 (Peprotech, Hamburg, Germany) was labelled with the fluorescent dye Alexa Fluor® 488 (tetrafluorophenyl) TFP ester using Alexa Fluor ® 488 Microscale Protein Labelling Kit (A30006) purchased from Thermo Fisher Scientific (Waltham, USA) (Figure C1). Here, 20 µg of lyophilized BMP-2 was dissolved in 20 µl PBS to a final concentration of 1 mg ml^{-1}. The labelling procedure was performed according to manufacturer's instructions. BMP-2 concentration before and after labelling was determined using NanoDrop 2000c (Thermo Fisher Scientific) at 280 nm.
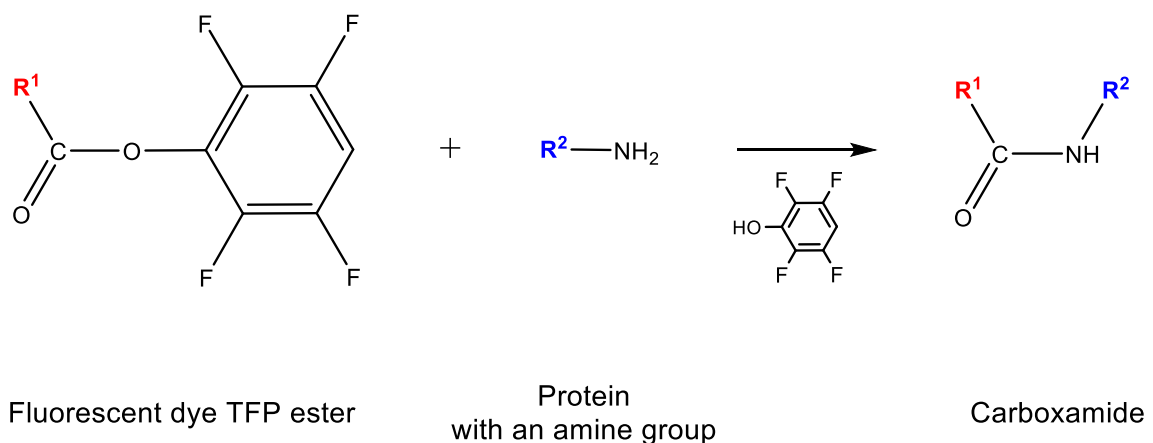

Fluorescent dye TFP ester   Protein with an amine group   Carboxamide

Figure C 1: Schematic illustration of the labelling of a protein with a fluorescent dye TFP ester.

Non-modified NPSNPs (5 mg) were suspended in 0.05 ml of PBS under ultrasound treatment for 10 mins using a VWR Ultrasonic Cleaner (45 kHz, 60 W). After that 0.05 ml of a fluorescent BMP-2 solution (60 µg ml^{-1}) in PBS was added to the particle dispersion, and the mixture was shaken at 350 rpm and 7 °C for 24 h in a thermomixer (Biozym Scientific GmbH, Germany) to produce BMP-2-loaded NPSNPs. Then, the BMP-2 loaded NPSNPs were separated by centrifugation, washed three times with fresh PBS and used for the subsequent release experiments. The supernatant and washing solutions for collected for BMP-2 quantification. Taken together, 3 µg of BMP-2 were offered for loading on the surface of 5 mg NPSNPs resulting in the theoretically adsorbed BMP-2 amount of 0.6 µg BMP-2 per 1 mg NPSNPs (0.6 µg mg^{-1}).

The release of the fluorescent BMP-2 was carried out with the previously BMP-2-loaded NPSNPs suspended in 0.1 ml of sterile-filtered PBS with 0.1% BSA and at 37 °C in a convection oven for a period of 10 days under aseptic conditions. At each time point, 100 µl of the supernatant was removed. The collected supernatant was replaced by 100 µl of the fresh PBS with 0.1% BSA. In general, BMP-2 amounts in the supernatants and washing solutions were quantified on the one hand, by ELISA (Peprotech, Hamburg, Germany) according to the manufacturer's instructions and on the other hand, by SPARK® fluorescence plate reader (Tecan Group ltd., Männedorf, Switzerland). For fluorescence spectrometry, the excitation and emission wavelengths were at 485 nm and 520 nm, respectively.

In addition, the photostability of the dye-labelled BMP-2 in PBS buffer was observed. For that, 100 µl of the fluorescent BMP-2 solution (30 µg ml^{-1}) was placed in a convection oven at 37 °C for a period of 10 days. At certain time points, the fluorescence intensity of the sample was measured using SPARK® fluorescence plate reader.

C3 Results and discussion

The theoretical BMP-2 concentration should be around 1 mg ml^{-1}. The actual concentration of BMP-2 was determined spectrophotometrically at 280 nm of about 0.23 mg ml^{-1} before the labelling procedure. After the labelling and purification step, a concentration of only 0.06 mg ml^{-1} could be quantified. We believe that these results provide a strong evidence for precipitation of BMP-2 in PBS resulting in decreased BMP-2 amount. The degree of labelling (DOL= mole dye/mole protein) was calculated to 1.3, which was optimal for BMP-2 molecules.

The initial dye-labelled BMP-2 amount and BMP-2 content in the supernatant and washing solutions after the loading on non-modified NPSNPs were determined by the fluorescence spectrometry and ELISA measurements (Figure C 2).
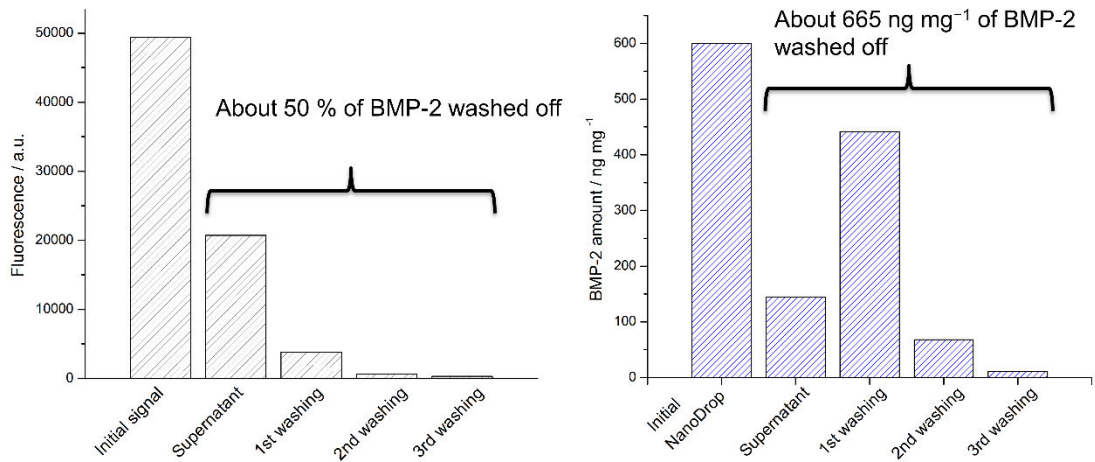
Figure C 2: Amounts of BMP-2 measured by fluorescence plate reader (left) and ELISA (right).

The results obtained from the fluorescence and ELISA measurements significantly differ from each other. While fluorescence measurements suggest that about 50% of initial BMP-2 is still present in the supernatant and washing solutions, ELISA measurements show that the entire BMP-2 could be washed off the surface of non-modified NPSNPs. There is no plausible explanation for the disagreement of these results. However, based on the results derived from ELISA and BRE-Luc assay from the main part of the thesis showing only low loading capacity of BMP-2 on non-modified NPSNPs, we hypothesize that the results obtained from ELISA are more reliable than those obtained from fluorescence measurements.

The released BMP-2 amounts determined by fluorescence and ELISA measurements were not in good agreement as well (Figure C 3).
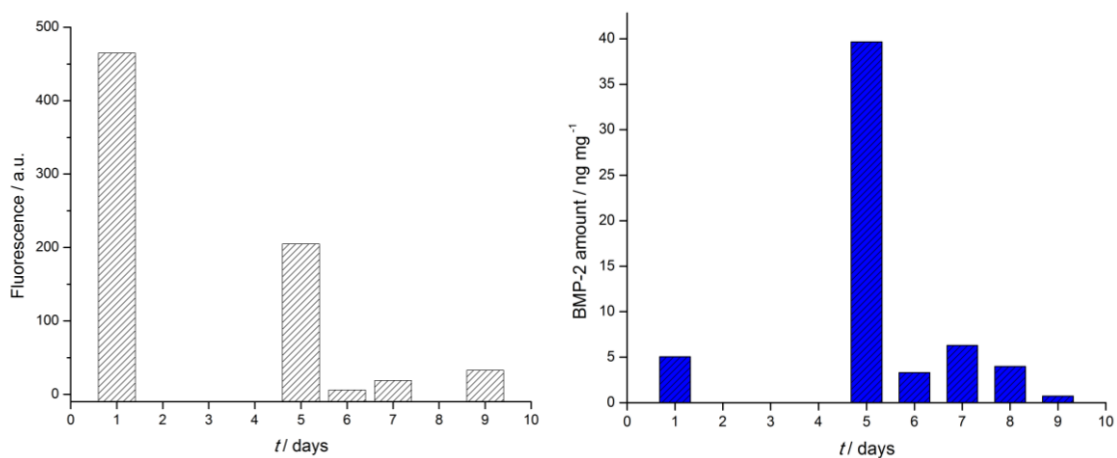

Figure C 3: Release BMP-2 amounts measured by fluorescence plate reader (left) and ELISA (right).

The photostability of the fluorescent BMP-2 over a period of 9 days was verified by fluorescence measurements (Figure C 4). The fluorescence intensity of the sample decreased over time evidencing low photostability of the Alexa Fluor 488 dye in PBS.
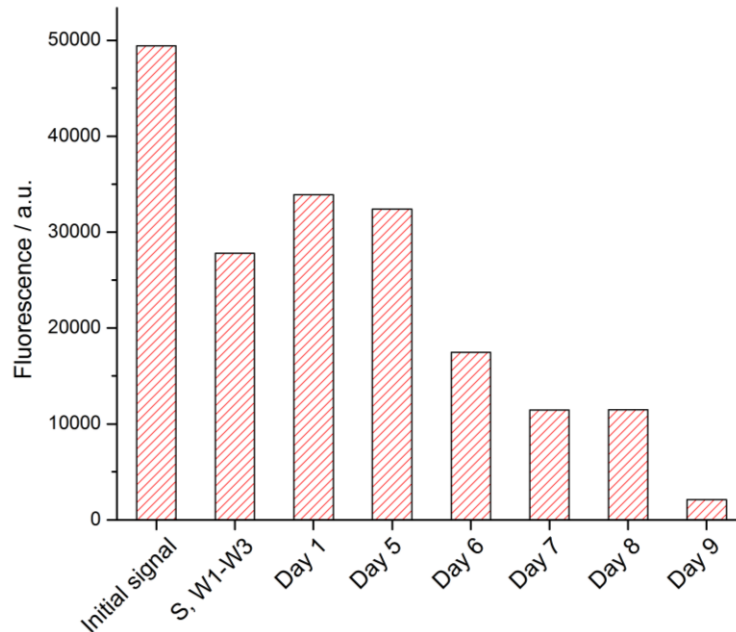

Figure C 4: Results of the photostability of the dye-labelled BMP-2 in PBS over a period of 9 days.

Taken together, we showed a successful labelling of BMP-2 with a fluorescent dye. However, due to the special requirements and conditions of the labelling such as the usage of a highly concentrated BMP-2 solution in PBS and purification step, 75% of the initial BMP-2 was lost after the procedure. In addition, we demonstrated disadvantages of dye-labelled BMP-2 quantification by fluorescence measurements. This method seems to be not suitable for quantification of released BMP-2 due to the fast photobleaching of the fluorescent dye in PBS. We propose that future labelling attempts should be performed with BMP-2 dissolved in an appropriate buffer such as MES or MOPS. In addition, the fluorescence intensity of dye-labelled BMP-2 adsorbed on NPSNPs should be measured rather than the dye-labelled protein in solution.

9   List of publications

<u>Publication</u>

S. Springer, **A. Satalov**, J. Lippke, M. Wiebcke, Microporous Mesoporous Mater, **2015**, *216*, 161-170.

<u>Conference contributions</u>

Abstract publication

A. Satalov, P. Behrens, Eur Cell Mater, **2016**, 32, Suppl. 5, 116.

Oral poster presentations

A. Satalov, M. Steindorff, E. Gellermann, H. Hartwig, M. Stiesch, P. Behrens, *„Multifunctionalized nanoporous silica nanoparticles for tooth regeneration"*, **2014**, 48. Tagung der Deutschen Gesellschaft für Biomedizinische Technik, Hannover, Germany.

A. Satalov, M. Steindorff, E. Gellermann, H. Hartwig, A. Winkel, M. Stiesch, P. Behrens, *„Sustained Release of Bone Morphogenetic Protein 2 (BMP-2) from Nanoporous Silica Nanoparticles for Tooth Regeneration"*, International Symposium Biofabrication and I$_4$A, **2015**, Hannover, Germany.

A. Satalov, M. Steindorff, E. Gellermann, H. Hartwig, A. Winkel, M. Stiesch, P. Behrens, *„Sustained release of bone morphogenetic protein 2 (BMP-2) from nanoporous silica nanoparticles and collagen matrices for tooth regeneration",* **2015**, Jahrestagung der Deutschen Gesellschaft für Biomaterialien e.V., Freiburg, Germany.

A. Satalov, P. Behrens, *"Novel delivery system of bone morphogenetic protein 2 (BMP-2) from nanoporous silica nanoparticles and collagen matrices for bone and tooth regeneration"*, **2016**, Jahrestagung der Deutschen Gesellschaft für Biomaterialien e.V., Aachen, Germany.

Poster presentations

A. Satalov, M. Steindorff, E. Gellermann, H. Hartwig, M. Stiesch, P. Behrens, *„Multifunctionalized nanoporous silica nanoparticles for tooth regeneration"*, **2014**, Biofabrication Retreat, Hannover, Germany.

A. Satalov, M. Steindorff, E. Gellermann, H. Hartwig, M. Stiesch, P. Behrens, *"Biocomposites for Tooth Regeneration based on Collagen Matrix, Nanoporous Silica Nanoparticles and Bone Morphogenetic Protein 2 (BMP-2)"*, **2014**, Deutsch-französisch-polnisches Symposium, French Embassy, Berlin, Germany.

A. Satalov, M. Steindorff, E. Gellermann, H. Hartwig, A. Winkel, M. Stiesch, P. Behrens, "*Biocomposites for Tooth Regeneration based on Collagen Matrix, Nanoporous Silica Nanoparticles and Bone Morphogenetic Proteins (BMPs)*", **2015**, Euro BioMAT, Weimar, Germany.

A. Satalov, M. Steindorff, E. Gellermann, H. Hartwig, A. Winkel, M. Stiesch, P. Behrens, „*Sustained release of bone morphogenetic protein 2 (BMP-2) from nanoporous silica nanoparticles and collagen matrices for tooth regeneration*", **2015**, Nanoday, LNQE, Hannover, Germany.

A. Satalov, P. Behrens, "*Novel Delivery System of Bone Morphogenetic Protein 2 (BMP-2) based on Nanoporous Silica Nanoparticles and Collagen Matrices for Bone and Tooth Regeneration*", **2016**, Biointerfaces International, Zürich, Switzerland.

A. Satalov, M. Jahns, K. Nolte, L. Burmeister, A. Hoffmann, P. Behrens, „*Surface modification of nanoporous silica nanoparticles to enhance non-covalent protein binding*", **2017**, 29. Deutsche Zeolith Tagung, Frankfurt am Main, Germany.

10 Curriculum Vitae

Name	Alexandra Satalov
Date of birth	25.06.1988
Place of birth	Aktjubinsk, Kazakhstan

<u>Education</u>

Feb. 2014 – Sept. 2017	Doctor thesis within interdisciplinary research consortium "Biofabrication for NIFE", Institut für Anorganische Chemie, Leibniz Universität Hannover, Germany
March 2013 – June 2013	Visiting scholar at the Institute for Superconducting and Electronic Materials (ISEM), Wollongong, Australia Research: Engineering of advanced cathode materials for Li-ion batteries
Jan. 2013 – March 2013	Research intern at the Institute of Material Science, Leibniz Universität Hannover, Germany Research: Investigations on coated and uncoated spheroidal graphite cast iron samples by means of impedance measurements
Dec. 2010 – Feb. 2013	Research assistant at the Institute of Material Science, Leibniz Universität Hannover, Germany
Oct. 2011 – Jan. 2013	Master of Science, Material and Nano chemistry, Institut für Anorganische Chemie, Leibniz Universität Hannover, Germany Title: "Composites based on natural polymers, nanoporous silica nanoparticles and bioactive molecules for biomedical applications"
Oct. 2008 – July 2011	Bachelor of Science, Chemistry, Institut für Anorganische Chemie, Leibniz Universität Hannover, Germany Title: "Synthesis of nanoscale Mg-Al-LDHs and characterization of their dissolution behaviour"
Aug. 2005 – June 2008	Abitur, Scharnhorst Gymnasium, Hildesheim, Germany
Jan. 2004 – June 2005	St. Augustinus Haupt- und Realschule, Hildesheim, Germany
Sept. 1994 – Dec. 2003	Comprehensive school, Kazakhstan